DIRECT LASER MICRO-FABRICATION BY ADAPTIVE OPTICS

Bangshan Sun

Jesus College

Trinity Term 2015

A thesis submitted for the degree of Doctor of Philosophy
at the University of Oxford

Direct Laser Micro-fabrication by Adaptive Optics

Submitted for the degree of *Doctor of Philosophy*

Bangshan Sun, Jesus College, Trinity Term 2015

Ultrafast lasers are widely used for the precise three-dimensional micro-fabrication inside transparent materials. The resolution of fabricated features depends upon the size of the focal spot, and the process efficiency depends upon the generation of short pulses at the focus. The performance is detrimentally affected by the presence of phase aberrations, which can be introduced by the optics of the system or by refraction at the surface of material. Efficiency can also be affected by other forms of aberration that are related to the ultra-short pulses, such as pulse front distortion or material dispersion.

Adaptive optics has in the past been introduced into laser material processing in order to overcome the problems caused by phase aberrations. However, there are related phenomena specific to systems using ultrashort pulses that have not been extensively studied, nor have benefitted from the application of adaptive optics. This thesis concerns the development of theoretical and practical techniques to address these issues and improve the performance of laser fabrication system. New applications are enabled with this technology.

Spatiotemporal modelling of laser focal intensity distribution is enabled by adopting the Fourier optics. The effects of phase aberrations and sample dispersion on the ultrafast laser focusing are studied in detail. Simulations for both conventional and temporal laser focusing methods are presented. I explore the significance of individual aberration and sample dispersion to investigate the benefit of their compensation in various practical scenarios.

A new method in controlling the ultrafast laser pulses - pulse front adaptive optics - is introduced. With the combination of a deformable mirror (DM) and a spatial light modulator (SLM), quadratic shape pulse fronts with different magnitudes are created. The results are demonstrated through wave-front sensor and auto-correlator measurements. In addition, I introduce the first application of this method into the pulse front correction for an two-photon microscope. An improvement of 1.4 times in the two-photon signal beyond the phase correction is demonstrated.

A series of new applications are enabled by adopting the adaptive optics into laser fabrication. In the adaptive laser fabrication in diamond, graphitic wires with any three-dimensional shapes are enabled. The resistivity of the wires is demonstrated to be reduced by more than 100 times compared to the previous reports. Non-reciprocal effects in the diamond fabrication are studied in detail. The influence of laser parameters, light polarization and pulse front tilt are investigated. I also explore several more advanced applications in the diamond fabrication. Specifically, initial results of the alternating conductor, micro-capacitor and electrode arrays for radiation detector are presented. Additionally, I discuss micro-fabrication of three-dimensional funnel structures in silica glass for applications in neuroscience research.

Acknowledgement

I am most indebted to my DPhil supervisor Professor Martin J. Booth, and my research guider Dr. Patrick S. Salter for their solid support and full responsibility in every aspect of my DPhil research. I cannot forget the time when I started my DPhil program, they always kept great patience in guiding me into this new research field. They explained to me all the relevant background knowledge and trained me the necessary experimental skills step by step. When I started my research, they tried every possible way to provide me the best apparatus and all the supports. When I encountered research problems, they always promptly found time and discussed with me, offering as many as possible solutions. Most valuably, each time when I was frustrated by the terrible results and started to question my research, they always kept patient, spent plenty of valuable time to encourage me in every possible way. Among all the things, I consider their instruction and encouragement as the most precious gifts I received in my DPhil study. It is a pride of my whole life that I can complete my DPhil study under their supervision !

Taking this opportunity, I also would like to thank my Jesus college advisor, Prof. Steve Morris, for the inspiring chats, his support and encouragement to my DPhil study. Thank Dr. Simon Tuohy in the assistance of my experiments, especially in preparing the two-photon fluorescence dye solution and various optical components. Thank Dr. Alexander Corbett in providing the autocorrelator for my experimental research of pulse front correction. Thank Dr. Brian Patton in providing generous and constructive suggestions in my research, especially in the diamond fabrication. I would like to thank the previous and current people in Dynamic Optics and Photonics Group: Dr. Daniel Burke, Dr. Maria Frade Rodriguez, Dr. Jun Guan, Leilei Huang, Dr. Debora Andrade, Dr. Mirella Koleva, Dr. Bei Li, Dr Iris Choi, Dr. Mantas Zurauskas and Xiang Liu. Without the friendship of our research group, the time spent in the lab should be less enjoyable.

I am also very grateful for the colleagues who are doing the research in the related area elsewhere. I am truly grateful to Grahame Faulkner and Dr. Crisanto Quintana Sanchez in providing the micropositioner rigs for the measurement of resistance in the graphitic wires.

Many thanks to Sharlayne Waller and Dr. Julian George in the help of glass etching and SEM imaging. Thank Steven Murphy and Dr. Alexander Oh in providing the diamond sample and idea of graphitic detectors. Thank Prof. Jason Smith for his constructive advices in my research of diamond micro-fabrication.

I would like to thank my supervisor Prof. Martin Booth again, and the Leverhulme Trust in providing me sufficient funding to cover stipend and the oversea student fees. This solid funding support gave me the chance to have my full concentration on the DPhil research. I always understand that a full support of oversea student fees is a rare case, and the only thing I can do to return back is to try my best to achieve the most outstanding research progress.

Finally, and always, I am truely thankful to my family - my parents and my sister. Even though they are not in UK, they keep providing me the warmest home for my heart. They are always making their best to support my study and career. They help me back to the best life and working status each time I experience emotional distortion. If without their help, I cannot even imagine how my life and study of DPhil would become.

Contents

Chapter 1

Ultrafast laser material processing and adaptive optics

Ultrafast lasers have been widely used in many research applications. One specific application that is attracting increasing interest is laser processing of micrometre-scale structures in transparent materials. Strong confinement of the laser focus in space and time creates various nonlinear optical effects that produce permanent modification to specific areas inside the material. Research in the field of lab-on-a-chip, telecommunications, quantum physics and material science has been enabled by such laser material processing methods. In laser focusing systems, aberrations are generated from inherent imperfections in the optical system or through interaction of the light with the material. This thesis describes investigation into these effects and the practical compensation of various focal distortions. Applications in laser material processing with adaptive optical correction are subsequently presented. In this first chapter of the thesis, I provide a brief introduction to the related background knowledge. The nature of ultrashort laser pulses, development of laser material processing and the principle of adaptive optics are discussed. The structure of the whole thesis is outlined at the end of this chapter.

1.1 Ultrashort laser pulses

1.1.1 CW and ultrafast lasers

The light emitted from continuous wave (CW) lasers has constant amplitude in infinite time duration. The CW lasers usually have narrow wavelength bandwidth. In the past, the spectral regions for CW lasers were usually covered by laser dyes, which may be excited by argon ion lasers, krypton ion lasers, Nd: YAG laser and its harmonics. Those dyes usually provided broad coverage for the visible spectrum. For longer wavelengths such as the infrared region, the development of tunable solid-state media greatly extended the spectral coverage for CW lasers.

On the other hand, with a mode-locking process [1], ultrafast lasers have a limited time duration for each laser pulse. The first ultrafast laser was a helium-neon laser built in 1964 with nanosecond pulses [2]. The development of ultrafast lasers can be roughly summarized into three generations [1, 3]. The first generation included mostly lamp-pumped solid-state lasers or gas lasers. They were mode-locked to generate pulses of tens of picoseconds duration. The second generation was engendered by the demonstration of the CW dye laser [4,5]. The strong gain/absorption saturation of dyes created pulses down to sub-picosecond time duration [5]. The third generation was the demonstration of the soliton laser [6]. The advanced mode-locking techniques were used to produce femtosecond pulses. One important example was the application of Ti: sapphire as a broadly tunable laser medium. The advancement of ultrafast laser in the future may be to develop new broadband gain media, increase the range of tunable spectrum (such as the advancement of liquid crystal lasers [7–9]), increase the robustness and reduce costs.

Several key parameters of the ultrafast lasers are: pulse duration, bandwidth and peak power. Among all the applications, the picosecond and femtosecond ultrashort lasers pulses are mostly adopted. They are used in different situations and there is no point to decide which one is better or easier to make. The bandwidth which characterizes the laser in spectral domain is related to the pulse duration which characterizes the laser in time domain. Their relationship is expressed by the one dimensional Fourier transform which will be discussed later. Ultrafast

lasers have much higher peak intensity than CW lasers. Considering a 100 mW output laser with 1 ps pulse duration and 1 MHz repetition rate, the pulse energy is calculated to be 100 nJ. It is then easy to calculate that the peak power of the ultrashort laser pulse is 100 kW. One can see how the mode-locking process significantly increases the peak power for ultrafast lasers.

To describe ultra-short laser pulses, the terms of "phase front" and "pulse front" are usually used. "Phase front" is sometimes called the "wave front". It represents the contour of constant phase across the laser pulse. In contrast, "pulse front" represents the contour of constant intensity in space and time.

1.1.2 Mode-locking process

An ultrafast laser consists of an optical cavity, inside which there is a material called gain medium [10]. With the way of stimulated emission by pumping energy, light of a specific wavelength that passes through the gain medium is amplified (increases in power). The optical cavity also consists of a pair of mirrors on either end of the gain medium. Light bounces back and forth between the mirrors, passing through the gain medium and being amplified each time. One of the mirrors is partially transparent, so that this allows some of the light escape in each round propagation through the cavity.

In general, a laser transition has a finite line width over which it can provide optical gain, and so laser emission has a finite spectral bandwidth $\Delta\upsilon$ [1, 11]. As shown in Figure 1.1, $\Delta\upsilon$ is usually defined as the FWHM of the Gaussian curve. Inside the laser cavity, the radiation of the laser light is presented as discrete frequencies, which are also called the "modes". The frequency difference between each modes is represented as $\delta\upsilon$. It is sometimes called the mode-spacing, which is decided by the round-trip time inside the cavity. The $\delta\upsilon$ can be calculated as,

$$\delta\upsilon = \frac{1}{T_{RT}} = \frac{c}{2L} \tag{1.1}$$

where T_{RT} is the cavity round-trip time, c is the speed of light and L is the optical length of the cavity.

If there is no control for the laser spectrum, the free-running laser modes oscillate independently with random phases [1]. The purpose to introduce the mode-locking is to produce

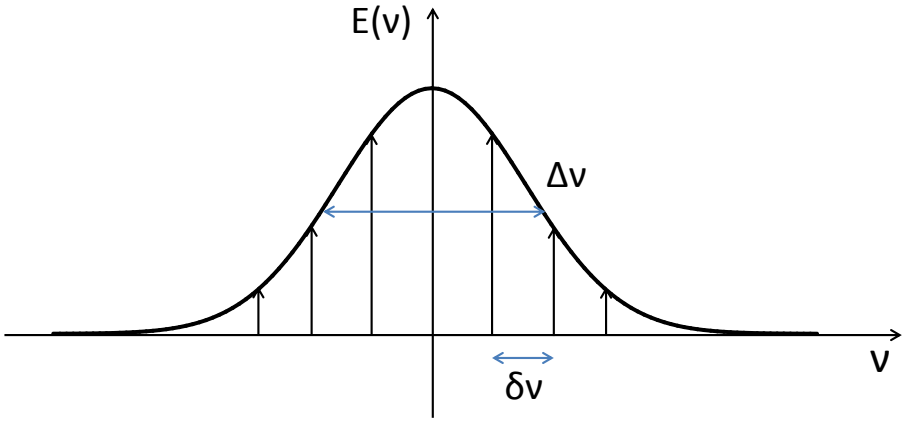

Figure 1.1: Schematic of laser emission in spectral domain. Each mode is represented as the perpendicular arrows, with a mode-spacing of $\delta\upsilon$.

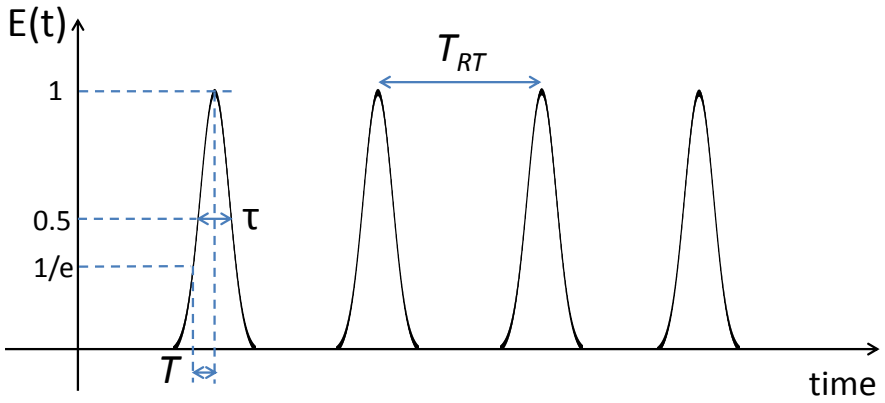

Figure 1.2: Schematic of mode-locked laser pulses emission in temporal domain. The period of the laser output T_{RT} is corresponding to the cavity round-trip time. Pulse duration τ is defined as the FWHM (full width at half maximum) of the temporal curve. Pulse width T is defined as the time when intensity of the light dropped to $1/e$ of the peak. Details of τ and T are discussed in Chapter 2.

the laser pulses which have a well determined phase profile with all of the energy confined to the time interval, corresponding to the resolution desired. With mode-locking, all the modes of the laser can be made to oscillate in phase (locked together). The temporal profile of this kind of mode-locked laser is shown in Figure 1.2. As the laser output becomes temporally well defined, the period of the laser output T_{RT} is corresponding to the cavity round-trip time, which is,

$$T_{RT} = \frac{2L}{c} \tag{1.2}$$

When all the modes are oscillating with a correct phase relationship between each other,

the laser output is described as “transform-limited”. In this situation, the bandwidth and pulse duration of the pulses are equal to a constant.

There are generally two kinds of mode-locking techniques [11,12], which are active mode-locking and passive mode-locking. In the active mode-locking, the radiation in the laser cavity is modulated by a signal derived from an external clock source. The time from the clock source is matched to the cavity round trip time. In the passive mode-locking, the laser radiation itself generates a modulation through the action of a non-linear device in the laser cavity. This modulation is thus automatically synchronized to the cavity round-trip frequency and requires no external clock signal. Passive mode-locking is often referred to as self-mode-locking.

Active mode-locking has a requirement to match the laser cavity length to the modulator drive frequency. With the additional weakness of the pulse compression mechanism, active mode-locking is only sufficient to generate picosecond pulses. Therefore, passive mode-locking method is more generally used. In the experiments described in this thesis, the laser source was a Newport Spectra Physics Ti: sapphire with 100 fs pulse duration and 790 nm central wavelength. The technique used is the passive mode-locking.

1.2 Ultrafast laser material interaction

1.2.1 Developments and advantages

Most applications of the ultrafast lasers involve the focusing of the pulses into a tight spot with a lens or mirror system. The ultra-short nature of the laser pulses provides high local intensities for spot sizes of micrometre dimensions, which opens a door to new physics and novel applications. There have been review articles which extensively describe nonlinear processes [13, 14], optical breakdown [15], surface micromachining [16, 17] and the history of femtosecond laser micromachining [18–21].

Since the end of 1980s, initial studies of ultrafast laser material modification were performed on polymer materials with ultrafast excimer UV lasers [22, 23]. Later, ablation of silica [24] and silver surfaces [25] was demonstrated using infrared femtosecond laser systems. After that, it was found that femtosecond laser processing in the bulk of transparent materials

could enable optical waveguiding structures written inside of silica glass [26]. The modification of refractive index was also demonstrated by the focusing of femtosecond lasers into Nd-, Er-Yb doped glasses or Nd:YAG crystal [27]. In addition, high resolution 3D structures were enabled by two-photon polymerization [28,29]. In the applications of bio-materials, academic and industrial developments involve laser materials processing for dental, orthopedic, neural, ophthalmic, cardiovascular, and transdermal applications [17, 21, 30].

Ultrafast laser micro-machining of transparent materials has unique advantages over other fabrication techniques [18, 31]. Firstly, the nonlinear nature of the absorption confines any induced changes to a small volume inside the focal area. This spatial confinement makes it possible to fabricate geometrically complex structures in three dimensions with ultra-small sizes. Secondly, the unique property of ultrafast laser focusing enables the processing of the material only at the focal area where the light intensity is above the threshold of material modification. This makes sure that the material in the regime other than the laser focal area is not affected. Thirdly, it uses simpler and less expensive device production equipment, avoiding photolithography and clean room facilities. Fourthly, it enables rapid prototyping. The device pattern can be easily changed by simple software control, with significant cost reduction with respect to standard techniques using photolithographic steps and requiring the production of a mask. Finally, the absorption process is independent and with different level for each unique material. This enables devices to be fabricated in compound substrates of different materials.

1.2.2 Energy absorption and ionizations

The bandgaps of transparent materials are typically much larger than the energy of a single photon of the infrared laser source. For example, the bandgap of fused silica is about 9 eV, while the photon energy at 1030 nm wavelength is 1.2 eV [32]. In the linear interaction regime, the bandgap of a photon with such energy $h\nu$ is much smaller than that of the material E_g and thus cannot be absorbed. However, if the light intensity is sufficiently high, absorption can take place through nonlinear phenomena. This includes multiphoton ionization, tunneling ionization and avalanche ionization [18].

Multiphoton ionization involves the simultaneous absorption of m photons of energy $h\nu$,

where m is the minimum integer such that $mh\nu > E_g$ is satisfied [18]. Tunneling ionization occurs when the very high electric field of the laser pulse lowers the Coulomb potential energy barrier and enables an electron to tunnel from the valence to the conduction band. Both the multiphoton ionization and tunneling ionization processes exist when the laser is with high intensities [24, 33, 34]. When femtosecond lasers are used to interact with dielectrics, multiphoton ionization usually dominates over tunneling. In avalanche ionization, an electron which is free at the bottom of the conduction band of the material is exposed to an intense light field. When its total energy which exceeds the conduction band minimum is more than the bandgap energy, it can ionize another electron from the valence band, resulting in two electrons near the conduction band minimum. These electrons can in turn be accelerated by the electric field, causing an avalanche in which the free electron density grows exponentially.

When the material is illuminated by a long pulse (such as several picoseconds or nanosecond duration), the peak intensity is too low to allow multiphoton or tunneling ionization. In this situation, avalanche ionization is the only possible mechanism. The initial seed electron is usually from the region with impurities and dislocations within the focal volume of the laser pulse. When femtosecond laser pulses are focused, the peak intensities are much higher, so that multiphoton ionization becomes significant. If the intensity exceeds a threshold, some free electrons are generated. These electrons act as a seed, further producing the avalanche ionization process. Therefore, only femtosecond pulses allow the unique combination of multiphoton and avalanche ionization. The permanent material modification can be generated in a small volume inside the bulk in a highly controlled and reproducible way.

1.2.3 Kerr Effect and Self-focusing

In 1875, physicist John Kerr found that when the applied electrical field changes, the refractive index of a material changes correspondingly. This effect was called as "Kerr effect" or quadratic electro-optic effect [35]. It has been found that this effect generally applies to all materials, and it is especially strong in liquids. As laser focusing properties inside material are highly related to the local refractive index, Kerr effect plays an important role in the research of laser material processing.

One specific case of Kerr effect is called Kerr electro-optic effect, or DC Kerr effect. In this case, when the applied electrical field slowly changes, the material become birefringence. The refractive index is different for the light whose polarization is parallel to the electrical field, and the light whose polarization is perpendicular to the electrical field. The difference in the refractive index is represented as,

$$\Delta n = \lambda K E^2 \tag{1.3}$$

where λ is the wavelength of the light, K is the Kerr constant, and E is the strength of the electric field.

Another general case in Kerr effect is called optical Kerr effect, or AC Kerr effect. In this case, the influence of electrical field is from the light itself. The variance of refractive index is proportional to the square of field amplitude of input light (which is light intensity). The refractive index is thus represented as,

$$n = n_0 + n_2 I \tag{1.4}$$

where n_0 is the original refractive index of material, n_2 is the non-linear part of refractive index, I is light intensity. As n_2 is usually positive in most materials, the refractive index becomes larger in the areas where the intensity is higher.

Optical Kerr effect is only significant when the beam intensity is strong, such as in the case of applying ultrafast laser light. It occurs if the light radiation power is greater than the critical power, which is defined as,

$$P = \frac{\alpha \lambda^2}{4\pi n_0 n_2} \tag{1.5}$$

where P is the critical power, α is a constant which depends on the initial spatial distribution of the beam. Optical Kerr effect contributes to a series of non-linear optical effects such as self-focusing, self-phase modulation, modulational instability and Kerr-lens mode-locking.

Self-focusing is caused by the variance of refractive index when the laser intensity have non-uniform local distribution (such as in lens focusing) [36]. Self-focusing caused by Kerr effect was firstly predicted in 1960s [37, 38], and experimentally verified in glasses and liq-

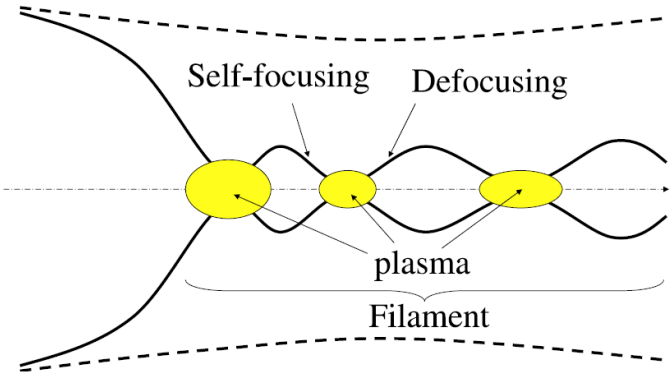

Figure 1.3: Sketch showing the focusing-defocusing cycles by the intense core of the beam [40]. The solid curves indicate the diameter of intense core, while dashed lines indicate the root mean square radius of the full beam.

uids [39]. In the focusing of ultrafast lasers, the laser intensity is higher at the center of focal point, while lower in the surround areas. Correspondingly, a variance profile of refractive index which generates at the focal area performs like a small focusing lens. The peak intensity in the self-focused region keeps increasing until defocusing effects or medium damage interrupt this process.

Due to the self-focusing, the beam collapses after the nominal focal point and gives rise to high intensities which lead to ionization of the medium. The resulting distribution of the free electrons, however, leads to a refractive index profile acting as a defocusing lens. This leads to formation of filaments, which is shown in Figure 1.3 [40]. When the beam becomes sufficiently intense, after the collapse at the nominal focus, a plasma is generated near the collapse location, which defocuses the beam core. Once defocused, the beam power may be still above critical power and undergo another focusing-defocusing cycle. The repetition of this scenario sustains a long range, self-guided propagation in the form of a filament.

1.2.4 Permanent material modification

Depending on the intensity, femtosecond laser processing can produce three types of modification in the bulk of transparent materials: isotropic refractive index changes (Type 1) [26], nanogratings (Type 2) [41], and voids (Type 3) [42]. For a lower pulse energy, the processed regime in the material usually maintains uniform quality, and there are permanent refractive

index changes. If the absorbed energy is too high, catastrophic material damage occurs, leading to the formation of voidlike structures. These three types of modification can be clearly distinguished only for laser pulses shorter than about 200 fs. At longer pulses, nanogratings appear even at relatively low fluences, just above a permanent modification threshold [43,44].

There have been enormous applications in isotropic refractive index changes (Type 1) of ultrafast laser fabrication. In silica glass, uniform increment of the refractive index can be achieved by ultrafast laser processing with a good control of the laser intensity [26]. The laser-written tracks exhibited positive refractive index change up to 0.035 (Δn). The optical waveguides with relatively low-loss ($<$0.15 dB/cm) were demonstrated through laser processing of silica glass [45, 46]. The processing in silica glass has found interesting applications in telecommunications and quantum physics [47–49]. On the other hand, in crystalline materials, femtosecond laser focusing generally produces a decrease in refractive index [50, 51]. This can be easily understood by considering that in a crystal the atoms are in the closest possible arrangement, and that any laser processing in the lattice order leads to a lower local density. For the laser processing in polymers, induced refractive index changes can be explained by a photochemical modification. This involves a direct cleavage of the polymer backbone and propagation via chain unzipping under the formation of monomers [52].

In addition, interesting applications in microfabrication were enabled by using high power ultrafast laser focusing to produce catastrophic material damage (Type 3). The most investigated material is silica glass. The applications in its fabrication involve the combination of laser processing and chemical etching methods [53]. The regions where the material is broken down by high power laser focusing could be dissolved in chemical solutions. Interesting 3D structures were therefore created in a silica glass substrate for various applications. These include lab-on-a-chip [54], micron actuators [55], micro-channels [56], micro-gratings [56], monolithic [57] and surface structuring [58]. For the high power laser processing in crystalline material, breaking down of the atom bond creates other optical or electrical applications. An example is the graphitization during the diamond fabrication. High intensity focused laser damages the atom bonds in diamond, changing the diamond into graphite [59]. The graphitization process releases free electrons, subsequently, conductive regions which are mainly

formed by graphite are created inside insulator. Applications within electronics [60, 61] and photonics [62] were enabled.

1.3 Adaptive optics

1.3.1 History

Adaptive optics (AO) was a method originally developed for telescopes for improving astronomical images [63]. In 1953, Babcock first introduced the idea of improving astronomical viewing by compensating for the atmosphere-induced aberrations. His proposal was to measure the deviations of the light rays from all parts of the mirror, and feed that information back so as to locally correct for the deviations. Although the idea was scientifically sound, it had a few minor technical complications, and it was not put into action until 20 years later when the first real-time AO system was used for national-defense applications [64]. AO might have been conceived for the purpose of improving astronomical imaging, but other scientists soon realized the importance of this technology in other areas of research. In particular, it has been considered that adaptive optics might have great potential in biomedical retinal imaging and various microscopic systems. With a few years' effort, Liang, Williams, and Miller [65] finally constructed the first closed-loop AO system. In the past decades, the researches in retinal and microscopic imaging systems have been greatly improved from the benefits of adaptive optics. Most recently, adaptive optics has been introduced to the research of laser material processing.

1.3.2 Adaptive optics elements

The main driving factor in the development of adaptive optics elements (AOEs) is the commercial availability for practical, affordable correction devices [66]. For the applications of laser material processing and microscopic imaging, two most commonly used adaptive optics elements are liquid crystal spatial light modulators (SLMs) and deformable mirrors (DMs).

Liquid crystal (LC) panels were extensively developed for displays, which also led to spatial light modulators (SLMs) for various research applications [67–70]. Besides the wider

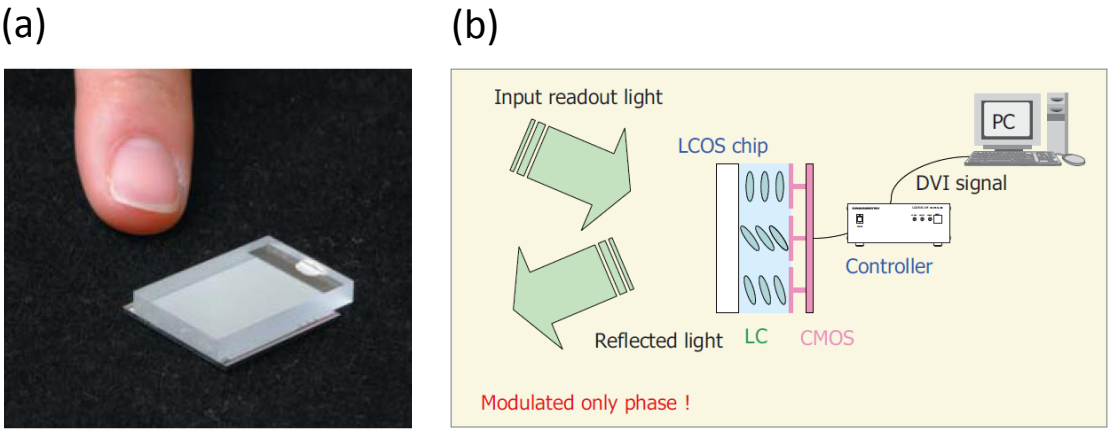

Figure 1.4: A liquid crystal spatial light modulator (SLM) manufactured by Hamamatsu (X10468 series) [72]. (a) SLM chip inside the head. (b) Sketch illustrating the modulation of the wavefront by the SLM.

application in optical data storage and optical trapping, SLMs have also found excellent ability in the pulse shaping and the modulation of the wavefront. The recently developed Multiphoton Intrapulse Interference Phase Scan (MIIPS) is a technique based on SLM that can correct the phase distortions of the ultrafast laser pulse in the spectral domain [71]. In this thesis, liquid crystal SLM is specifically used to compensate various phase aberrations generated in the optical system. Figure 1.4 show the SLM used in our experiments that is based on the Liquid Crystal on Silicon (LCOS) technology, in which liquid crystal is controlled by an accurate voltage. The refractive index of the liquid crystals is changed by the different applied voltage. Subsequently, the wave front of the reflected laser light can be modulated. The SLMs can usually be controlled by a personal computer using the Digital Video Interface (DVI). A LCOS chip usually has a parallel-aligned nematic liquid crystal layer to modulate light. It only changes the phase of light without any change of intensity and rotation of polarization state.

Different from SLMs, DMs are constructed by a certain number of mirror actuators [66, 73–75]. The angle or shape of each actuator can be electrically controlled. With the combination of different status for each actuator, a specific mirror shape (mode) can be achieved. Both the wavefront and pulse front can be tuned when the laser light is reflected from the mirror surface. An example of a DM is shown in Figure 1.5.

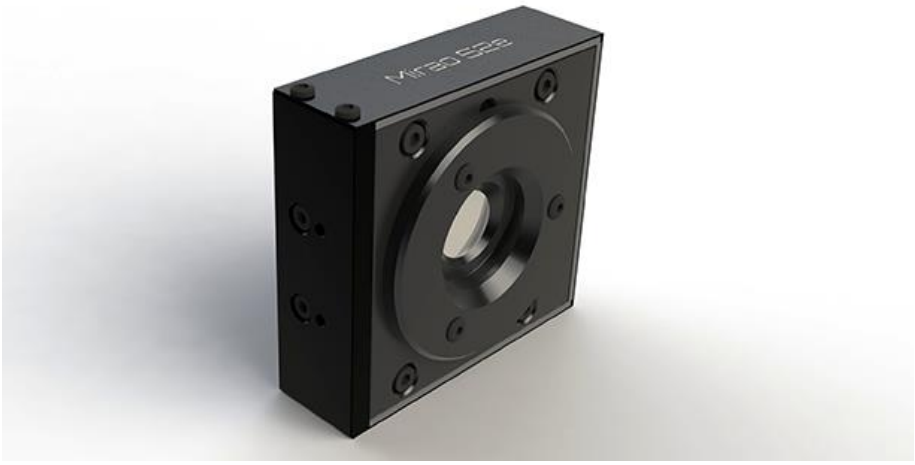

Figure 1.5: A deformable mirror manufactured by Imagine Optics (Mirao 52E) [76]. The DM mirror is in the center of the device.

Unlike the liquid crystal SLMs, the technique for the development of DMs is more complicated. The most widely used DMs have continuous reflective surfaces, while others are with segmented MEMS mirrors [77]. Electrostatically actuated membrane DMs consist of a thin membrane with a reflective coating mounted above an electrode array [78]. The DM surface shape can be pulled towards the electrodes by applying a potential between the membrane and the electrode. A transparent electrode can also be included above the membrane to permit pushpull deformations [79]. There are other electrostatically actuated MEMS DMs which are based upon microstructured silicon [78]. A supporting structure below the reflective membrane ensures that the influence of each actuator on the DM shape is spatially more confined than for a membrane DM. Piezo-electric actuators have been employed in DMs both using direct actuation of the mirror surface [80] and through curvature control using bimorph actuators [81]. Magnetically actuated DMs have also been demonstrated [82]. These DMs have been complemented by more exotic technologies such as thermally actuated [83], fluidic [84] and ferromagnetic devices [85].

Both SLMs and DMs have the capability to control the wave front of the laser light. They are however used in different situations. SLMs usually have more pixels than the total number of actuators in DMs. This means that SLMs often obtain a better resolution in the wavefront

control. It can be concluded that the SLMs are generally easier to use within its application range. However, SLMs are usually wavelength and polarization dependent. They are applied to the lasers with a certain wavelength range, and they can only react to the specific polarization status. In addition, SLMs can only operate when the laser pulses are with relative lower power. In comparison, the DMs do not have these limitations, but are more difficult to control.

1.3.3 Adaptive optics in laser material processing

The first applications of adaptive optics in laser material processing involved various beam shaping technique. SLM was usually used to generate holographic laser processing [86–88]. In contrast, this thesis concentrates on the correction of phase aberration by adaptive optics technology. The sample being processed is usually a transparent material with uniform refractive index. There is however a difference between refractive indices of the objective immersion and fabricated sample material. Distortion of the focus is then generated due to the refraction of laser light at the sample interface. In addition, there are usually other misalignments in the optical system. Therefore, there is a need to use adaptive optics to correct these aberrations, thus improve the quality of laser material processing.

There have been researches regarding the adaptive correction of phase aberrations in laser material processing. A way of measuring aberrations based upon the super-continuum emission of plasma created in the beam focus was proposed in [89]. A detailed study about the spherical aberration compensation scheme and parallel fabrication was shown in [90]. Parallel processing was also demonstrated by using a micro-lens array in conjunction with a SLM [91]. Later on, in the fabrication of lithium niobate [92], the size of written structures was demonstrated to decrease dramatically, and fabrication depth and stopgap strength were increased by a factor of two to three. By using a DM in parallel with a SLM, three dimensional structures were fabricated deep in the bulk of diamond [93]. Additionally, an improved method by using SLM for controllable beam shaping was studied for waveguide fabrication [94].

1.4 Structure of thesis

The target of this thesis is to advance the direct laser fabrication by adaptive optics. This was realized by first studying of existing problems in laser fabrication system, then finding proper methods to address those issues, and finally exploring new applications of this technology. As the first step to investigate existing problems in laser fabrication system, the commonly encountered phase aberrations, dispersion of material and pulse front distortions were studied in detail. The effects of these three facts on the ultrafast laser focusing were explored in various practical scenarios. Secondly, demonstrated as the proper methods to solve those discussed problems, the pulse front adaptive optics and the phase front adaptive optics were respectively presented. These methods were experimentally demonstrated to be able to resolve the phase aberration and pulse front distortions in optical systems. Finally, based on the discussed adaptive optical methods, various new applications of adaptive laser fabrication were explored and discussed.

The structure of this thesis is divided into three parts. First part (Chapter 2) introduces mathematical models that are used throughout the thesis. Second part (Chapter 3 - 6) describes various imperfections and their possible compensation in the laser fabrication system. Third part (Chapter 7 - 10) concentrates on the new applications of adaptive laser micro-fabrication.

Chapter 2 of this thesis concerns various theoretical models in the ultrafast laser focusing, including Fourier optics, focusing methods and lens dispersion. These models are used throughout the descriptions in the whole thesis.

Chapter 3 and 4 report the effects of phase aberrations and sample dispersion on the ultrafast laser focusing. These theoretical investigations are very useful in determining how the aberrations and sample dispersion affect the laser focusing. In addition, Chapter 5 and 6 describe another undesired factor: pulse front distortion. A new adaptive optics method: pulse front adaptive optics is developed to correct this distortion, and its application is demonstrated in a two-photon microscope.

Chapter 7, 8 and 9 concerns various applications of adaptive laser micro-fabrication. Chapter 7 concentrates on the improvements in the quality of laser graphitized wires in diamond. Chapter 8 discusses non-reciprocal effects in diamond fabrication. Chapter 9 explores several

potential applications in diamond fabrication.

The Appendix includes the fabrication of three dimensional structures in glass for applications in neuroscience.

Chapter 2

Theoretical models for laser focusing

2.1 Introduction

In this chapter, the optical theories behind the ultra-fast laser micro-fabrication are summarized. These include several important mathematical models which are used throughout the thesis for characterization of laser focusing. The mathematical representation of ultrashort laser pulses is first discussed. Fourier optics was then introduced to simulate the intensity distribution at the focal plane. Various focusing methods including the conventional point focusing, conventional line focusing, temporal line focusing and temporal widefield focusing are discussed based on different pupil illuminations (the intensity distribution in the back focal plane of the objective lens). Later on, the mathematical description of the phase aberrations are presented. Two most common aberrations are in the forms of Zernike modes and refractive index mismatch. Finally, the dispersion effects from the optical lens are presented. Chromatic aberration, propagation time difference (PTD) and group velocity dispersion (GVD) are discussed in detail.

2.2 Temporal and spectral field distribution of laser pulses

The output from a mode-locked laser consists of a series of periodic pulses. Considering a Gaussian-shaped laser pulse train with a central frequency of ω_0, the temporal field amplitude

is represented by [95],

$$E(t) = \exp(-i\omega_0 t) \sum_{n=1}^{\infty} \exp\left[-\left(\frac{t-t_n}{T}\right)^2\right] \tag{2.1}$$

where t is the local time coordinate and t_n corresponds to the time when pulse train reaches the peak. T represents the time when amplitude drops to 1/e of the peak amplitude (defined as "pulse width"). The first factor corresponds to a fast oscillation of the light field with a central frequency ω_0, while the second factor gives the envelope of the oscillation change. The temporal "pulse duration" τ, which is defined as the FWHM of the temporal Gaussian curve, can be expressed as,

$$\tau = 2T\sqrt{\ln 2} \tag{2.2}$$

Both pulse width and pulse duration are marked Figure 1.2 of Chapter 1.

On the other hand, the field distribution in the spectral domain can be obtained as,

$$E(\omega) = \sqrt{\pi} T \exp\left[-\left(\frac{T(\omega-\omega_0)}{2}\right)^2\right] \tag{2.3}$$

The spectra width $\Delta\Omega$, which is defined as the FWHM of the spectral Gaussian curve, can be represented by,

$$\Delta\Omega = 4\sqrt{\ln 2}/T \tag{2.4}$$

It is interesting to note that, $\tau\Delta\Omega = 8ln2$, which is a constant.

2.3 Modelling of focal field distribution

2.3.1 Fourier optics

The propagation of the light through the lenses could be represented by Fourier theory. This enables the simulation of the light intensity distribution at the focal plane of the lens. The modeling method is extremely useful for all the optical systems involving laser focusing. Any aberration and dispersion effects can be included and analyzed.

Different from ray optics, Fourier optics belongs to the category of physical optics which

considers the light in forms of electromagnetic radiation. As discussed in the previous chapter, ultra-fast lasers include laser light with different wavelengths which is limited by a bandwidth. It is much easier to understand pulses by decomposing laser pulse into monochromatic components with interference of many spectral components with a certain phase relationship. The one dimensional Fourier transform is adopted to transmit the light in the time domain into spectral domain,

$$E(\omega, x, y, z) = \int_{-\infty}^{+\infty} E(t, x, y, z) \exp(-i\omega t) dt \tag{2.5}$$

where $E(\omega, x, y, z)$ and $E(t, x, y, z)$ represent the electromagnetic field of the ultrafast laser light in spectra domain and time domain, respectively. ω is the frequency of the laser light, t is the time, x, y and z are the three dimensional spatial coordinates, i is the imaginary unit ($i^2 = -1$).

Similarly, inverse one dimensional Fourier transform transmits the representation of ultrafast laser light from spectral domain into time domain,

$$E(t, x, y, z) = \frac{1}{2\pi} \int_{-\infty}^{+\infty} E(\omega, x, y, z) \exp(-i\omega t) d\omega \tag{2.6}$$

Two dimensional Fourier optics is used to calculate the light distribution after the propagation of lens, from the distribution at the back focal plane of the lens (which is also called "pupil illumination"). If we assume that the distribution in the back focal plane of the lens is $E(\omega, p_x, p_y)$, then the distribution at the focal plane $E(\omega, x, y, z_f)$ is obtained by solving the Rayleigh-Sommerfeld diffraction integral [96],

$$E(\omega, x, y, z_f) = \frac{\omega}{i2\pi c} \int E(\omega, p_x, p_y) \frac{\exp(ikR)}{R} \cos\gamma dp_x dp_y \tag{2.7}$$

$$R = \sqrt{f^2 + (x - p_x)^2 + (y - p_y)^2} \tag{2.8}$$

where p_x, p_y are the coordinates at the back focal plane of the lens. x, y and z_f are the coordinates at the focal plane of the lens. c is the speed of light and k is the wave number

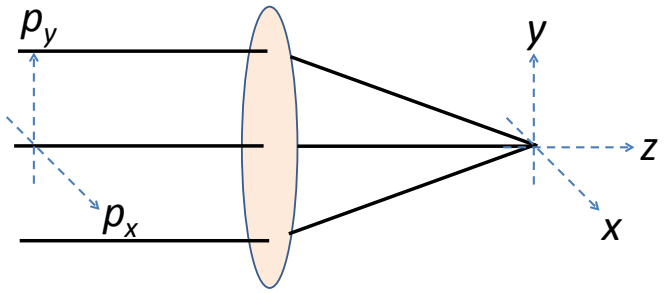

Figure 2.1: Optical coordinates in the Fourier optics model.

($k = \omega/c = 2\pi/\lambda$). f is the lens focal length. R is the radius of curvature for the spherical waves and γ is the angle of the ray with respect to the optical axis. Figure 2.1 presents the optical coordinates used in the Fourier optics calculation.

Here, the optical propagation through the lens is treated as propagation between two planes. Then we can have an equivalent plane of a reference sphere as the pupil. After doing so, the angles γ defines the derivation from the radius R of the sphere which becomes a small angle approximation [97]. The focal field distribution is simplified and re-written as,

$$E(\omega, x, y, z_f) = \frac{\omega}{i2\pi cf} \exp(ikf) \exp\left[\frac{ik(x^2+y^2)}{2f}\right] \times F\left[E(\omega, p_x, p_y)\right] \tag{2.9}$$

where $F[\,]$ represents the two-dimensional Fourier transform.

In most cases, it is also very important to investigate the field distribution other than the focal plane. Considering a plane $z_s = z_f + \Delta z$, which has an axial distance of Δz away from the focal plane, the field amplitude at the plane z_s can be obtained by applying the Angular Spectrum of Plane Waves (ASPW) starting from the focal plane [96],

$$E(\omega, x, y, z_s) \propto F\left[p_s E(\omega, p_x, p_y)\right] \tag{2.10}$$

$$P_s = \exp\left[ik\Delta z\sqrt{1 - \frac{p_x^2 + p_y^2}{f^2}}\right] \tag{2.11}$$

By solving the above equations, the field amplitude of the laser light in and around the focal plane can be calculated for each wavelength. One dimensional inverse Fourier transform (Equation 2.6) can be used to transmit the light field distribution from spectral domain into

time domain. The light intensity is with a square relationship with the field amplitude,

$$I(t,x,y,z) = |E(t,x,y,z)|^2 \tag{2.12}$$

2.3.2 Diffraction-limited focus

Beside various effects of imperfections in the optical system, there is a fundamental maximum to the resolution of any optical focusing which is due to diffraction. An optical system with the ability to produce resolution as good as the system's theoretical limit is said to be diffraction limited.

Early in 1873, Ernst Abbe found that light with wavelength λ, traveling in a medium with refractive index n and converging to a spot with angle θ will make a spot with radius r,

$$r = \frac{\lambda}{2n\sin\theta} \tag{2.13}$$

where $n\sin\theta$ is called the numerical aperture (NA). This approximation is also known as Abbe's Law [98].

Later on, Airy pattern (or called Airy disk) is used for a more accurate description of the best focused spot of light that a perfect lens with a circular aperture can make. The intensity in the Airy pattern is a derivation result from the two-dimensional Fourier transform discussed in above subsection. In lateral focal plane (xy focal plane), the physical distance between the two first minimum intensity beside the peak value can be expressed by [95],

$$d_{lateral} = \frac{1.22\lambda}{NA} \tag{2.14}$$

This equation describes the lateral size of perfect focal spot. Similarly, based on the derivation of the Fourier optics, the axial (z direction) size of the focal spot can be represented by [95],

$$d_{axial} = \frac{4n\lambda}{NA^2} \tag{2.15}$$

where n is the refractive index of the sample material.

2.4 Methods of laser focusing

In the previous section, it is understandable that the intensity distribution of the laser light in and around the focal plane is decided by the pupil illumination. In this section, we present several typical ultrafast laser focusing methods which could be distinguished by their pupil illuminations. These focusing methods include the conventional point focusing, conventional line focusing, line simultaneous spatial and temporal focusing (line SSTF) and widefield simultaneous spatial and temporal focusing (widefield SSTF).

The conventional focusing and temporal focusing are distinguished by whether there is a spatial chirp at the objective pupil. Spatial chirp of the ultrafast laser pulses is a concept which means different wavelength components of the pulse are spatially separated with each other. The conventional focusing methods do not include the spatial chirp of the input laser light, while in SSTF, spectra components are separated in the pupil of the objective lens.

2.4.1 Conventional focusing methods

The most typical conventional focusing methods are the point focusing and the line focusing. Point focusing is a method that has been generally used in most applications of laser light. Using this method, the laser beam is expanded into a circular shape and illuminated to the pupil of objective lens. The pupil illumination of the conventional point focusing method is shown in Figure 2.2 (a). In this case, the field distribution at the focus should be a single Airy pattern.

One single wavelength component is sufficient to represent continuous-wave (CW) point focusing. It is easy to calculate the field distribution profiles within the time domain by the method described above. The pupil illumination of CW laser in the back focal plane is represented by,

$$E(\omega, p_x, p_y) = E_0 \times u\left(p_x, p_y\right) \tag{2.16}$$

$$u\left(p_x, p_y\right) = \begin{cases} 1 & , \sqrt{p_x^2 + p_y^2} \leq R \\ 0 & , \sqrt{p_x^2 + p_y^2} > R \end{cases} \tag{2.17}$$

where E_0 is a constant of field amplitude assuming a uniform field distribution across the

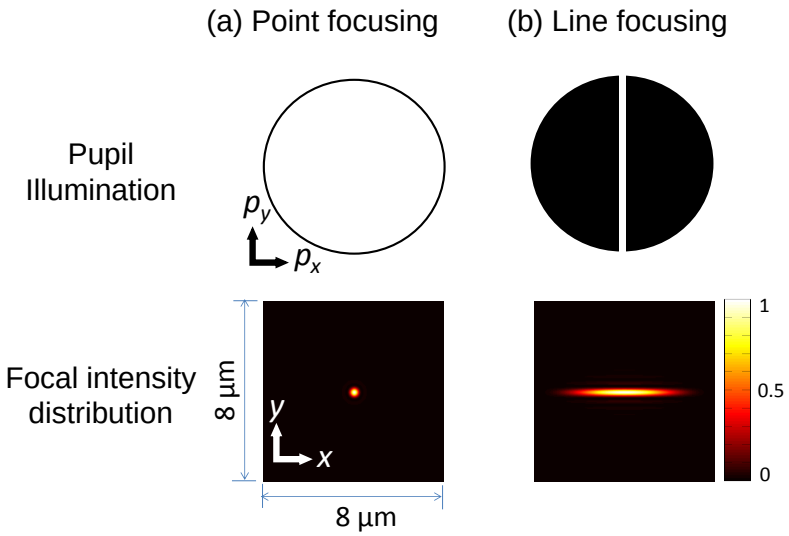

Figure 2.2: Pupil illumination (top images) and lateral focal field distribution (bottom images) for the conventional focusing methods. The light is assumed to be focused by a 1.4NA oil immersion objective lens. Color bar shows the normalized field amplitude. (a) Conventional point focusing method. (b) Conventional line focusing method.

pupil, R is the radius of the pupil.

When the laser beam becomes pulsed, the spectrum stretches. For pulsed laser point focusing, the pupil illumination with all single wavelengths in the back focal plane of the objective lens (pupil illumination) is represented by,

$$E(\omega, p_x, p_y) = E_0 \times \exp\left[-\frac{T^2(\omega-\omega_0)^2}{4}\right] \times u\left(p_x, p_y\right) \tag{2.18}$$

in which, T is the pulse width (the time when amplitude drops to 1/e of the peak amplitude). The contribution by each single wavelength is calculated individually, and then combined together with the one dimensional inverse Fourier transform. With the conventional point focusing method, both the CW laser and pulsed laser can be focused into a single Airy disk at the focal plane. This is shown by the Fourier Optics simulation results in Figure 2.2 (a).

In some laser focusing applications, it is needed to generate a line shape focus. In laser material processing, line focusing is a very useful method to increase the fabrication dimension in lateral plane. This could be realized by creating a line shape pupil illumination. In this

situation, the field amplitude at the pupil of the objective lens is,

$$E(\omega, p_x, p_y) = E_0 \times \exp\left[-\frac{T^2(\omega-\omega_0)^2}{4}\right] \exp\left[-\frac{{p_x}^2}{s_{BFP}^2}\right] \times u\left(p_x, p_y\right) \tag{2.19}$$

where s_{BFP} represents the physical dimension of line shape light strip at the pupil, which is defined as the distance for the field amplitude to drop to 1/e of the peak value. In our simulation, it is set to be 0.06 times of the pupil radius in the calculation. The pupil illumination of line focusing is shown in Figure 2.2 (b). The lateral field distribution at the focal plane presents a line shape, which is in opposite direction of the illumination strip.

2.4.2 Temporal focusing methods

Simultaneous spatial and temporal focusing (SSTF) is also known as temporal focusing (TF). It is realized by spatially separating the spectral components of a short pulsed laser beam across the illuminated pupil of a colour corrected objective lens, thus ensuring that these components recombine into an ultrashort pulse only at the focus [99, 100]. This can be practically realized by aligning a grating or a prism into the optical system. A sketch showing the optical set-up for the SSTF is in Figure 2.3. It has become a useful method in microscopy and laser fabrication, relying on the fact that a focused ultrashort pulse is a superposition of many spectral components in space time, which gives rise to a high instantaneous peak intensity. SSTF has been applied to multiphoton microscopy for both harmonic generation [101, 102] and two-photon fluorescence imaging [103, 104], in which high axial resolution and video-rate speed were demonstrated. There are extensive subsequent investigations using SSTF in imaging, such as adjusting group velocity dispersion for refocussing [105], imaging of biological samples [106], the creation of novel excitation patterns for biological photoactivation [107, 108], as well as theoretical treatment [109]. Concurrently, SSTF has also been implemented in laser fabrication, where demonstrations include the generation of hollow microfluidic channels [110], control of the pulse front tilt (PFT) for directional laser writing [111, 112], 3D lithographic micro-fabrication [113], patterned excitation [114] and longer pulse envelope fabrication [115].

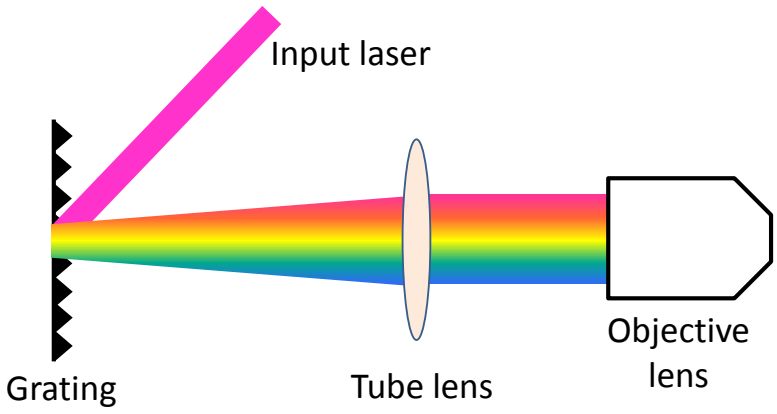

Figure 2.3: Sketch showing the optical set-up for SSTF. A grating is used to create the spatial chirp at the pupil of objective lens.

There are generally two types of temporal focusing methods. According to the shape of the focus, they are named as line SSTF which has a line shape focus, and wide-field SSTF which has focus with relatively large area. The wide-field focusing method is extremely useful to increase the efficiency in ultrafast laser fabrication.

For an example of line SSTF focusing, each spectral component is located at a different position along the p_x direction and fills the entire pupil along p_y direction, as shown in Figure 2.4 (a). We can represent such pupil illumination by,

$$\begin{aligned} &E(\omega, p_x, p_y) = \\ &E_0 \exp\left[-\frac{T^2(\omega-\omega_0)^2}{4}\right] \exp\left[-\frac{(p_x-p_{x0})^2}{s_{BFP}^2}\right] u\left(p_x, p_y\right) \end{aligned} \tag{2.20}$$

in which, p_{x0} is a function of ω (proportional to $(\omega - \omega_0)$). It represents the central wavelength position for each spectral component.

It is seen in Figure 2.4 (a), the simulation for the field distribution of line SSTF presents similar lateral focal shape as the conventional line focusing (Figure 2.2 (b)). However, they are in different principle, thus have different properties in their pulse fronts, and different sensitivities to phase aberrations and sample dispersion. These will be discussed in later chapters in this thesis.

For an example of wide-field SSTF, the pulse is spectrally spread along the p_x direction, while being spatially confined in p_y direction in the back focal plane of the objective. The

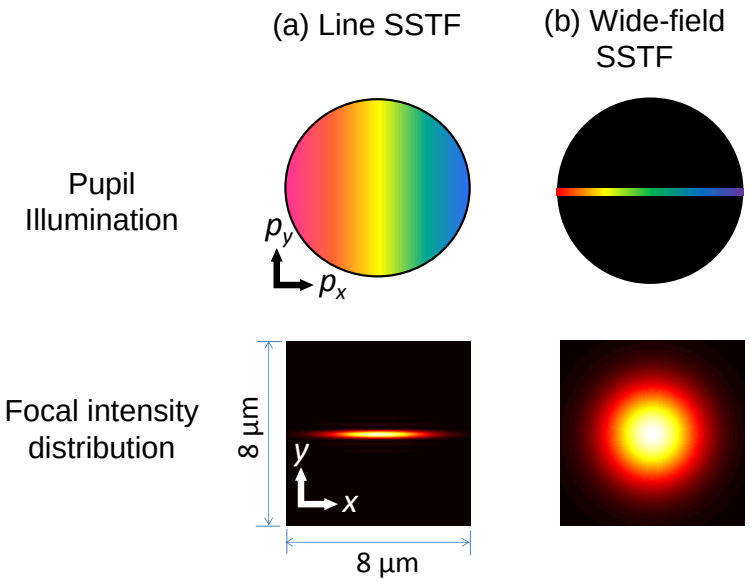

Figure 2.4: Pupil illumination (top images) and lateral focal field distribution (bottom images) for the temporal focusing methods. The light is assumed to be focused by a 1.4NA oil immersion objective lens. (a) Line SSTF. (b) Wide-field SSTF.

pupil illumination is shown in Figure 2.4 (b), which can be represented by,

$$E(\omega, p_x, p_y) = \\ E_0 \exp\left[-\frac{T^2(\omega-\omega_0)^2}{4}\right] \exp\left[-\frac{(p_x-p_{x0})^2+p_y^2}{s_{BFP}^2}\right] u\left(p_x, p_y\right) \tag{2.21}$$

As the simulation result shown in Figure 2.4 (b), the focal field distribution of wide-field SSTF presents a much larger area than other focusing methods.

In Equation 2.19, 2.20 and 2.21, s_{BFP} is used to represent the physical dimension of a single spectral component at the pupil. It is defined as the physical distance for the field amplitude to drop to 1/e of the peak value. The value of s_{BFP} can be controlled by the optical system prior to the objective lens. It is calculated from the size of each monochromatic beam input to the grating s_0,

$$s_{BFP} = \frac{4\lambda_0 f_{TL}}{\pi s_0} \tag{2.22}$$

where f_{TL} is the focal length of tube lens before objective lens, λ_0 is the central wavelength of the input laser light. The value of s_{BFP} affects the lateral distribution of the focus for both conventional line and SSTF focusing, with a smaller value leading to a greater lateral spread

of the focus.

In SSTF, p_{x0} represents the spatial spreading of different frequencies in the pupil, and it is important to control of both the axial and lateral extent of the focal intensity distribution. The value of p_{x0} can be effectively set by the optical system prior to the objective lens, such as a combination of a diffraction grating and a tube lens. p_{x0} is defined by,

$$p_{x0} = \frac{f_{TL}\gamma(\omega - \omega_0)}{k} \tag{2.23}$$

where k is the wavenumber, $k = \omega/c$, and c is the light speed. γ is a variable that is used to control the spread of each monochromatic light. If a grating is used in the optical system, γ is physically defined as,

$$\gamma = \frac{2m\pi}{k_0 c d_{grat} \cos\theta} \tag{2.24}$$

where d_{grat} is the period of grating, m is the diffraction order, θ is the angle of the pulse spectrum disperses from the grating.

In most practical cases, it is needed to determine the value of γ by the requirement of spatial chirp at the pupil for temporal focusing. Here, we present how to calculate γ if the wavelength component at the edge of the pupil is required to have a field amplitude ratio of q compared to the field amplitude of central wavelength light. For an example, $q = 5\%$ means that the wavelength component at the edge of the pupil has field amplitude of 5% to that of central wavelength. In this situation,

$$\frac{f_{TL}\gamma(\omega_e - \omega_0)}{k} = R \tag{2.25}$$

where ω_e represents the frequency of the light at the pupil edge, R is the pupil radius. Solving this equation, we have,

$$\omega_e = \frac{c f_{TL}\gamma\omega_0}{c f_{TL}\gamma - R} \tag{2.26}$$

As the edge field amplitude equals to q times of the central wavelength, thus,

$$E_0 \times \exp\left[-\frac{T^2(\omega_e - \omega_0)^2}{4}\right] = q \times E_0 \tag{2.27}$$

Combine Equation 2.26 and 2.27, we have,

$$\exp\left[-\frac{T^2\omega_0^2(\frac{R}{cf_{TL}\gamma-R})^2}{4}\right] = \exp\left[\ln(q)\right] \tag{2.28}$$

By solving this quadratic equation, the γ is obtained and represented by,

$$\gamma = \frac{\frac{T\omega_0 R}{2}\sqrt{\frac{-1}{\ln(q)}} + R}{cf_{TL}} \tag{2.29}$$

In practice, Equation 2.29 is used to calculate to desired γ value to obtain the required spatial chirp for the target temporal focusing, while Equation 2.24 is used to experimentally align the grating into the system to generate the spatial chirp for the laser light.

2.5 System induced phase aberrations

In a perfect optical system, light focuses without distortion to a diffraction-limited focus, the form of which essentially determines the resolution of the microscope or laser fabrication system. However, inherent imperfections or misalignments in optical systems, refractive index differences between the objective immersion medium and specimen, and optical inhomogeneity in the specimen cause additional unwanted refraction of the light. This refraction introduces phase variations, or aberrations, which can severely affect the quality of imaging and laser fabrication, particularly when high NA objective lenses are employed.

A phase function ϕ in the pupil of the objective can be used to represent the aberrations arising from focusing into the specimen, such that the aberrated pupil function becomes,

$$E_a(\omega, p_x, p_y) = E(\omega, p_x, p_y)e^{-j\phi(\omega,p_x,p_y)} \tag{2.30}$$

In this section, two most typical methods describing the phase aberrations are presented, that is the Zernike mode aberration and refractive index mismatch (RIM) aberration.

2.5.1 Zernike mode aberrations

The wavefront phase ϕ can be represented by the expansion of an infinite sum of weighted orthogonal functions. The Zernike circle polynomials are often used in optics as they form an orthogonal set of functions defined over a unit circle and have simple properties of invariance [116]. Some low-order Zernike polynomials correspond to aberrations such as astigmatism, coma and spherical aberration that are commonly encountered in most optics systems. An aberrated wavefront can be expressed as the weighted sum of Zernike polynomials, defined in polar coordinates as,

$$\phi(\omega, \rho, \theta) = \sum_{k=1}^{\infty} c_k(\omega) Z_k(\rho, \theta) \tag{2.31}$$

where c_k is the modal coefficient, ρ and θ are the polar coordinates in a unit circle describing the same pupil as (p_x, p_y). As ultrafast laser pulse contains various different frequencies, the magnitude of the Zernike modes for each spectral component is defined as,

$$c_k(\omega) = c_k(\omega_0) \times \omega/\omega_0 \tag{2.32}$$

This model accounts for aberrations that are induced by the propagation of the light through specimens with an inhomogeneous refractive index. Neglecting any dispersion within the specimen, the phase aberration is proportional to the frequency of the light. A mathematical description of the most common modes is included in Table 2.1. The azimuthal frequency m and radial polynomials of degree n [116] are also shown. Orthogonal Zernike polynomials have been normalised so that each polynomial has a root mean square (RMS) value of one radian over the unit circle, which is defined by the hard edge aperture found in objective lenses. It is notable that the lower order Zernike modes (piston, tip, tilt, and defocus) are not included in this table, as they have either no effect on the focusing process (piston), or represent displacement of the focus (tip, tilt, defocus). Piston adds a constant phase to the pupil function, so it is generally disregarded as it does not distort the phase shape. Tip and tilt add a linearly varying phase to the pupil. This does not result in any distortion of the focal spot, but shifts the focus from its original position to another position in the lateral focal plane. In paraxial optics (such as focusing with relative low NA objective), defocus also does not distort the focus, but

displaces the focal position along the axial direction.

Table 2.1: The Zernike polynomials k = 5 to 11

k	n	m	$Z_k(\rho, \theta)$	Aberration term
5	2	2	$2\sqrt{3}\rho^2 \cos(2\theta)$	astigmatism
6	2	-2	$2\sqrt{3}\rho^2 \sin(2\theta)$	astigmatism
7	3	1	$2\sqrt{2}(3\rho^3 - 2\rho)\cos(\theta)$	coma
8	3	-1	$2\sqrt{2}(3\rho^3 - 2\rho)\sin(\theta)$	coma
9	3	3	$2\sqrt{3}\rho^3 \cos(3\theta)$	trefoil
10	3	-3	$2\sqrt{3}\rho^3 \sin(3\theta)$	trefoil
11	4	0	$\sqrt{5}(6\rho^4 - 6\rho^2 + 1)$	spherical

2.5.2 Refractive index mismatch (RIM) aberration

A very common aberration that we also consider arises when light is focused into a uniform medium through a planar interface between which of different refractive indices. Even a small refractive index difference between the objective lens immersion medium and the sample can lead to a significant spherical aberration [117]. This form of aberration is the major phase distortion encountered in laser material processing. The index mismatch between the immersion medium of the objective lens (n_1) and the specimen (n_2) is characterized by introducing a phase aberration function $\phi(d, \rho)$ into the pupil function of the imaging lens. $\phi(d, \rho)$ is defined as [90, 117],

$$\phi(d, \rho) = -k \cdot d \cdot NA \left(\sqrt{\frac{n_2^2}{NA^2} - \rho^2} - \sqrt{\frac{n_1^2}{NA^2} - \rho^2} \right) \tag{2.33}$$

where k is the wavenumber, and d is the nominal focusing depth of the light in the specimen (the position of the geometrical focus, if the rays were not refracted at the interface). The aberration caused by the refractive index mismatch not only axially shifts the focus to a greater depth (if $n_2 > n_1$), but also causes a distortion of the intensity distribution at the focus.

Equation 2.33 contains both a defocus element (causing an axial shift of the focus) and a spherical aberration element (causing focal shape distortion). In practice, we are mainly interested in the focal distortion, so the phase that causes the axial shift is removed in the modelling. Practical aberration correction usually removes any focal distortion without re-focusing the system. This is because in order to minimise the phase range required on the adaptive element, it is desirable to refocus the system by specimen translation, rather than including the defocus component in the phase correction function. This is useful to maintain the dynamic range for any AOE (adaptive optics element). With a high NA objective lens, we employ a spherical term rather than a quadratic term to describe the defocus phase element,

$$D(d,\rho) = k \cdot d \cdot NA\sqrt{\frac{n_2^2}{NA^2} - \rho^2} \tag{2.34}$$

The process to obtain defocus-free phase $\hat{\phi}(d,\rho)$ can be expressed as,

$$\hat{\phi}(d,\rho) = \phi(d,\rho) - \frac{\langle \phi'(d,\rho), D'(d,\rho)\rangle}{\langle D'(d,\rho), D'(d,\rho)\rangle} D(d,\rho) \tag{2.35}$$

$\phi'(d,\rho)$ and $D'(d,\rho)$ represent spherical aberration and defocus with subtracted mean values,

$$\phi'(d,\rho) = \phi(d,\rho) - \frac{1}{N}\sum\nolimits_{\rho} \phi(d,\rho) \tag{2.36}$$

$$D'(d,\rho) = D(d,\rho) - \frac{1}{N}\sum\nolimits_{\rho} D(d,\rho) \tag{2.37}$$

where N is the total number of the calculation pixels. The calculation $\langle .,. \rangle$ defines an inner product over the pupil,

$$\langle \phi'(d,\rho), D'(d,\rho)\rangle = \frac{1}{N}\sum\nolimits_{\rho} \phi'(d,\rho) \cdot D'(d,\rho) \tag{2.38}$$

It is notable that with the removal of the defocus element, the simulation of intensity distribution for a RIM aberrated focus still shows additional shifts in the on-axis peak intensity even after removal of this defocus component. The reason for this additional shift is that the defocus removal relies upon the minimization of the rms phase error, which does not necessarily mean the maximum intensity point resides in the nominal focal plane for large aberrations.

2.6 Dispersion of optical lenses

The most important part of the optical system - optical lenses, are made of some sort of transparent material. The refractive index of the transparent material is different for laser light with different wavelengths, forms the effect of dispersion. Dispersion generally exists in all transparent materials, generating distortions in the focal plane. Especially in recent years, numerous methods have been developed to obtain ultra-short pulses with durations down to several femtoseconds [118–120] and even attoseconds [121, 122]. Short pulse durations are accompanied with large spectral bandwidths thus enlarge the effect of dispersion. In this section, we first describe various common dispersion effects in a singlet lens. These effects include chromatic aberration, propagation time difference (PTD) and group velocity dispersion (GVD). Spatial and temporal distortions of the focuses generated from these effects are presented. Achromatic doublets are then introduced for the compensation of these lens dispersion effects.

2.6.1 Chromatic aberration

The light of longer wavelength usually refracted with a different angle with the light of shorter wavelengths inside the lenses. This causes spatial distortion to the lens focusing, which is decided by the curvature of the lens surface.

Planoconvex lens has one side plane and the second side curved. A spherical surface for the curved side is the easiest solution because it can be described by just one parameter the radius of curvature R. On the other hand, a biconvex or a concave-convex lens is with both

surfaces of some sort of curvature. There are many ways of describing lens surfaces, so that such mathematic expressions can become quite complex, e.g. for an asphere, surfaces are described by polynomials. In order to keep matters as simple as possible, we will stick to singlet plano- and biconvex lenses with spherical surface profiles in this section.

The spatial distortion of chromatic aberration is reflected in the variation of focal length for different wavelengths. The focal length f for the light with wavelength λ can be expressed by the lens-makers formula [96],

$$\frac{1}{f(\lambda)} = [n(\lambda) - 1]\left(\frac{1}{R_1} - \frac{1}{R_2}\right) \tag{2.39}$$

where n is the refractive index of the lens material, R_1 and R_2 are the radii of curvature with the following sign convention: the values are positive (negative) for surfaces concave (convex) towards the incident side, which is usually the left hand side.

In Equation 2.39, it is seen that the focal length difference for each wavelength is related to the first order of the material dispersion. This variation in the focal length is also called the chromatic aberration. The effect of chromatic aberration is an expansion of the focal region along the optical axis, because the lens does not focus in just one focal plane anymore. To estimate the influence of chromatic effect, it is necessary to calculate the change of the focal length Δf, for a given lens and pulse duration τ. After differentiating and resolving Equation 2.39, the expression of Δf can be derived as follows,

$$\Delta f = \frac{f(\lambda)}{n(\lambda) - 1}\left[-\frac{dn}{d\lambda}\right]\Delta\lambda \tag{2.40}$$

In most practical cases, the pulse duration τ instead of the spectral width $\Delta\lambda$ is known and therefore we derive another expression for band-limited Gaussian pulses with a center wavelength λ. From the relationship,

$$\Delta\lambda \cdot \tau = \frac{2\ln 2 \cdot \lambda^2}{\pi c} \tag{2.41}$$

It is easy to obtain,

$$\Delta f = \frac{2\ln 2 \cdot \lambda^2}{\pi c} \cdot \frac{f(\lambda)}{(n(\lambda)-1)\,\tau} \left(-\frac{dn}{d\lambda}\right) \tag{2.42}$$

Through these derivations, it is seen that the chromatic aberration is a direct consequence of first order material dispersion.

2.6.2 Propagation time difference (PTD)

Now we look at another interesting effect, which causes pulse front distortion, but is depending on the lens parameters only. While light with different wavelength propagates inside a transparent material, there is a mismatch between phase and group velocity. Thereby, the phase velocity v_ϕ is determined by the refractive index as,

$$v_\phi = \frac{c}{n(\lambda)} \tag{2.43}$$

whereas the group velocity v_g is given by,

$$v_g = \frac{c}{n(\lambda) - \lambda\frac{dn}{d\lambda}} \tag{2.44}$$

Compared the two equations with each other, one can see that the phase velocity is larger than the group velocity. This effect causes propagation time difference (PTD) [123]. Moreover, the delay of pulse and phase front depends on the material path within the lens. Thus, the more glass to pass, the later the pulse front arrives. Therefore, the pulse front in the middle of a convex lens is delayed more than at the edges. The PTD effect is illustrated in Figure 2.5. The radially varying group delay lengthens the pulse temporally and distorts the pulse front in the focal plane.

With a few derivation, the propagation time difference between the phase front and pulse front for a singlet can be expressed by,

$$\Delta t(r) = \frac{R^2 - r^2}{2cf(\lambda)^2} \left(\lambda\frac{df}{d\lambda}\right) \tag{2.45}$$

it is clear that the magnitude of the PTD is in a quadratic relationship with the normalized

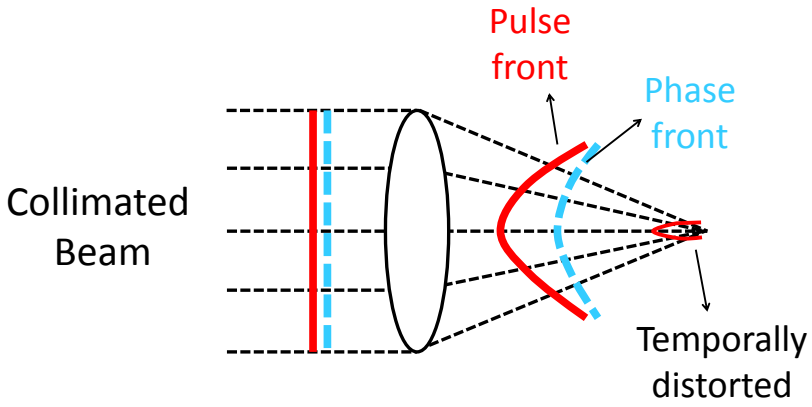

Figure 2.5: Sketch illustrating the effect of propagation time difference (PTD). When collimated beam with flat pulse and phase front propagates through a chromatic lens, the pulse front is delayed and distorted compared with the phase front. Temporal distortion occurs at the focus.

radius.

2.6.3 Group velocity dispersion (GVD)

The light of longer wavelength usually propagates in a different speed with the light of shorter wavelengths inside the lenses. This causes temporal distortions (stretching) to the lens focusing, which are called group velocity dispersion and even higher orders.

To investigate the temporal pulse broadening effect, the input ultrafast laser pulse with a duration of τ (FWHM) is assumed to propagate through a singlet lens. Therefore, the increased pulse duration according to the GVD effect τ_{GVD} can be presented by [123],

$$\tau_{GVD} = \tau \times \left[1 + \left(\frac{4\ln 2 \cdot GVD}{\tau^2}\right)^2\right]^{0.5} \tag{2.46}$$

in which,

$$GVD = \frac{\lambda^3}{2\pi c^2}\left(\frac{d^2 n}{d\lambda^2}\right) L \tag{2.47}$$

where L is the optical length through the lens. It is seen that the increase pulse duration, which is also called the temporal distortion is related to the second order of the material dispersion.

Both PTD and GVD cause a temporal spread of the laser pulse in the focal plane. Therefore, it is interesting to know which of these effects is the dominant one. Here we use a ratio

between magnitudes of temporal pulse broadening effects of PTD and GVD to characterize the level of time delays. If the ratio is larger than one, it means the existence of PTD effect introduces more time delay than the GVD effect of the lens.

Sellmeier equation is generally used to represent the refractive index of the transparent material. The derivation from the Sellmeier equation describes the relationship between the material refractive index and wavelength,

$$\frac{d^2n}{d\lambda^2} = -\frac{C}{\lambda} \cdot \frac{dn}{d\lambda} \tag{2.48}$$

where the magnitude of the constant factor C depends on the actual material and is typically in the order of unity. The ratio between temporal pulse broadening effects of PTD and GVD can be expressed by,

$$\frac{PTD}{GVD} = \frac{1}{\Delta\lambda} \cdot \frac{dn/d\lambda}{d^2n/d\lambda^2} = \frac{\pi}{2\ln 2 \cdot C} \cdot \frac{c\tau}{\lambda} \tag{2.49}$$

For an example, for a 100 fs laser pulse centered at 800 nm, PTD is about one order of magnitude larger than GVD.

2.6.4 Achromatic doublets

It has been shown that for singlet convex lens, chromatic aberrations enlarge the focal region, PTD distorts the pulse front, and causes together with GVD an increase of the pulse duration. As a solution to these effects, achromatic doublets have been designed and widely adopted in various applications.

As shown in Figure 2.6, an achromatic doublet is a combination of two lenses made of different sorts of glass with different refractive indices. It is able to offer the same optical path to all incoming rays. As a result, it should lead all the optical rays to meet at the focus again and therefore lead to higher intensity in the focal plane. In addition, the effects of propagation time difference could be resolved.

The focal length of the light with different wavelengths propagating through an achromatic doublet can be expressed by,

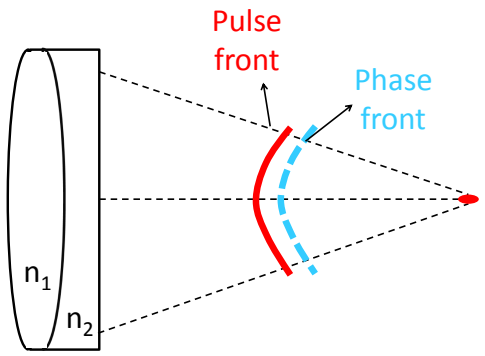

Figure 2.6: Sketch illustrating the effects of achromatic doublets. The undesired effects of spatial focal distortion and propagation time difference can be resolved.

$$\frac{1}{f(\lambda)} = [n_1(\lambda) - 1]\left(\frac{1}{R_1} - \frac{1}{R_2}\right) + [n_2(\lambda) - 1]\left(\frac{1}{R_2} - \frac{1}{R_3}\right) \tag{2.50}$$

With a proper design of the curvature of the lens surface, it is able to lead $f(\lambda)$ to be approximately constant, which does not change with the wavelength. Therefore, the achromatic doublet can be designed to fully cancel the spatial distortion from the chromatic aberration.

Interestingly, with the proper design, the optical path length for the light transmitted with different radius can be the same. That is to say, the radially distortion for the pulse front can also be resolved. The constant delay between the pulse front and phase front can be expressed as,

$$\Delta t_{doublet} = \frac{d_1}{c}\left(-\lambda\frac{dn_1}{d\lambda}\right) + \frac{d_2}{c}\left(-\lambda\frac{dn_2}{d\lambda}\right) \tag{2.51}$$

The benefits of an achromatic doublets can be summarized as follows. Firstly, an achromatic doublet focuses all colors, within a certain spectral range, in one focal point. Secondly, the PTD is constant over its cross-section, which prevents pulse front distortion and leads to a flat pulse front in the focal plane. Thirdly, the GVD is constant over the cross-section too, since the achromatic design offers the same optical path lengths for all colors. Therefore, the GVD can be compensated externally by pre-chirping the laser pulse.

2.7 Conclusions

As a brief summary of this chapter, several mathematical models regarding the focusing of ultrafast lasers have been described in detail. These models include mathematical representation of laser pulses, Fourier optics for the simulation of focal field distribution, various focusing methods based on the pupil illumination, system induced phase aberrations and the dispersion effects of the lenses. All these models were extensively applied to the research works and referenced throughout the thesis.

Chapter 3

Effects of phase aberrations on ultrafast laser focusing

3.1 Introduction

In Chapter 2, the phase aberrations are described in the form of Zernike modes and refractive index mismatch. These aberrations exist in nearly all optical systems, therefore it is important to characterize how these aberrations affect the laser focusing, and subsequently develop methods for their necessary compensation. There have been numerous studies documenting the detrimental effects of phase aberrations in conventional focusing (also described as the conventional spatial focusing (SF), Section 2.4.1, Chapter 2). However, until now, there has been no systematic analysis for the effects of aberrations in simultaneous spatial and temporal focusing (SSTF) (Section 2.4.2, Chapter 2). In this chapter, I study both the spatial and temporal effects of aberrations in SSTF and compare with that of conventional focusing. Both line and wide-field foci are analysed. The results are useful to illustrate the potential of aberration correction for SSTF microscopy, laser fabrication and any similar applications.

3.2 Temporal evolution of focal intensity distribution

In this section, the intensity distribution of the focus at various times for conventional line spatial focusing and line SSTF is presented. The profiles for focusing with and without phase

aberrations are compared.

3.2.1 Line SSTF and line SF

In the previous chapter, the conventional line focusing (line SF) and temporal line focusing (line SSTF) are defined according to their pupil illuminations (Section 2.4). The similarity of line SSTF and line SF is that they generate similar line shape focus when the focal intensity is considered in time averages. The difference is that the wavelength components in line SSTF spread in the pupil and propagate with different optical path, generating a pulse front tilt in the focal plane, while all the wavelength components in line SF propagates with similar optical path to the focal plane, generating the line shape focus completely.

Line SSTF is created by using a spatially chirped beam at the back focal plane of the objective lens. In effect, this creates a single focal spot at one instant time, and the position of the focal spot shifts along x axis temporally. This apparent motion of the focus in the x direction is a consequence of the pulse front tilt (PFT). The term of "pulse front tilt" represents the distorted pulse front with a tilted shape in time domain [124]. The first column in Figure 3.1 (a) shows the temporal distribution of the focal point for SSTF, at the time of -1.5 ps, 0 ps and 1.5 ps, relative to the time of maximum focal intensity using 150 fs pulsed laser light illumination (pulse width $T = 150\ fs$). It is clear that the focal point shifts along x axis, and the intensity increases to the peak at the central focus, and then decreases when it moves away. The time average xz profile shows an obvious line along x axis.

Conventional SF uses spectrally uniform illumination, which directly generates a line along the x axis in the focal plane. This focal shape is a consequence of the reduced numerical aperture in one dimension (along p_x) of the objective pupil. The line exists at all points in time (-0.15 ps, 0 ps and 0.15 ps) with different intensity, as shown in the first column of Fig 3.1 (b).

Aberrations affect both the spatial and temporal intensity distribution of line focusing. As an example, we consider the aberration arising from a mismatch in the refractive index (Section 2.5.2, Chapter 2) between an objective immersion (n_1 = 1.52) and a diamond sample (n_2 = 2.4) when the wavelength of laser is 790 nm. This is relevant for laser machining

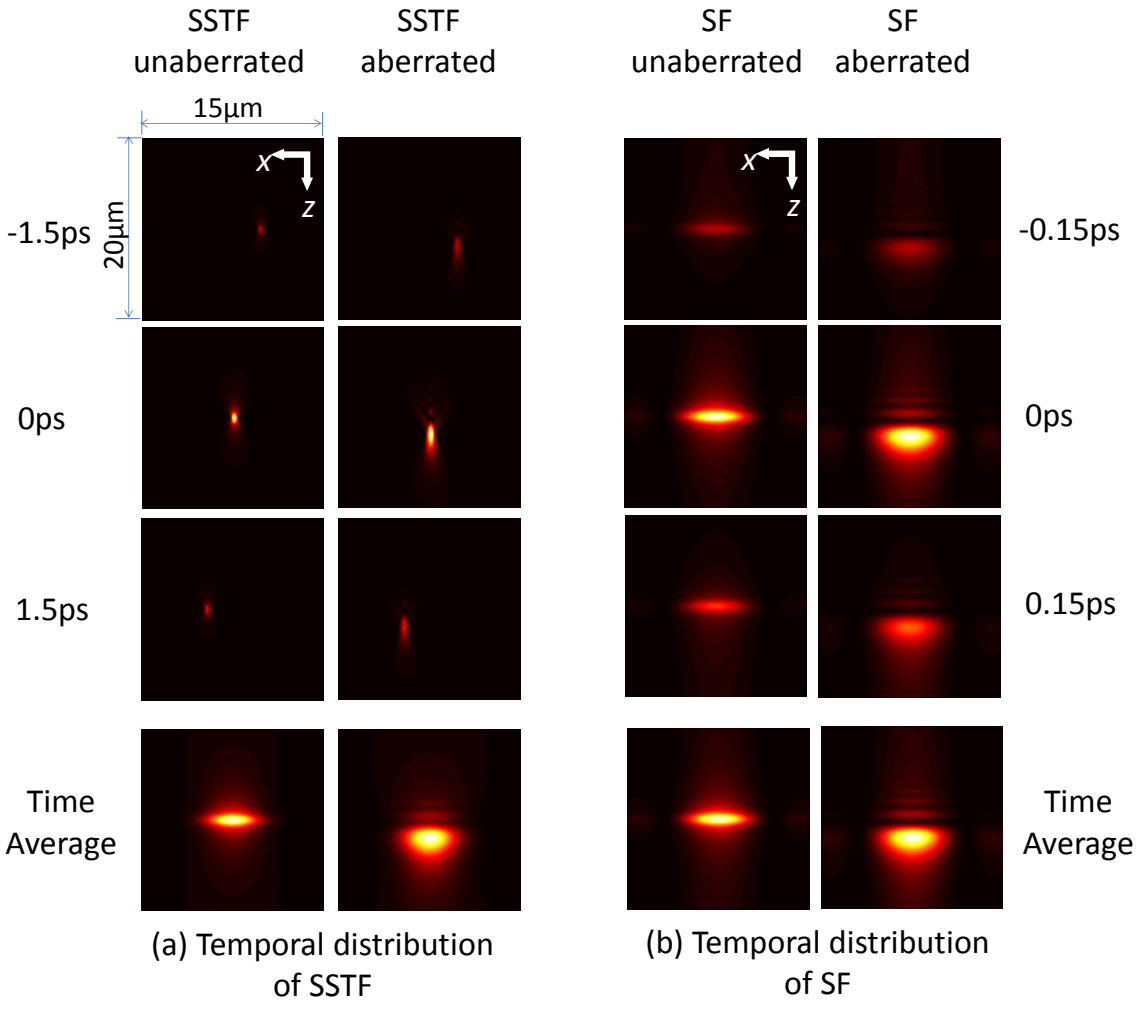

Figure 3.1: Effects of aberration on the temporal focusing properties for line SSTF and line SF. In the images of the aberrated focus, the 150 fs pulsed laser light (pulse width $T = 150\ fs$) with a central wavelength of 790 nm is focused into diamond (refractive index 2.4) with a nominal focus depth of 25 μm by a 1.4NA oil immersion objective lens. Each column is individually normalized. (a) Temporal intensity distribution of SSTF at the time of -1.5 ps, 0 ps and 1.5 ps, as well as the time average profile. (b) Temporal intensity distribution of line SF at the time of -0.15 ps, 0 ps and 0.15 ps, as well as the time average profile.

applications [93]. The second columns in Fig 3.1 (a) and (b) show the cases when the laser light is focused into diamond with a nominal focusing depth of 25 μm. It can be seen that the temporal shapes of both SSTF and SF are distorted and the peak intensity points shift. Sidelobes are generated at lower depths beside the peak intensity points. We note that the sidelobes of SF are larger than that of SSTF, which can be seen in both temporal and time average profiles.

These results were calculated for specific conditions, but the qualitative effects are similar for other focusing configurations and materials. In general, there are some scenarios where the temporal profile at the focus needs to be considered, however, the time average result will be more important for most applications.

3.2.2 Pulse front tilt in SSTF

Pulse front tilt generally exists in most ultrafast laser systems, as the complex optical systems in laser source usually introduces a certain amount of tilt to the pulse front. Also, the pulse front tilt can be easily generated or controlled by a prism or a grating. Diffractive adaptive optics elements, such as a SLM can operate as a variable grating, thus can be used to tune the amplitude of the PFT [125]. Simultaneous spatial and temporal focusing usually creates a spatial chirp of the laser beam by a grating or a prism, thus it also introduces pulse front tilt. This has been seen in previous papers [111, 112, 126]. It is also seen in Figure 3.1 that the focal point shifts along the x direction with time for line SSTF. In this subsection, we investigate this pulse front tilt effect for both line SSTF and wide-field SSTF. The effect of refractive index mismatch aberration on PFT is discussed.

From now on, all the intensity profiles are calculated as the time average of the squared intensity,

$$\left\langle I^2 \right\rangle = {}^{1}\!/_{T_{RT}} \int_0^{T_{RT}} I^2(t)dt \tag{3.1}$$

where T_{RT} is the repeat period of the laser light. This corresponds to the excitation probability for a second order process, such as two-photon fluorescence microscopy. Although in general other non-linear processes may be used, this quantity provides adequate illustration of the focusing effects.

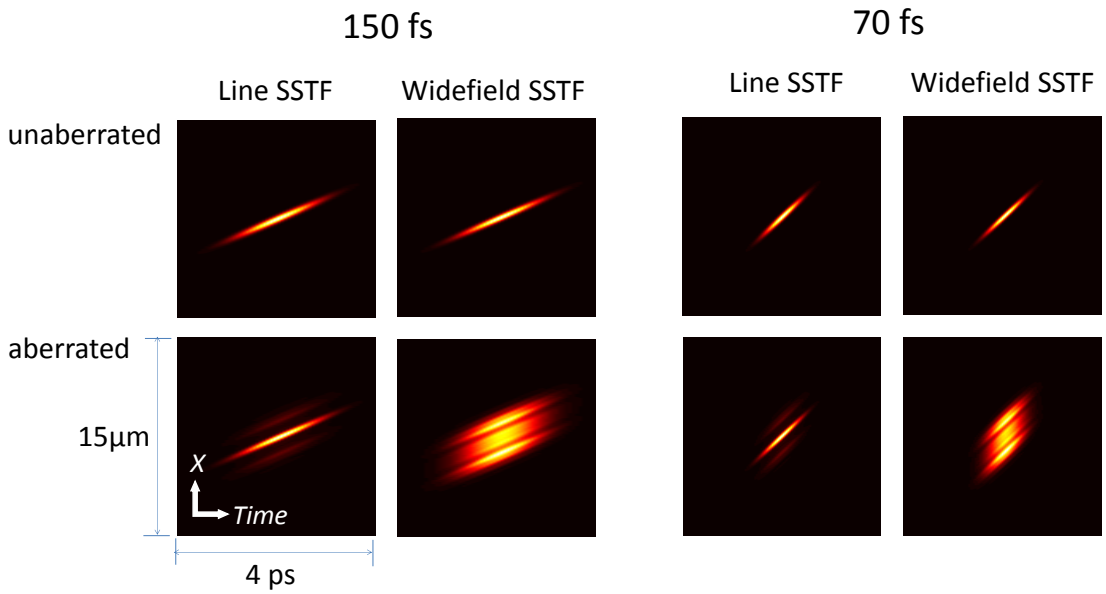

Figure 3.2: Effects of aberration on the temporal pulse front tilt effect for line SSTF and wide-field SSTF. The intensity is calculated at the nominal focal plane. The images on the left hand show the laser with 150 fs pulse width, while the images on the right hand show 70 fs pulse width. In the images of the aberrated focus, the laser light with a central wavelength of 790 nm is assumed to be focused into diamond (refractive index 2.4) with a nominal focus depth of 25 μm by a 1.4NA oil immersion objective lens. Each image is individually normalized to its own peak intensity.

Figure 3.2 presents the calculation for the intensity distribution along the x direction and $time$ axis. Each image is individually normalized to its own peak intensity. For an example of the unaberrated line SSTF, it is seen that the focus shifts along x direction when the time increases. An obvious pulse front tilt is seen. For the laser with the same pulse width, the temporal intensity distributions of line SSTF and wide-field SSTF have no difference when the intensity profile is unaberrated. When the laser is focused into a diamond sample, aberration arises from the refractive index mismatch. Sidelobes are generated along the focus. Comparing the aberrated profiles of line SSTF and wide-field SSTF, the mismatch aberration has much more obvious influence for the temporal focus of wide-field SSTF. It is notable that the peak intensity point shifts with the existence of refractive index mismatch aberration, however, the calculation in this figure is only conducted at the nominal focal plane. In addition, the calculations for laser with a pulse width of 70 fs is compared with the laser of 150 fs. With the same scales for the x and $time$ axis, the pulse front tilt presents different angles for different pulse widths. However, the physical distance for the focal movement along x direction is the

same for both laser pulse widths.

3.3 Line focusing

In this section, we investigate the effects of lower-order Zernike modes and refractive index mismatch phase aberrations on the line spatial focusing (SF) and line SSTF. The focal distortion and the intensity reduction effect are presented. The pupil illuminations of the investigated line focus are shown in Figure 2.2 (b) and Figure 2.4 (a) in Chapter 2. The $\langle I^2 \rangle$ distribution along y and z direction is studied (at the plane where $x = 0$), because it gives a better view of the distortion both along the axial and lateral directions.

3.3.1 Zernike mode aberration

Figure 3.3 and 3.4 shows the distortions occurring in SSTF (a)-(c) and SF (d)-(f) in the presence of individual Zernike modes. Each image (including both unaberrated and aberrated cases) is individually normalized to its own peak intensity. The SSTF pupil illumination profile is shown in the first inset in (a); plots of the Zernike modes in the pupil are shown as the remaining insets. While the unaberrated line focus stretches as a line along the x direction, it has a good confinement along both the z and y directions, which are shown as the first profile in (a). The $\langle I^2 \rangle$ profiles show different distortions when Zernike modes are considered. Mode 6 (astigmatism) and mode 11 (spherical) cause the peak $\langle I^2 \rangle$ to shift along the axial direction, while other modes, especially mode 8 (coma), mode 10 (trefoil) and mode 11 (spherical), produce various amounts of focal distortion. These effects are also characterized by the plots in row (b), which show how the peak $\langle I^2 \rangle$ in the y direction changes along z direction (where we define $I_p(z) = \text{Max}_y \left[\langle I^2 \rangle (y, z) \right]$). The effects of particular Zernike mode aberrations can be understood by comparison of the pupil illumination profile and phase plots (the insets in row (a)) in each case. For example, mode 6 creates a defocus-like phase distortion for each spectral component in the pupil, which shifts the focus for each component by a different amount along the z axis; modes 8, 10 and 11 cause more complex phase deviations for each spectral component, which leads to distortion at the focus. The peak $\langle I^2 \rangle$ of the distorted

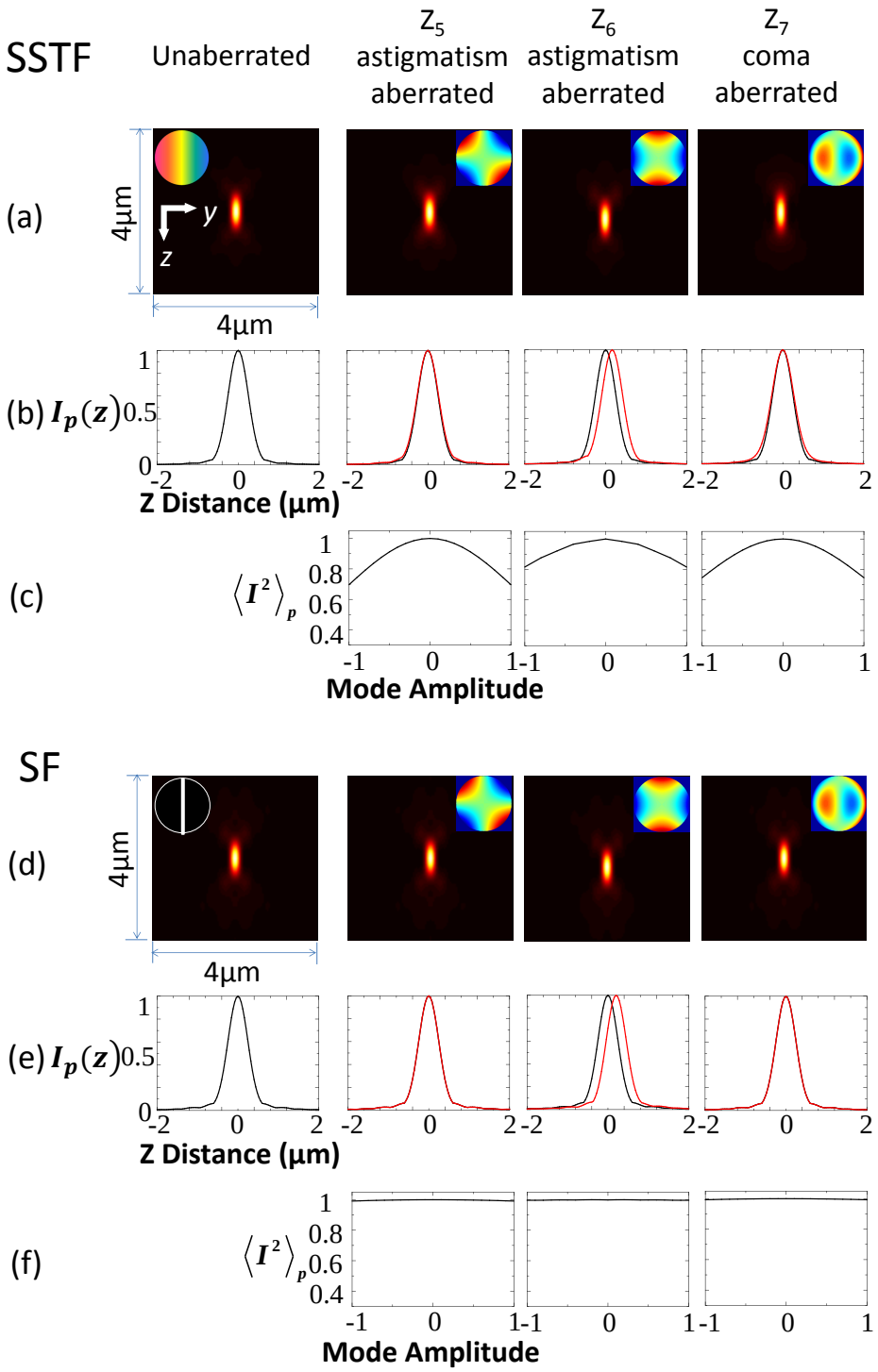

Figure 3.3: Effects of Zernike mode aberrations (modes 5-7) on line focus. Each image is individually normalized to its own peak intensity. (a)-(c) Simultaneous spatial and temporal focusing (SSTF). (a) Comparison of the $\langle I^2 \rangle$ yz profiles between the unaberrated case and with Zernike modes 5-11 aberrated cases. The inset in the first profile is the pupil illumination, and the insets in the remaining profiles show the phase of the Zernike modes. (b) Normalized plot of the variation of $I_p(z)$ (red curve). The black curve is the unaberrated case included for comparison. (c) Peak $\langle I^2 \rangle$ changes with Zernike mode amplitude (rad. (rms)) of the central wavelength. (d) - (f) The effects of Zernike modes on conventional spatial focusing (SF). Each row indicates the same comparison as above.

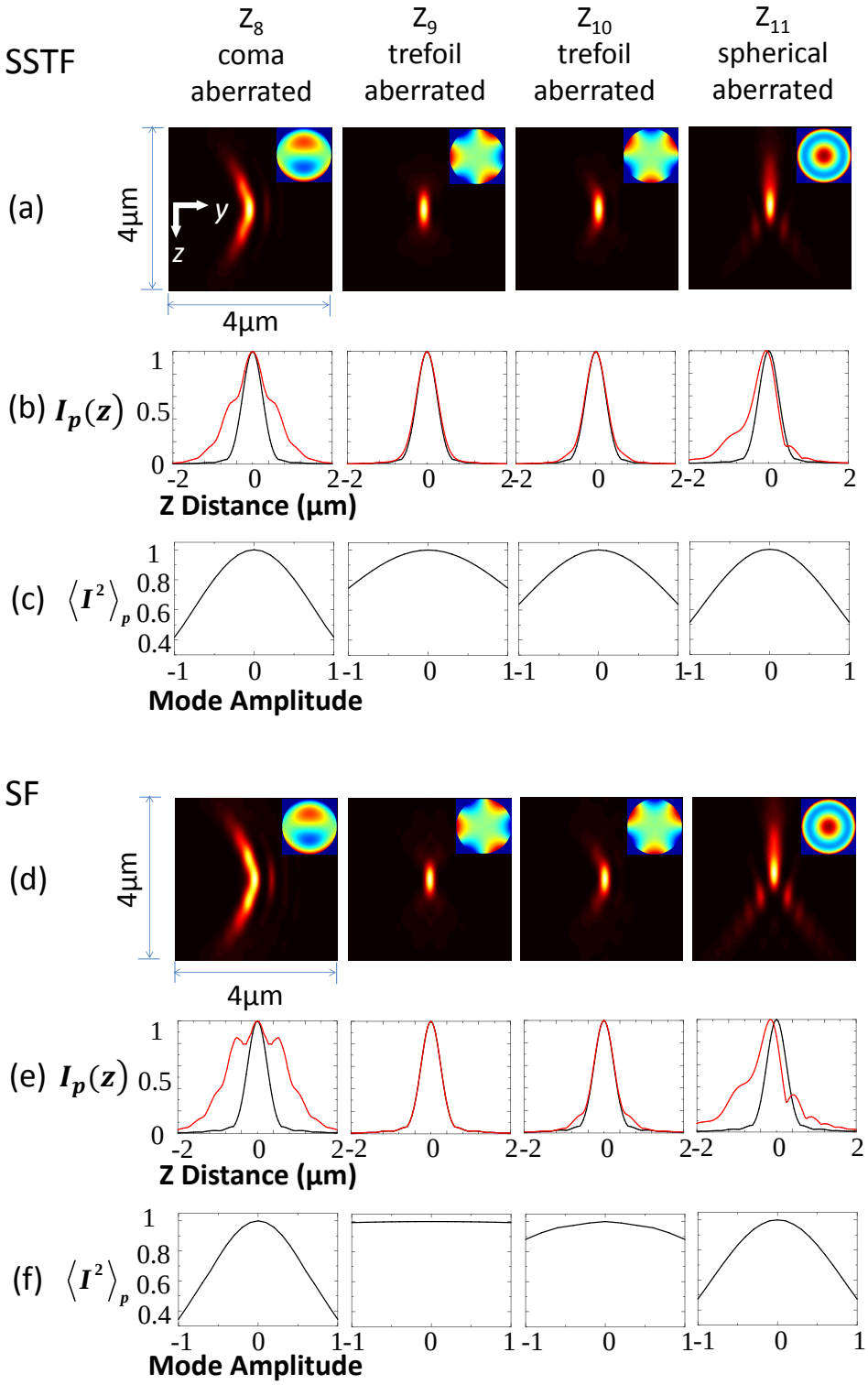

Figure 3.4: Effects of Zernike mode aberrations (modes 8-11) on line focus. Each profile is calculated as the time average of the squared intensity $\langle I^2 \rangle$, and normalized to its own peak intensity. (a)-(c) Simultaneous spatial and temporal focusing (SSTF). (d) - (f) The effects of Zernike modes on conventional spatial focusing (SF). All the figure indications are the same with Figure 3.3.

focus as a function of the amplitude of the Zernike mode (measured in rad. (rms) at the central wavelength) is also illustrated in row (c). As the SSTF uses full pupil illumination, all the Zernike modes have effects on the focusing, and thus cause reduction in the peak $\langle I^2 \rangle$.

A comparison of these results with line SF is shown in Figure 3.3 and 3.4 (d)-(f). Similarly, mode 8 (coma), mode 10 (trefoil) and mode 11 (spherical) produce various amounts of intensity distortion. As shown in row (f), these three modes cause a drop in the peak intensity. From the $\langle I^2 \rangle$ profiles and the axial $I_p(z)$ distribution, it is seen that the sidelobes of the distorted SF are stronger than that of SSTF. The larger drop in peak $\langle I^2 \rangle$ is because the pupil illumination of SF is a single line, and the Zernike modes 8, 10 and 11 have a more significant phase distortion along this line than in other areas. Mode 6 (astigmatism) and mode 11 (spherical) cause a focus shift along the z direction, but mode 6 exhibits a very slight drop in peak intensity. By comparing the pupil illumination of line SF and the phase plots of each Zernike mode, it is easy to find that modes 5, 7 and 9 have little effect on the line SF, because the phase in these three modes is nearly flat in the area along line illumination in the SF pupil. Through these investigations, we can conclude that, the value of $\langle I^2 \rangle$ in SSTF line focusing is more sensitive to certain Zernike aberrations than the equivalent value for SF line focusing. However, the effects on spatial resolution are similar in both cases.

3.3.2 Index mismatch aberration

In many laser fabrication and microscopy applications, a high NA objective lens is used to focus laser light deep into a sample with a refractive index differing to the lens immersion medium. This scenario is modelled in Figure 3.5 (a) (b) for both SF and SSTF, where we consider the aberration arising when the light is focused with a 1.4 NA oil (n_1 = 1.52) lens into a diamond sample (n_2 = 2.4) with a nominal focusing depth of 50 μm [93]. Each image is individually normalized to its own peak intensity. The focus is distorted generating several sidelobes above the peak intensity point, with a corresponding reduction in peak $\langle I^2 \rangle$. Figure 3.5 (c) shows the $I_p(z)$ distribution along the axial direction for unaberrated and aberrated line SSTF as well as line SF foci, and each curve is individually normalized. The FWHM of the $\langle I^2 \rangle$ along the z direction becomes wider, and the on-axis peak intensity points are obvi-

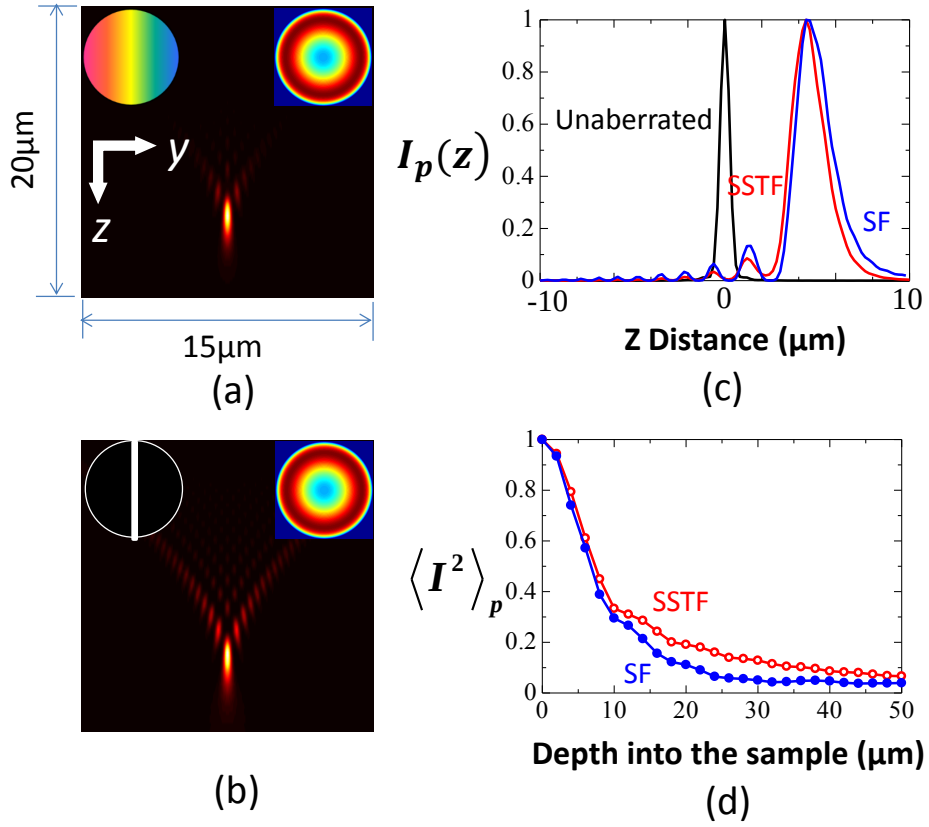

Figure 3.5: Effects of refractive index mismatch on a line focus. Each image is individually normalized to its own peak intensity. The sample is diamond with the refractive index of 2.4. The light is focused by using a 1.4 NA oil immersion lens. The nominal focus depth is 50 μm. (a) Aberrated $\langle I^2 \rangle$ yz profile for line SSTF. Insets are the pupil illumination (left) as well as the phase induced by the index mismatch (right, with defocus element removed). (b) Aberrated yz profile for line SF. (c) Comparison of the axial $I_p(z)$ distribution for unaberrated and index mismatch aberrated SSTF and SF. Each curve is individually normalized. (d) Peak $\langle I^2 \rangle$ changes with the nominal focus depth into the sample for line SSTF and SF. Each curve is individually normalized.

ously shifted because of the distortion. We note that this shift in the on-axis peak intensity is in addition to the axial shift due to the defocus component of the phase aberration function (described in the end of section 2.5.2). These aberration phenomena have been widely observed in modelling of refractive index mismatch induced aberrations in conventional focusing systems [127]. The $\langle I^2 \rangle$ profiles and curves show that the sidelobes of SSTF line focusing are smaller than that of SF. Figure 3.5 (d) shows the peak $\langle I^2 \rangle$ dropping with the increase in nominal focus depth into the sample. As a conclusion, the effect of index mismatch is slightly smaller on line SSTF than that on line SF, which suggests that line SSTF might be a better

choice for the cases involving deep focusing into high index sample considering the amount of aberration.

3.4 Wide-field focusing

In this section, we investigate the effects of lower-order Zernike modes and refractive index mismatch phase aberrations on the wide-field SSTF. The pupil illumination of the wide-field SSTF is shown in Figure 2.4 (b) of Chapter 2.

3.4.1 Zernike mode aberration

In the widefield SSTF, a symmetric focusing shape is obtained both along the axial and lateral directions, which is shown by the unaberrated xz profile in Figure 3.6 (a). The widefield area experiences different peak intensity shifts or intensity stretches when Zernike mode aberrations are considered. The xz $\langle I^2 \rangle$ profiles (at y = 0) in the presence of Zernike modes 5-11 are shown in Figure 3.6 (a), the variation of $I_p(z)$ is presented in Figure 3.6 (b), and Figure 3.6 (c) shows how peak $\langle I^2 \rangle$ changes with each Zernike modes amplitude. Each image (including both unaberrated and aberrated cases) is individually normalized to its own peak intensity. The pupil illumination of widefield SSTF is such that the components of the spectrum are distributed along p_x direction, but only have a narrow extent in the p_y direction. Comparing the pupil illumination to each Zernike mode plot in the pupil (the insets in Figure 3.6 (a)), it is understandable that modes 5, 8, and 10 have little effect on the focusing properties. The input energy is spread as a line along the p_x axis in the pupil, where, for these modes, the phase is essentially constant. The axial $\langle I^2 \rangle$ distribution is nearly the same as the unaberrated profile, and the peak $\langle I^2 \rangle$ shows negligible change with increasing mode amplitude. Mode 6 slightly shifts the axial position of the widefield area, but does not cause intensity reduction; this is a consequence of the quadratic, defocus-like form of phase along the illumination axis of the pupil. Modes 7, 9 and 11 distort the focus, and cause a decrease in focal intensity. It is notable that mode 11 (spherical) not only stretches the focus, but also causes large shift in peak intensity along the axial direction.

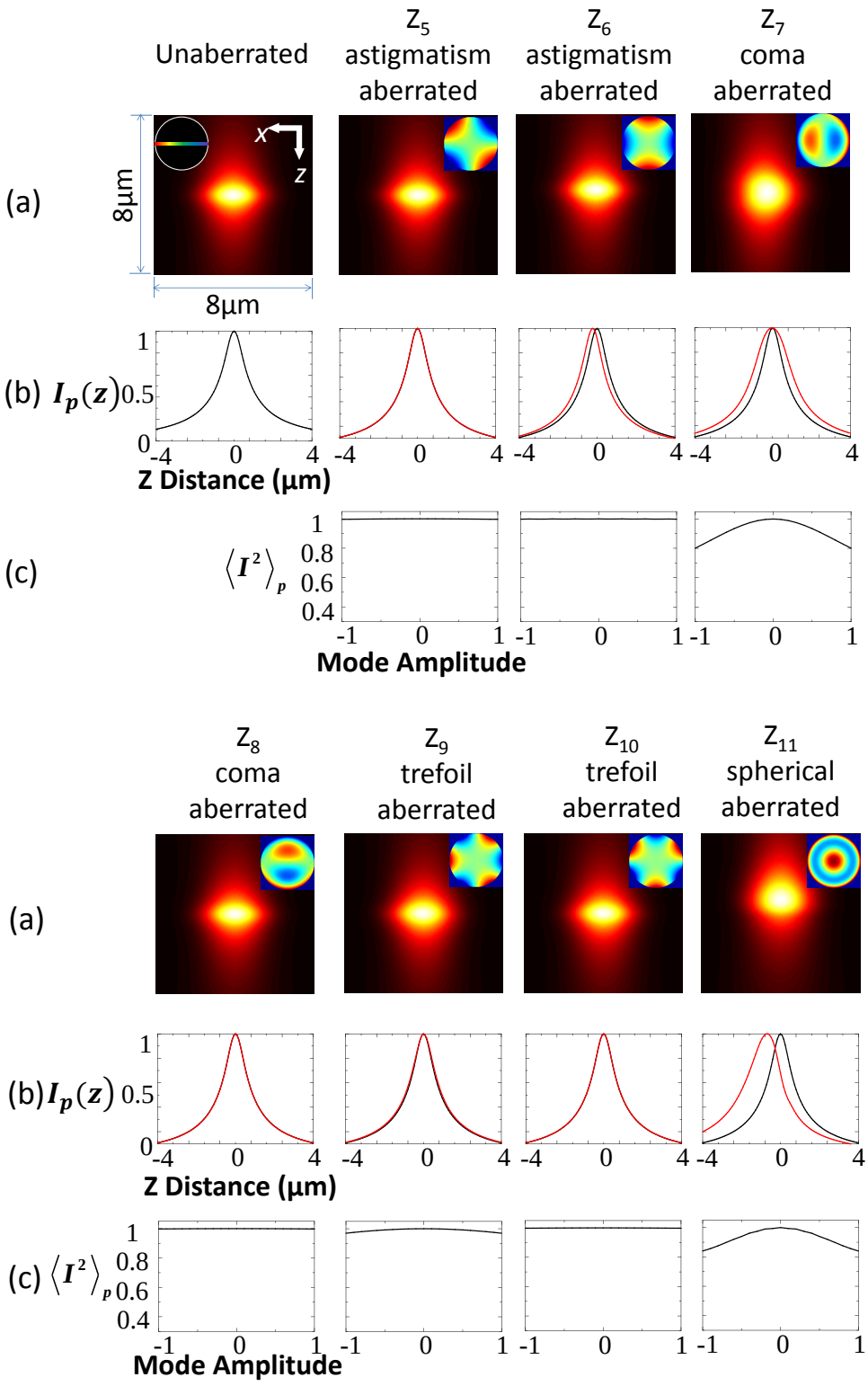

Figure 3.6: Effects of Zernike mode aberrations on widefield simultaneous spatial and temporal focusing (SSTF). Each image is individually normalized to its own peak intensity. (a) Comparison of $\langle I^2 \rangle$ xz profiles between unaberrated and Zernike mode 5-11 aberrated (central wavelength amplitude equals to 1 rad. (rms)) widefield SSTF. The inset in the first figure is the pupil illumination, and the insets in the aberrated figures are the Zernike modes phase plot in the pupil. (b) Normalized plot of the variation of $I_p(z)$ (red curve). The black curve is the unaberrated version included for comparison. (c) Peak $\langle I^2 \rangle$ changes with Zernike mode amplitude (rad. (rms) of the central wavelength).

3.4.2 Index mismatch aberration

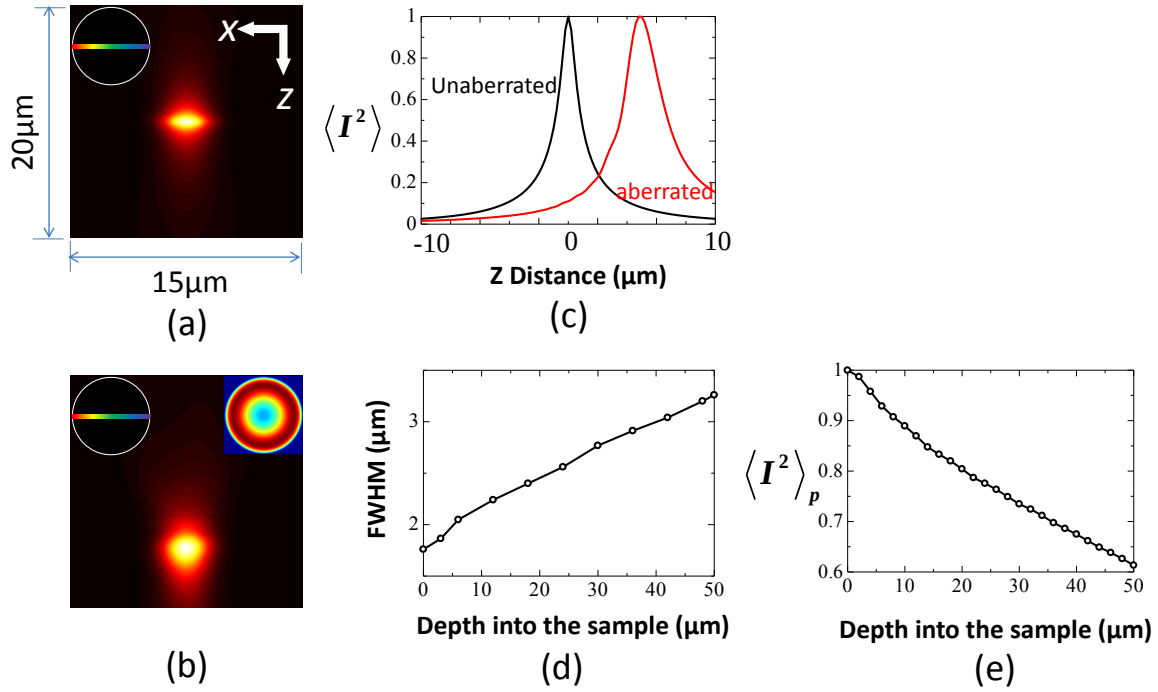

Figure 3.7: Effects of refractive index mismatch on widefield SSTF. Each image is individually normalized to its own peak intensity. The sample is diamond with the refractive index of 2.4. The nominal focus depth is 50 μm. (a) Unaberrated $\langle I^2 \rangle$ xz profile for widefield SSTF. (b) Aberrated $\langle I^2 \rangle$ xz profile. Insets are the pupil illumination (left) as well as the phase induced by the index mismatch (right, with defocus element removed). (c) Comparison of axial $\langle I^2 \rangle$ distribution for unaberrated and index mismatch aberrated widefield SSTF. Each curve is individually normalized. (d) FWHM of the $\langle I^2 \rangle$ distribution along axial direction versus nominal focus depth into the sample. (e) Peak $\langle I^2 \rangle$ changes with the focusing depth into the sample for SSTF.

When the laser light is focused in widefield SSTF by a high NA lens deep into a high index sample, the index mismatch causes focal distortion and consequently a reduction in axial resolution. Comparison of the unaberrated xz $\langle I^2 \rangle$ profile in Figure 3.7 (a) and the index mismatch aberrated profile in Figure 3.7 (b) indicates an obvious change in the shape and the position of the focusing area. Each image is individually normalized to its own peak intensity. The $\langle I^2 \rangle$ distribution along the axial direction for the two profiles is shown in Figure 3.7 (c). We find the FWHM increases for aberrated focusing. The FWHM increases from 1.76 μm at the surface to 3.26 μm at a nominal focus depth of 50 μm. The axial FWHM of the $\langle I^2 \rangle$ distribution as a function of nominal focus depth into the sample is shown in Figure 3.7 (d). The FWHM continues to broaden with increasing depth, with a corresponding reduction in

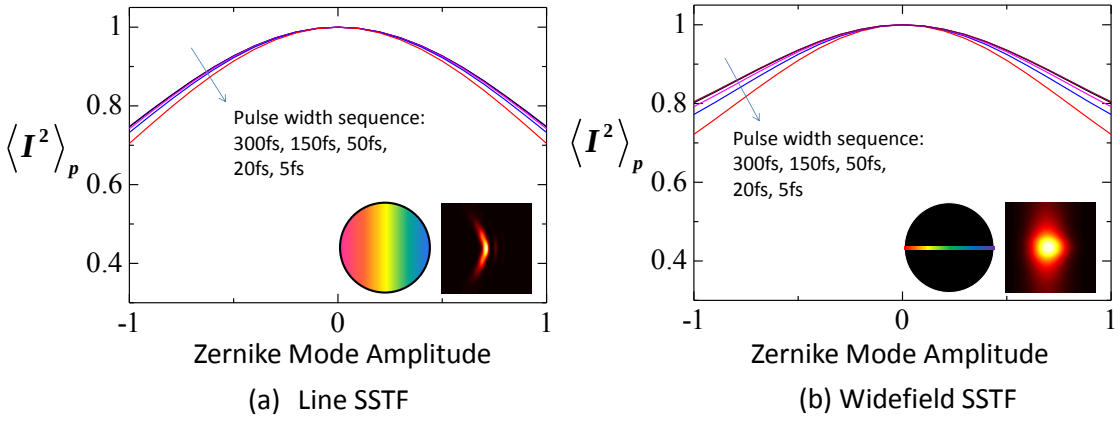

Figure 3.8: The effect of a coma aberration (mode 7) with different pulse widths (T). The graphic shows the peak $\langle I^2 \rangle$ changes with Zernike mode amplitude (rad. (rms)) of the central wavelength. Insets are the pupil illumination and aberrated $\langle I^2 \rangle$ profile. (a) Line SSTF. (b) Widefield SSTF.

peak intensity, as shown in Figure 3.7 (e). It is notable that with the same focusing depth into a sample, the peak intensity of widefield SSTF is not as sensitive to aberrations as the line focus (Figure 3.5 (d)). For example, when the light is focused into diamond with a depth of 50 μm, the peak $\langle I^2 \rangle$ dropped to 61% for widefield SSTF, 7% for line SSTF, 4% for line SF and 0.6% for point SF.

3.5 Aberration effect for different pulse widths

The Zernike mode amplitude is a parameter dependent on frequency, while the spectral range of the laser light is set by the pulse width, suggesting that the pulse width should have an influence on the effects of aberrations. The qualitative effects are similar for different pulse widths, but the level of distortion varies for each specific focusing method. We take the example of coma aberration to illustrate the effects of changing the pulse width. Peak $\langle I^2 \rangle$ versus Zernike mode amplitude is calculated for different pulse widths, while p_{xo} is adjusted for each width in order to maintain the same axial and lateral resolution. Figure 3.8 shows the influence of the pulse width on line SSTF and widefield SSTF. Focusing with shorter pulse widths is slightly more affected by the aberrations. For example, in Figure 3.8 (b), when the coma aberration is applied with amplitude of 1 rad. (rms) at the central wavelength, the peak $\langle I^2 \rangle$ using 300 fs

pulses drops to 80%, but for 5 fs pulse the peak $\langle I^2 \rangle$ drops to 72%. This is because the magnitude of the phase aberration varies with the light wavelength, so that the laser with broad band-width (lower pulse width) is affected more by the phase aberrations.

3.6 Discussion

The reason for the robustness of line SF and widefield SSTF to some Zernike modes, for example modes 5, 7 and 9 for line SF and modes 5, 8 and 10 for widefield SSTF, is that only part of the pupil is illuminated. The focus will be less distorted if this illuminated part of the pupil has less phase aberration for particular Zernike modes. We note that one can use this observation to draw conclusions about other modes that we have not studied directly here.

When the laser light is focused into a sample with a refractive index mismatch, the FWHM is broadened and peak intensity is reduced. These trends for either line or widefield SSTF are also applicable for other different materials and lenses, other than used for the calculations in this paper.

We should also note that in this chapter, we mainly use a second order excitation probability to model focal aberration effects. However, the trends observed will also be relevant for higher order processes, such as in harmonic generation for microscopy or high-order non-linear fabrication processes.

In this chapter, non-linear refractive index variation due to Kerr effect is neglected. It is notable that self-focusing and other non-linear effect would bring additional focal distortion when high power laser is used.

These results provide the basis for understanding the effects of aberrations on SSTF systems and the performance improvement that might be achieved through aberration correction. Several SSTF systems now include complex illumination structuring to create photo-activation patterns [107, 108], or for patterned laser fabrication [113, 114]. Further work will illustrate how aberrations affect these more complex illumination systems. Furthermore, we also note that in applications of SSTF multiphoton microscopy, imaging of the generated fluorescence onto the detector will also be affected by the aberrations, whereas our modelling so far has involved only the excitation effects.

3.7 Conclusions

Phase aberrations affect the focal distributions in SSTF and SF systems. This has been shown for lower order Zernike modes and refractive index mismatch aberrations in line and widefield focusing systems. The particular aberrations cause reduction of the axial and lateral resolution, reduction in peak intensity, or shift of the focus. Compared to line SF, line SSTF is more sensitive to Zernike modes aberrations, while slightly less sensitive to index mismatch aberrations. Widefield SSTF is much more robust to both Zernike modes and index mismatch aberrations than line focusing.

Chapter 4

Effects of sample dispersion on ultrafast laser focusing

4.1 Introduction

In Chapter 3, the effects of phase aberrations on laser focusing are discussed. In addition to phase aberrations, the dispersion of various optical components in the system also introduces focal distortions. The dispersion of lens, including chromatic aberration, PTD and GVD have already been discussed in Section 2.6 of Chapter 2.

In the focusing of ultrafast lasers, the sample material also brings undesired dispersion effect. The impact is especially significant when laser pulses with shorter duration are focused into sample at larger depths. However, there has until now not been a study for this type of sample dispersion effects. This chapter describes an investigation into spatial and temporal distortions caused by the dispersion of sample materials. To begin with, conventional focusing is studied, and the dispersion effects when focusing with high and low numerical aperture (NA) objective lens are compared. Simultaneous spatial and temporal focusing (SSTF) with both line and wide-field configurations [99, 103] are then investigated. I conclude with a discussion of the effects of different laser parameters and sample materials.

4.2 Theory

This section describes the analytical approach to characterize the effects of sample dispersion on ultrafast laser focusing. The spectral phase maps at the objective pupil introduced by the sample dispersion are presented.

4.2.1 Dispersion effect

It has been shown in Chapter 2 that Fourier optics [97, 128] is adopted to calculate the focal intensity distribution when the laser light is focused by an objective lens into a dispersive medium. When the laser light is focused into a sample, light refraction at the interface of the objective lens immersion medium (refractive index n_1) and the specimen (refractive index n) is represented by a phase function in the objective pupil (details in Section 2.5.2, Chapter 2):

$$\phi(\lambda, n) = -\frac{2\pi}{\lambda} \cdot d \left(\sqrt{n^2 - \rho^2 NA^2} - \sqrt{n_1^2 - \rho^2 NA^2} \right) \tag{4.1}$$

where d is the nominal focusing depth, that is the focal depth ignoring the effect of refraction at the specimen interface, NA is the numerical aperture of the objective lens and ρ is the normalized radius in the pupil of the objective lens. The phase in Equation (4.1) contains a spherical element $\widehat{\phi}$, which causes distortion of the focus, and a defocus element D, which causes focal position shift:

$$\phi(\lambda, n) = \hat{\phi}(\lambda, n) + D(\lambda, n) \tag{4.2}$$

The distortion from RIM aberration is much more significant than the sample dispersion effect. For the simulations presented in this chapter, we assume that an adaptive optics element (AOE) such as a deformable mirror (DM) has been used to compensate the RIM aberration. However, an AOE can provide ideal correction across all spectral components of the laser pulse only assuming the refractive index of the sample is a constant. If dispersion is present, then only partial correction is possible, for example by implementing perfect correction at the center wavelength; the other wavelengths in the laser spectrum are then only partially compensated. By subtracting the influence of the RIM aberration of the center wavelength,

we are able to concentrate on studying the residual sample dispersion effects. In this case, the effect of the sample dispersion could be expressed by the phase term,

$$\Phi_{dispersion}(\lambda) = \phi(\lambda, n_\lambda) - \phi(\lambda, n_0) \tag{4.3}$$

where n_λ and n_0 are the refractive indices of the sample at the wavelength λ and at the central wavelength λ_0, respectively. $\phi(\lambda, n_0)$ represents the correction phase introduced by the AOE. According to Equation (4.2), Equation (4.3) can be re-written as:

$$\Phi_{dispersion}(\lambda) = \hat{\phi}(\lambda, n_\lambda) - \hat{\phi}(\lambda, n_0) + D(\lambda, n_\lambda) - D(\lambda, n_0) \tag{4.4}$$

We define the spherical aberration difference $\hat{\phi}_{spherical}(\lambda)$ as,

$$\hat{\phi}_{spherical}(\lambda) = \hat{\phi}(\lambda, n_\lambda) - \hat{\phi}(\lambda, n_0) \tag{4.5}$$

while the focal shift difference $D_{shift}(\lambda)$ is expressed as,

$$D_{shift}(\lambda) = D(\lambda, n_\lambda) - D(\lambda, n_0) \tag{4.6}$$

In Equation (4.4), the effect of sample dispersion is contributed by both the spherical aberration difference $\hat{\phi}_{spherical}(\lambda)$, which represents a small amount of focal distortion, and the focal shift difference $D_{shift}(\lambda)$ which represents the axial shift of the peak intensity for a given wavelength component away from the nominal focal point.

As this chapter investigates the dispersion effects of the sample, the dispersions of the objective lens and other optical elements in the optical system are therefore not included. The field function at the pupil of the objective lens including the wavelength dependent aberration due to sample dispersion could be expressed as:

$$\widetilde{E}(\lambda, p_x, p_y) = E(\lambda, p_x, p_y) e^{-j\Phi_{dispersion}(\lambda)} \tag{4.7}$$

4.2.2 Phase maps

Several commonly used optical materials which have different levels of dispersion are studied: lithium niobate ($LiNbO_3$) [129, 130], which is an important material for optical waveguides, sensors and modulators; SF11 glass, which is popular in various optical components (such as lenses, prisms); water (H_2O) [131, 132], which forms the basis for many biological specimens studied in non-linear optical microscopy; fused silica (SiO_2) [133], which is well known for its applications in semiconductors and optical devices; and diamond [134, 135], which is attractive for photonic and quantum technologies. Lithium niobate ($LiNbO_3$) is used as an example for the calculations of Sections 4.3 and 4.4, while all the materials are compared later in Section 4.5. The Sellmeier refractive index equations of these materials are presented in the Appendix of this Chapter.

Most optical materials have dramatic dispersion in ultraviolet region and relatively smaller dispersion in the near infrared region. In Sections 4.3 and 4.4, we consider laser light with a central wavelength of 520 nm to illustrate the distortion patterns. The corresponding femtosecond lasers around this wavelength region with short pulse durations can be either frequency-doubled passively mode-locked solid-state bulk lasers (such as Diode-pumped lasers and Titanium-sapphire lasers) [1, 136]. The observed phenomenon is similar for lasers within other wavelength regions. The influence of laser central wavelength with different magnitude of sample dispersion effect is discussed later in Section 4.5.

To illustrate the sample dispersion effect, examples of the spectral phase map at the pupil [128] are plotted in Figure 4.1. The calculation assumes the laser is focused into $LiNbO_3$ with a 0.5 NA oil immersion lens. The phase maps are spatially symmetric about the center of the pupil (along vertical axis), while varying with the wavelength of the light (along horizontal axis). In each phase map, the greater phase variation at shorter wavelengths is a consequence of higher sample dispersion in this wavelength region. It is seen that when the laser is focused with a high depth, the generated phase variation is greater than that for focusing at a low depth. This is easily understandable that a higher depth of focusing creates larger difference in the optical path length for the wavelength components. The focusing with 0.5NA objective lens is compared with the focusing with 1.35NA objective lens. It is seen that with the same focusing

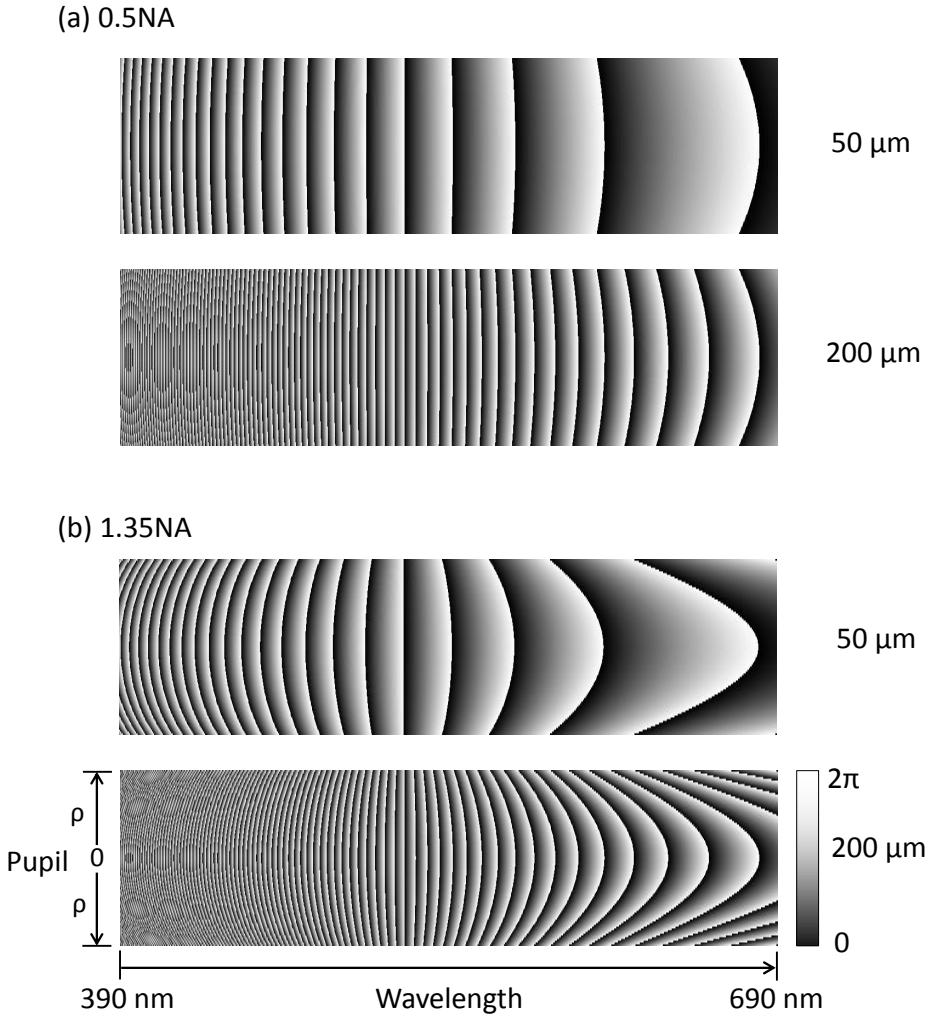

Figure 4.1: Spectral phase maps due to sample dispersion. (a) The calculation assumes the laser is focused 50 μm or 200 μm into $LiNbO_3$ with a 0.5 NA oil immersion lens. (b) The calculation assumes the laser is focused 50 μm or 200 μm into $LiNbO_3$ with a 1.35 NA oil immersion lens.

depth, focusing with higher NA lens generates more phase variation than the focusing with lower NA lens.

4.3 Conventional point focusing

In this section, we study the effect of dispersion on conventional point focusing. In the discussion below, the laser pulse duration (FWHM of the temporal pulse) is chosen to be 25 fs when investigating the temporal pulse broadening and overall intensity reduction effects, whereas 10 fs pulse duration is used to illustrate the spatial focal distortion effects. Spatial distortion

is usually less obvious, thus the shorter pulse duration is adopted to reveal the details of the effect. The influence of laser pulse duration is discussed later in Section 4.5. The effects when focusing with low (0.5) and high (1.35) NA lenses are compared in this section. We note that the immersion medium (such as water or oil) of a high NA lens and any other intervening materials (such as a cover glass) may contribute additional dispersion effects, although these are not included in the analysis of this chapter.

4.3.1 Spatial focal distortion

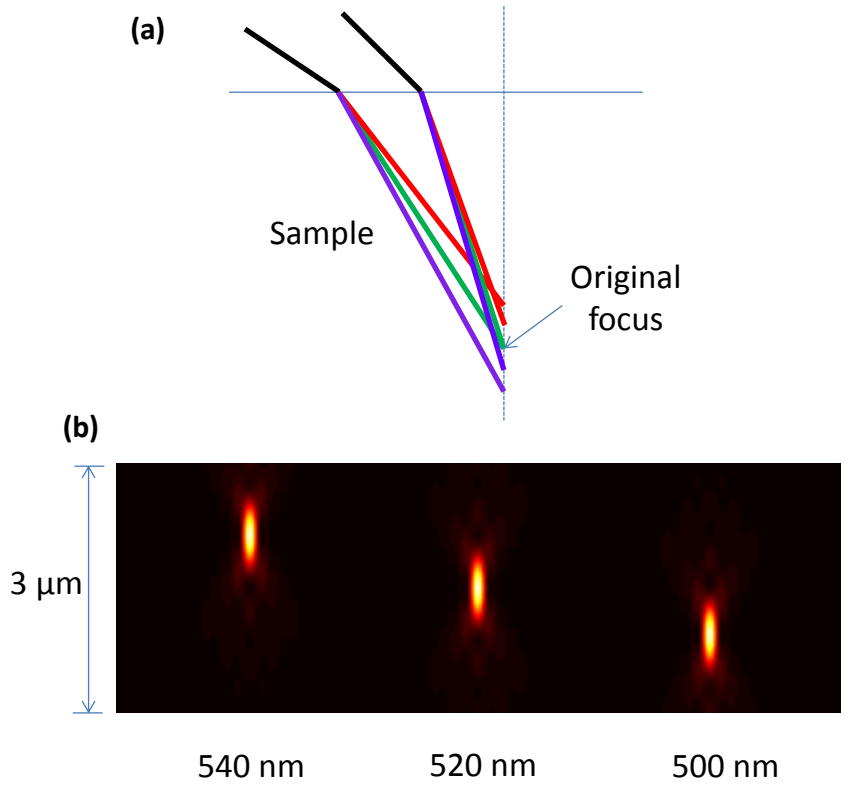

Figure 4.2: (a) A sketch showing the angles of refraction for different wavelength components inside the sample. Two optical rays at the sample interface with different incident angles are illustrated. (b) Simulation of the focal intensity distribution for single wavelength components. The laser is assumed to focused by a 1.35 NA lens.

Figure 4.2 explains the effect of sample dispersion on the axial spatial profiles. Equation (4.4) suggests that dispersion contributes different amounts of spherical aberration and focal shift for each spectral component. As illustrated in the sketch of Figure 4.2 (a), the focal shift, which is the major reason for axial elongation, can be explained by the fact that light of

different wavelengths propagate into the sample with different angle of refraction. This causes the different wavelength components to have different focal shifts relative to the nominal focal position. The contribution to the focal intensity from three single wavelength components (500 nm, 520 nm and 540 nm) is calculated for an input laser centered at 520 nm wavelength, shown in Figure 4.2 (b). For the illustration, each focus is normalized to its own peak intensity, though the practical intensity amplitude for 500 nm and 540 nm wavelength components are about 40% to that of central wavelength 520 nm component. It is obviously seen that the focal positions of 500 nm and 540 nm wavelength components are shifted away from the nominal focal point by about 0.5 μm.

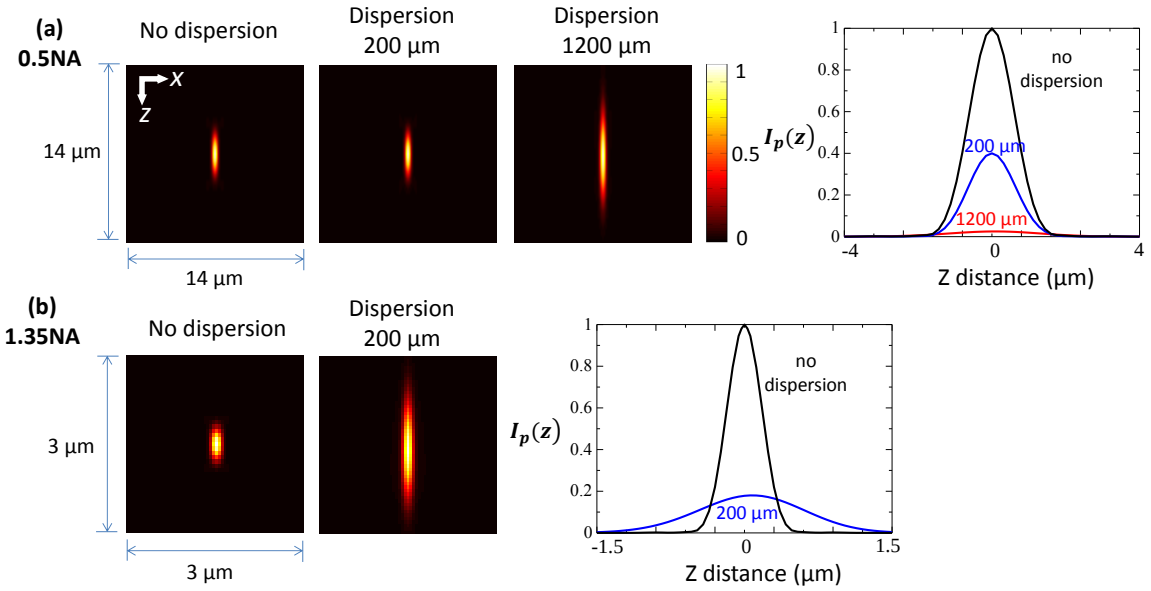

Figure 4.3: (a) Effects of sample dispersion on the spatial focal intensity distribution of conventional point focusing. Original pulse duration is 10 fs. Each profile is normalized independently to its peak intensity. Axial $\langle I^2 \rangle$ profiles and axial peak $\langle I^2 \rangle$ plot when the laser is focused by (a) a 0.5 NA lens and (b) a 1.35 NA lens.

In the calculation below, the intensity is calculated as the time average of the squared intensity (Equation (3.1)). The left profiles in Figure 4.3 (a) and (b) show the laser focused into the sample when there is no dispersion. As the index mismatch aberration is corrected by the AOE, the spatial profile does not change with focal depth. With sample dispersion, the focus is elongated along the axial direction. When the laser is focused with a depth of 200 μm, there is no obvious spatial distortion for the 0.5 NA lens, while there is a significant spatial elongation for the 1.35 NA lens. This shows the spatial distortion is more severe when

focusing with a high NA lens, which should be expected, when one considers the effects of dispersion on the refraction angle of different spectral components (Figure 4.2 (a)). The normalized peak $\langle I^2 \rangle$ along the axial z direction (defined as $I_p(z) = \text{Max}_{\ x}\left[\langle I^2 \rangle (x,z)\right]$) is plotted in the right hand figures of Figure 4.3 (a) and (b). The drop in intensity due to the sample dispersion is clearly seen.

4.3.2 Temporal pulse broadening

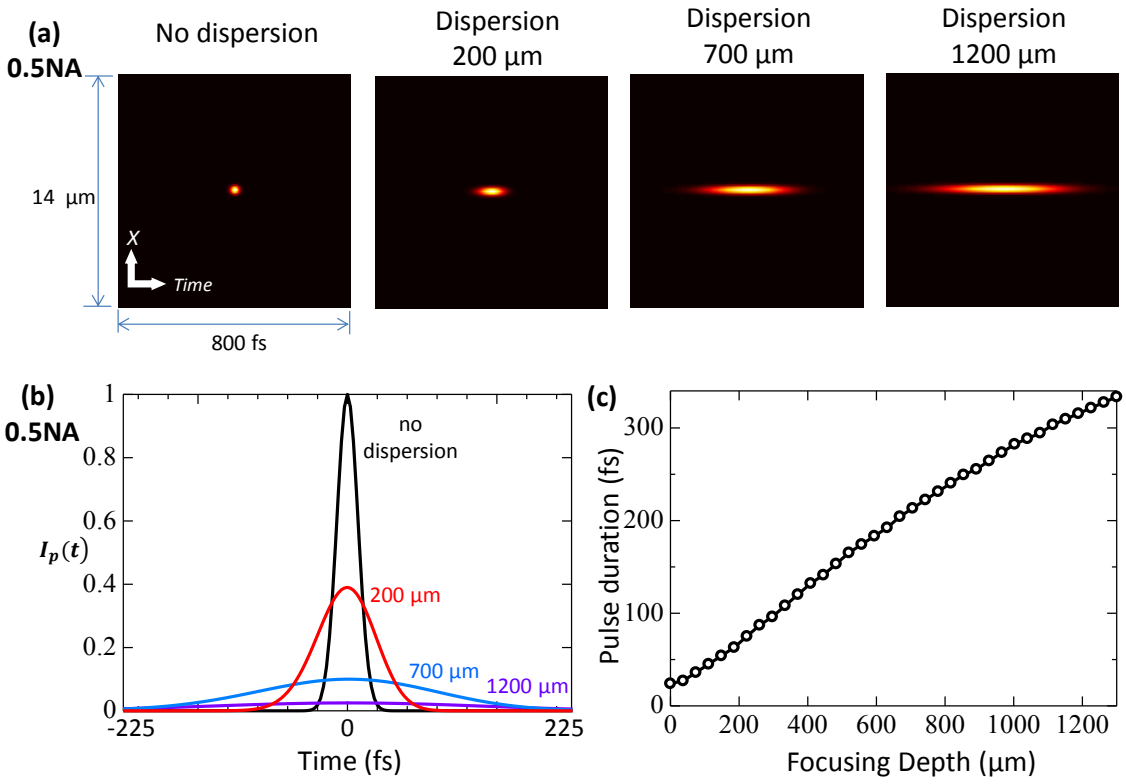

Figure 4.4: Effects of sample dispersion on the temporal profile of conventional point focusing. A laser with pulse duration of 25 fs is focused with a 0.5 NA lens. (a) Temporal profiles at the nominal focal point. Each profile is normalized independently to its peak intensity. (b) Temporal peak $\langle I^2 \rangle$ plot when the laser light is focused into the sample without dispersion (black curve) and with dispersion at different focusing depths. (c) Pulse duration at the focus versus focusing depth with sample dispersion.

Another effect of the sample dispersion is the temporal pulse broadening of the focus. Shown in Figure 4.4 (a), the pulse temporal profile is elongated along time axis and the pulse duration at the focus is significantly broadened (from 25 fs to 320 fs) by the sample dispersion. The normalized $\langle I^2 \rangle$ along the time axis with a present of intensity reduction is plotted

in Figure 4.4 (b). The pulse durations at the focus are calculated for different focusing depths in Figure 4.4 (c) and a continuous pulse broadening is clearly seen. The temporal pulse broadening effect is caused by the spatial and temporal chirp of the laser pulse. The light travelling speed and phase difference of each wavelength component (Figure 4.1) can also affect the temporal profile.

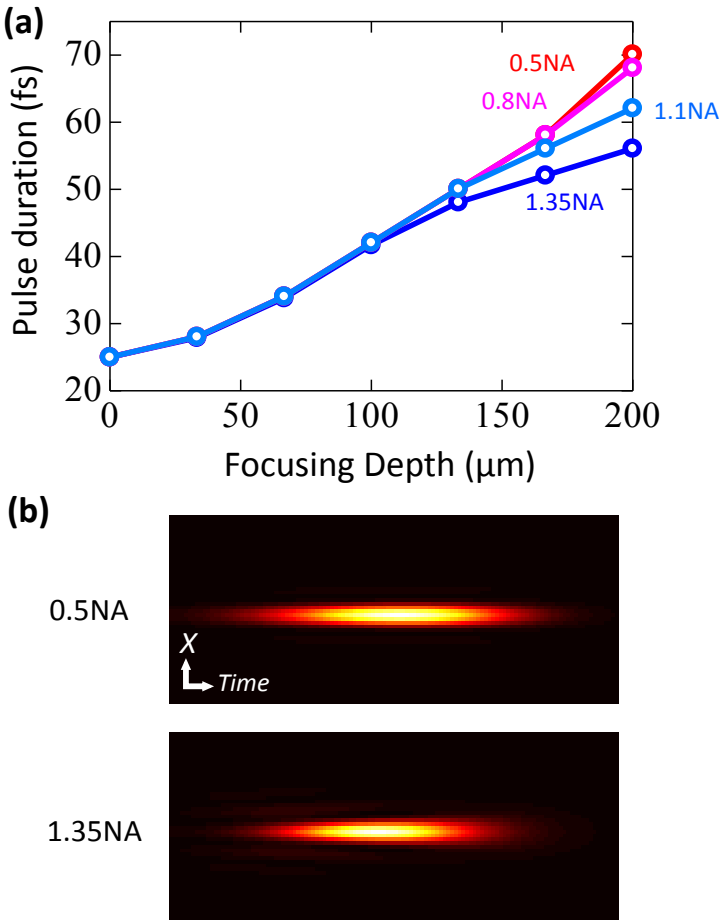

Figure 4.5: Pulse broadening effect caused by sample dispersion for the objective lens with different NA. (a) Pulse duration versus laser focusing depth. (b) Temporal intensity profiles when the laser is focused into 200 μm by a 0.5 NA lens or a 1.35 NA lens. Each image is individually normalized to its own peak intensity.

The temporal pulse duration broadening effect is calculated for the objective lens with different NA. Shown in Figure 4.5 (a), the pulse duration at the nominal focal point is plotted with the increasing focusing depth. It is seen that when the focusing depth is smaller than $\sim$100 μm, the temporal pulse duration is similar for the lenses with different NAs. However, when the depth is larger than $\sim$100 μm, the pulse duration for the higher NA lens is smaller

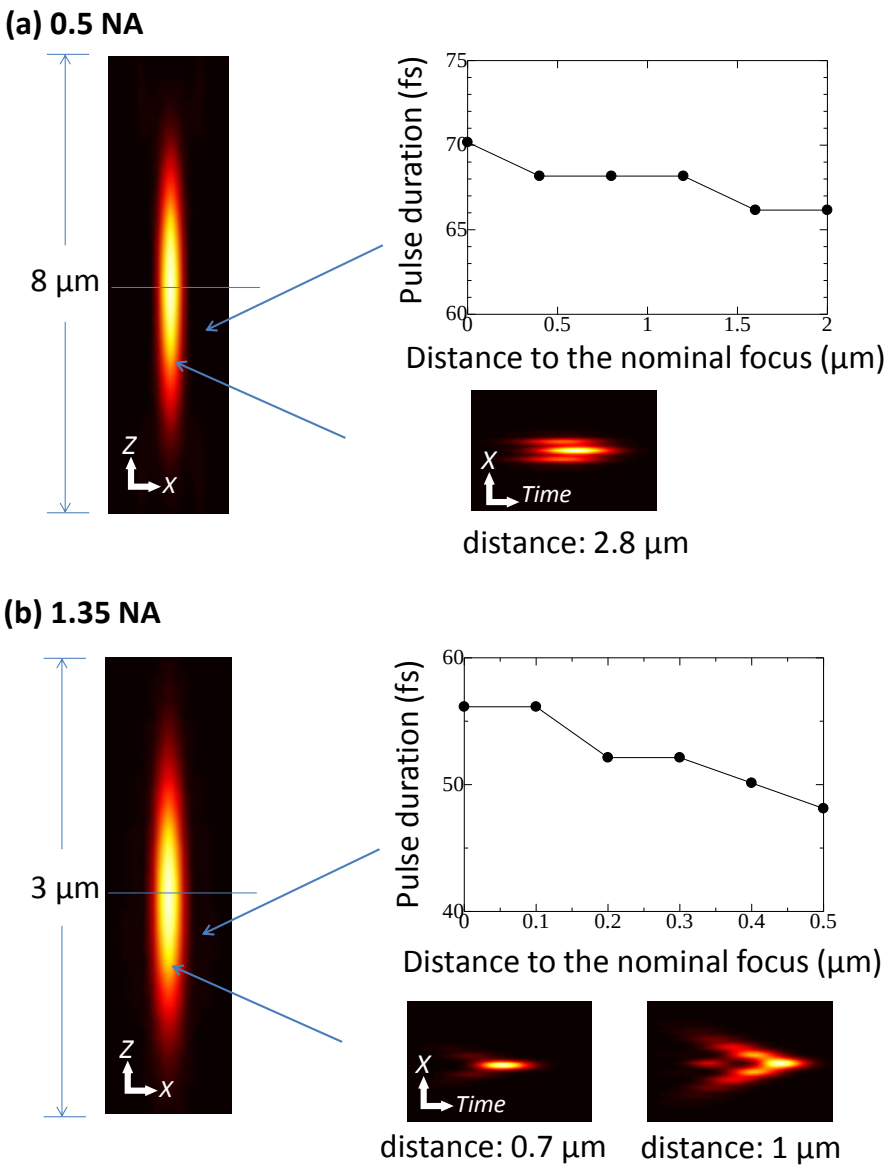

Figure 4.6: The pulse duration and temporal intensity profiles for the investigated points along the axial direction. (a) The laser is focused by a 0.5 NA lens. (b) The laser is focused by a 1.35 NA lens. Each image is individually normalized to its own peak intensity.

than that of lower NA lens, and this difference of pulse durations increases with the focusing depth. This interesting phenomenon can be explained as follows: when the focusing depth is larger than $\sim$100 μm, the temporal intensity profile at the focal point for higher NA lenses is more seriously distorted. So that in this case, the temporal intensity does not follow a perfect Gaussian distribution. This effect is shown in Figure 4.5 (b), it is seen when the laser is focused into 200 μm by a 0.5 NA lens, the temporal profile is fairly like a Gaussian distribution in temporal axis. In contrast, when the laser is focused by a 1.35 NA lens, the

temporal distribution is more seriously distorted, and does not follow a Gaussian distribution. In the case of 1.35 NA, the more distorted temporal profile however leads to a smaller FWHM in time. The serious distortion of the profile makes it difficult to directly characterize the temporal profile by the pulse durations in the form of FWHM.

The temporal pulse durations and intensity profiles are only calculated at the nominal focal point in the above cases. It is also interesting to study the temporal pulse broadening effect at other points of the focus. Figure 4.6 presents the simulated results for the temporal pulse duration and intensity profiles along the axial direction for both 0.5 NA lens and 1.35 NA lens. It is seen in both cases, the temporal pulse duration becomes smaller when the studied point has a larger distance away from the nominal focal point. It is also seen that the temporal intensity profile is seriously distorted at the edge of the focus. Similarly, the reduction in the temporal pulse duration can be explained by the non-Gaussian intensity distribution of the temporal profile, which results in a smaller FWHM.

4.3.3 Intensity reduction

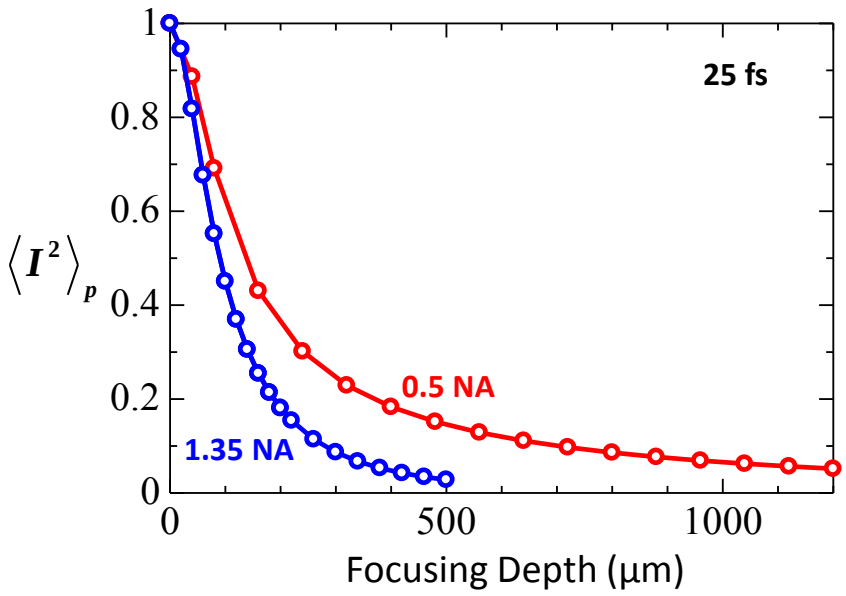

Figure 4.7: Peak $\langle I^2 \rangle$ versus focusing depth in the presence of sample dispersion.

In Figure 4.7, the peak $\langle I^2 \rangle$ of the focus versus the focusing depth for both high and low NA lenses are presented. It is clear that the peak $\langle I^2 \rangle$ decreases more rapidly with depth when

focusing with a 1.35 NA lens, which suggests the effect of sample dispersion is more dramatic for a higher NA lens. The sample dispersion effect when the laser is focused into 200 μm with a 1.35 NA lens is nearly equivalent to that when the laser is focused into 400 μm with a 0.5 NA lens.

4.4 Simultaneous spatial and temporal focusing (SSTF)

As described in Chapter 2.4, simultaneous spatial and temporal focusing (SSTF) [102, 103] can provide advantages to both microscopy [107, 108] and laser fabrication [111, 112]. In the calculation below for both wide-field and line SSTF, pupil illumination is initially adjusted to make the light at the edge of the pupil has a field amplitude of 10% compared to the amplitude of the central frequency at the centre of the pupil (Section 2.4.2). The reason to use 10% to position less wavelength components inside the pupil is that it can enhance the axial resolution which is useful to illustrate the distortions discussed below. A NA of 1.35 is used for the calculation for the rest of the chapter.

In this section, the spatial focal distortion is presented for both line and wide-field SSTF. The temporal pulse broadening and intensity reduction effects are compared with conventional point focusing.

4.4.1 Spatial focal distortion of line SSTF

The effect of sample dispersion on the spatial profile of line SSTF is shown in Figure 4.8. The pupil illumination of line SSTF in Figure 4.8 (a) shows how the spectral components are distributed across the pupil. Light of different wavelengths is represented with different colours. The corresponding field amplitude distribution across the pupil is presented, showing the edge of the pupil has a field amplitude of 10% compared to the amplitude of the central frequency at the centre of the pupil. Figure 4.8 (b) and (c) present the $\langle I^2 \rangle$ distribution in three orthogonal planes. The corresponding positions of the second and third profiles (yz and xy) are marked with the dotted lines in the first xz profile. Each profile is normalized independently to its peak intensity. Without sample dispersion (Figure 4.8 (b)), the line focus

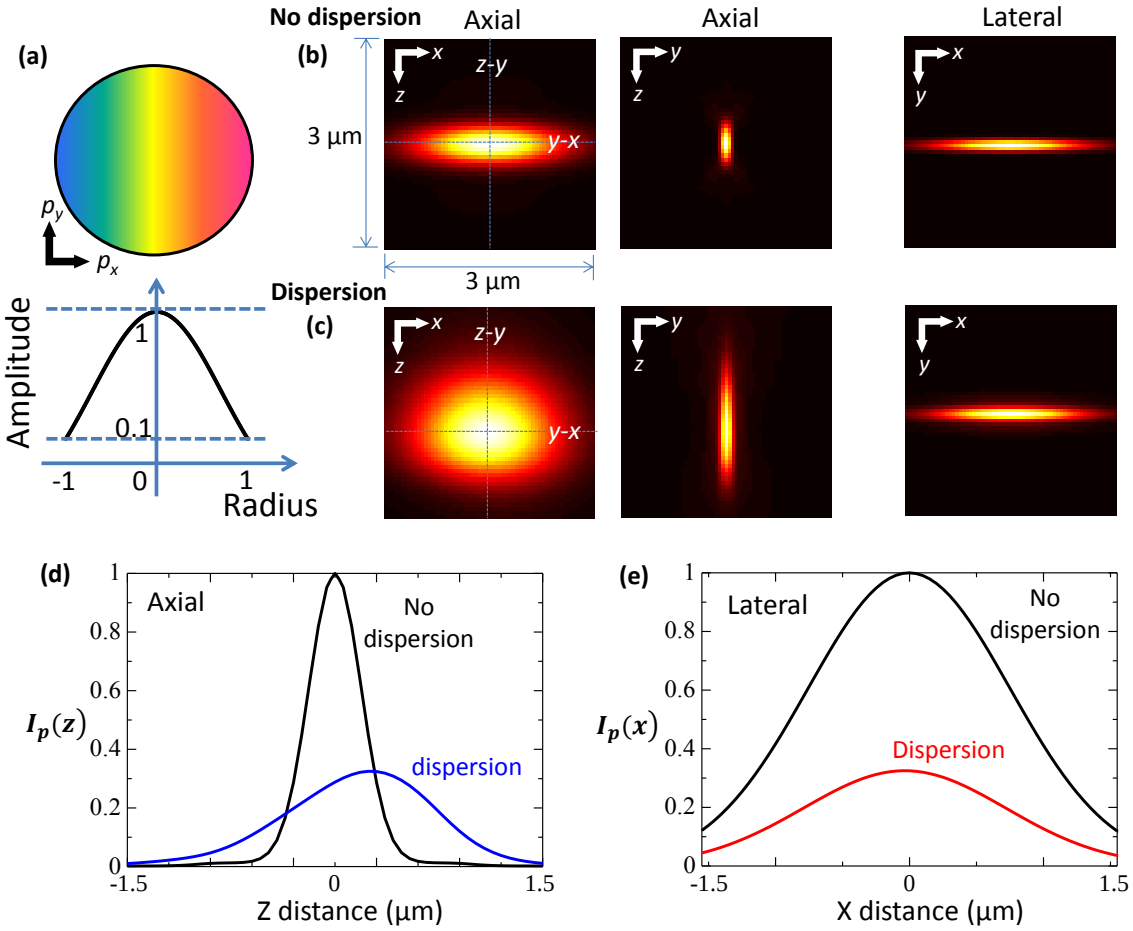

Figure 4.8: Effects of sample dispersion on the spatial focal intensity distribution of line SSTF. Original pulse duration is 10 fs. Each image is individually normalized to its own peak intensity. (a) Pupil illumination of the line SSTF. (b) Axial (xz, yz) and lateral profiles (xy) of the focus without sample dispersion. (c) Axial (xz, yz) and lateral profiles (xy) of the focus with sample dispersion. (d) Normalized peak plot for the axial profile (yz). (e) Normalized peak $\langle I^2 \rangle$ plot for the lateral profile (xy).

has axial resolution similar to that with conventional point focusing (compare with Figure 4.3 (b)). When sample dispersion is included (Figure 4.8 (c), focusing depth is 200 μm), the focus is distorted and elongated along the axial direction. The axial resolution is reduced by a factor of around three when focusing to a depth of 200 μm. This reduction in resolution is similar to that with conventional focusing, which is discussed in section 4.3.1. The lateral profile does not have a noticeable change from the sample dispersion. Figure 4.8 (d) shows the peak $\langle I^2 \rangle$ changes along the z direction for the axial profile. Figure 4.8 (e) shows the peak changes along the x direction for the lateral profiles. Noticeable drops in the focal intensity are clearly seen.

4.4.2 Spatial focal distortion of wide-field SSTF

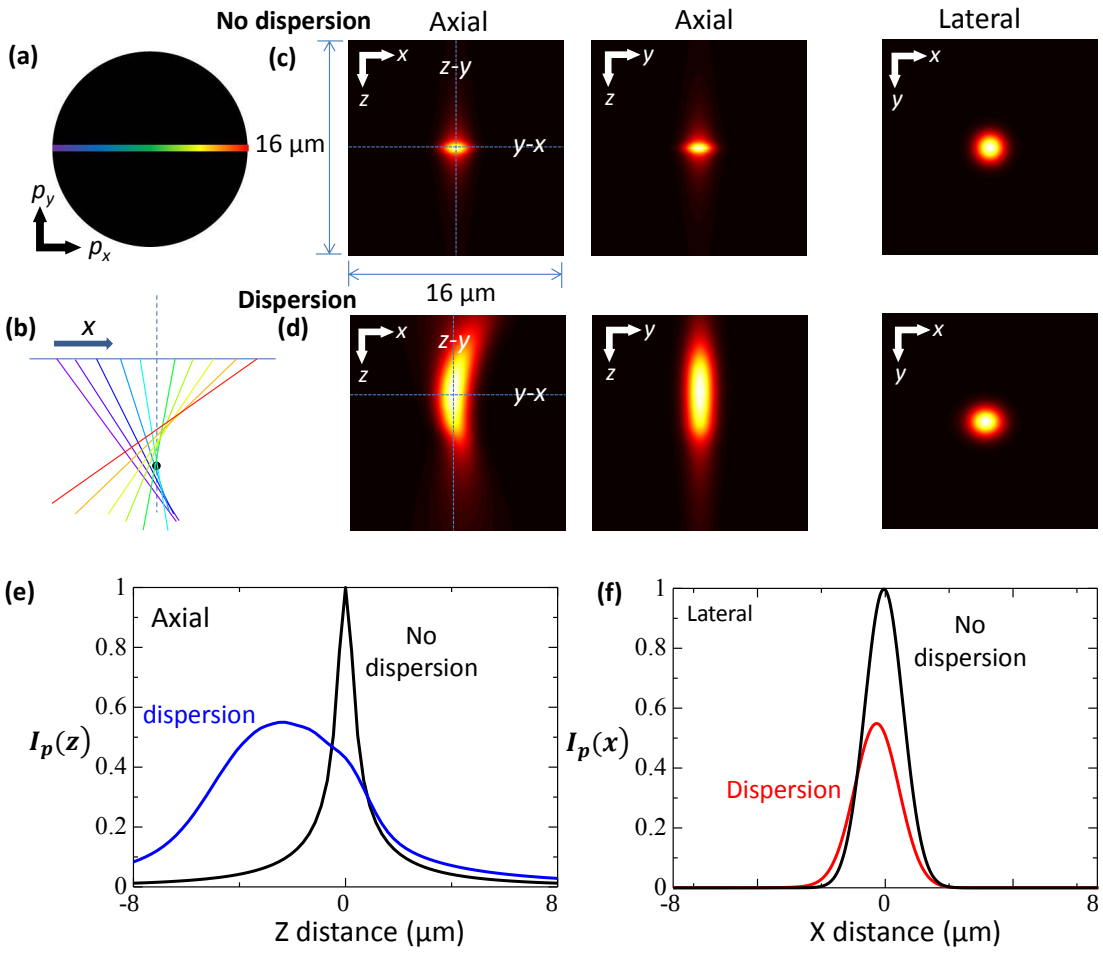

Figure 4.9: Effects of sample dispersion on the spatial focal intensity distribution of wide-field SSTF. Original pulse duration is 10 fs. Each image is individually normalized to its own peak intensity. (a) Pupil illumination of the wide-field focusing. (b) A sketch shows the propagation of different wavelength components inside the sample. (c) Axial (xz, yz) and lateral profiles (xy) of the focus without sample dispersion. The corresponding positions of the second and third profiles (yz and xy) are marked as dotted lines in the first xz profile. Each profile is normalized independently to its peak intensity. (d) Axial (xz, yz) and lateral profiles (xy) of the focus with sample dispersion at the focusing depth of 200 μm. (e) Normalized peak $\langle I^2 \rangle$ plot for the axial profile (yz). (f) Normalized peak $\langle I^2 \rangle$ plot for the lateral profile (xy).

The effect of sample dispersion on the spatial profile of wide-field SSTF is shown in Figure 4.9. As shown in (a), the illumination is spatially chirped to form a line at the pupil. A sketch of the propagation of each wavelength component inside a dispersive sample is shown in Figure 4.9 (b). The dark point marks the original nominal focal position without sample dispersion. For the purposes of illustration, we assume each ray represents a different wave-

length and the refraction angle of each ray is adjusted due to dispersion. One property of TF is that a higher intensity is achieved at the position where the different spectral components recombine with the right phase. It is seen from Figure 4.9 (b) that the region of peak intensity for wide-field TF may be expected to shift leftwards and upwards from the nominal focal point. This hypothesis is confirmed by the simulation results shown in Figure 4.9 (d). The focus is distorted and elongated along the axial direction, and the peak intensity point has both an axial shift and a lateral shift. The axial resolution is significantly reduced (about seven times) when the dispersion is considered. For the lateral profile, the sample dispersion introduces a slight broadening along the x direction (about 1.17 times). The drop in the intensity due to the sample dispersion is presented Figure 4.9 (e) and (f). As a comparison, a smaller spatial distortion of the line TF from sample dispersion benefits from its full pupil illumination, which brings better focal confinement in both the lateral and axial directions.

4.4.3 Temporal Pulse Broadening

One advantage of temporal focusing is that the pulse duration varies with the light propagation after the objective lens, but the shortest pulse is only achieved at the peak intensity point where the spectral components of the laser pulse recombined with the right phase. We show that this characteristic makes the temporal property of SSTF much more robust against the effect of sample dispersion than conventional focusing. As discussed above, the peak intensity point shifts when sample dispersion is considered, thus we only investigate the temporal property of the peak intensity point instead of the original nominal focus. It is seen in Figure 4.10 (a), there is no significant temporal broadening when the sample dispersion is considered. The comparison with conventional focusing in Figure 4.10 (b) shows the advantage of reduced temporal pulse broadening in SSTF. We note the pulse duration is still slightly broadened for SSTF, because even at the peak intensity point, there are residual spreads of different wavelengths both spatially and temporally. We therefore conclude the SSTF is more robust against the sample dispersion than conventional focusing in the temporal domain.

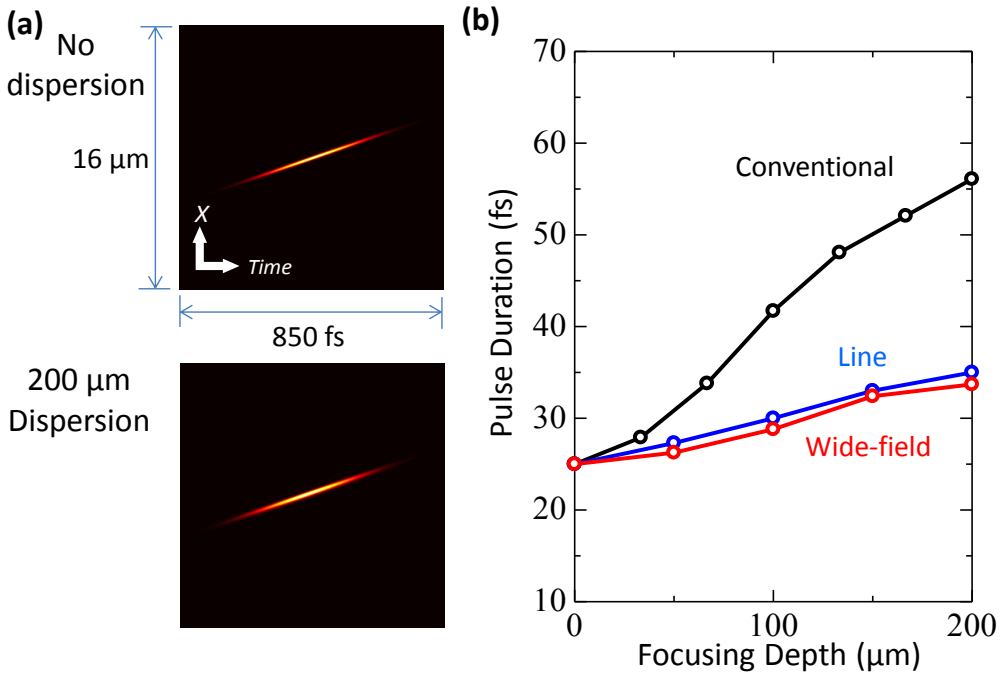

Figure 4.10: Effects of sample dispersion on the temporal profile of SSTF. Original pulse duration is 25 fs. (a) An example of temporal profiles at the peak intensity point for wide-field SSTF without and with sample dispersion. An obvious pulse front tilt is seen [111]. Each profile is normalized independently to its peak intensity. (b) Comparison of pulse duration for conventional focusing, line SSTF and wide-field SSTF with sample dispersion.

4.4.4 Intensity reduction

The comparison of intensity effects for conventional point focusing, line SSTF and wide-field SSTF is shown in Figure 4.11. It is seen the SSTF are more robust to sample dispersion than conventional focusing in maintaining the focal intensity. It is interesting to note that these results of the sample dispersion effect on SSTF, including the different magnitude of distortions and intensity reduction between line and wide-field focusing, show the similar trends with the effects from sample scattering [137]. Both the sample dispersion results presented in this chapter and the scattering effects presented in reference [137] show that the wide-field SSTF is good at maintaining the peak intensity, however, bad at maintaining the focal resolution. This could be explained by both effects are introducing a slight change of the refraction angle to the incident optical rays. The difference is that the light scattering introduce a random angle change, while the sample dispersion introduces monotonous angle change.

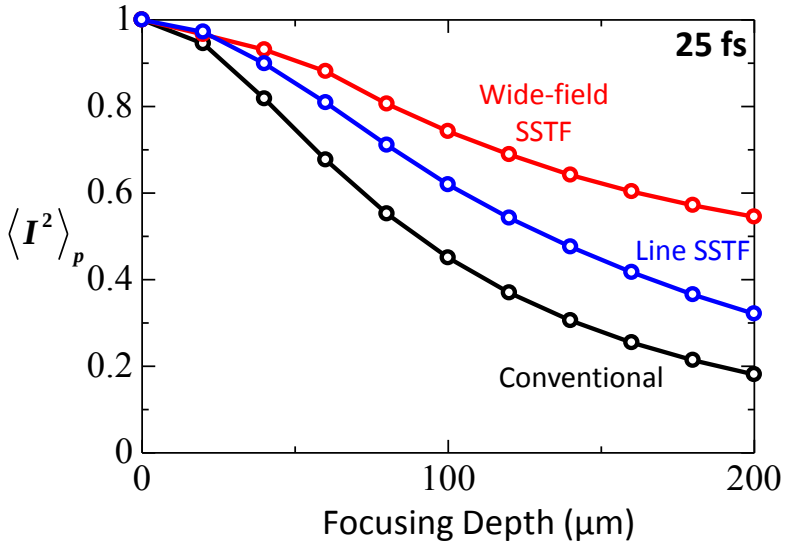

Figure 4.11: Intensity reduction caused by sample dispersion. Conventional point focusing, line SSTF and wide-field SSTF are compared together.

4.5 Influence of laser parameter and sample material

The effect of the material dispersion is strongly related to the spectral bandwidth of the laser light. A laser with shorter pulse duration has larger bandwidth, and therefore results in more severe dispersion effects. The dispersion effects for the 520 nm centered laser light with pulse duration of 80 fs, 40 fs, 25 fs and 10 fs are calculated and shown in Figure 4.12 (a). It is obvious that a shorter pulse duration significantly exacerbates the dispersion effect. When focusing the laser to a nominal depth of 200 μm, the $\langle I^2 \rangle_p$ decreases to 80%, 40%, 20% and 2% for the laser with 80 fs, 40 fs, 25 fs and 10 fs pulse duration, respectively.

The near infrared is a common wavelength region for the ultra-short lasers pulses. The dispersion effects are investigated for different pulse durations centered at the wavelength of 800 nm, as shown in Figure 4.12 (b). Because most materials including lithium niobate are less dispersive in near infrared region, the intensity reduction effect appears less significant. These results suggest the sample dispersion is not a very severe problem if an 800 nm laser light with pulse duration $> \sim 50$ fs is focused into a nominal depth $< \sim 200$ μm with a high NA lens ($< \sim 400$ μm for low NA lens, refer to Section 4.3.3). However, dispersion effects are still significant if shorter pulses (e.g. < 50 fs) are used or the laser is focused to a greater depth.

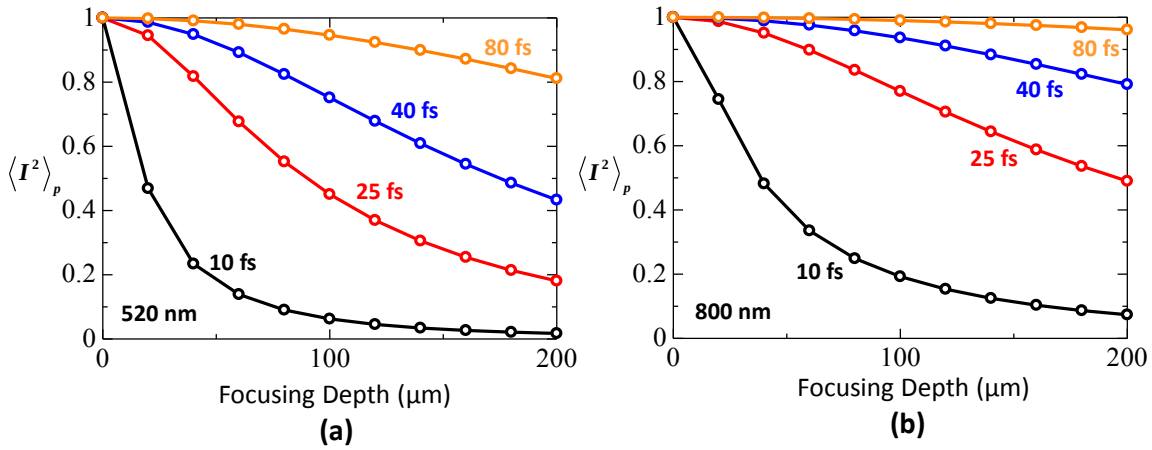

Figure 4.12: Effect of sample dispersion for focusing of ultra-short pulsed laser with different pulse durations. The sample is lithium niobate and the objective used has a NA of 1.35. Central wavelength of the laser light is (a) 520 nm (b) 800 nm.

The sample material investigated above is lithium niobate, which has a refractive index of around 2.3 and high dispersion. Several other commonly used optical materials with different levels of sample dispersion have also been investigated. These materials are SF11, water, fused silica and diamond whose refractive indices are around 1.8, 1.33, 1.46 and 2.5. The corresponding intensity reduction effects from sample dispersion are shown in Figure 4.13 (a). It is seen that the peak $\langle I^2 \rangle_p$ drops to 60% when a 25 fs laser is focused 200 μm into fused silica or diamond. This suggests that sample dispersion is still problematic when focusing into a low-dispersion material if the laser has very short pulse duration or the focusing depth is large.

The sample dispersion effect of water is specifically studied in Figure 4.13 (b). These calculations are relevant for nonlinear optical microscopy, where specimens are often water-based. The effect of the dispersion of water is investigated for various wavelength regions from ultra-violet to infrared. It is seen that the effect is significant in ultra-violet and visible regions, but smaller in the near infrared region. The peak $\langle I^2 \rangle_p$ drops to 60% when a 25 fs laser with a central wavelength at 800 nm or 1060 nm is focused into water with a depth of 200 μm. This suggests the sample dispersion effect of water is not negligible if a very short pulsed laser is used, especially in the applications of multi-photon microscopes, where short pulse laser is often used.

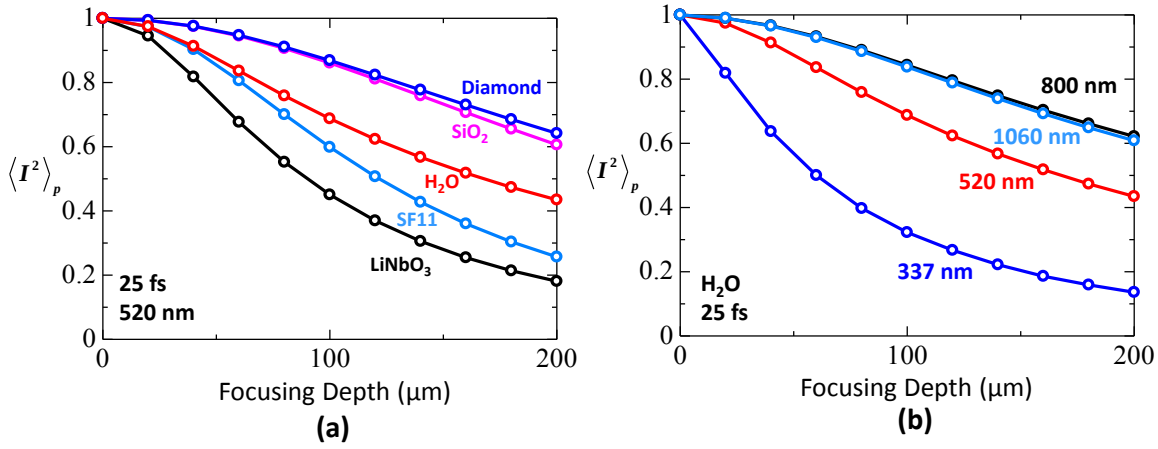

Figure 4.13: Effect of sample dispersion for several commonly used optical materials. (b) Effect of sample dispersion when the ultra-short laser pulse with different central wavelength is focused into water.

4.6 Discussion

The investigation in this chapter addresses the focusing of ultrafast laser into a dispersive sample. It is notable that this effect of material dispersion is different to the effect when the collimated laser beam propagates through a dispersive material. The latter phenomenon is solely caused by a different propagation speed of each spectral component. For an example, after transmitting through lithium niobate with optical length of 200 μm, a collimated 25 fs laser is broadened to 33 fs. As a comparison, focusing by a 0.5 NA lens with the same depth into the sample, the laser is broadened to 70 fs (Section 4.3.2). The pulse broadening effect for the focusing of laser into a dispersive sample is much more significant.

There have been well established methods correcting the GVD effect for optical components, such as lenses. These include the pre-compensation by a prism pair or a grating pair [138, 139]. However, these methods are not able to cancel the dispersion effects when the ultrafast laser is focused into a dispersive sample.

We assume a linear refractive index for the calculation in this chapter. In those high power laser focusing, refractive index of the material changes with laser intensity in focal region, introducing additional distortions in addition to the effect of material dispersion.

For the purposes of illustration, we have used particular combinations of lasers and materials. However, the broader trends in the results will also be seen for other practical scenarios.

4.7 Conclusions

In summary, the effect of sample dispersion in ultrafast laser focusing has been studied in detail for different focusing methods, objective lenses, materials and laser wavelengths and pulse durations. Spatial distortion, temporal pulse broadening and overall intensity reduction have been investigated.

Sample dispersion generally reduces the axial spatial resolution of the focus. This effect is more significant when focusing with a high NA lens, or in the wide-field SSTF. In SSTF, the peak intensity point shifts both along axial and lateral direction. The sample dispersion also introduces temporal pulse broadening at the focus. SSTF is much more robust than the conventional focusing in this respect.

Overall, the sample dispersion effect is more significant for conventional point focusing method and a high NA objective lens. Both the parameters of the input laser and the sample materials affect the magnitude of dispersion effect, but the trends observed in the results here will also be seen for other combination of laser and material parameters.

4.8 Appendix: Sellmeier refractive index equations

The fitting Sellmeier equations for the refractive index of Lithium Niobate ($LiNO_3$) [129], SF11 glass [140], water (H_2O) [131, 132], Fused silica (SiO_2) [133] and Diamond [134] are expressed as follows:

$$n_{LiNO3} = \left(1 + \frac{2.6734 \times \lambda^2}{\lambda^2 - 0.01764} + \frac{1.2290 \times \lambda^2}{\lambda^2 - 0.05914} + \frac{12.614 \times \lambda^2}{\lambda^2 - 474.60}\right)^{0.5} \tag{4.8}$$

$$n_{SF11} = \left(1 + \frac{1.73759695 \times \lambda^2}{\lambda^2 - 0.013188707} + \frac{0.313747346 \times \lambda^2}{\lambda^2 - 0.0623068142} + \frac{1.89878101 \times \lambda^2}{\lambda^2 - 155.23629}\right)^{0.5} \tag{4.9}$$

$$n_{H2O}(0.182-1.129\mu m) = \left(1+\frac{5.684027565\times10^{-1}\times\lambda^2}{\lambda^2-5.101829712\times10^{-3}}+\frac{1.726177391\times10^{-1}\times\lambda^2}{\lambda^2-1.821153936\times10^{-2}}+\frac{2.086189578\times10^{-2}\times\lambda^2}{\lambda^2-2.620722293\times10^{-2}}+\frac{1.130748688\times10^{-1}\times\lambda^2}{\lambda^2-1.069792721\times10}\right)^{0.5} \tag{4.10}$$

$$n_{H2O}(0.5-1.6\mu m) = \left(1+\frac{0.75831\times\lambda^2}{\lambda^2-0.01007}+\frac{0.08495\times\lambda^2}{\lambda^2-8.91377}\right)^{0.5} \tag{4.11}$$

$$n_{SiO2} = \left(1+\frac{0.6961663\times\lambda^2}{\lambda^2-0.0684043^2}+\frac{0.4079426\times\lambda^2}{\lambda^2-0.1162414^2}+\frac{0.8974794\times\lambda^2}{\lambda^2-9.896161^2}\right)^{0.5} \tag{4.12}$$

$$n_{Diamond} = \left(1+\frac{0.3306\times\lambda^2}{\lambda^2-0.1750^2}+\frac{4.3356\times\lambda^2}{\lambda^2-0.1060^2}\right)^{0.5} \tag{4.13}$$

in which, the wavelength is with a unit of μm.

Chapter 5

Pulse front shaping by dual adaptive optics elements

5.1 Introduction

In previous chapters, it has been shown that phase aberrations and dispersion effects bring distortions to laser focus. Beside these two, another important source of error in ultrafast laser focusing is the distortion to the laser pulse front (contour of constant intensity) [123,141–143]. This form of distortion arises from variation in group delay (GD) across the beam profile with a consequent spreading of the arrival times of pulses at the target.

Beam shaping using two dimensional reflective elements, such as parabolic mirrors or deformable mirrors (DMs), can provide spatial deformation of the pulse front, but only with a concomitant distortion of the phase front, which makes the laser pulse inappropriate in most applications. In another way, temporal pulse shaping can be employed, whereby the whole beam is spectrally dispersed and the temporal shaping is conducted for each individual spectral component [69, 144–146]. Whilst an essential tool for creating ultra-short pulses, this mode controls the pulse front solely within the temporal (or equivalently spectral) domain, resulting in a modulation which is spatially uniform across the beam. Until now, there has been no realization of flexible spatial pulse front modulation, which has limited the ability to control ultrashort laser pulses.

Currently, adaptive optics elements have only been applied to control the phase of the laser pulse. In this chapter, I present a new concept of adaptive optics: harnessing extra spatial degrees of freedom for pulse front shaping, through the combination of a diffractive and a reflective adaptive optics element (AOE). Effectively, the phase front and the pulse front for an ultra-short pulse become decoupled allowing independent spatial control of each across a beam. We demonstrate that through adaptive control of the pulse in an ultrafast laser system, a beam could be generated with an arbitrarily shaped pulse front, whilst the phase front remains flat. Autocorrelation measurements using an annular intensity distribution were adopted to demonstrate the relative temporal delay between different parts of the beam. The potential applications for this new adaptive optics method are discussed.

5.2 Diffractive and reflective AOEs

In this section, we introduce the function of two different types of adaptive optics elements: diffractive (SLM) and reflective (DM) AOEs. The basic principle of pulse front shaping method by a combination of these two AOEs is explained.

It has previously been realised that combining diffractive and reflective/refractive optics can be a useful concept for static shaping of pulse fronts from an ultrafast laser. The design of specialist optics has allowed the focusing of ultra-short pulses at high numerical aperture with minimal increase to the pulse duration [147, 148]. This static concept can be extended to dynamic control through the inclusion of two adaptive optics elements, one diffractive and another either refractive or reflective. We show here this hybrid dynamic optical system permits adaptive control of both phase and pulse fronts in an ultrashort pulse.

We outline the concept in Figure 5.1. A diffractive element, such as a liquid crystal spatial light modulator (SLM), invokes a phase delay on the beam within an interval of 2π radians for a monochromatic wavelength. Large phase shapes can still be implemented through discontinuous jumps in the phase profile where the phase is wrapped from 2π to zero radians between adjacent pixels (Figure 5.1(a)). Operating as a phase grating, the device is capable of changing the direction of propagation (the k vector) for the beam. However, the impact of this modulation on the optical path length followed by the light across the beam is negligible; for

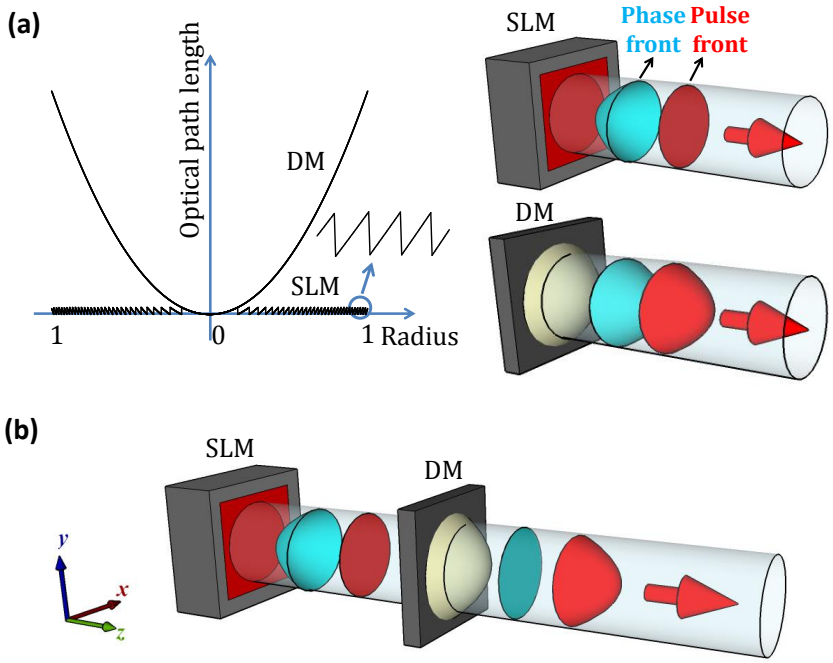

Figure 5.1: The principle of adaptive pulse front control. (a) The graph (left) shows the impact of the SLM and DM on the optical path length of the incident light, while the images (right) reveal the associated influence on the phase front and pulse front for an ultrafast beam. (b) The method of combining the SLM with DM to decouple and exert independent control over the phase front and pulse front.

the pulse front, the SLM behaves essentially like a plane mirror. Hence on reflection from the SLM, the phase front of the pulse (which is perpendicular to the k vector) can be reoriented, while the pulse front is nearly unaffected. An angle is introduced between the pulse front of the beam and the phase front: a local pulse front tilt is created. The spatial multiplexing capability of the SLM may be exploited to generate a local pulse front tilt that varies in both magnitude and orientation for different parts of the beam cross-section, distorting the phase front but without affecting the pulse front shape.

Other adaptive elements, such as a reflective membrane deformable mirror (DM), can implement a large phase distortion in a continuous manner, through the introduction of a correspondingly large difference in optical path length (Figure 5.1(a)). Thus, both the phase front and pulse front are affected by the DM, such that although distorted, they remain parallel. By combining a reflective DM with a diffractive SLM, it is possible to cancel out any phase front distortion, whilst maintaining the local pulse front tilt. As shown in Figure 5.1(b), applying

opposite phase shapes to the two adaptive devices, we are able to maintain a flat phase front while generating a spatially variant local pulse front tilt across a collimated beam. Effectively, the pulse front and the phase front have become decoupled within the beam, and through appropriate shaping of the AOEs, it is possible to control each of them independently.

5.3 The experimental system

The complete system for all the optical measurements is shown in Figure 5.2. The laser source used for the experiments was a Titanium Sapphire oscillator (Newport Spectra Physics Maitai), with central wavelength of 790 nm, 80 fs pulse duration and maximum output power of $\sim$ 300 mW. The power was controlled using neutral density (ND) filters. A pair of prisms [139] was aligned directly after the ND filter to compensate the group velocity dispersion (GVD) effect arising from the optical system [123]. The position of the prism pair was finely adjusted to ensure the duration of the pulse exiting the optical system was 80 fs.

The laser beam was expanded before illuminating a liquid crystal SLM (Hamamatsu X10468-02). The laser beam expansion was sufficient for the effective region on the SLM to be considered as illuminated with an approximately flat intensity distribution. A 4f lens system was used to image the phase pattern on the SLM onto a large stroke DM (Imagine Optic MIRAO 52-e). 4f system is an imaging system which can be formed using two lenses where the back focal plane of one forms the front focal plane of the other. It is useful to maintain the correct phase of the laser light, and also provide a way to change the size of the laser beam.

An autocorrelator (A.P.E Pulsecheck) or a Shack-Hartmann Wave-front Sensor (SHWS; Thorlabs WFS150-7AR) could be coupled in after another 4f system. The autocorrelator was used to demonstrate distortion of the pulse front, while the SHWS was used to verify the correction of phase front aberration. A different 4f lens system was chosen to introduce an appropriate beam size for the autocorrelator or SHWS. A pinhole on an adjustable mount was inserted into the Fourier plane of the DM to block any un-modulated light from the SLM (which forms the zero diffraction order) generated when a large phase pattern was applied. Achromatic doublets were used throughout the system to minimize the system-induced pulse front distortions, enabling us to explore the pulse front solely created by the adaptive optics

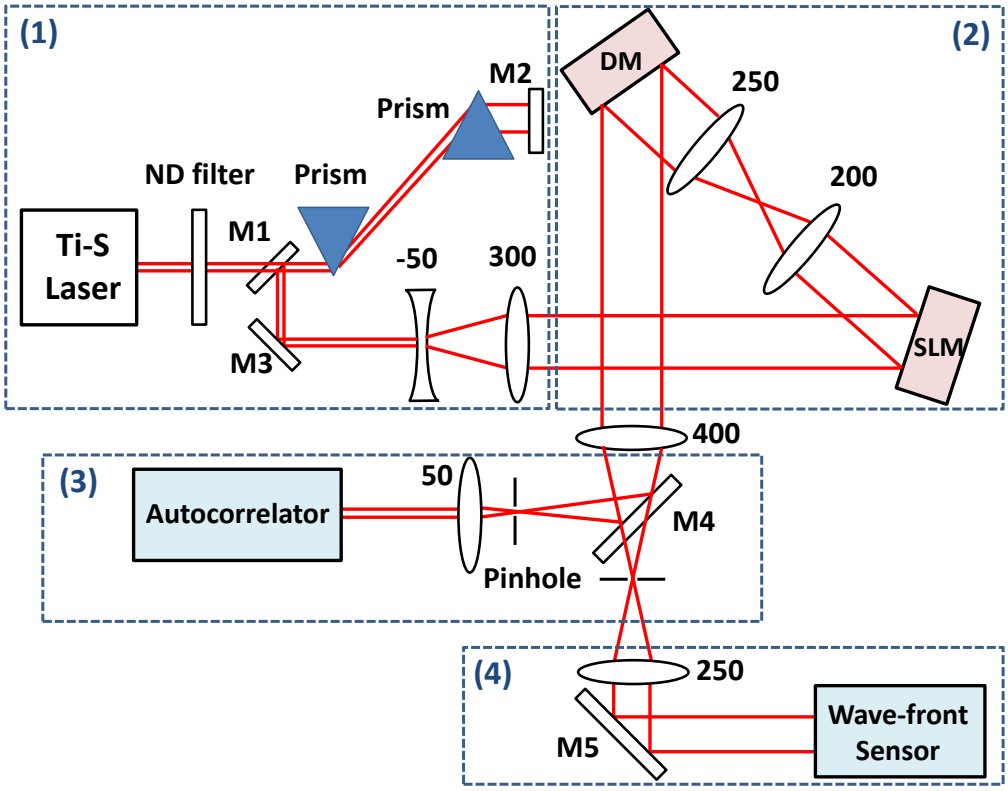

Figure 5.2: The optical systems for pulse front shaping and characterization. The pulse front shaping system: (1) the power control and GVD pulse duration compression, (2) the adaptive pulse front control system. The characterization system: (3) autocorrelation measurement, (4) the wave-front measurement. The focal lengths (mm) of the achromatic doublets are shown in the adjacent number. ND filter: neutral density filter, M1 – M5: mirror No. 1 to No. 5, SLM: spatial light modulator, DM: deformable mirror.

elements.

5.4 Phase front characterization

To demonstrate the shaping technique, we generated a quadratic temporal delay of the pulse front with respect to radial position in the beam, since this corresponds to the propagation time difference (PTD) induced on ultra-short pulses by a simple chromatic lens [123] (Section 2.6.2, Chapter 2). To implement such a pulse front distortion, it is necessary to apply a quadratic phase of equal magnitude but opposite sign to the SLM and DM. We denote the phase applied for the central wavelength of the laser in the form of the Zernike polynomial [116] $Q(r) = Z_4(r) = \alpha \cdot \sqrt{3}(2r^2 - 1)$, where α determines the total amplitude of the

phase and r is the normalised radius of the objective pupil. We use the equivalent optical path length ($EOPL$) introduced by dual AOEs to characterize the applied phase magnitude, which is represented by: $EOPL = \lambda \cdot (Q_{\max} - Q_{\min}) \,/\, (2\pi)$, where λ is the wavelength of the laser light.

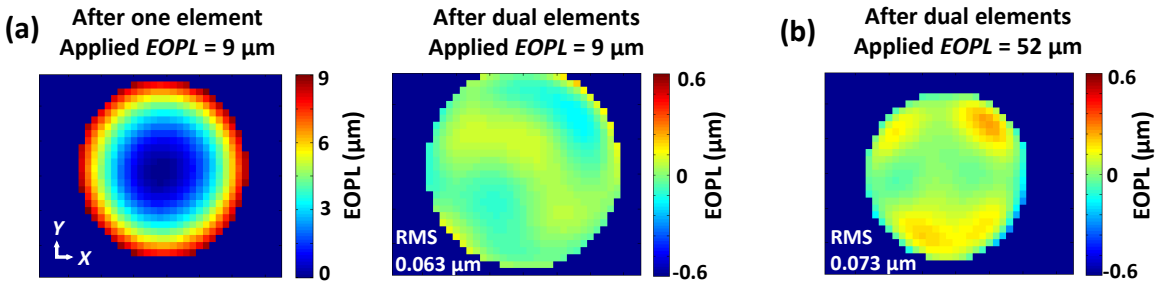

Figure 5.3: (a) Example phase fronts measured by Shack-Hartmann Wave-front Sensor, when quadratic phase of $EOPL$ = 9 μm was applied to one adaptive optics element (SLM) (left) and dual adaptive optics elements (SLM and DM) (right). (b) The phase front measured for the light when quadratic phase of $EOPL$ = 52 μm was applied to SLM and DM.

To generate a pure pulse front distortion while maintaining a flat phase front, it is essential to make sure the phase introduced by the SLM and DM perfectly cancels with each other. Therefore, a Shack-Hartmann wave-front senor (SHWS) was used to monitor the phase front following the SLM and DM. Figure 5.3(a) shows the phase front measured by the wave-front sensor when a quadratic phase shape of $EOPL$ = 9 μm was applied. It is seen after opposite phases were applied to the dual adaptive elements, an approximately flat phase front (Root-Mean-Square (RMS) of $EOPL$ = 0.063 μm) was measured. This is also the case when a large quadratic phase shape was applied to the SLM and DM. An example is shown in Figure 5.3(b) with phase of $EOPL$ = 52 μm applied to SLM and DM, and phase front with RMS of 0.073 μm was measured for the output beam. It is also seen with increasing the phase amplitude, small amounts of high order residual phase front aberrations may be generated, due to limited actuator resolution of the DM [149]. In our experiments, both the SLM and DM were finely adjusted to remove these high order aberrations, and the total equivalent path length of the phase front measured by the wave-front sensor was kept to be smaller than 0.08 μm RMS, even when applying shapes of $EOPL > 50$ μm.

5.5 Method for the pulse front characterization

In this section, we introduce the method to characterize the shape and amplitude of laser pulse front. The theoretical simulations for the temporal property of quadratic pulse front, and the modelling of the autocorrelation for both the whole beam and annulus beam are presented. Annulus phase displayed in SLM creates the annulus intensity distribution for the laser beam. The measured autocorrelation traces are discussed.

5.5.1 Temporal intensity distribution of quadratic pulse front

The temporal intensity profile of the laser beam with a quadratic shape can be approximated using a Gaussian distribution in time. We initially consider a constant flat spatial intensity distribution across the beam cross-section. The spatial and temporal intensity vibration of the laser light can then be expressed as,

$$I(r,t) = \exp\left(\frac{-4\ln 2 \cdot (t - t_D(r))^2}{\tau^2}\right) \tag{5.1}$$

where I is the intensity of the laser light, r is the normalized radius, t is time, τ is the pulse duration of the original laser (FWHM of the intensity-time curve). For a laser pulse with a flat pulse front, the time delay $t_D(r) = 0$.

Figure 5.4 shows a sketch of the temporal profile of the quadratic-shaped pulse front. The central contour of the laser pulse, corresponding to the point of peak intensity, is represented by a quadratic relationship between the time and radius,

$$t_D(r) = T_{PF} \cdot r^2 \tag{5.2}$$

where T_{PF} is the total amount of quadratic pulse front (the time delay between a point at the edge of the beam and a point at the center of the beam, $T_{PF} = EOPL/c$, where c is the speed of light). Therefore, the temporal intensity of the laser pulse with a quadratic-shaped pulse front becomes,

$$I(r,t) = \exp\left(\frac{-4\ln 2 \cdot (t - T_{PF} \cdot r^2)^2}{\tau^2}\right) \tag{5.3}$$

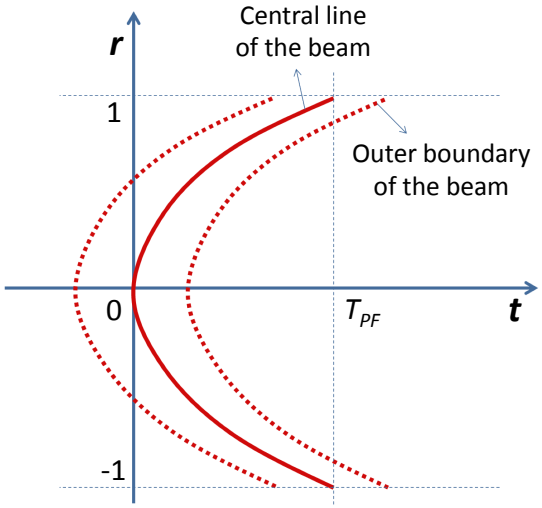

Figure 5.4: A sketch showing the temporal intensity profile of a quadratic-shaped pulse front.

Finally, the spatially integrated global temporal intensity profile of the whole beam is calculated by integration over the two dimensional spatial plane of the beam, which is,

$$I(t) = \int_0^1 I(r,t) \cdot 2\pi r \cdot dr \tag{5.4}$$

The global temporal profile of the quadratic-shaped pulse front is dictated by both the original pulse duration τ and the total amount of quadratic pulse front T_{PF}. Figure 5.5 shows simulation results. It is seen that when the original pulse duration is small (Figure 5.5 (a)), the pulse is very sensitive to quadratic pulse front distortions, with a significant increase in the spatially integrated pulse width. In contrast, for pulses with larger durations τ (Figure 5.5 (b) and 6(c)), only a small proportional difference is seen when a same quadratic pulse front distortion is applied.

5.5.2 Annulus intensity generation

The quadratic pulse front generated by dual AOEs was verified by measuring the pulse autocorrelation. In the above subsection, we noticed that the quadratic pulse front distortion has little effect on the temporal intensity distribution of the whole beam if a 80 fs laser pulse is used. Therefore, to accentuate the effect of the pulse front distortion on the autocorrelation mea-

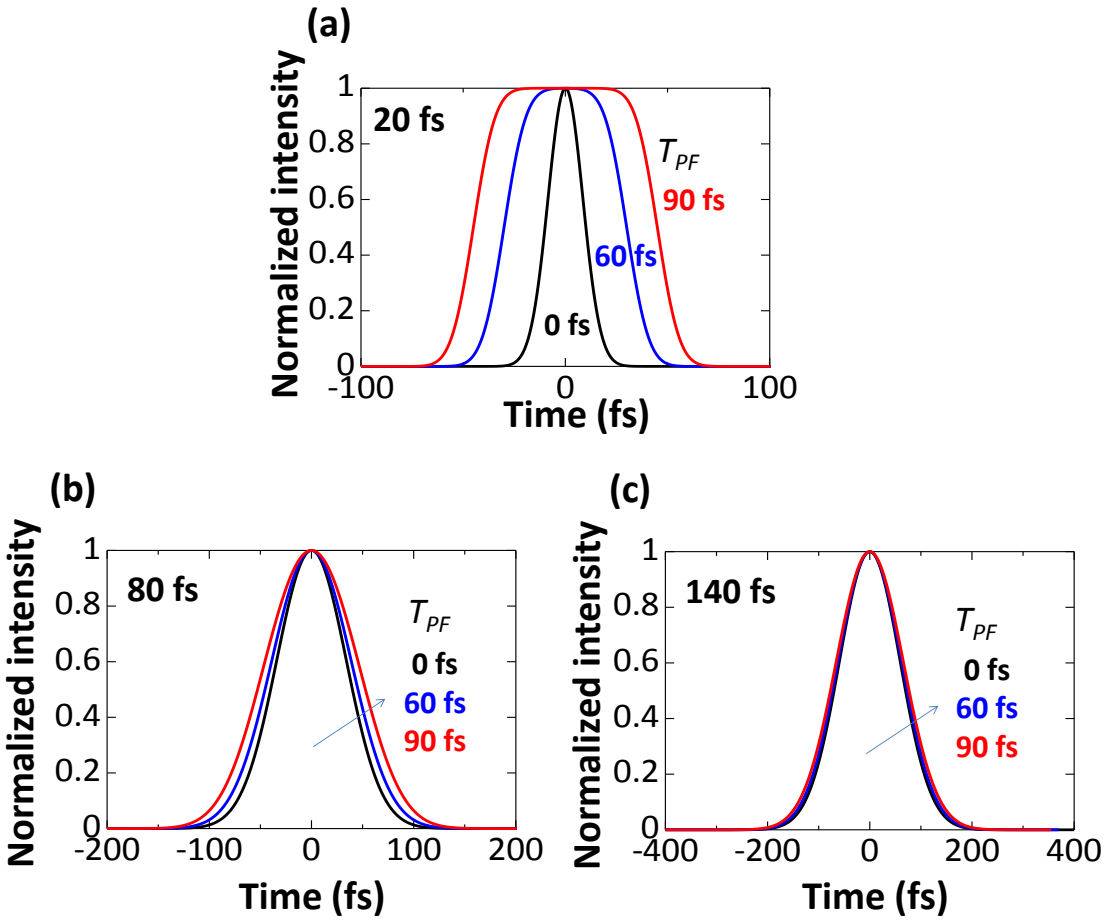

Figure 5.5: Calculated global temporal profiles for beams with a quadratic-shaped pulse front. The original pulse durations of the laser τ is: (a) 20fs, (b) 80 fs, (c) 140 fs. The total amount of quadratic pulse front delay T_{PF} is marked in the figures.

surement in out system, we implemented a scheme to mask parts of the beam cross-section, measuring only the autocorrelation between two annular regions of differing radius [150].

A phase pattern displayed on the SLM, which is shown in the left image of Figure 5.6, was applied to separate the annular intensity distribution from the original laser beam. A quadratic phase opposite to that introduced by the DM, was displayed only within a circular and an annular region of the beam. After reflection from both the SLM and the DM, only the light incident onto these active regions of the SLM has a flat phase front (corresponding to the first diffraction order). Light incident elsewhere on the SLM (corresponding to the zero order) propagated with an uncompensated quadratic phase front. A pinhole was aligned in the Fourier plane of the DM to spatially filter the strongly defocussed zero order. The resultant intensity distribution within the beam is presented in the right image of Figure 5.6.

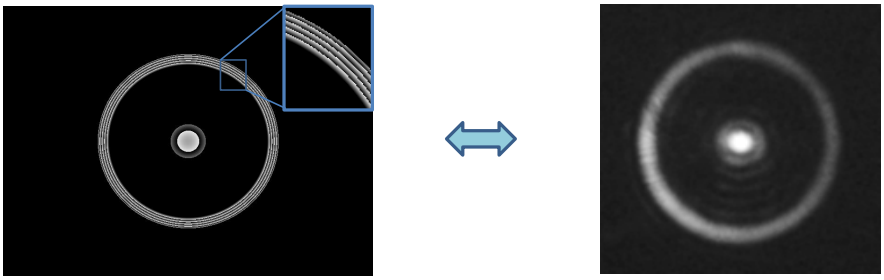

Figure 5.6: The phase pattern on SLM to generate double ring-shaped pulses. (left) the phase pattern on the SLM, (right) the corresponding intensity measured by CCD camera.

When measuring the pulse duration for a single ring of intensity with varying radius, a further two SLM phase patterns were applied, as shown in Figure 5.7. When the SLM phase pattern consisted of a single ring, as shown in the left image of Figure 5.7 (b), there was a residual leakage of the zero order light through the pinhole. This is because the central part of the beam acquires only a relatively small phase modulation, and thus part of it could still transmit through the pinhole. Therefore, we used a beam block (as shown in the sketch of Figure 5.7 (b)) to prevent the transmission of the central part of zero order to the autocorrelator.

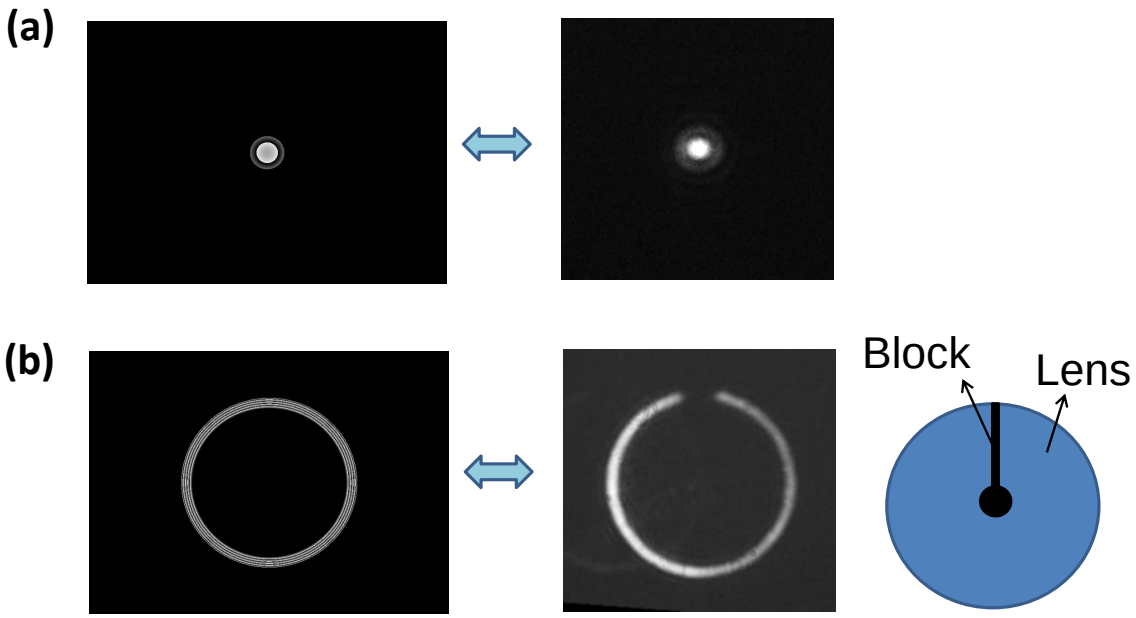

Figure 5.7: The phase pattern on SLM to generate single ring-shaped pulse. (left) the phase pattern on the SLM, (right) the corresponding intensity measured by CCD camera. The sketch in (b) shows the beam block placed at the surface of the lens after DM.

With a quadratic pulse front, there is a time delay between the two rings of intensity in the beam, as shown in Figure 5.8. We use T_D to represent the time delay between the two rings, and T_{PF} to represent the time delay between the edge and the center of the beam. Each ring was narrow enough that it contained minimal pulse front distortion within its width and, hence, the pulse duration within the ring was roughly equal to that of the original laser pulse (80 fs). The two rings were controlled to have similar integrated power, which was achieved by finely adjusting the width of each ring in the experiment. This was also confirmed by measuring the autocorrelation trace intensity for each ring.

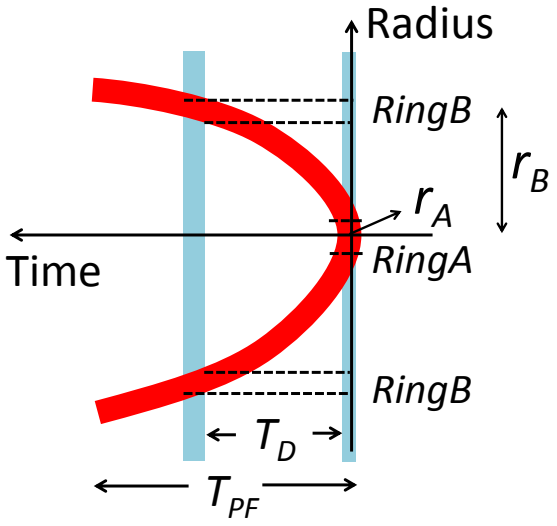

Figure 5.8: A sketch explaining the time delay between pulses from the ring shaped intensity within the beam.

5.5.3 Autocorrelation methods

Autocorrelation is an important method in characterizing the temporal property of an ultrashort laser pulse. It is the cross-correlation of a signal with itself at different points in time. In this subsection, the autocorrelation process for the whole beam, and for two annulus intensity distribution are compared. Two cases with shorter and longer laser pulse durations are considered.

The autocorrelation process can be expressed by the integration of two split input pulses,

variably delaying one with respect to the other,

$$Trace(t) = \int_{-\infty}^{\infty} I(t) \cdot I(t - \tau_D) \cdot d\tau_D \tag{5.5}$$

where τ_D is the delay between the two split input pulses.

Figure 5.9 shows the simulated autocorrelation of both the whole beam and an annular intensity beam for the case when the original pulse duration is 20 fs. The time average intensity of the beam is assumed to be constant with respect to radius (a flat-top beam profile). If the whole beam is measured, the autocorrelation trace shows a single peak and its width obviously broadens with an increase in T_{PF}. In contrast, the autocorrelation trace would have two side peaks if the ring-shaped pulse were measured with an equivalent T_{PF} [150].

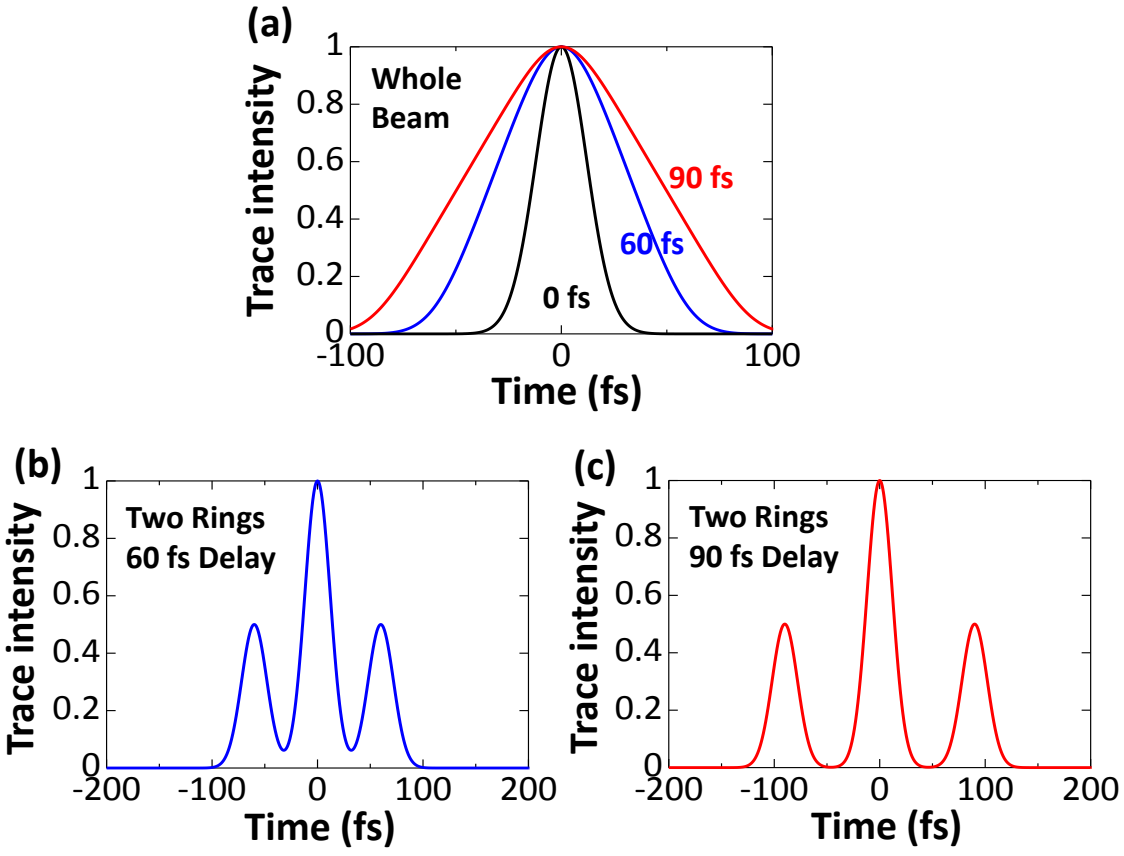

Figure 5.9: The simulated autocorrelation for a laser pulse with 20 fs duration. (a), The autocorrelation of the whole beam with T_{PF} of 60 fs and 90 fs. (b) and (c), The autocorrelation of the ring-shaped pulse with a delay T_D of 60 fs and 90 fs.

In our experiments, where the original pulse duration was 80 fs, the simulated autocorre-

lation of the whole beam and ring-shaped pulse are shown in Figure 5.10. The trace width broadening effect with increasing quadratic pulse front is not very obvious when the entire beam is incorporated into the autocorrelation measurement. The broadening effect would be even weaker if the time averaged beam has a Gaussian spatial intensity distribution across the beam. When the pulse with annular intensity distribution is used for the autocorrelation, it is seen that the trace width has a noticeable broadening, but a pulse front delay of T_{PF} = 90 fs is not sufficient to resolve the two additional side peaks.

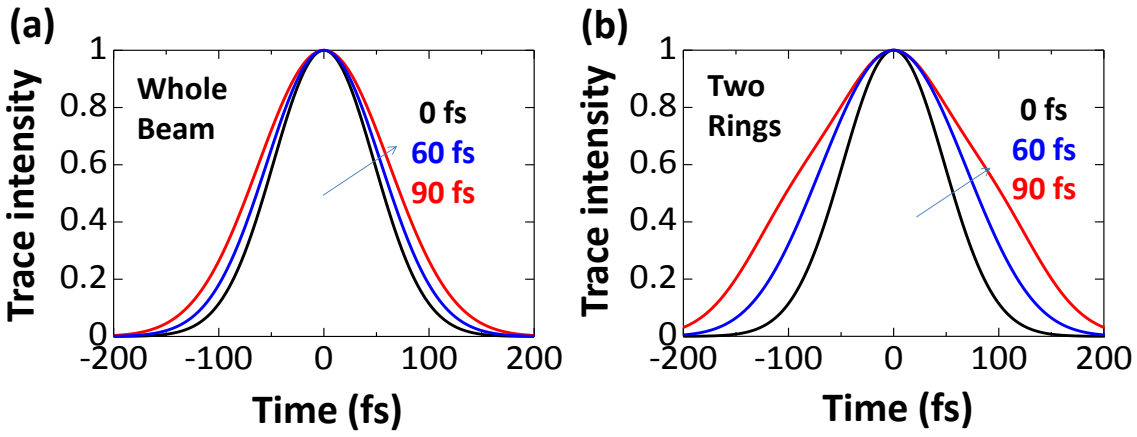

Figure 5.10: The simulated autocorrelation for laser pulses with 80 fs duration. (a), The autocorrelation of the whole beam. (b), The autocorrelation of the ring-shaped pulse.

These simulations show that when the original pulse duration is small compared to the total pulse front delay T_{PF}, both the autocorrelation of the whole beam and the autocorrelation of the annular beam can be used to obtain the value of T_{PF}. However, the autocorrelation of the whole beam would be preferable in this case as it is much easier to realise experimentally. When the pulse duration is comparable to or larger than T_{PF}, measuring the autocorrelation of the annular beam appears to be the better choice since it accentuates the effect of the quadratic pulse front.

In our experiments using a laser with 80 fs pulse duration, the dual ring illumination would be better for experimental characterization of quadratic-shaped pulse front distortion. Figure 5.11 shows the comparison of the experimental autocorrelation traces. It is seen that the width of the autocorrelation signal for the annular beam is more sensitive to the quadratic pulse front than for the whole beam. It is also notable that the time delay between the two

rings (T_D) in our experiments was too small to generate the two distinct side peaks (shown in Figure 5.10) in the autocorrelation trace.

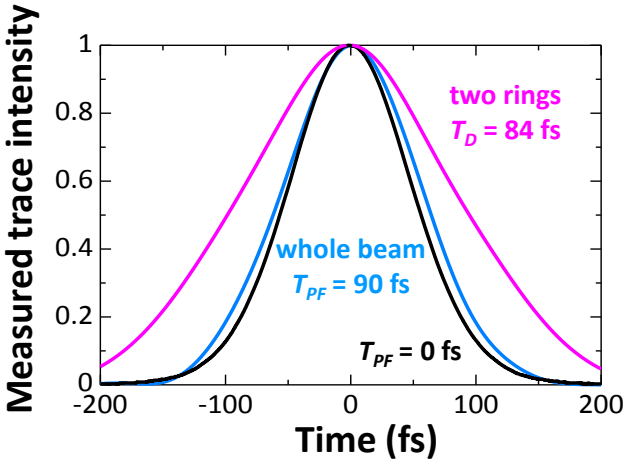

Figure 5.11: Experimentally measured autocorrelation traces with 80 fs pulse duration. The autocorrelation methods using the whole beam and the ring-shaped pulse are compared. The beam had a flat spatial intensity distribution across the pupil.

5.5.4 Autocorrelation traces

When the pulses with intensity in both $RingA$ and $RingB$ propagated into the autocorrelator, the width of the autocorrelation trace (characterized as full width at half maximum, FWHM) was determined by the amount of the time delay T_D between the two rings. The experimental results of the intensity autocorrelation trace for two rings with different time delays T_D are presented in Figure 5.12. Quadratic phase of $EOPL$ = $\pm$43 μm were applied to SLM and DM. A normalized radius of 0 was used for $RingA$, and 0.8/0.76 for $RingB$, respectively, predicting T_D to be -93 fs and 84 fs (a positive value represents that $RingB$ was delayed with respect to $RingA$). There was an obvious broadening of the autocorrelation trace when the equal and opposite phase shapes were applied to the SLM and DM, demonstrating the presence of pulse front delay. The experimentally measured curves showed close agreement with the simulated autocorrelation trace assuming T_D is equal to 90 fs.

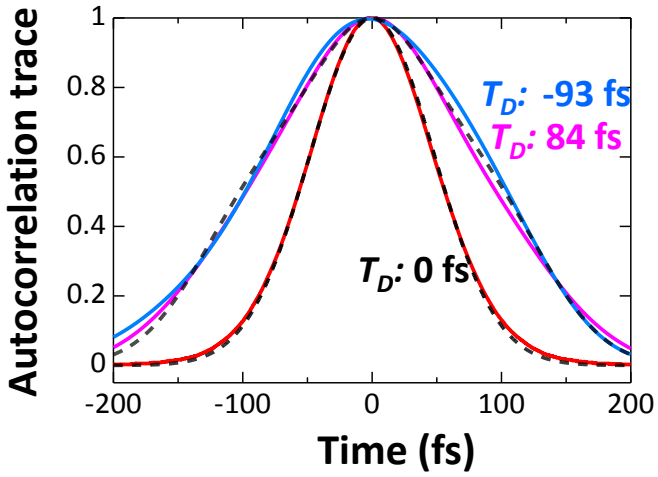

Figure 5.12: The autocorrelation measurement for pulses with delays of -93 fs, 0 fs and 84 fs. The measured intensity was normalized for each trace. Dashed curves show the theoretical simulation with T_D set to be $\pm$90 fs and 0 fs.

5.6 Pulse front shaping

By keeping the position of $RingA$ fixed at the center of the beam and varying the normalized radius of $RingB$, we were able to probe the relative temporal delay with respect to position for the rotationally symmetric pulse front distortion. In the experiments of Figure 5.13, quadratic phase shapes with different amplitudes were applied to dual AOEs. The generated quadratic pulse front was expected to be with magnitude of T_{PF} = 160 fs, 100 fs and 30 fs, respectively. As shown in the three main curves in Figure 5.13, it is seen that the autocorrelation trace widths obviously increase with the radius of $RingB$. The three solid curves are the simulation assuming the pulse fronts are with perfectly quadratic shapes. The strong match between the experimental and theoretically predicted results proves the creation of quadratic pulse fronts.

Measurements were also performed with just a single ring of intensity, as shown in the inset of Figure 5.13. The blue dots show the auto-correlation trace width for only $RingB$ with an increasing radius, while the trace widths for both rings together ($A + B$, black dots) are added for a comparison. Importantly, the autocorrelation width for a single ring stayed constant at $\sim$114 fs (corresponding to pulse duration of $\sim$80 fs based on simulation) for all the different radii of $RingB$. This strongly suggests that the pulse duration at each particular radius within the beam was roughly equal to that of the original laser pulse, and the broadening

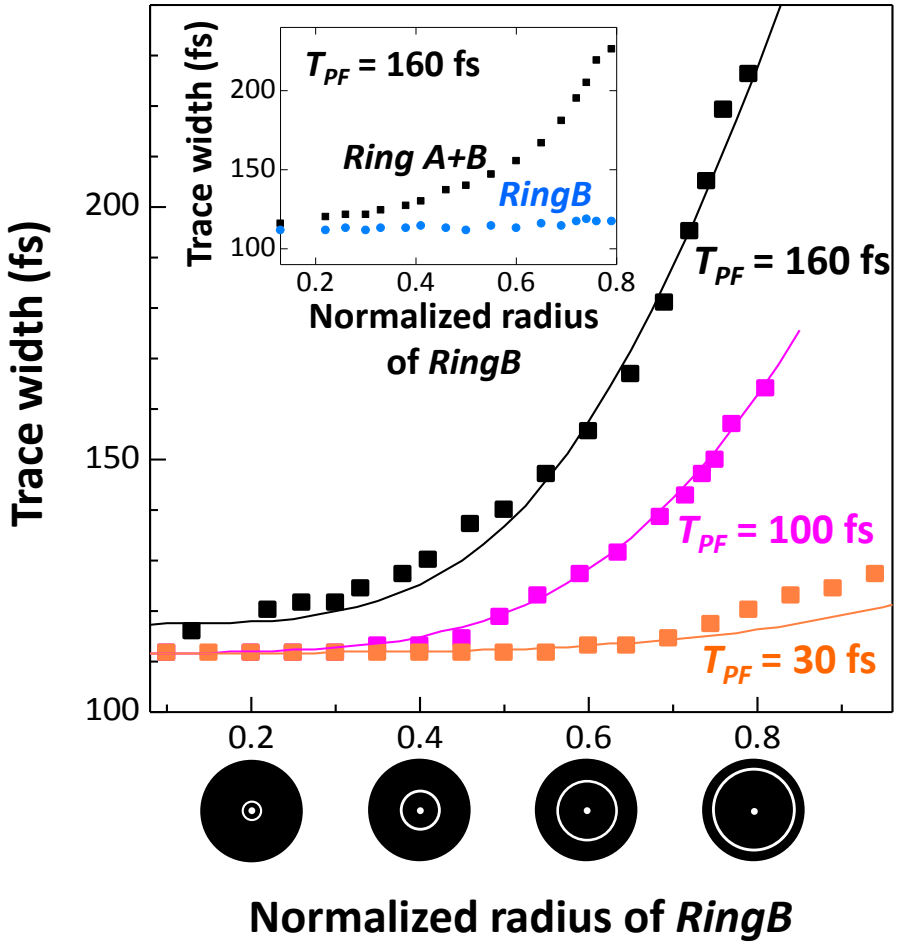

Figure 5.13: Graph showing the changes of the autocorrelation trace width with the normalized radius of $RingB$, while $RingA$ was fixed at the center of the beam. Dots show measurements; curves are theoretical predictions. Inset: Autocorrelation trace width measured for $RingB$ alone, and for $RingA$ and $RingB$ together. The measurement uncertainty for data points was estimated to be $\pm 5\%$.

of the autocorrelation trace width was solely introduced by the radially dependent time delay from the quadratic-shape pulse front implemented by dual AOEs.

Due to the adaptive nature of the pulse front shaping, it was straightforward to flexibly adjust the magnitude of the quadratic pulse front. In Figure 5.14, the created total amount of quadratic pulse front T_{PF} is plotted against measured autocorrelation width. The normalized radius of $RingB$ is fixed to be 0.67. The strong match between the experimental and theoretically predicted data demonstrates controllability of the pulse front over a large range: the maximum T_{PF} created was 175 fs by applying a phase with $EOPL$ = 52 μm to the SLM and the DM.

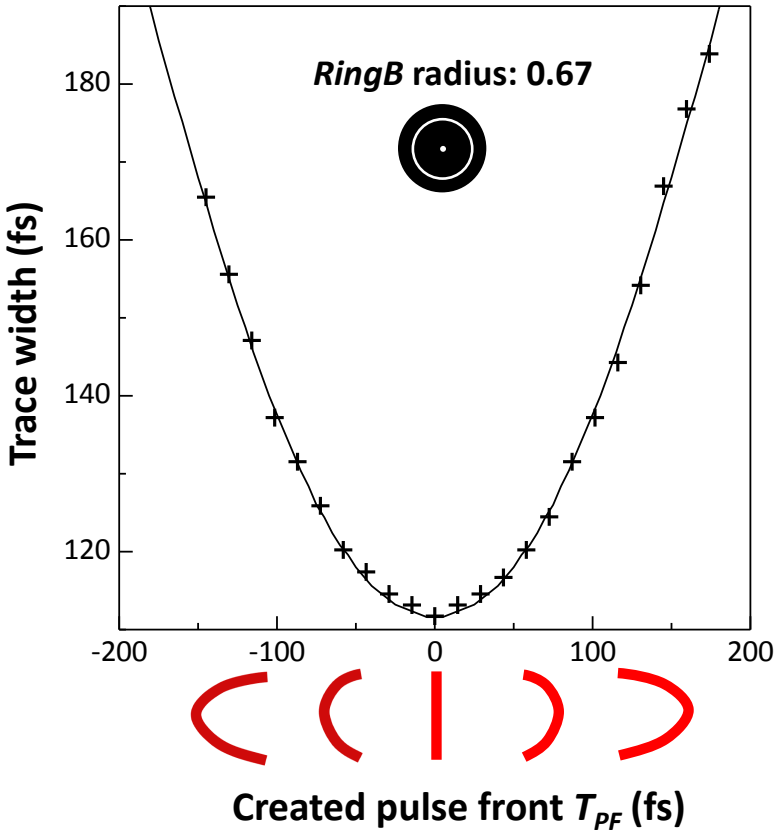

Figure 5.14: The measured autocorrelation trace width (cross data points) for $RingA$ and $RingB$ together ($RingB$ radius is 0.67), versus the magnitude of created quadratic pulse front. Solid curve is the theoretical prediction. The measurement uncertainty for data points was estimated to be $\pm 5\%$.

We therefore conclude that it is possible to shape the pulse front through applying equal but opposite phase fronts to a SLM and DM, and that the pulse front distortion is controllable by varying the magnitude of the phase shape. We note that since the level of pulse front distortion T_{PF} was of the similar order to the original pulse duration, the spatially integrated temporal envelope of the whole beam did not exhibit a significant change. Direct measurement of the entire beam [150] without any annular spatial masking still revealed a broadening of the autocorrelation trace, but the broadening was too small resulting in a much lower resolution for the characterization of pulse front in our situation.

5.7 Discussion

The quadratic shaped pulse front is an important study, since it is the most commonly encountered pulse front distortion in an optical system − the well-known propagation time difference (PTD) [151, 152] (Section 2.6.2, Chapter 2). However, this technique of pulse front shaping is not simply limited to quadratic profiles. Through proper choice of phase for SLM and DM, in principle pulse fronts with any desired shape and magnitude can be created. Beside the quadratic phase, we additionally applied astigmatism and coma phase with opposite amplitudes to SLM and DM. Flat phase fronts were verified by the wavefront sensor, indicating the pulse front with astigmatism and coma shapes were created, although those complex pulse front shapes could not be measured easily by the autocorrelation process.

Although specific lenses or static optical components may be designed to minimize the pulse front distortion in a specific system [147, 148, 153, 154], a significant benefit of this technique allows both the shape and magnitude of the pulse front to be adaptively tuned for any practical scenario. Once fully calibrated, the dynamic response depends on the employed AOEs, and is similar to any adaptive optics optimization routine [63]. Rather than a specific case, this technique could be widely used in any systems with any form of pulse front distortion. Furthermore, the use of adaptive optic elements gives the ability for simultaneous control over the pulse front and phase front in one single system. While creating a desired pulse front, one can introduce an additional phase front through applying a phase pattern to the SLM. In this way, the pulse front and phase front can be manipulated at the same time independently of each other.

While these experiments were conducted for the laser with 80 fs pulse duration and 790 nm central wavelength, this pulse front modulation technique is, of course, applicable to lasers of other pulse duration operating in different wavelength bands. A limiting factor moving to lasers of shorter pulse duration will likely relate to dispersion within the SLM. With such effect, the phase front of laser pulses would not be perfectly cancelled by the dual AOEs for all spectral components. However, assuming typical values for the liquid crystal dispersion at a central wavelength of 790 nm, there is expected to only be $\pm\ 2\%$ variation in the $EOPL$ over a 200 nm bandwidth. Therefore, this effect is usually considered to be negligible for most

of the lasers. In the future, the advent of new adaptive elements, such as segmented mirror SLMs, are expected to increase the usable bandwidth of the pulse front modulation scheme.

It is well known that the correction of phase front aberrations is beneficial in the applications of ultrafast lasers [66, 90, 155]. In addition, numerous studies have demonstrated the pulse front distortions generally exist in an optical system, and bring undesired effects, especially when using pulses with shorter durations [123,150,156–159]. However, there have until now been limited studies on the correction of these distortions − primarily due to the absence of an effective method for adaptive pulse front control. The demonstrations in this chapter suggest a promising method for the correction of various forms of system-induced pulse front distortions. In addition, the ability to create more complex pulse fronts could possibly bring new and interesting applications in laser material processing, where it is already known that pulse front tilt can strongly affect the light-matter interaction [125, 160].

5.8 Conclusions

In summary, a new technique using adaptive optical elements to shape the pulse front of an ultrafast laser has been demonstrated. The phase front of the laser pulses was characterized by the measurement of a wavefront sensor. The pulse front was characterized by autocorrelation of two angular beams. Quadratic shape pulse fronts with various magnitudes were demonstrated. This new ability with, in principle arbitrary pulse front shaping, could be applied to the correction of wide forms of pulse front distortions, and open new windows for applications requiring advanced manipulation of ultrashort laser pulses.

Chapter 6

Compensation of pulse front distortion in two-photon microscope

6.1 Introduction

In Chapter 5, a new adaptive optics concept that is able to arbitrarily shape the pulse front of the laser light was introduced. With the compensation of opposite phase fronts introduced by a deformable mirror (DM) and a liquid crystal spatial light modulator (SLM), collimated beams with any desired pulse front shape can be created. In this chapter, I present a first practical application of this new pulse front adaptive optics method.

The fact that the pulse front distortion (spatial variation in group delay (GD) across the beam) generally exists in optical systems has been reported by numerous studies [123, 141, 150, 156]. However, until now, dynamically pulse front correction has not yet been realized. There is also very limited investigation for the effect of pulse front correction in practical applications. Optical microscopy is a vital tool for multi-dimensional non-invasive imaging in various research areas. The two-photon fluorescence microscope confines the non-linear nature of the excitation fluorescence excitation to a small focal volume, thus enabling high-resolution and three-dimensional imaging deep inside specimens [161]. In two-photon microscopy, the pulse front distortion could introduce temporal aberration to the laser focus, thus broadening the focal pulse duration and reducing the focal intensity. These effects are

dramatic when laser pulses with short duration are used. In this chapter, I show adaptive correction of system-induced pulse front distortion in two-photon microscopy, and demonstrate further improvement beyond conventional phase correction.

6.2 Pulse front distortion in the optical system

In a two-photon microscope, the major system-induced distortion arises from the propagation time difference (PTD) of the lenses (Section 2.6.2, Chapter 2). The magnitude of the distortion is dependent on the optical path length, which is related to the lens radial position. As shown in Figure 6.1 (a), after propagating through a chromatic lens, the pulse front is radially distorted, forming focal distortion in the time domain. Conventional singlet lenses or aspheric lenses usually have a large distortion, while achromatic doublets are designed to minimize the distortion. Objective lenses were found to have a residual amount of pulse front distortion [156,162,163], which can become serious for more complex lenses containing more elements [164].

In a paraxial model, the PTD has a quadratic relationship with the radius r [123] (Equation 2.45, Chapter 2). We therefore chose to demonstrate adaptive correction of pulse front distortion by introducing a quadratic shape pulse front to the laser light. If the introduced pulse front perfectly cancels the pulse front distortion, we are able to maintain a temporally undistorted focal point (Figure 6.1 (b)).

As it is impractical to calculate the magnitude of pulse front distortion in a whole system, it was necessary to create a series of quadratic pulse fronts with different magnitudes, and apply a sensorless adaptive optics routine, whereby the shape giving the highest focal intensity is considered to approach the optimal correction. In the description below, we first discuss a three-stage procedure to effectively remove phase aberrations. By creating 20 quadratic shapes with different magnitudes, we then used the two-photon signal as the feedback metric to demonstrate the effect of pulse front correction. Finally, we present improvements in the two-photon imaging of biological samples. Similar to the previous chapter, we use the equivalent optical path length ($EOPL$) to represent the peak-to-valley magnitude of the phase front applied to the dual AOEs, and T_{PF} to represent the peak-to-valley time delay for the pulse

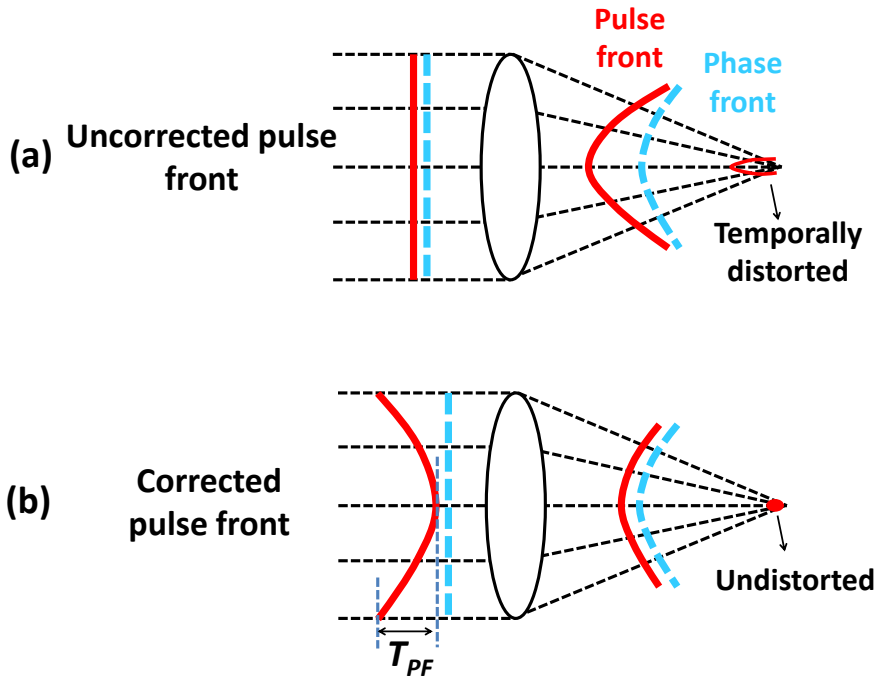

Figure 6.1: (a) Focusing of the laser light with uncorrected pulse front. The focus is distorted in time domain by the spatially variant propagation time difference (PTD) of the lens. (b) Focusing of the laser light with corrected pulse front. Temporal distortion is removed by the correction.

front ($T_{PF} = EOPL/c$, where c is the speed of light, shown in Figure 6.1 (b)).

6.3 Optical system

In the two-photon microscope set-up, the laser source and pulse front adaptive optics arm were the same as that described in Section 5.3, Chapter 5. The laser was with central wavelength of 790 nm and 80 fs pulse duration. A high numerical aperture oil immersion objective (Olympus oil lens: 60, 1.4 NA, PLAPON60XO) was used to focus the laser light into either a fluorescent sea containing Alexa594 dye, or biological samples. A PMT was aligned to measure the two-photon emission. Achromatic doublets were adopted throughout the system to reduce the pre-existing system-induced pulse front distortion.

A pair of prisms was aligned to compensate the group velocity dispersion (GVD) effect arising from the optical system. The duration of the pulse at the pupil of the objective lens was kept to be 80 fs with the verification of autocorrelator measurement. We note that the GVD

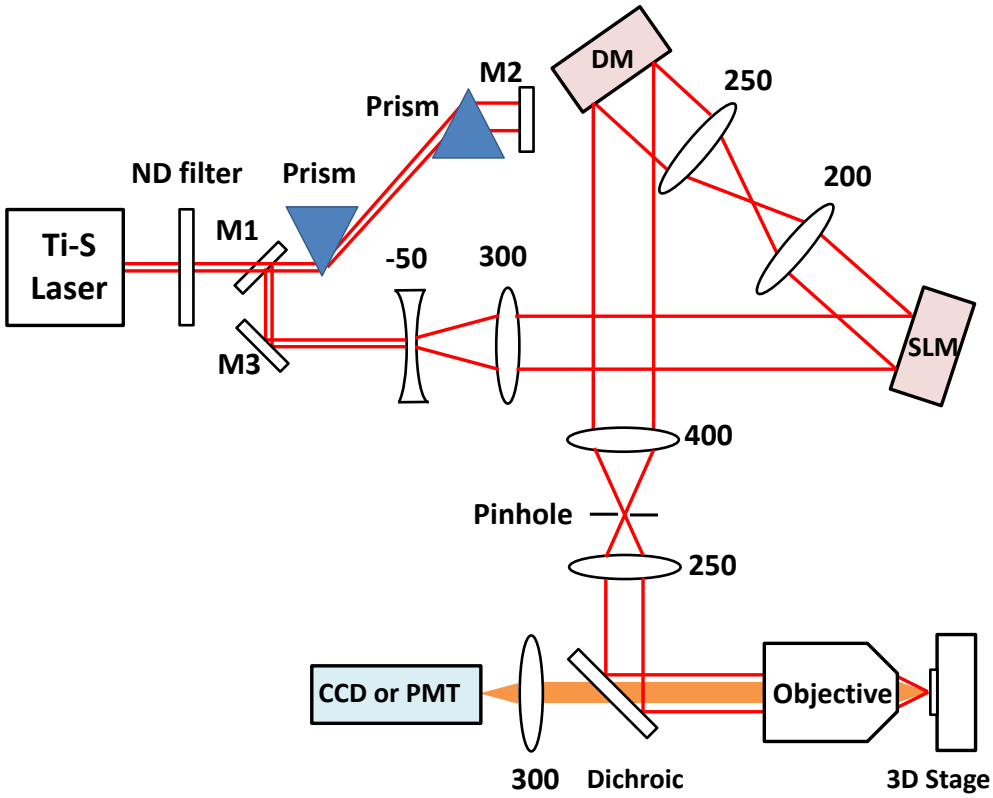

Figure 6.2: The optical system of two-photon microscope with a pulse front correction arm. The focal lengths (mm) of the achromatic doublets are shown in the adjacent number. ND filter: neutral density filter, M1 − M3: mirror No. 1 to No. 3, SLM: spatial light modulator, DM: deformable mirror. Dichroic: dichroic mirror.

and any other high order dispersions only affect the laser pulse duration, but have no effect on the pulse front. The whole system is shown in Figure 6.2.

6.4 Correction of phase aberrations

Phase aberrations have a pronounced detrimental influence on the magnitude of any non-linear fluorescence generation at the focus [165]. In order to use the two-photon signal as a metric to demonstrate the correction of pulse front distortion, it was imperative to ensure that any residual phase aberrations in the system were effectively removed when opposite phase patterns were applied to the SLM and DM.

6.4.1 Three-stage phase correction

We followed a three-stage procedure to make sure all possible phase aberrations were extensively canceled. Initially, a Shack-Hartmann wave-front sensor was aligned after the dual AOEs. There is detailed discussions for adopting the wavefront sensor in correcting the phase aberrations in the last chapter (Section 5.4, Chapter 5). The SLM and DM were updated until the wave-front sensor confirmed that the phase front aberration was below 0.08 μm ($EOPL < 0.08$ μm) for the light entering the objective lens [166]. This stage compensated the majority of the large phase aberrations.

Subsequently, by aligning a mirror at the focal position, the laser light is strongly reflected back to the dichroic mirror. As the dichroic mirror did not fully block the laser light, a small proportion of the reflected laser propagated through the dichroic mirror. Therefore, the 3D focal intensity distribution was able to be imaged onto a CCD camera. Using a phase-diversity approach [167], the SLM and DM were further updated to provide compensation for small magnitude phase aberrations.

In the final stage, we used a PMT to measure the two-photon emission from the fluorescent dye. Any residual small phase aberrations were finely corrected using a sensorless adaptive optics scheme [168]. In this stage, the major Zernike mode aberrations, which are mode 5 - 11 and high order spherical aberrations of mode 22 and 33, were corrected. After this stage, individual maximum two-photon signal was found for each pulse front shape.

These three methods are currently the major techniques used in the adaptive optics to correct the phase aberrations. All the three methods were conducted following the order to correct the larger aberrations to smaller aberrations. It fully makes sure that all the phase aberrations were extensively removed.

6.4.2 Effectiveness of phase correction

One method to verify the phase aberration correction result is to introduce aberrations with different magnitudes, and characterize the response in the two-photon intensity. Examples to show this method are in Figure 6.3. The verification was conducted after the three stage phase correction. Astigmatism (mode 6) and spherical (mode 11) aberrations were taken as

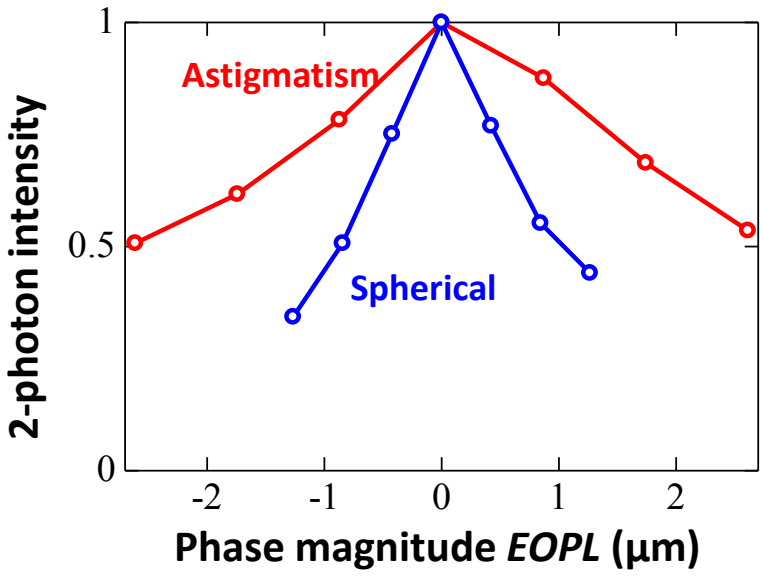

Figure 6.3: The two-photon intensity versus magnitudes of phase aberrations. The magnitudes of astigmatism (mode 6) and spherical (mode 11) were controlled by applying a phase pattern to the SLM. The calculation of $EOPL$ is presented in Section 5.4, Chapter 5.

the examples. The magnitude of the aberrations was controlled by applying a phase pattern to SLM. It is seen in the figure, that the two-photon fluorescence intensity has maximum value when the applied aberrations are equal to zero. When the aberrations were applied with either positive or negative magnitudes, the two-photon intensity presents a decreasing trend. This verification confirms that the aberrations have been extensively removed, so that any additional phase change introduces a reduction in the focal intensity.

An additional verification to show the effectiveness of this three stages phase correction is to measure the focal intensity distribution by the light scattering from a 100 nm gold bead. The intensity of scattering light, which was measured by a PMT, was proportional to the laser light illuminated onto the gold bead. The gold bead was scanned by the 3D stage through the laser focus to generate three dimensional images [169]. Figure 6.4 presents both the axial and lateral images of the foci, when quadratic pulse fronts with T_{PF} equal to -90 fs, 0 fs and 90 fs were introduced (note that a T_{PF} of 90 fs is equivalent to 34 wavelengths of distortion). The dimensions of foci with quadratic pulse fronts of -90 fs and 90 fs were slightly larger, caused by a reduced effective NA arising from the lower illumination power at the edge of the pupil (more details discussed later). From the quality of the imaged foci which were compared

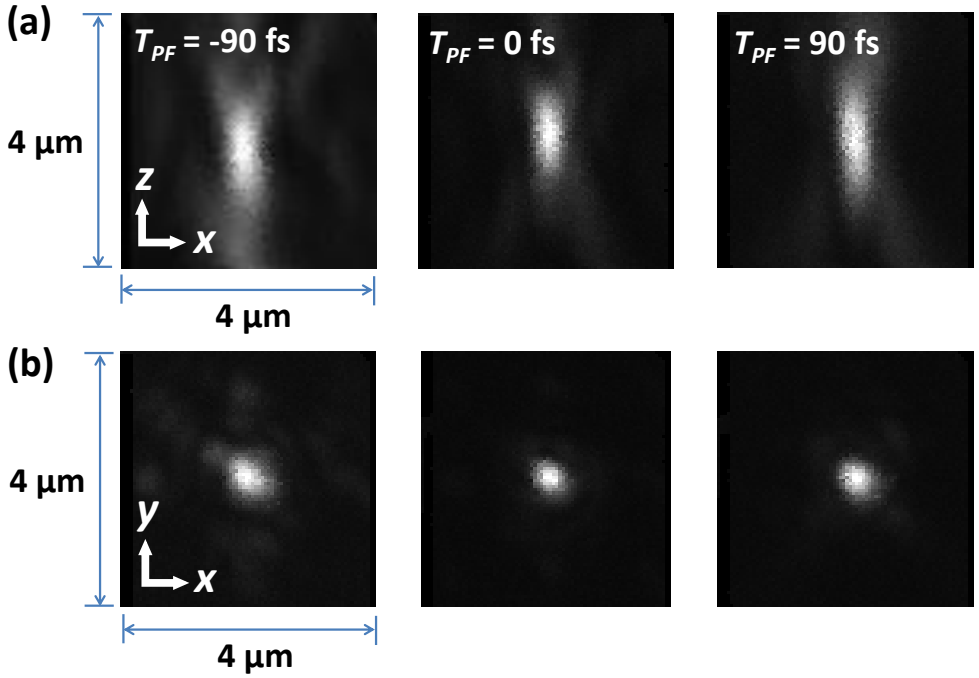

Figure 6.4: (a) Axial and (b) lateral focal intensity distribution measured by the light scattering from a gold bead. Each image is normalized by its own peak intensity. The images show that residual phase effects were minimal, even in the presence of significant pulse front distortion.

with theoretical simulations [170], and the maximum two-photon signal confirmed in the third stage of phase correction, we consider that the residual phase aberrations were negligible in our demonstration.

The initial three-stage correction makes sure that all the experiments afterwards were conducted under the minimum phase aberrations. With the three-stage phase correction, we consider the system was initially set-up, and ready for the next pulse front correction experiments.

6.5 Pulse front correction

To demonstrate the effects of pulse front correction, 20 quadratic pulse fronts with different magnitudes were created for the focusing of laser light. Each pulse front shape was finely produced with the three stage compensation of phase aberrations discussed above.

6.5.1 Pupil intensity

For a fair comparison, the input laser power contributing to the focal two-photon excitation should be exactly the same for these 20 shapes. The first factor that needs to be considered is the reflection efficiency of the SLM. Large phase patterns displayed on the SLM reduced the diffraction efficiency, particularly at the edge of the beam where the required phase gradient was largest [171]. As shown by the images of the intensity distribution at the objective lens pupil in Figure 6.5, with a flat phase distribution (T_{PF} = 0 fs), the intensity was fairly uniform across the beam. However, when we applied a quadratic pulse front with T_{PF} = 90 fs, the intensity at the edge of the pupil became smaller than that at the centre. Therefore, for the same input power from the laser source, larger phase patterns reduced the total integrated power contributing to the two-photon excitation.

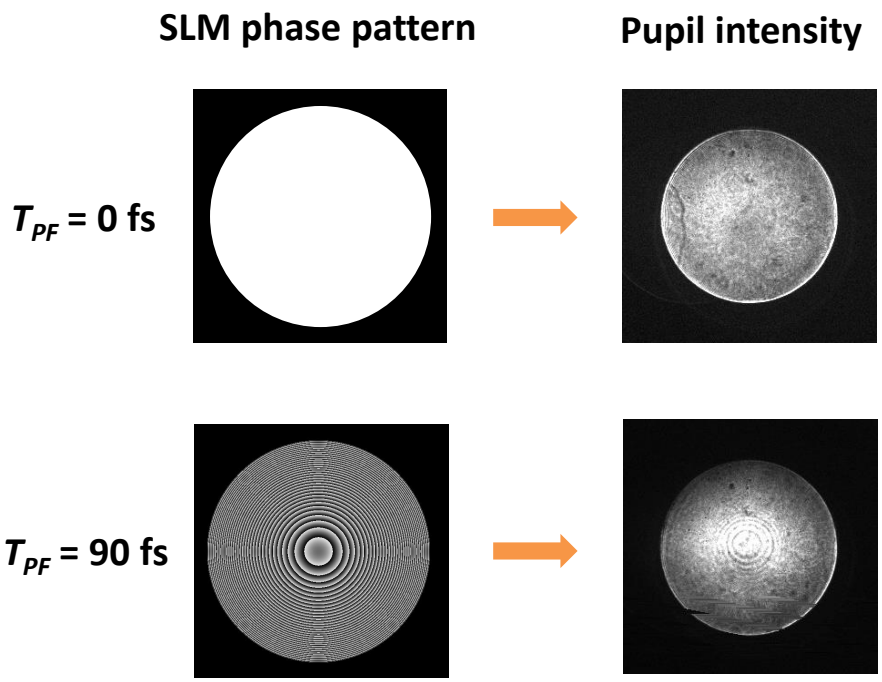

Figure 6.5: Phase pattern in SLM and pupil intensity distribution measured by a CCD camera. For the intensity distribution, each image is normalized by its own peak intensity. The top images show that the SLM is with a flat shape (T_{PF} = 0 fs), while the bottom images show the case when the adaptive optics elements create a quadratic pulse front with T_{PF} = 90 fs.

6.5.2 Total internal reflection

When the light was focused through a cover glass into a water-based sample using a high numerical aperture (1.4NA) oil immersion objective, consequently, some of the excitation light at the beam periphery was lost due to total internal reflection (TIR). Total internal reflection (TIR) occurs at the interface of the cover glass (refractive index = 1.5) and the specimen (water solution, refractive index = 1.33) (refractive indices are quoted at wavelength of 790 nm). This reduces in effect the available numerical aperture of the objective to a value below that of the specimen refractive index. Therefore, it is needed to determine the effective aperture angle.

The relationship between the incident angle θ_i and the refraction angle θ_r of an optical ray is calculated by Snells Law [116]:

$$n_1 \sin\theta_i = n_2 \sin\theta_r \tag{6.1}$$

The reflection coefficient of the optical ray (assuming circularly polarised light) at the interface is defined via Fresnel equations [116] as,

$$R = 0.5 \cdot (R_s + R_p) = 0.5 \cdot \left(\frac{\sin(\theta_i - \theta_r)^2}{\sin(\theta_i + \theta_r)^2} + \frac{\tan(\theta_i - \theta_r)^2}{\tan(\theta_i + \theta_r)^2} \right) \tag{6.2}$$

Although the laser illumination is polarised, the wide range of angles in the focusing cone mean that the proportions of s and p polarised light vary across the beam, as would the reflection coefficients. For this reason, we adopt the coefficient of Equation 6.2 as a rotationally invariant approximation to the actual reflection properties. A plot of the reflection coefficient versus incident angle is shown in Figure 6.6 (a). Here we define the effective aperture angle as the incident angle for which the reflection coefficient is 50%. We assume that rays with an incident angle larger than the half coefficient reflection angle are not transmitted. In our case, the effective aperture angle for the light transmitting from the cover glass into water is 62.1°.

The incident angle of the optical ray at the edge of the full objective pupil can be calculated by,

$$\sin\theta_{edge} = \frac{NA}{n_1} \tag{6.3}$$

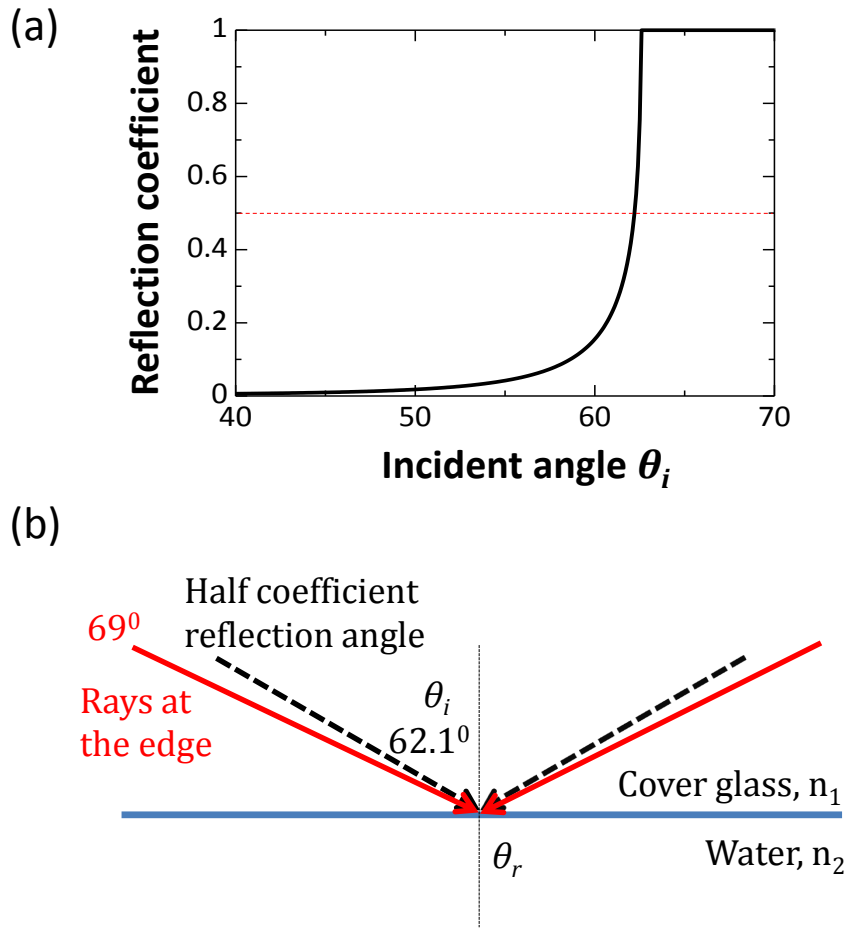

Figure 6.6: TIR effect of the oil objective lens focusing into water. (a) The reflection coefficient of the optical rays transmitted from the cover glass into water with different incident angle. (b) A sketch shows the TIR effect when the laser was focused from cover glass into fluorescence dye.

NA is the numerical aperture of the objective lens. This angle is 69° for a 1.4 NA oil objective lens, and 71.2° for a 1.42 NA oil objective lens. For the system where TIR occurs at the cover glass, the extent of the effective pupil can be calculated as,

$$r_{TIR} = \frac{\sin\theta_{TIR}}{\sin\theta_{edge}} \tag{6.4}$$

Only light passing through this effective aperture contributes to the focal intensity, and as such was considered when measuring the power incident on the objective. This is important when ensuring that the input pupil power was constant for all the measurements of the two-photon florescence emission with varying pulse front distortion. In the experiments in this chapter, the effective pupil radius is calculated to be 0.95 of the full radius for the 1.4NA objective lens, and 0.93 for the 1.42NA objective lens.

Considering the above two effects (pupil intensity and TIR effect), to achieve a fair comparison, the integrated laser power within 0.95 of the normalized objective pupil radius was tuned to be 3.2 mW for all the 20 quadratic pulse front shapes investigated. This was realized by the control with a neutral density filter directly after the laser source, and the measurements of laser power within 0.95 pupil radius by a silicon power meter.

6.5.3 Two-photon measurements

Measurements of the two-photon signal generated from the fluorescent sea containing Alexa594 dye are shown as the red curve in Figure 6.7. When the T_{PF} was increased from a flat input pulse front (T_{PF} = 0 fs), the two-photon signal presented a rising trend, until peaked at 90 fs input pulse front (signal increased by a factor of 1.4). On both sides of 90 fs, the two-photon signals decreased. To validate the data, we conducted four different sets of experiments, each with separate realignment and re-calibration of the two-photon microscope system. The four sets of measured data are presented as the error bars in the curve, proving a high repeatability for the correction effect. Additionally, the experiments were repeated with another comparable objective lens (Olympus oil lens: 60×, 1.42NA, PLAPON60XO), and it was found to have the similar trends with the presented curve. We therefore conclude that introducing a quadratic

pulse front with a magnitude of T_{PF} = 90 fs, to a certain extent, corrected system-induced pulse front distortion.

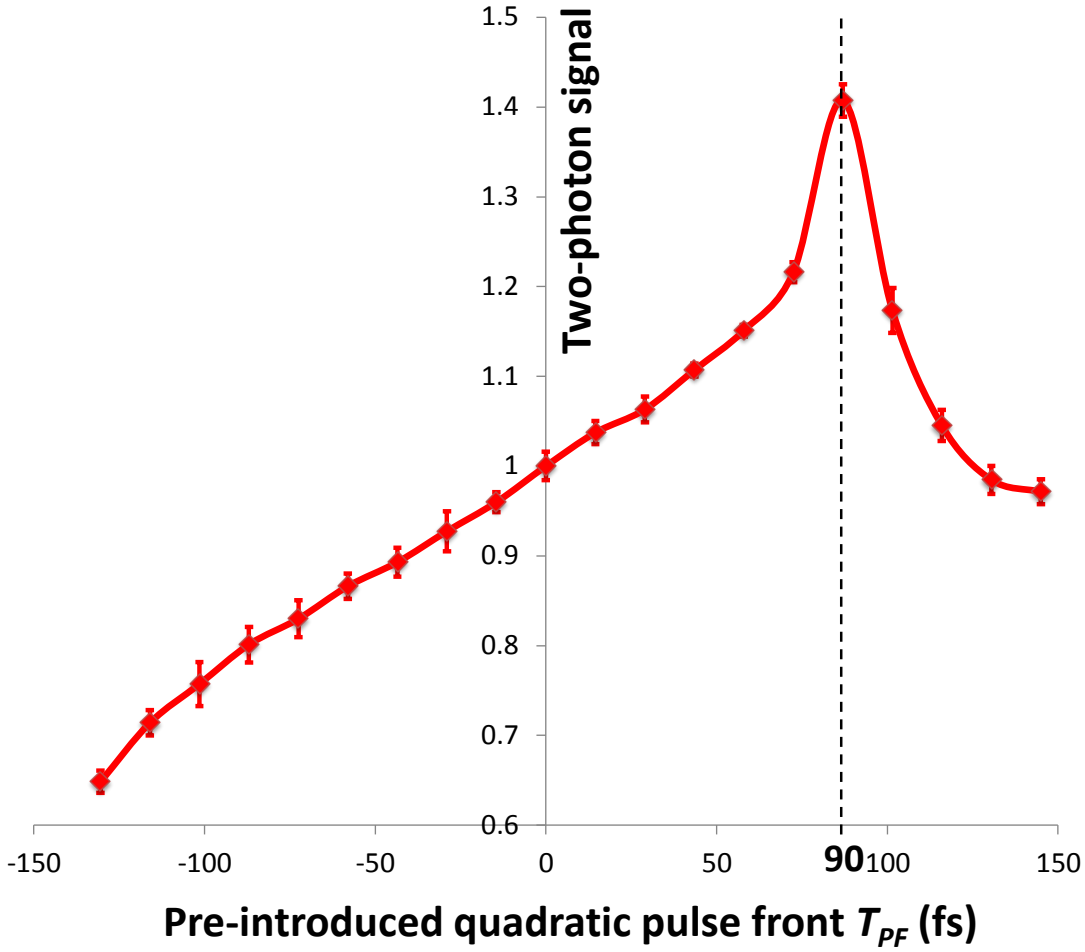

Figure 6.7: Effect of pulse front correction on two-photon fluorescence generation at the focus of an objective lens. The sample was the fluorescent sea containing Alexa594 dye. Two-photon signals are normalized to the case when no pulse front correction was introduced. The error bars for each point were based on four different sets of measurements.

6.5.4 Discussion

Figure 6.8 (a) presents the power dependence for the signal measurement, while T_{PF} was set to be 0 fs and 90 fs. The perfect quadratic dependence of the signal on input laser power confirmed the measured signal was solely from the non-linear two-photon interaction. It also demonstrate that the improvement in the two-photon intensity applies to all the incident laser powers.

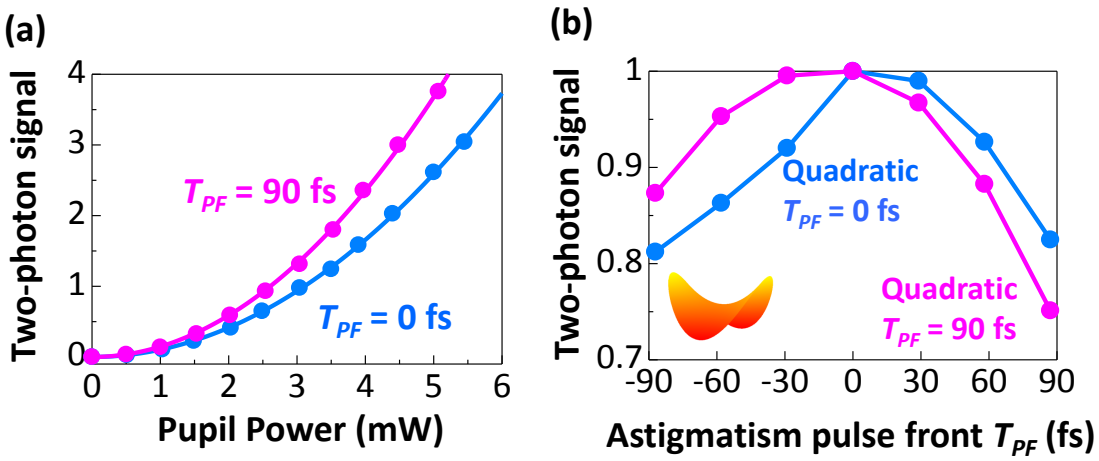

Figure 6.8: (a)Two-photon signal versus different input pupil power. Dots are measurements, while curves are quadratic fitting. (b) The effect of astigmatism shaped pulse front on the two-photon emission for two different settings of the quadratic pulse front.

We further investigated whether pulse fronts with other shapes affected the magnitude of two-photon fluorescence emission. Through application of opposite astigmatic phase patterns to the SLM and DM, we created a pulse front shape with an opposite quadratic temporal delay between orthogonal directions in the beam cross-section. The phase front was checked to be flat by the same three stages described above. The magnitude of two-photon emission was found to decrease monotonically as the level of astigmatic pulse front distortion increased, as shown in Figure 6.8 (b). Two cases were examined: in the first case, the starting point was a flat pulse front; in the second, an additional quadratic-shaped pulse front of amplitude 90 fs was applied. The astigmatic pulse front, which is orthogonal to the quadratic shape, uniformly reduced the focal intensity through an increase in the focal pulse duration as expected. This strongly indicated that the improvement in fluorescence signal when using quadratic-shaped pulse fronts alone is related to a correction of a system-induced pulse front distortion, as opposed to an anomaly introduced by the pulse front control scheme.

6.6 Two-photon images of pollen grain

We further demonstrated the benefits of pulse front correction on the two-photon imaging of biological samples. The images were acquired (Figure 6.9) for pollen grain samples (Blades

Biological Ltd, CBS040) with a fixed pupil power of 3.2 mW. Phase aberrations were fully corrected by the same three-stage procedure as discussed above. When we applied pulse front control to remove the system induced distortion, the images (Figure 6.9, right side) became brighter as should be expected from the data in Figure 6.9 (a). Following pulse front correction, the image contrast was noticeably improved; this can also be seen in the line plots of the intensity taken from the images. It has been well known that the correction of phase aberrations can increase the signal level and contrast in such microscopes. However, for all the images shown in Figure 6.9, the phase aberrations were all ideally corrected within the capabilities of the adaptive optics used. Furthermore, one would expect that any residual aberrations would be worse in the "pulse front corrected case, as the phase settings of the dual adaptive elements are larger, leading to larger residual phase aberrations (Figure 6.4). The fact that the pulse front corrected images exhibit greater contrast is therefore a clear indication of the benefits of the pulse front correction.

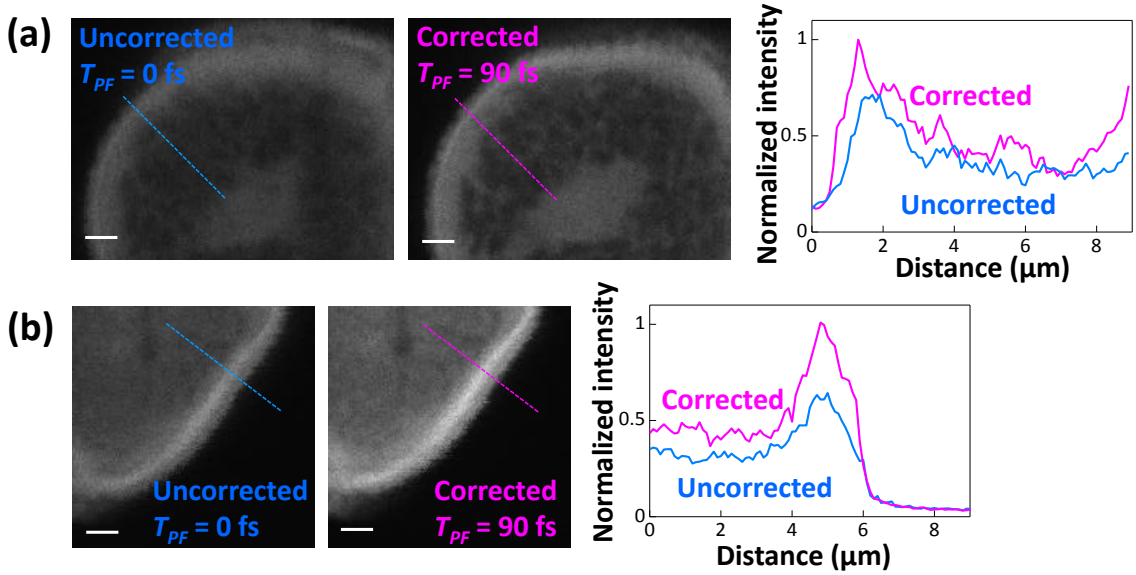

Figure 6.9: Effect of pulse front correction on two-photon microscope imaging of pollen grain samples. Two sets of images were taken with the uncorrected (T_{PF} = 0 fs) or corrected (T_{PF} = 90 fs) pulse front. The scale bar is 2 μm. Normalized two-photon intensity plots along the lines marked in images are also shown.

6.7 Pulse front correction for different pulse durations

Assuming a PTD of 90 fs is introduced by a singlet lens, the ratio for the two-photon intensity arising from a PTD corrected focus over the uncorrected focus can be calculated for input pulses of varying duration. The detailed calculation method was in reference [143]. As shown in Figure 6.10, the increment ratio increases dramatically with shorter pulse duration. The benefits of pulse front correction are much more significant when using shorter pulses. We expect a similar trend would be present in our experimental system, whereby the two-photon fluorescence is maximised when applying a pulse front with T_{PF} = 90 fs. We expect the modest improvement ratio in fluorescence yield of 1.4 to be increased significantly when a laser with shorter pulse duration is employed. It is notable that in the calculation of Figure 6.10, the pulse durations are for the laser pulses at the focus. In contrast, the pulse duration in the two-photon microscope discussed above is for the laser at the objective pupil. The 80 fs laser pulse would be broaden to more than 100 fs after propagating the objective lens due to the GVD effect.

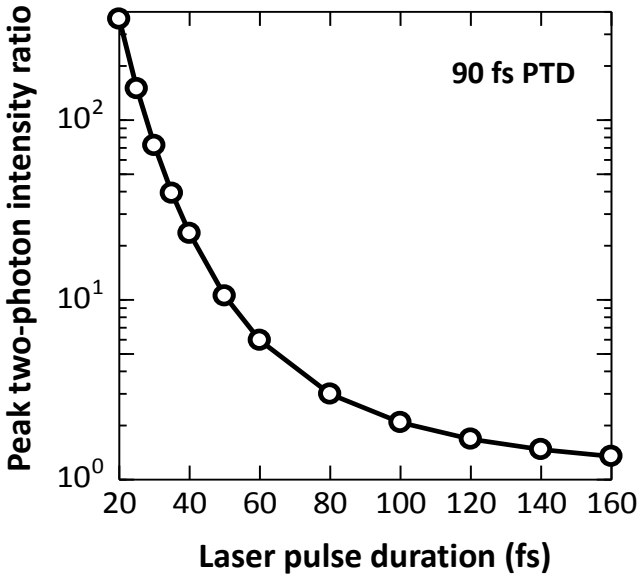

Figure 6.10: The peak two-photon intensity increment ratio after the correction of PTD for the laser with different pulse durations. The pulse durations presented at the horizontal axis are for the laser pulsed at the focus.

6.8 Conclusions

In conclusion, this chapter demonstrates the adaptive correction of pulse front distortion in a two-photon microscope. With the phase aberrations fully removed, the pulse front correction offers further improvements for the two-photon signal. In our demonstration, distortions with quadratic shape may also arise when the laser was focused through the objective immersion and sample cover-glass, however, they were all corrected as the "system-induced" pulse front distortion in our case. Besides the two-photon microscope, one pronounced benefit of this method is that, it can introduce the pulse front correction with any shapes and magnitudes which is able to be adapted to any applications using ultrafast laser. The two-photon signal was increased by 1.4 times for a 80 fs laser in our demonstration, however, this ratio enhancement will be significantly more if lasers with shorter pulse duration were adopted.

Chapter 7

Laser fabrication of high conductivity graphitic wires in diamond

7.1 Introduction

Chapter 3-6 discuss several forms of imperfection in an ultrafast laser focusing system. Effects of focal distortions and methods to correct them are investigated. One of the distortions, the phase aberration effect arising from the refractive index mismatch has been discussed. This form of distortion is mostly encountered in laser material processing. From this chapter onwards, I apply the adaptive optics to several real applications in laser micro-fabrication. The correction of focal distortions leads to significant improvements in the quality of laser fabricated structures.

Chapter 7 specifically concentrates on graphitic wire fabrication in diamond, which is a truly remarkable material, from both aesthetic and scientific points of view, due to the scope of exemplary material properties [135]. It has a high Young's modulus with a low thermal expansion coefficient and high thermal conductivity [172]. The high biocompatibility creates opportunities for biotechnology applications [173, 174]. It is optically transparent over a wide spectrum and a highly diverse mix of color centers render diamond attractive for photonic and quantum technologies [175]. Advances in CVD doping technology have created interesting electrochemical applications with conductive diamond electrodes [176, 177]. Another very

promising route for the functionalization of diamond is the generation of buried electrically conductive graphitic microstructures. This graphite fabrication in diamond has various applications, such as all-carbon diamond radiation detectors [60, 61, 178–181], metallo-dielectric photonic crystals [62], ohmic contacts [182], infrared radiation emitters [183], field emitters [184] and bolometers [185]. One method to fabricate the subsurface graphite structure is through the implantation of heavy ion beam into the diamond lattice [186–190], capable of fabricating ultra-thin graphite layers with a very uniform surface [187, 188], as well as 3D graphitic structures through micro-patterning [190]. After annealing the diamond, the resistivity of the irradiated regions was found to have a similar value to polycrystalline graphite [190, 191]. However, this fabrication procedure is usually complex and time consuming, and the graphitic structures are limited to a depth within $\sim$5 μm from the diamond surface. On the other hand, laser processing, which has previously been demonstrated as a powerful tool in the micro-fabrication of various materials [192–196], offers another way to create graphitic structure in diamond. The focused ultra-short intense laser pulses create a high electric field magnitude, inducing subsequent transformation of the diamond lattice into graphite [59]. The graphitisation is confined to the laser focus, and by translating the diamond through the focus it is easy to trace out the conductive wires, which are presented in this chapter. Compared to other methods, laser processing intrinsically presents a much easier and quicker way to generate graphitic wires in diamond, and the fabrication can be conducted much deeper within the diamond substrate ($>$1.5 mm [62]).

Nevertheless, different from laser processing in other low-index transparent materials, high-quality laser fabrication inside diamond experiences some significant challenges that have persisted over the last decade. In order to generate high quality, homogeneous and uniform graphitic wires with controllable thin sizes, the width of the employed laser pulse should be short enough (such as using a fs/ps laser) [61, 181, 197]. However, until now, ultra-short pulsed laser processing has had very limited success in fabricating uniform conductive wires inside diamond: i) with low resistivity; ii) following arbitrary 3D paths. Despite numerous efforts, current fs/ps laser induced wires still have resistivity more than two orders higher than that of polycrystalline graphite [61, 62, 181, 198], and it is only possible to fabricate the

uniform conductive wires along the direction of the laser beam propagation, perpendicular to the diamond surface (defined here as the z axis) [59, 62, 197–203]. If laser processing is going to progress as a promising technique for fabrication of high-quality conductive micron/submicron wires in diamond, it is essential to carefully address these two existing problems. Recently, there have been numerous valuable studies investigating ways to improve this laser graphitic wire fabrication technique [59, 62, 197–203]. However, effective methods to overcome these two challenges have not yet materialized.

The current applications of graphitic wires [60–62, 178–185] are dependent upon their electrical properties. Therefore, a reduction of resistivity is crucially important to obtain superior performance for the graphitic devices. On the other hand, the ability to induce wires along any 3D path is extremely important not only to maximise the potential of existing devices, but to also introduce new applications through the fabrication of highly complex graphite structures.

In this chapter, I show an advanced fs-laser fabrication scheme that simultaneously resolves those two problems. This scheme adopts the dynamically adjust of the input wave front. It enables the laser writing of high quality wires along any orientation, greatly expanding the fabrication capabilities by allowing the wires to follow any 3D path. The adaptive fs-laser fabrication generates highly conductive, homogeneous, uniform wires with controllable dimensions down to at least 400 nm. Furthermore, the increased control over the laser induced material modification leads to a significant reduction in the resistivity down to 0.022 Ω cm. This advanced technique enables the versatile design of high quality, complex, 3D graphitic structures within a large accessible volume inside diamond, and promises to benefit a wide range of applications in diamond science and technology.

7.2 Laser fabrication process

This section outlines the optical system for the laser fabrication of graphitic structure inside diamond. The effect and adaptive compensation of refractive index mismatch aberration are discussed.

7.2.1 Fabrication system

Previously, fabrication with nanosecond pulse width lasers was found to have a reduction in the resistivity of the graphitic wires, but at the expense of increased structural inhomogeneity [61, 181]. Even for small laser powers around the graphitization threshold, large irregular features are generated and there is extensive crack formation in the surrounding diamond [197]. Additionally, long pulsed lasers (such as $>\sim$100 ps) usually generate a large damaged volume, which makes it very difficult to fabricate wires either with ultra-thin sizes or with precise 3D shapes. As this chapter aims at high quality, homogeneous thin 3D wire fabrication, a femtosecond pulsed laser source was therefore necessarily employed. The ultrashort nature of the femtosecond pulse is important in minimizing any additional graphitization in regions surrounding the focus and allowing much more precise size control.

Laser fabrication in the bulk of diamond is much more challenging than at the surface. A large refractive index mismatch between the immersion medium of the objective lens (n_L = 1.52 for oil, n_L = 1 for air) and the diamond (n_H = 2.4) leads to refraction of incident rays at the diamond surface and generates spherical aberration (Section 2.5.2, Chapter 2; refractive indices are quoted at wavelength of 790 nm). To remove this aberration, a liquid crystal spatial light modulator (SLM) was adopted to dynamically control the wave-front of the incident laser light. By applying a phase to the SLM which is opposite to any induced aberrations, diffraction limited performance could be maintained throughout the diamond substrate.

The optical system is shown in Figure 7.1. The laser source was a Newport Spectra Physics Solstice, central wavelength 790 nm, 100 fs pulse duration, repetition rate 1 kHz. A half-wave plate and a Glan-Taylor polarizer were aligned to control the laser power. To fabricate inside the diamond, the SLM (Hamamatsu X10468-02) was imaged using a 4f lens system onto the pupil plane of an Olympus 60$\times$ 1.42 NA oil immersion objective lens. For the fabrication of the diamond surface, a Zeiss 20$\times$ 0.5 NA dry objective lens replaced the oil immersion objective. A LED, which was located under the specimen, provided illumination for a transmission microscope, which consisted of the fabrication objective lens and an additional doublet lens, allowing the fabrication process to be viewed in real time. A single crystal CVD diamond (5 mm $\times$ 5 mm $\times$ 3 mm, Element Six) with polished side surfaces was used as the sample.

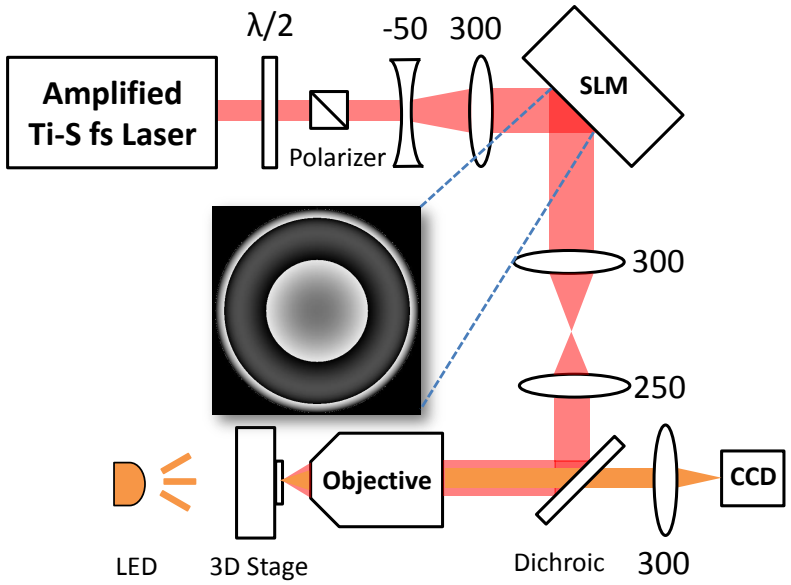

Figure 7.1: Optical system for fabrication in diamond sample with dynamic adaptive wavefront introduced by SLM. The focal lengths (mm) of the achromatic doublet lenses are shown adjacent to each component. The inset shows an example phase shape applied to SLM when fabricating the wire at a depth of 20 μm inside diamond.

To confirm the ultrafast laser processing turns diamond into graphite, we conducted Raman spectrum measurements [204] for both fabricated region and unfabricated diamond sample. The measurement for laser fabricated region was performed on the surface area, as significant refractive index aberration made it difficult to conduct Raman characterization deep inside the sample. The measurement results are shown in Figure 7.2. It is seen in the measurement curve (dark) of the diamond bulk, the SP^3 peak at 1332 cm^{-1} is extremely strong, confirming a strong portion of diamond in the original sample [205]. It is shown that there is a SP^2 peak at around 1420 cm^{-1} (D peak) in the dark curve, which indicates there is also small amount of amorphous carbon in the sample. This is probably because the manufacture of diamond sample did not bring a perfect purity for the diamond. After the laser processing, it is seen in the red curve that the SP^3 peak at 1332 cm^{-1} is in a low intensity, while the SP^2 peak at around 1420 cm^{-1} disappeared. Another SP^2 peak at 1580 cm^{-1} (G peak) became strong. This confirms that the diamond has been turned into graphite in the fabricated region [205]. The SP^3 peak still existed in the red curve, which means there is still remaining diamond in the graphitized region, though the proportion should be low.

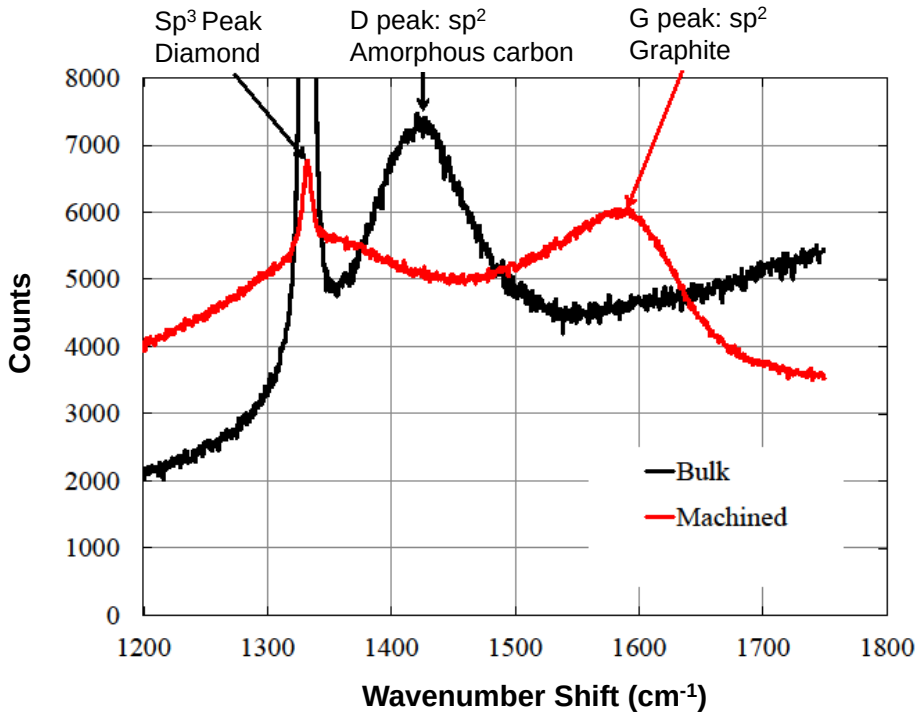

Figure 7.2: The Raman spectrum measurement of diamond bulk (dark curve) and laser fabricated region on the surface of diamond (red curve).

7.2.2 Refractive index mismatch aberration

The fabrication scheme is explained in Figure 7.3 (a) and (b). Typically in conventional laser fabrication, a flat wave-front is incident on the pupil of the objective lens. As demonstrated by the theoretical focal energy distribution in Figure 7.3 (a1), which is simulated for a 1.4 NA oil immersion lens focusing 20 μm beneath the surface of diamond, the focus is seriously distorted, elongated and non-uniform along the z axis (Kerr effect is neglected in the calculation). This distortion increases with fabrication depth [170]. With the use of a SLM (Figure 7.3 (b1)), the incident wave front was dynamically adjusted to remove the aberration enabling a highly confined laser focus at different target depths. The appropriate phase for aberration compensation at a particular depth was predicted by theory given knowledge of the material refractive index (Section 2.5.2, Chapter 2). Implementing such aberration correction in experiment was achieved by using position feedback from the sample translation stages to update the phase patterns displayed on the SLM. To ensure this was the case, we verified that the aberration correction was indeed optimum by monitoring the threshold pulse energy for material modification as a function of the SLM phase [206].

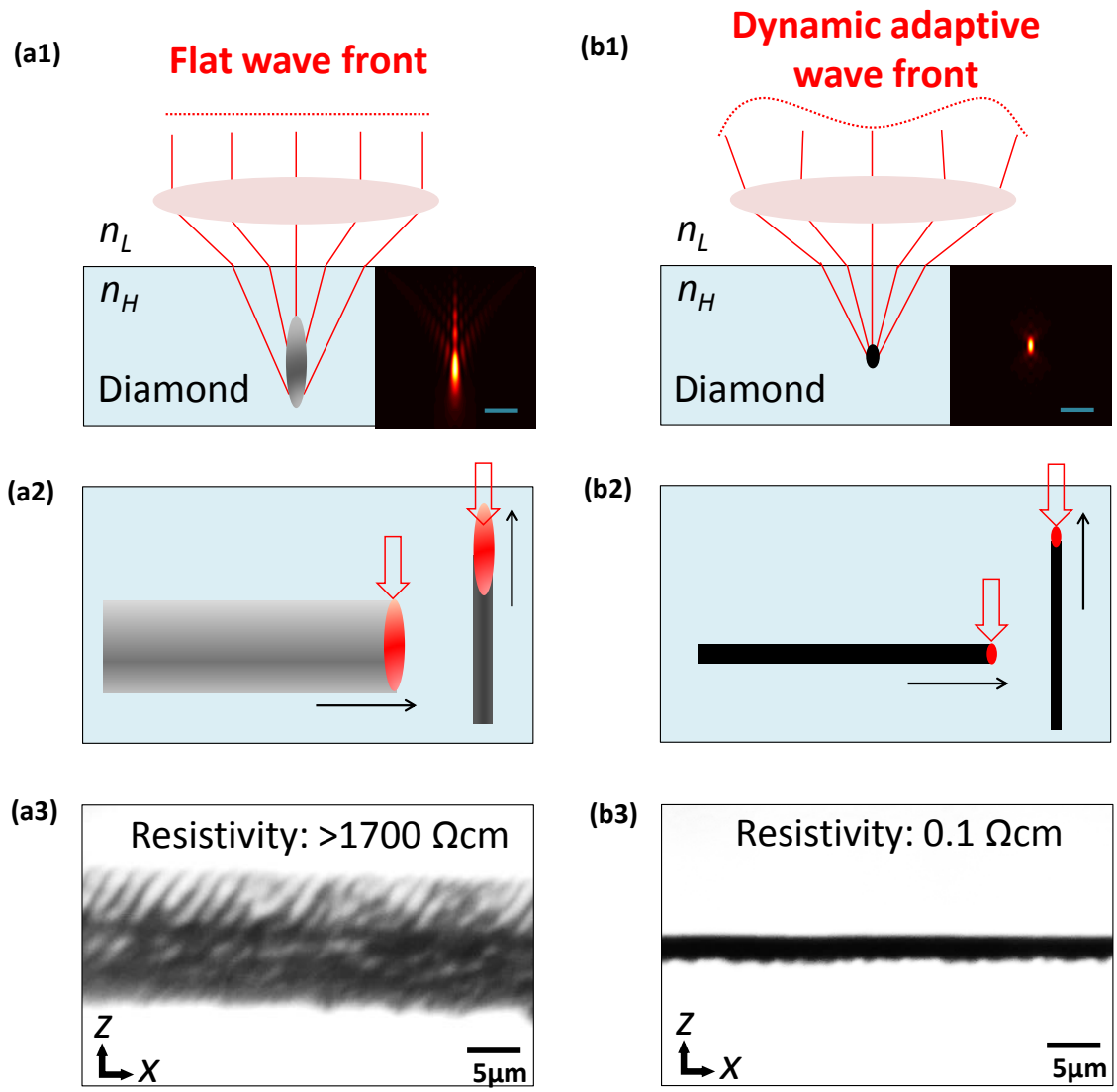

Figure 7.3: Fabrication of graphitic wires without (a) and with (b) aberration compensation. (a1) (b1) Schematic of the focusing geometry and theoretical calculation of the focal intensity distribution (scale bar is 2 μm). (a2) (b2) Illustration of fabrication perpendicular and parallel to the diamond surface. (a3) (b3) Experimental transmission microscope images showing associated wires fabricated parallel to the surface at a depth of 20 μm in diamond.

Comparing the sketches in Figure 7.3 (a2) and (b2), we can see that while fabrication along all directions seems to be possible for a beam without any aberration correction (a2), the corrected beam (b2) offers far better control over the fabrication process and wire size. The major focal distortion in (a) is along the z direction, while the focal dimensions are not as seriously affected along the x or y axis. This indicates the reason why previous laser fabrication in diamond has always been successful along the direction of beam propagation (z axis) [59, 62, 197–203], but very limited in all other directions. If we look at the fabrication

parallel to the surface in an experiment, the structural modifications in (a3) from the uncorrected beam are much larger and crucially give rise to high non-uniformity in the conversion from diamond to graphite. There appear to be regions inside the laser processed area along the irradiated path where the diamond is unaffected by the laser. In contrast, the structural modification arising from an undistorted focus (b3) shows good confinement along the z axis and a high level of uniformity. There are no obvious regions where the diamond lattice remains unmodified following fabrication. The relative resistances give the most telling comparison though (resistance measurement details are described in the next section). Both have a length of 70 μm in the x direction, but the resistance for the wire fabricated with the distorted focus (a3) is found to be beyond the range of our measurement apparatus ($>$30 MΩ, corresponding to a resistivity $>$1700 Ω cm). In contrast, the wire fabricated with the corrected focus (b3) has a measured resistance of 20 kΩ (resistivity $\sim$0.1 Ω cm). The following discussion will firstly concentrate on wires fabricated parallel to the diamond surface, since these have not been previously realized in established laser fabrication. Then we will expand the directions to fabricate single three dimensional wires with arbitrary trajectories.

7.3 Method for resistance measurement

The electrical performance of the conductive wires was studied in detail for different fabrication parameters. In order to measure the resistance of the wires inside the diamond, two graphitic pillars with a cross-section size of about $\sim$5 $\times$ 5 μm were fabricated to connect the wire to the surface. Surface contacts with a size of about $\sim$12 $\times$ 12 μm were also fabricated subsequently using a dry objective lens (this avoids problems associated with boiling of immersion oil when using an oil immersion objective for fabrication very close to the surface). The structure is shown in Figure 7.4 (a). A micro-positioner rig with probe tips (diameter 10 μm) was used to make electrical contact with the embedded graphitic wires. The resistance was measured by an Agilent 4192A LF Impedance Analyzer. The resistance was found to be $>$30 MΩ if one probe touched the graphite contact when the other probe touched the diamond surface; the resistance was about 0.5 Ω if the two probes touched the surface of a gold contact separated by a distance of 100 μm.

The sample wires shown in Figure 7.4 (b) and (c) were fabricated at a depth of 20 μm, speed of 10 μm/s with a laser power of 20 μW (pulse energy 20 nJ). In order to control the size of the cross-section, one wire was fabricated by several passes of the diamond through the laser focus with a slight axial shift in the focal position between each pass. Each pass was separated by an axial shift of 0.5 μm. Transmission microscope images of the top view and side view of the graphitic wire fabricated with four passes of the laser beam are presented. The approximately elliptical cross-section of such a wire was measured to have minor and major axes of 1.4 μm and 3.2 μm respectively. As the dimensions were measured from the microscope images, there is approximately $\pm \sim 5\%$ error for the values of cross-section sizes.

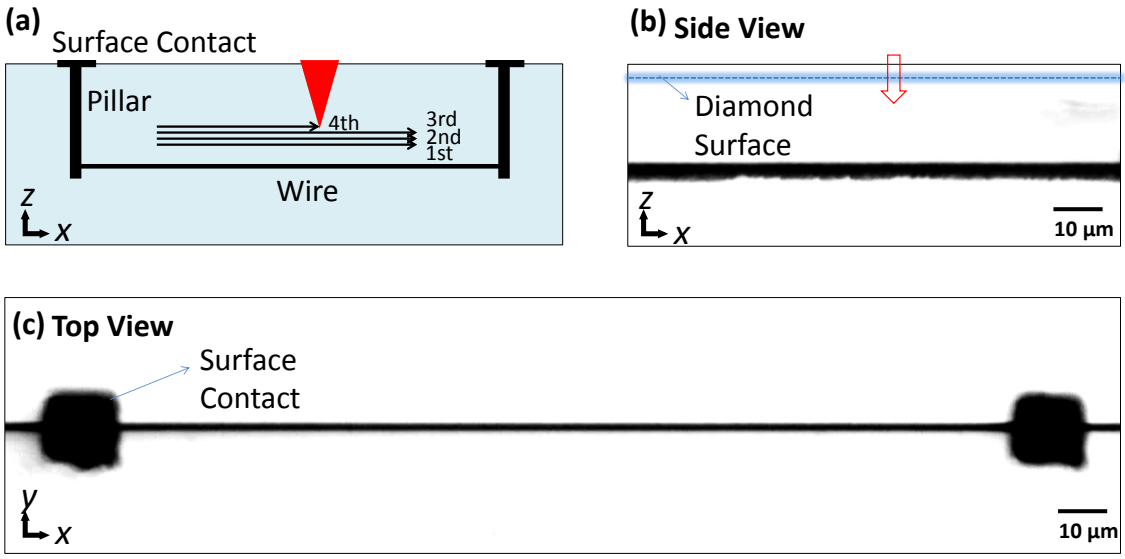

Figure 7.4: Scheme for electrical characterisation of the graphitic wires. (a) The structure of embedded wire contacts. (b) Side view and (c) Top view transmission microscope images of the wire for resistance measurement. The wires were fabricated with four passes shifted along z direction and are at a depth of 20 μm below the diamond surface.

The pillars were fabricated from higher depth to lower depth through the diamond. At each depth, a square shape graphitic structure was generated by transmitting several passes of the diamond through the laser focus. While the fabrication depth changed, the compensation phase for the correction of refractive index mismatch aberration was adjusted and applied to SLM. When the laser focus approached the diamond surface, cracking occurred and the immersion oil of objective lens was partly boiled. A side view microscope image of the pillars which were connected to the wires is shown in Figure 7.5 (a). It is seen that the pillars

are uniform across the axial direction, and this confirms a good aberration correction at each depth. The cross-section size of the pillar can be controlled by modifying the size of the square shaped graphitic structure.

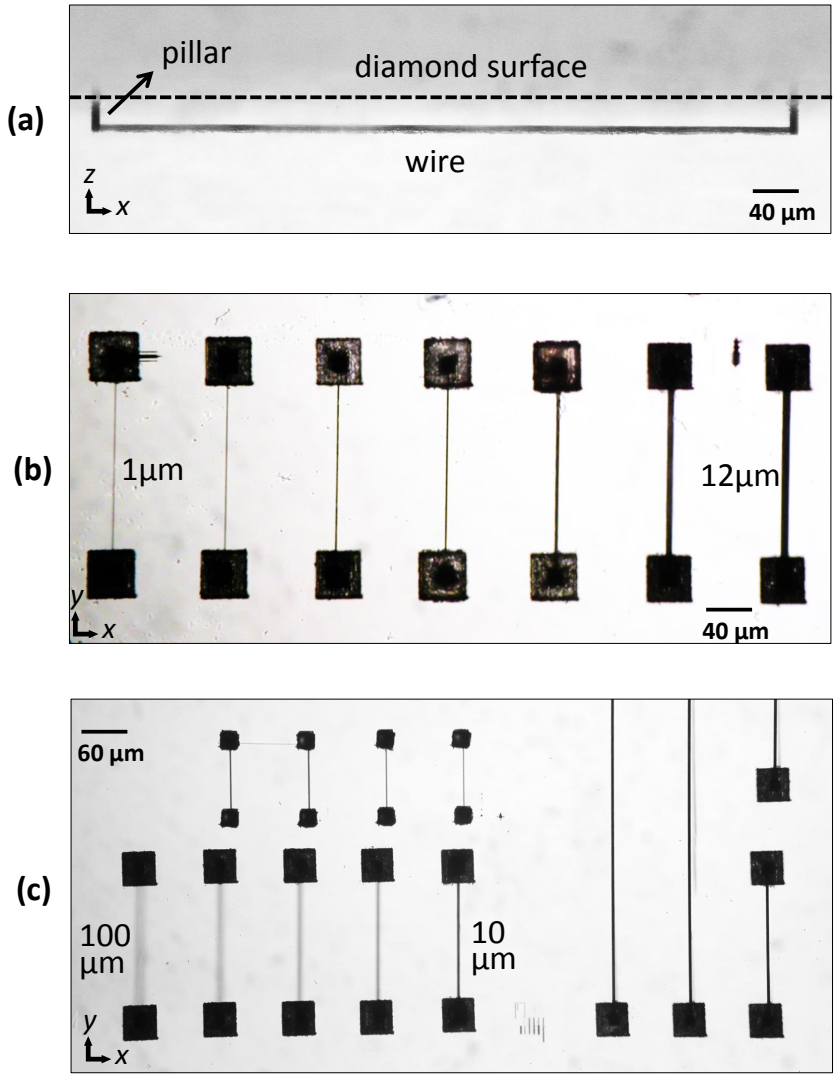

Figure 7.5: (a) Side view optical microscope image of a wire which was connected to two pillars. Surface contacts were not fabricated. The length of the pillar is 20 μm. (b) Wires fabricated with different cross-section sizes. The lateral width range is from 1 μm to 12μm. (c) Wires fabricated with various depth and lengths. The depth range is from 10 μm to 100μm. The size of surface contact was adjusted according to the length of the wire.

Similarly, the cross-sectional size of the graphitic wire can be controlled by changing the total number of the passes of diamond through the laser focus, as well as the distance between the passes. This method could be used to modify both the lateral and axial section sizes. The distance between each passes is a very important parameter, as it affects the resistivity of the

wire. Normally, a larger distance brings unmodified regions between each pass, thus increases the resistivity. On the other hand, a smaller distance increases the fabrication time and reduces the fabrication efficiency. Through an investigation, we found a lateral shift of 0.5 μm, and an axial shift of 0.8 μm would be a good choice considering both the resistivity and fabrication efficiency. The wires with different cross-section sizes are shown in Figure 7.5 (b). We note, when the cross-section size of the wire becomes larger, cracks could be generated beside the wire. This is because the graphite has smaller density compared to that of diamond, so that the strain increases along the graphitization area due to the increased volume.

The surface contact cannot be fabricated by a high NA oil lens (lens with oil immersion), as the power of the laser focus usually boils the oil. A dry lens has to be re-aligned for the surface graphitization. A relatively higher laser power is usually used. The size of the surface contact should be larger than the cross-section size of the pillar, and large enough for an appropriate contact with the micro-probe. Figure 7.5 (c) shows a series of wires connected with surface contacts with different sizes. The size of the surface contact does not have a significant influence on the resistance measurement. In Figure 7.5 (c), the wires with different fabrication depthes are also shown. With increasing depth, the phase applied to SLM becomes larger, and perfect compensation becomes more and more difficult.

7.4 Resistivity of graphitic wires

In this section, we investigate effect of the improved fabrication method on the resistivity of graphitic wires. The resistivity was characterized by the resistance measurements and physical sizes of the wire. Wires with various lengths and cross-section sizes are discussed. We demonstrate an axial multi-fabrication scheme, which could significantly reduce the resistivity of the graphitic structure.

7.4.1 Axial multi-fabrication scheme

During laser fabrication of diamond, the existing graphitic structure could block the propagation of laser light. This usually affects the graphitization of diamond in the area below the

existing graphitic structure. This effect is negligible for the fabrication of wires perpendicular to the diamond surface, as the laser focus could be translated from greater depth to shallower depth, thus the later graphitization only happens above the existing graphitic structure. However, during the fabrication of the wire parallel to the diamond surface, this effect could have an influence. Figure 7.6 shows the side view images of the wires fabricated with different laser power. During fabrication, the top region of the wire (with lower depth) usually has sufficient illumination of the laser light, thus it could be easily turned into graphite. On the contrary, the bottom region of the wire (with higher depth) usually has less laser illumination because the blocking from the existing graphite beside the target area. As a result, the lower graphitization of the bottom region could bring a much higher resistivity, which is undesired in our fabrication. Comparing Figure 7.6 (a) and (b), we could notice that the less graphitized region seems smaller for the wire fabricated with lower power. We thus developed an axial multi-fabrication scheme for an advanced control of the resistivity of the wires.

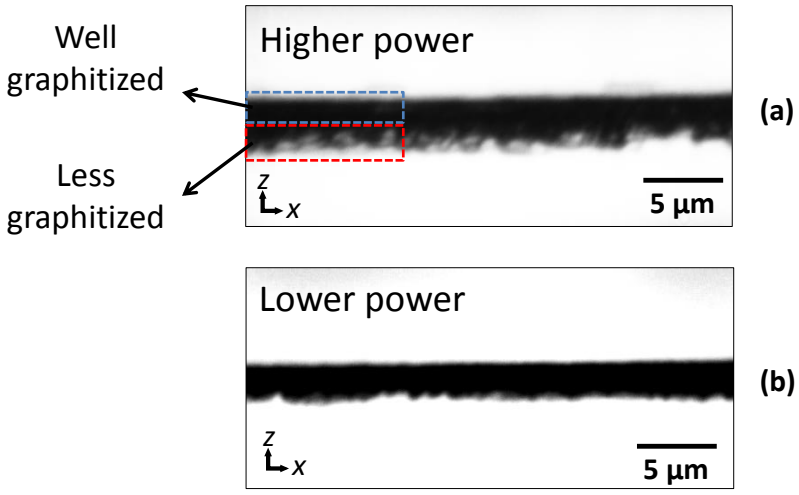

Figure 7.6: Images show the different level of graphitization of the wire along the axial direction. (a) The wire fabricated with a higher laser power (about 30 μW). The area marked with blue dashed square shows the well-graphitized region, while the area marked with red dashed square shows the less-graphitized region. (b)The wire fabricated with a lower laser power (about 20 μW).

The details of the multi-fabrication scheme is explained in Figure 7.7. With traditional method, the laser focus is scanned with one pass parallel to the diamond surface, producing a wire with well graphitized area on the top and less graphitized area on the bottom. In the

multi-fabrication scheme, we use a relatively low laser power to fabricate a wire with a first pass, and then slightly reduce the fabrication depth (with step less than the axial focal size), translating the laser focus for more passes on the top of the existing wire. With this procedure, the well fabricated graphite is gradually added on the top of the existing wire. The proportion of the well graphitized area should increase with the total number of the passes, as shown in the sketch of Figure 7.7 (a). Therefore, the resistivity of the whole wire should decrease with this method. To compare the wires fabricated with one pass and with multiple passes, we took a microscope image which is shown in Figure 7.7 (b). The left part of the wire was fabricated with four passes with a shift of axial focal position of 0.5 μm, while the right part was fabricated with one single pass. The demonstration of this resistivity reduction effect with axial multi-fabrication scheme will be discussed in detail in next subsection.

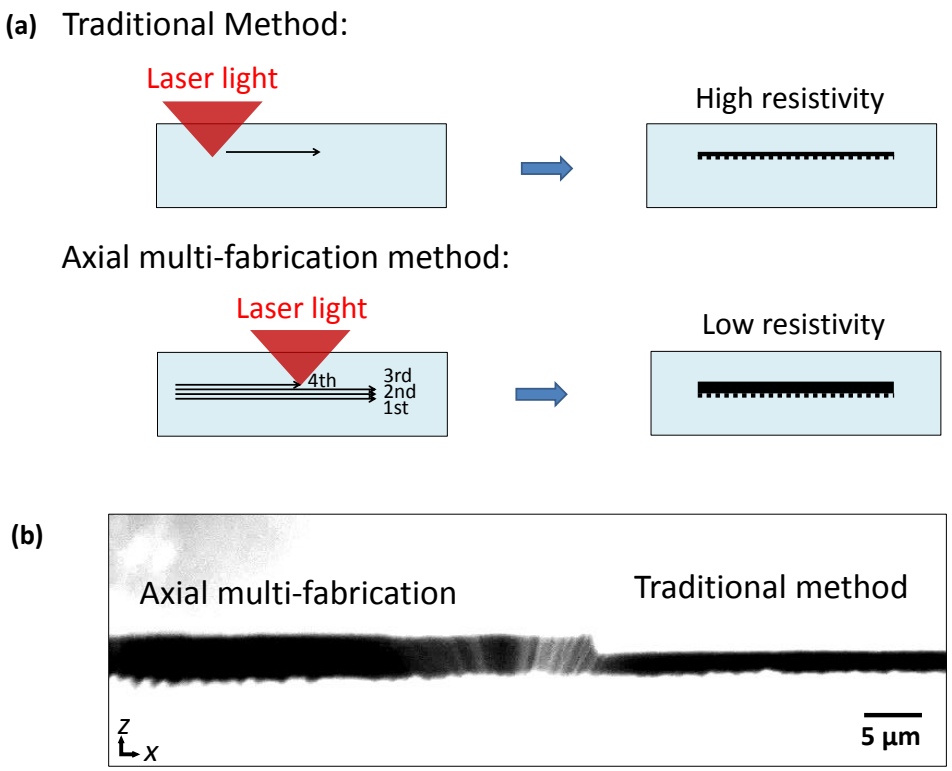

Figure 7.7: (a)Sketches showing the comparison of traditional single pass fabrication (top), and the axial multi-fabrication scheme (bottom). (b)Microscope image showing the wire fabricated with multiple passes (left part), and single pass (right part). Note the thin white strips in the middle of the image is due to illumination error in the optical microscope.

7.4.2 Resistivity measurements

We firstly study the resistance of the wires versus the wire lengths. The sample wires were fabricated at a depth of 20 μm, speed of 10 μm/s with a laser power of 20 μW (pulse energy 20 nJ). The fabrication was with four passes with each pass separated by an axial shift of 0.5 μm. The transmission microscope images of the top view and side view of the graphitic wire fabricated with four passes of the laser beam are shown in Figure 7.4 (b) and (c). The approximately elliptical cross-section of such a wire was measured to have minor and major axes of 1.4 μm and 3.2 μm ($\pm$ $\sim$5%) respectively. A set of wires were fabricated, each with equal cross-section but different lengths ranging from 50 μm - 1000 μm, The resistance of each wire was measured and is shown in Figure 7.8 (a). There is a linear increase in resistance R with wire length L as would be expected from the relationship: $R = L\rho/S$, where ρ is the resistivity and S is the cross-sectional area. This allows us to obtain the resistivity of 0.052 Ω cm ($\pm$ $\sim$5%) from the gradient of the linear fit. From the linear fit, it is seen that there exists an additional resistance of 19.7 kΩ when the wire length was equal to zero, arising from the resistance of the pillar and surface contact, as well as any additional contact losses between the measuring probe tips and surface contacts. The pillars and surface contacts for each of the wires were fabricated in sequence under identical conditions. Therefore, this additional loss is considered to be a fixed constant for all the wires.

Wires of varying cross-section were also generated by changing the number of spatially shifted passes of the laser beam during processing. The measured resistance is shown in Figure 7.8 (b), as marked points. As a guide, several theoretically calculated curves are also shown for different values of the material resistivity. The resistivity values used for the calculation are marked at the left side of the curves, having taken into account the additional contact losses of 19.7 kΩ. It is interesting to note that the resistivity is reduced from $\sim$0.069 Ω cm to $\sim$0.022 Ω cm by increasing the number of passes of the laser beam. In fact, as discussed in the above subsection, by gradually increasing the number of additional laser passes above the initial wire along z direction, the proportion of well-formed graphite increased, resulting in a reduction of resistivity for the whole wire. The effect of increasing the number of passes on the resistivity is more pronounced for a low number of passes (up to 6), and then the re-

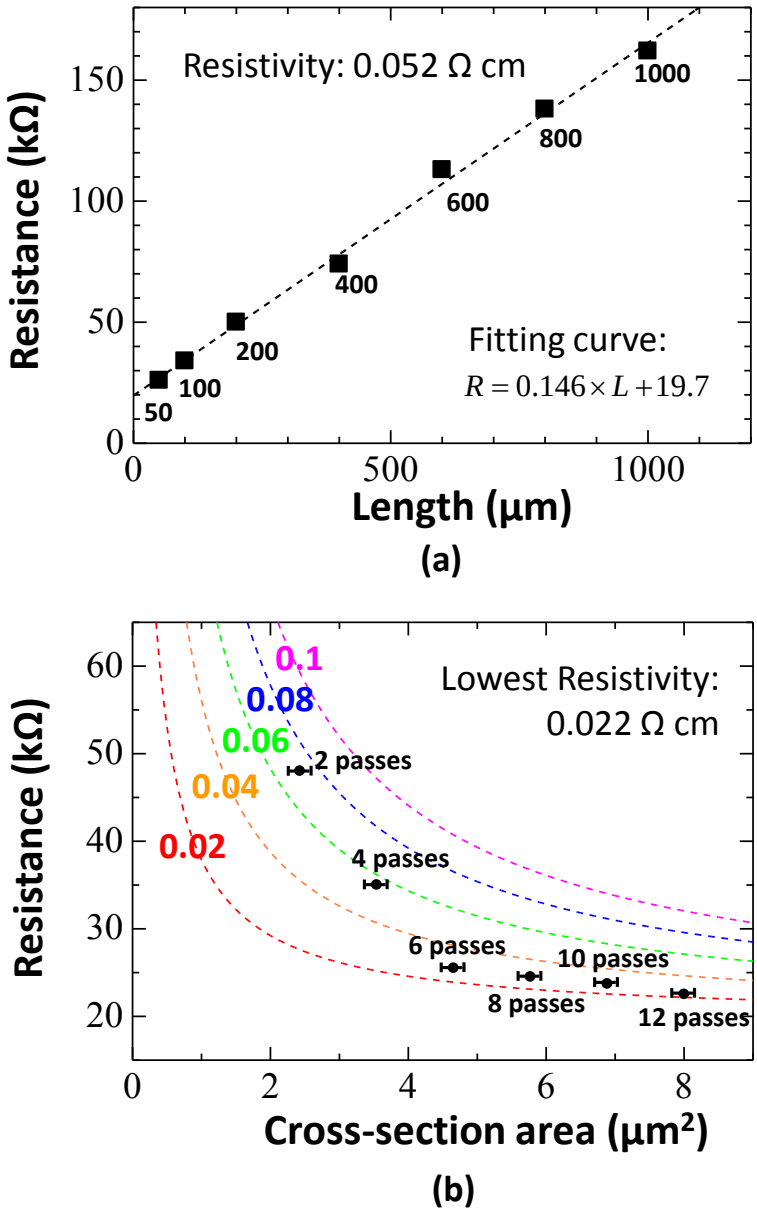

Figure 7.8: The measured resistance of the wires with various physical dimensions. (a) Resistance as a function of wires length. Wires were fabricated with four passes with axial shift of 0.5 μm. (b) Resistance as a function of cross-sectional area of wires. The dashed colored curves show the theoretical prediction for wires of different resistivities (in unit of Ω cm).

sistivity value becomes relatively stable (from 6 to 12 passes). This minimum resistivity we obtained here (0.022 Ω cm, corresponding to a conductivity of 4545 S/m) was reduced by a factor of 40 to 180 times compared to previously reported resistivities of fs/ps induced wires: 1.6 Ω cm (Shimizu *et al.* [62]), 3.9 Ω cm (Kononenko *et al.* [198]) and 0.9 Ω cm (Lagomarsino *et al.* [61, 181]). We therefore conclude this was the lowest resistivity ever achieved for a laser

written graphitic wire inside diamond.

7.5 Fabrication power

We note that the incident laser power used for the fabrication affect both the cross-section size and resistivity of the wire. A lower power always introduces smaller cross-section size. This should be expected, as a lower power reduces the dimension of the focal area whose intensity is above the diamond graphitization threshold, thus leading to a smaller graphitized area. Therefore, controlling the input laser power is an alternative method to introduce different cross-section sizes for the wire.

It should be taken into consideration that the laser power also affects the wire resistivity. According to our investigation, there should be an optimal power that can bring the lowest resistivity. Any power above or below this optimal value results in a larger resistivity. This could be explained that with a low power, the graphitization is less significant, so that more part of the diamond within the wire is not completely turned into graphite; while with high power, the proportion of less graphitized area at the bottom of the wire increases, leading to higher resistivity for the whole wire. The optimal fabrication power is related to the laser system, objective lens and diamond sample, and could be found by trying a series of different power experimentally. In our system, the laser power of 20 μW (pulse energy 20 nJ) is a good choice to reach the lowest resistivity.

We should note that the intensity threshold of diamond graphitization is low, thus the power used for the laser diamond processing is of a small value. Additionally, the generated graphite has a strong absorption to the near infrared laser light. Therefore, the self-focusing effect is negligible in the research for laser processing of diamond.

7.6 The effect of anneal process

The resistivities reported in this paper lie between the value for amorphous carbon (ρ= 8×10^{-2} Ω cm) and for polycrystalline graphite (ρ= 3.5×10^{-3} Ω cm) [207]. In recent wire fabrication using heavy ion implantation, the resistivity was found to be 10^2 Ω cm immediately following

the ion implantation [191, 208]. Nevertheless, a subsequent high temperature anneal process reduced the resistivity of the wires by several orders of magnitude to the level of polycrystalline graphite [190]. However, our preliminary experimental results following an anneal process where the diamond was maintained at 1100 ^oC for one hour in a vacuum of at least 10^{-5} mbar did not show a noticeable reduction in resistivity for the laser induced graphitic wires following an anneal process. This may be related to the different underlying mechanism behind graphitization in ion beam implantation and laser fabrication, but is subject to further investigation. One possible explanation may be the difference in the heat of the graphitization for these two mechanism. The ultrafast laser produces high peak intensity at the focus, thus generates much higher heat than the ion beam implantation. This possibly means that the graphitic area has already been annealed in the laser focusing process.

7.7 Ultra-thin wires at deep depth

In this section, we explore the limits of this adaptive fabrication method. The wires with ultra-thin cross-section size and at deep depth are demonstrated.

The diamond is transformed into graphitic material when the local electric field magnitude at the laser focus is above a threshold value. Therefore, the size of the fabricated wire can be reduced by taking advantage of this threshold effect with fine control over the laser power [34, 209]. An ultra-thin wire with a width 400 nm was fabricated with a power of 6 μW (pulse energy 6 nJ), making it the smallest reported laser-induced graphitic wire inside diamond. An image of such a wire is shown in Figure 7.9 (a). We note the size was approaching the resolution limit of the transmission microscope used for inspection, and thus 400 nm places an upper limit on the actual size. Furthermore, the resistivity of this ultra-thin wire was measured as $<$0.4 Ω cm. This is already an improvement over any other reported wires written with ultra-short lasers $-$ even those of much larger cross-section size, whose reported resistivity varied from 0.9 to 3.9 Ω cm [61, 62, 181, 198].

Even though the induced aberration increases with the fabrication depth in the diamond, the tightly confined focus can still be maintained using appropriate phase compensation by the SLM. The wires fabricated at a depth of 100 μm below the diamond surface (Figure 7.9 (b))

were found to have comparable physical properties to those at shallower depths. The resistivity of the wires fabricated at different depths within the diamond was found to be similar, indicating that the nature of material modification in our system did not depend upon the fabrication depth, in a contrast to previous findings using established laser processing techniques [203].

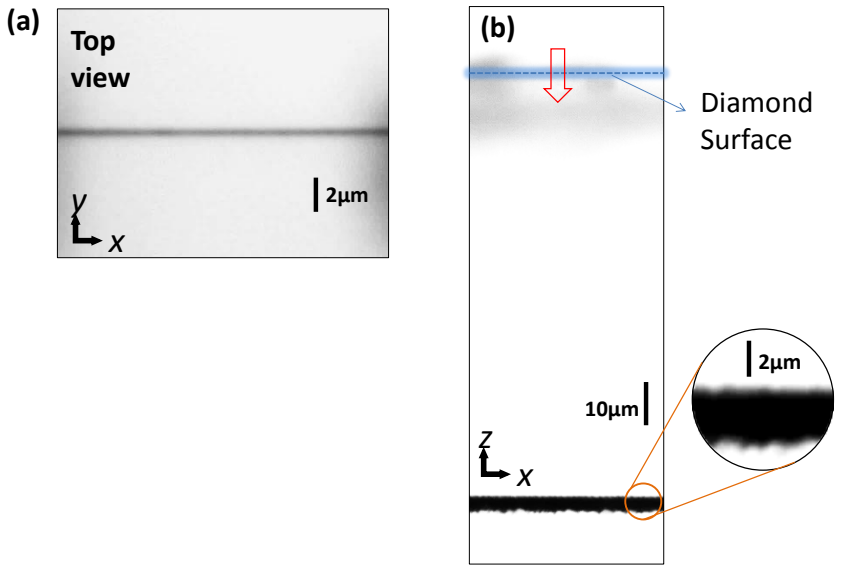

Figure 7.9: (a) An ultra-thin graphitic conductive wire with a width of 0.4 μm. (d) A conductive wire fabricated parallel to the surface with aberration compensation at a depth of 100 μm in diamond. The fabrication laser beam was incident along the negative z direction.

7.8 Wires with complex 2D/3D shapes

A unique advantage of this advanced adaptive laser writing is the ability to fabricate with high precision along any direction, which enables the creation of highly conductive single 3D wires inside diamond with arbitrary shape. To demonstrate this ability, we show two representative shapes: a spiral and a helix.

Figure 7.10 (a) shows a transmission microscope image of the spiral wire, prior to the fabrication of the vertical conductive pillars. The spiral wire was fabricated with four passes of the laser focus and has an inner radius that increases from 10 μm to 24 μm. After fabricating pillars at the central tip of the spiral and at the surrounding straight part, the resistivity was measured to be 0.05 Ω cm ($\pm \sim 5\%$), which is close to that measured for the straight four-pass

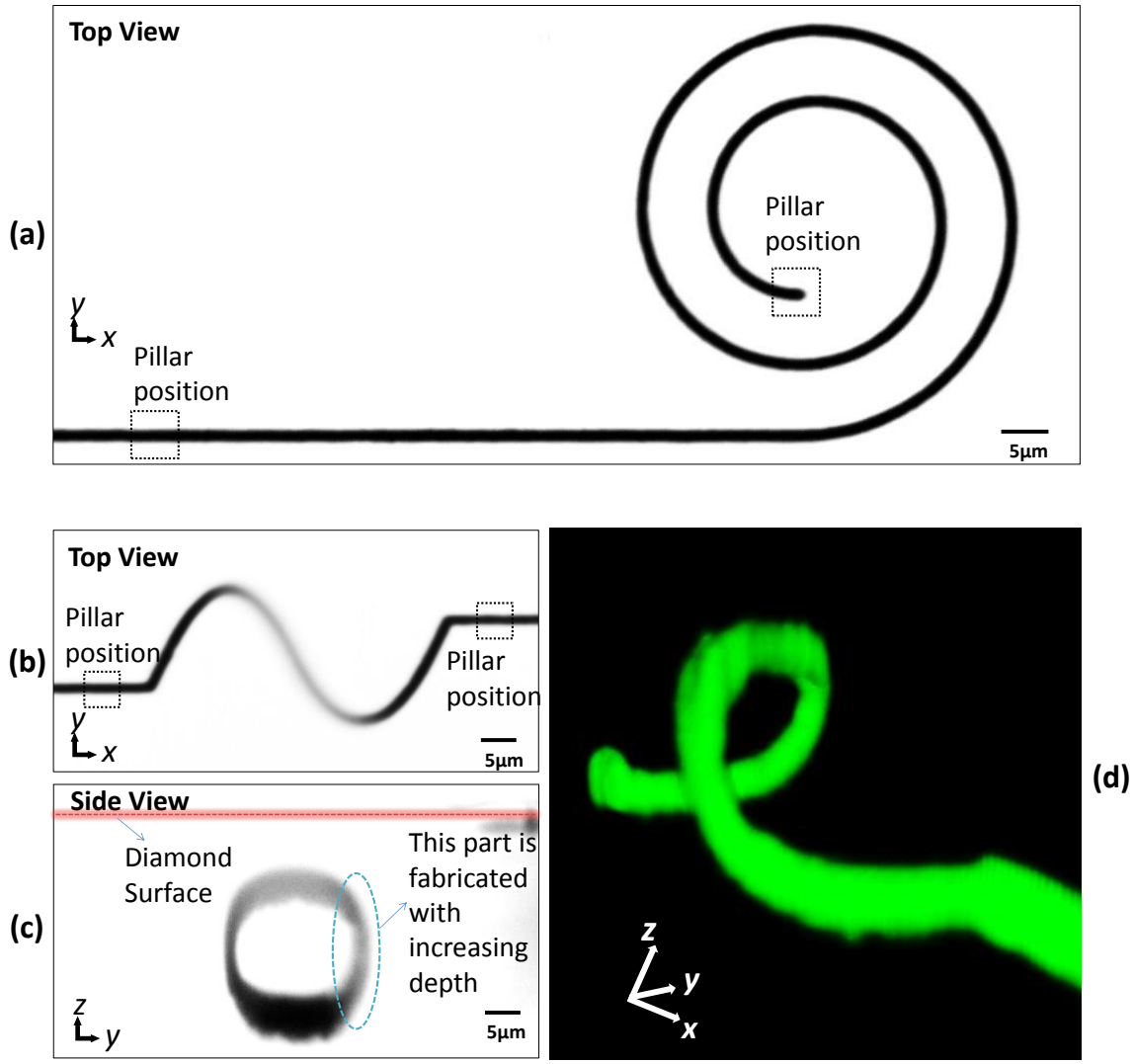

Figure 7.10: Examples of single micro wires with spiral and helical shapes. Both wires were fabricated with four shifted passes of the laser beam along the z direction. The depth of the helical wire ranged from 10 to 30 μm. The positions of subsequent pillar fabrication are marked in the images. (a) Transmission image of the spiral wire. (b) Top and (c) side view of helical wire. (d) 3D SHG (second harmonic generation) microscope image of the helical wire.

wires in Figure 7.10 (0.052 Ω cm). Top view and side view transmission microscope images of a helical wire are shown in Figure 7.10 (b) and (c). The helix dimensions along the x, y and z directions are 40 μm, 20 μm and 20 μm, respectively. Since the amount of spherical aberration changes with fabrication depth, the compensation phase displayed on the SLM was controlled to simultaneously update with the axial depth when fabricating the helical part. The central part of the helix, which appears blurred in the image of Figure 7.10 (b), is closer to the surface than the other parts of the structure. Both the whole spiral and helical wire are

homogeneous and uniform. A SHG (second harmonic generation [210]) microscope image clearly shows the 3D structure in Figure 7.10 (d). It is worth noting that the fabrication also caused stress in the surrounding diamond, due to the lower density of the generated graphitic phase, and the stressed region was also detected by the SHG scanning microscope. Thus, the cross-section in the SHG image appears larger and surface rougher than the transmission image. Further investigations are being undertaken to ascertain the effect of the generated stress field on the surrounding properties of the diamond. The measured resistivity of the helical wire was 0.13 Ω cm ($\pm \sim 5\%$). Compared to the straight wires, one potential cause for the slight rise in resistivity is that part of the wire (marked in Figure 7.10 (c)) was fabricated by translating the focus downward through the diamond, such that previous material modification partially obscured the incident beam from the updated focal position. This problem could be circumvented by adopting a straightforward bottom up fabrication strategy.

7.9 Conclusions

In this Chapter, I have demonstrated that dynamic wavefront control enables critically important new capabilities in laser writing of micron/submicron wires inside diamond. To the best of our knowledge, we have achieved: (i) the first laser induced graphitic wires inside diamond that are not only highly conductive, but also able to follow any 3D paths; (ii) the lowest reported resistivity of 0.022 Ω cm, approaching that of polycrystalline graphite; and (iii) the smallest laser written conductive nano-wire with a width of $<$400 nm, resistivity $<$0.4 Ω cm.

The simple fabrication process, considerably extending the operating depth, flexibility in generating arbitrary 3D shapes and the low resistivity of the graphitic wires make this advanced laser writing method highly promising for the preparation of more complex, high quality, conductive structures in diamond. This could benefit the wide range of emergent applications that combine diamond's properties with electrical measurement and control, from quantum enhanced technologies [211, 212], semiconductor research [213], to sensor based devices either for the detection of ionizing radiation [61, 181] or for use in harsh environments [214]. The ability to precisely graphitize the diamond also offers potential for the creation of 3D diamond micro-structures through a subsequent etching process [187].

Chapter 8

Non-reciprocal effects in diamond fabrication

8.1 Introduction

In Chapter 7, it has been demonstrated that the laser fabrication with adaptive correction of aberrations significantly improves the process of diamond graphitization. The quality of graphitization was demonstrated by the resistivity and physical dimensions of the wires. In this chapter, interesting phenomenons of non-reciprocal effect during the diamond graphitization are discussed. The laser processed area presents different graphitized features when the fabrication direction is reversed. These phenomenons have never been reported else where. The non-reciprocal effects are significantly determined by the laser power, the fabrication speed, the light polarization and pulse front tilt. The detailed influences of these factors are studied.

8.2 Non-reciprocal effects in laser material processing

During the investigations on straight graphitic wire fabrication, we noticed an interesting phenomenon correlated with the graphitization process. The appearance of the wires presented in the microscope looked different when we fabricated the wires with laser translated along different directions relative to the sample. This interesting phenomenon could be caused by

either properties of the laser beam, or the diamond crystal itself. There have been various reports on directional effects in laser processing of other materials. These effects are usually caused by two possible reasons: one is the pulse front tilt (PFT, details in Section 3.2.2, Chapter 3) of the laser beam, another is due to properties of the transparent material, such as its crystallography.

There have been extensive reports on the effects of pulse front tilt in laser fabrication, among them, most effects were investigated in fused silica. In chapter 5, we introduced a technique to control the pulse front of the laser light, where especially a quadratic shaped pulse front was created by the combination of SLM and DM. This technique is also able to create PFT for laser pulses.

It has been demonstrated that the pulse front tilt has non-reciprocal effects in the fabrication of non-crystal transparent material, such as fused silica. Figure 8.1 (a) presents the non-reciprocal fabrication effect [125]. The quality of laser material processing is significantly dependent on the fabrication direction. This phenomenon was first introduced by Kazansky etc. that the ultrafast laser beam could be used for calligraphic inscription similar to writing with a quill pen [160]. The more detailed mechanism, especially anisotropic bubble formation was later introduced [215]. There are also reports on the influence of the PFT which was generated by temporal focusing, on the fabrication with low NA objective lenses [111, 112]. The magnitude of the PFT was tunable in the temporal focusing, and the non-reciprocal effect was found in a large range of focusing depths. It was reported that the magnitude of PFT could be controlled by the grating phase patterns displayed in SLM, and the non-reciprocal effects could also be introduced by a non-symmetric intensity distribution in the pupil of the objective lens [125].

While the non-reciprocal fabrication effects of PFT were mostly found in the fabrication of non-crystalline materials, there were also reports of the directional phenomenon in the crystal fabrication. One famous paper reports this effect in the fabrication of $LiNbO_3$ crystal [216]. It has been demonstrated that when the direction of the femtosecond laser beam was reversed from the $+z$ to $-z$ direction, the structures written in a $LiNbO_3$ crystal when translating the beam along the $+y$ and $-y$ directions were mirrored. This phenomenon only happens

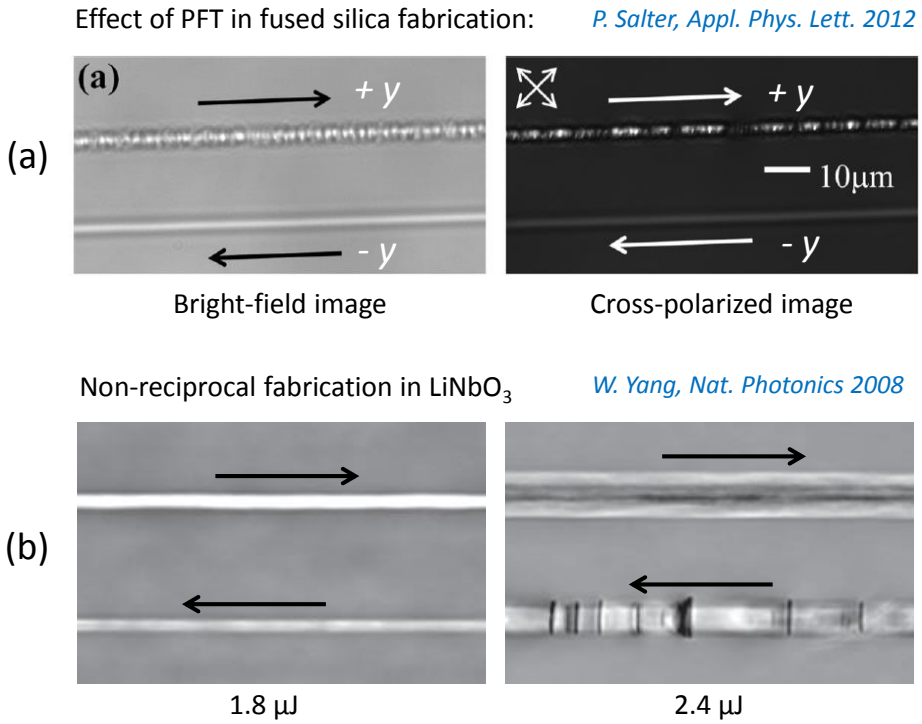

Figure 8.1: Previous reports of non-reciprocal fabrication effects. (a) Effects of pulse front tilt in the fabrication of fused silica [125]. Bright-filed image (left) and cross-polarized image (right) are shown. (b) Non reciprocal effects in the fabrication of $LiNbO_3$ crystal [216]. Fabrications with different pulse energy are shown. The arrows in the figures represent the fabrication directions.

when the pulse energy is above a certain threshold, and different pulse energy presents a different non-reciprocal phenomenon (shown in Figure 8.1 (b)). Different from the directional effect in the fabrication of non-crystal material of fused silica, the non-reciprocal effects in the fabrication of $LiNbO_3$ crystal are related to neither the pulse front tilt, nor the birefringence. The phenomenon was interpreted in terms of light strain at the front of an ultrashort pulse, photon drag effect and the associated light-induced thermal current in crystalline media [216].

Until now, there has been no investigation on the directional effects in the graphitization of diamond crystal. In this section, the non-reciprocal effects for fabrication in diamond along crystal directions of <100> and <110> are presented. The influence of the diamond crystallography, laser power, fabrication speed, light polarization and pulse front tilt are discussed in detail.

8.3 Diamond crystallography

One of the simplest shapes of crystal structure is the cubic crystal system. It has three major varieties of the crystal structures, which are primitive cubic, body-centered cubic (BCC) and face-centered cubic (FCC) [217]. Diamond crystal follows the face-centered cubic system which is constructed by two tetrahedrally bonded atoms in each primitive cell. A model of the diamond crystal is shown in Figure 8.2 (a). Each carbon atom connects to other four individual atoms in four planes.

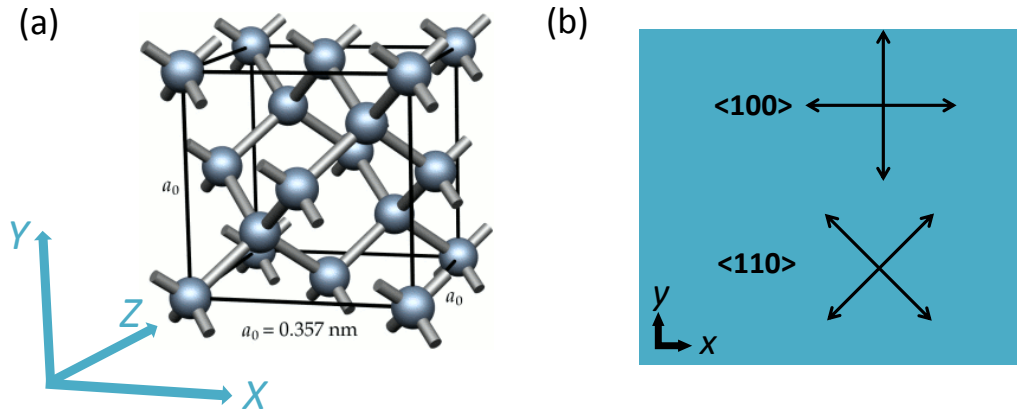

Figure 8.2: (a)A model showing the diamond crystal. (b)The direction families of <100> and <110> parallel to the top surface of a diamond sample. <100> represents either the direction along x axis or the direction along y axis. <110> represents either the direction of 45° relative to $+x$ axis, or the direction of 135° relative to $+x$ axis.

The coordinates in crystallography is represented by a specific notation system. Coordinates in square brackets such as [100] denote a direction vector. For an example, [100] could represent a direction along x axis, and [010] represents a direction along y axis. Coordinates in angle brackets such as <100> denote a family of directions which are related by symmetry operations. In the cubic crystal system for example, <100> would mean [100], [010], [001] or the negative of any of those directions. Indices in parentheses such as (100) denote a plane of the crystal structure. Indices in braces such as $\{100\}$ denote a family of planes.

In our investigations of the directional fabrication in diamond, the directions of <100> and <110> are studied, as these two direction families are mostly common seen in diamond fabrication. Figure 8.2 (b) shows these two direction families which are parallel to the top surface of a diamond sample. <100> represents either the direction along x axis or the direction

along y axis. $<110>$ represents either the direction of 45° relative to $+x$ axis, or the direction of 135° relative to $+x$ axis.

8.4 Fabrication along $<100>$

In this section, we introduce the specific non-reciprocal phenomenon which is only seen when the laser focus is translated along $<100>$ directions (namely either x or y directions). We call this phenomenon as "feathering effect". In all the fabrication described below, SLM was used to compensate the refractive index mismatch aberration. The system set-up is the same as the graphitic wire fabrication shown in Figure 7.1 of Chapter 7.

8.4.1 Feathering effect

In most laser processing of transparent materials, without the vibration of the sample stage, the processed region should be uniform at the edge of the written feature. We present here that, in specific conditions, the graphitization in diamond could lead to a non-uniform surface edge.

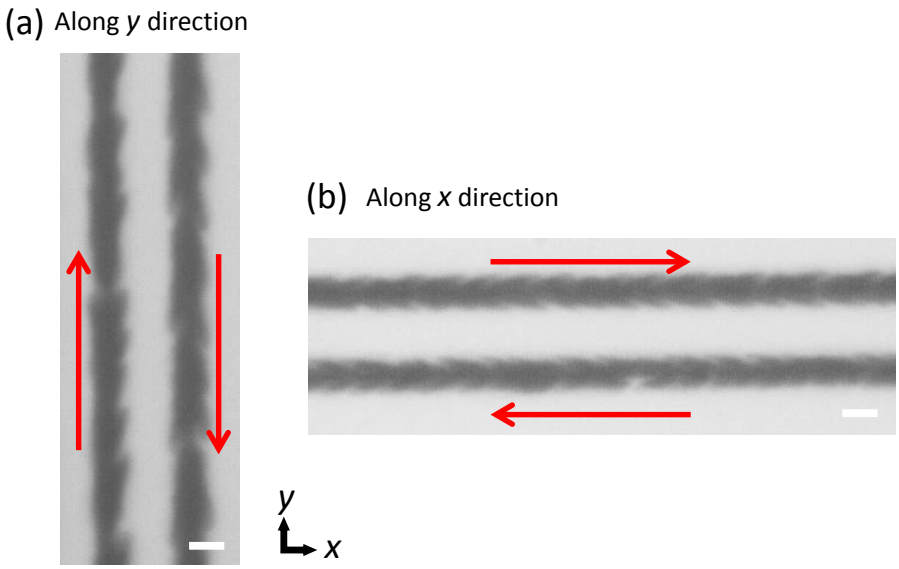

Figure 8.3: The feathering effect along the edge of the graphitic wires in diamond. The fabrication is along $<100>$ direction. Red arrows represent the fabrication directions. (a)Fabrication along y direction. (b) Fabrication along x direction. Images were captured from a conventional optical microscope. Scale bar is 2 μm.

Examples are shown in Figure 8.3, where the fabrication in diamond was conducted at a depth of 20 μm. The laser power is 40 μW (pulse energy 40 nJ), while fabrication speed is 250μm/s. The distance between each pulse is calculated as: $v/rate$, where v is the translating speed, $rate$ is the repetition rate of the ultrafast laser. In this situation, the laser source had a repetition rate of 1 kHz, leading to a pulse distance of 0.25 μm/pulse. It is seen that there are feathering effects generated along the graphitic wires. The direction of the feather is about 15° relative to x or y direction. Interestingly, when the fabrication direction (marked as the red arrows) was reversed, the direction of the feather changed correspondingly. This interesting phenomenon could be seen in the fabrication along either the y (Figure 8.3 (a)) or x (Figure 8.3 (b)) direction.

8.4.2 Laser power

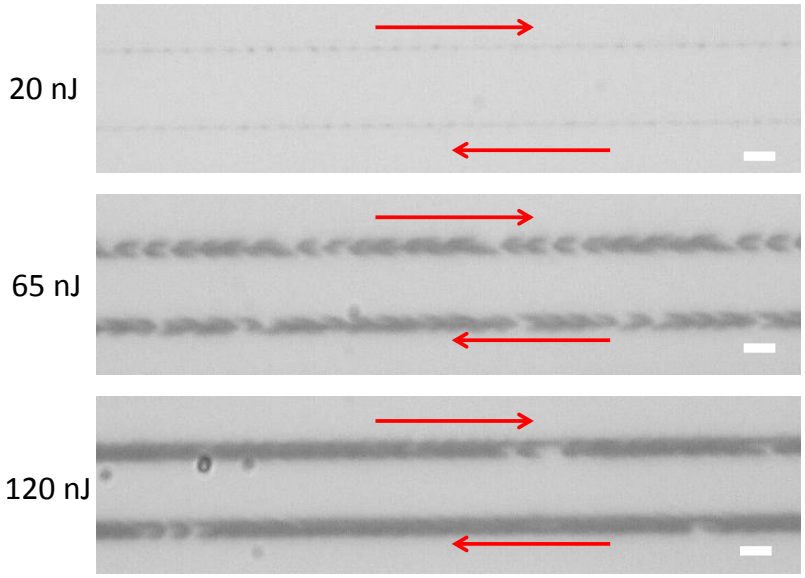

Figure 8.4: The influence of laser power on the feathering effect. Ultrafast laser with pulse energy of 20 nJ, 65 nJ and 120 nJ were investigated. The fabrication speed was 0.6 μm/pulse. Red arrows present the fabrication directions. Images were captured from a conventional optical microscope. Scale bar is 2 μm.

To begin with, we had a proposal that the feathering effect may be a result of the effect of heat flow. Therefore, it could be reasonable that the properties of laser light have an influence on this phenomenon. Figure 8.4 presents the fabrication with different laser power. The

fabrication speed was 600 μm/s (0.6 μm/pulse), with a depth of 20 μm. A fast fabrication speed was chosen, as it was able to spatially separate each laser pulse. In this way, it is able to show the formation of the feathering effect. It is seen that when the laser pulse has a small energy of 20 nJ, the graphitization was very slight. Each laser pulse only generated a small graphitic point. These small points are discrete, and the feathering effect could not be seen. When the laser power was raised to 65 nJ, each discrete graphitic point became larger, and the feathering effect became obvious. When we continue to raise the laser power to 120 nJ, the graphitic points began to connect with each other, and a wire was gradually formed. However, the feathering effect is not very obvious in this case. We believe the feathering effect is still there, but covered by the graphitic connections between each points.

8.4.3 Fabrication speed

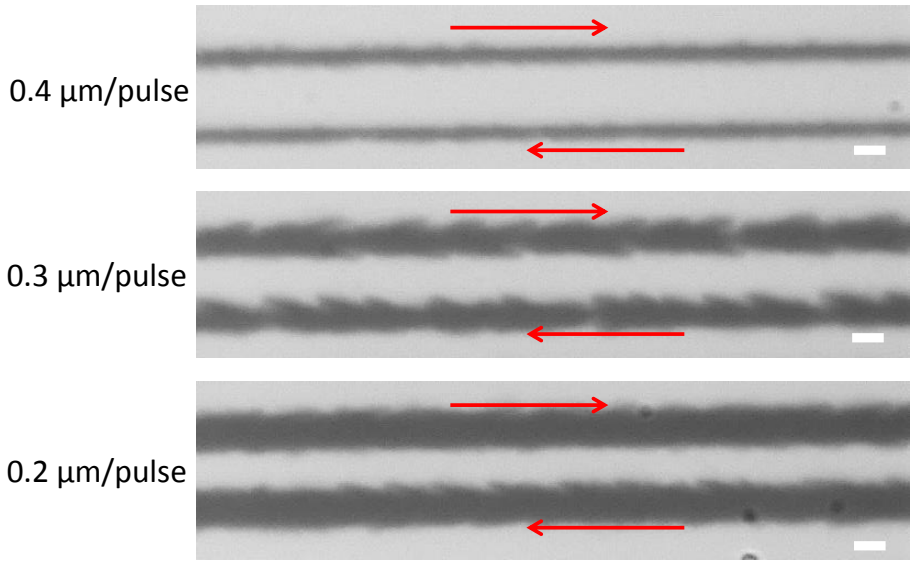

Figure 8.5: The influence of fabrication speed on the feathering effect. Ultrafast laser focus with fabrication speeds of 0.4 μm/pulse, 0.3 μm/pulse and 0.2 μm/pulse were investigated. The pulse energy was 65 nJ. Red arrows present the fabrication directions. Images were captured from a conventional optical microscope. Scale bar is 2 μm.

The effect of fabrication speed on feathering effect was investigated and presented in Figure 8.5. The laser power was chose to be 65 nJ, which was the power bringing the most obvious feathering effect in Figure 8.4. As shown in Figure 8.5, when the fabrication was with a large

speed (0.4 μm/pulse), the wire was pretty uniform at the edge. When we reduced the speed to 0.3 μm/pulse, the feathering effect became obvious. After the fabrication speed was further reduced to be 0.2 μm/pulse, the wire became fatter (with larger width), the feathering effect was covered by a strong graphitization even at the edge, and became less obvious.

Through these investigations, we can conclude that the feathering effect is only obvious when the laser pulse energy is above a certain threshold, while the fabrication speed is below a certain value. If any of these two conditions were not satisfied, the feathering effect will be too slight to be seen in a conventional optical microscope. On the other hand, either when the laser power is further raised, or the fabrication speed is further reduced, the feathering effect became less obvious because of a strong graphitization along the edge of the wire.

8.4.4 Light polarization

The polarization state of the ultrafast laser was found to have an influence on the non-reciprocal effect in the silica glass fabrication [160]. It is therefore also investigated to see if it has an influence on the diamond fabrication along $<100>$. The SLM, which was used as the adaptive optics element to correct the RIM aberrations, is polarization dependent. As the input laser light before and after SLM has to be of a linear polarization state, the discussions in the above sections are in fact for linear polarized laser light. To study whether the angle of linear polarization affects the feathering effect, we aligned a half wave-plate after the SLM, before the objective lens, to control the linear polarization angle. Fabrications with a series of laser powers and fabrication speed were conducted. As a result, we did not notice any difference in the feathering effect when the angle of the linear polarization was changed.

We further investigate whether the circular polarization could affect the feathering effect. A quarter wave-plate was aligned before the objective lens instead of the half wave-plate to change the linear polarization state to circular polarization state. Figure 8.6 presents the wires fabricated with different power, while the laser light was of a circular polarization. It is seen that the feathering effect exist when the laser power was 65 nJ or 150 nJ. Compared to linear polarized light, there is no obvious difference in the feathering effect when the laser light was changed to circular polarization. We therefore conclude that the polarization state of the laser

light has no effect on the feathering effect in the fabrication along <100>.

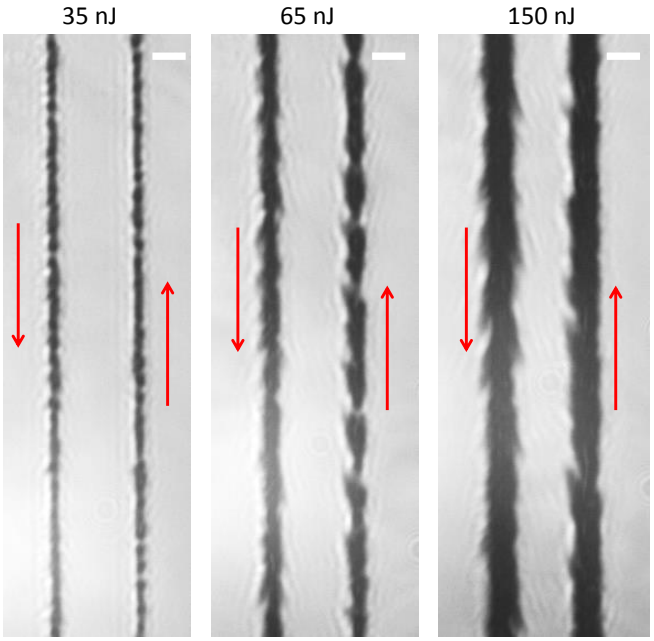

Figure 8.6: The influence of circular polarization state on the feathering effect generated in the laser fabrication along <100>. Ultrafast laser with pulse energy of 35 nJ, 65 nJ and 150 nJ were investigated. The fabrication speed was 0.25 μm/pulse. Red arrows present the fabrication directions. Images were captured from a conventional optical microscope. Scale bar is 2 μm.

While there has not been a reliable explanation for the generation of the feathering effect, one possible reason as discussed above could be the difference in the thermal conductivity of graphite and diamond. Diamond is an extremely efficient thermal conductor, and has higher thermal conductivity than graphite. Correspondingly, the graphitized feathering effect is easier to be formed close to the diamond side. This could be one reason that the feathering effect always point to the fabrication direction. If this hypothesis is correct, it could also be the explanation to the fact that the feathering effect is only generated when the laser pulse energy is higher, while the fabrication speed is lower than certain values. It can also explain why the polarization state has no effect, as polarization status of the laser light does not affect the heat flow in the fabrication. However, we believe the feathering effect is a complex process, and the explanation should take other factors into consideration, such as the strain distribution along the graphitized region, crystal structure and material absorption etc.

8.5 Fabrication along <110>

In this section, we introduce another specific non-reciprocal effect when the fabrication is conducted along <110> directions (45 degree relative to x or y axis). This effect is different from the feathering effect when the fabrication is along <100>, but it is also related to the laser power, fabrication speed and light polarization.

8.5.1 Linear polarization

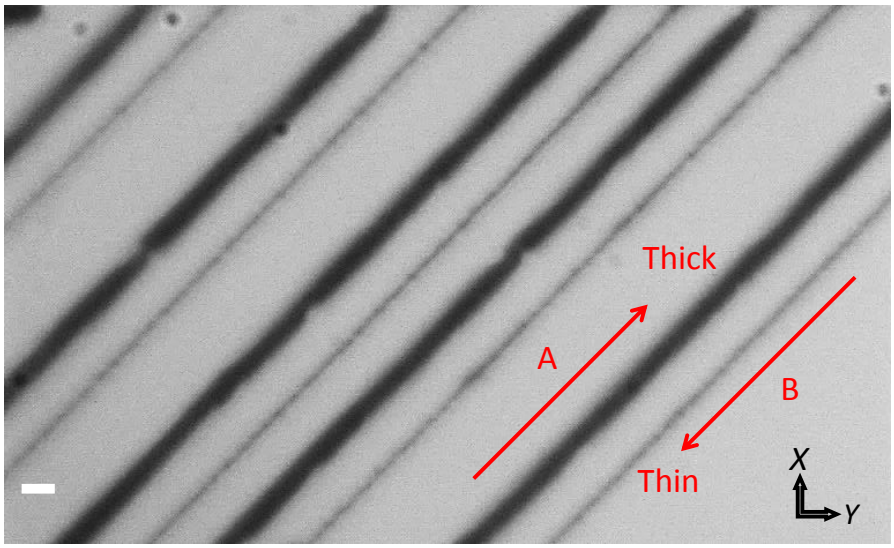

Figure 8.7: The wires fabricated with linear polarized laser light along <110> direction. All the wires were fabricated with same power (pulse energy 65 nJ), and same speed (0.28 μm/pulse). Red arrows show the fabrication directions. Images were captured from a conventional optical microscope. Scale bar is 2 μm.

We first investigate the fabrication with linear polarized laser light. All the fabrication was conducted with laser power of 65 μW (pulse energy 65 nJ), while the fabrication speed was 0.28 μm/pulse. The focal shape was confirmed to be fairly symmetric in the lateral plane. The image of the fabrication results are shown in Figure 8.7. Interestingly, the wires fabricated along the direction from bottom-left to top-right (direction A) appear to be much thicker than the wires fabricated in the reversed direction (direction B), while all the wires were fabricated with the same speed and power. Apparently, the diamond area fabricated along direction A were much more graphitized than the area fabricated along direction B, even though both the

fabrications were with exactly the same process and parameters. In addition, it is seen that all the graphitic wires are with uniform edge surfaces. Different from the fabrication along <100>, no feathering effect exists in the fabrication along <110>. This non-reciprocal phenomenon was also found in the other <110> directions (90 degree relative to the direction shown in Figure 8.7). During the experiments, several linear polarization with different directions was investigated. As a result, this non-reciprocal fabrication effect existed for all kinds of linear polarization directions.

Pulse Energy (nJ)	35	50	65	80	100	125
Speed (μm/pulse)	0.25	0.27	0.28	0.33	0.35	0.36

Table 8.1: The specific combinations of laser power and fabrication speed that can present most significant non-reciprocal graphitization when the fabrication is along <110> directions.

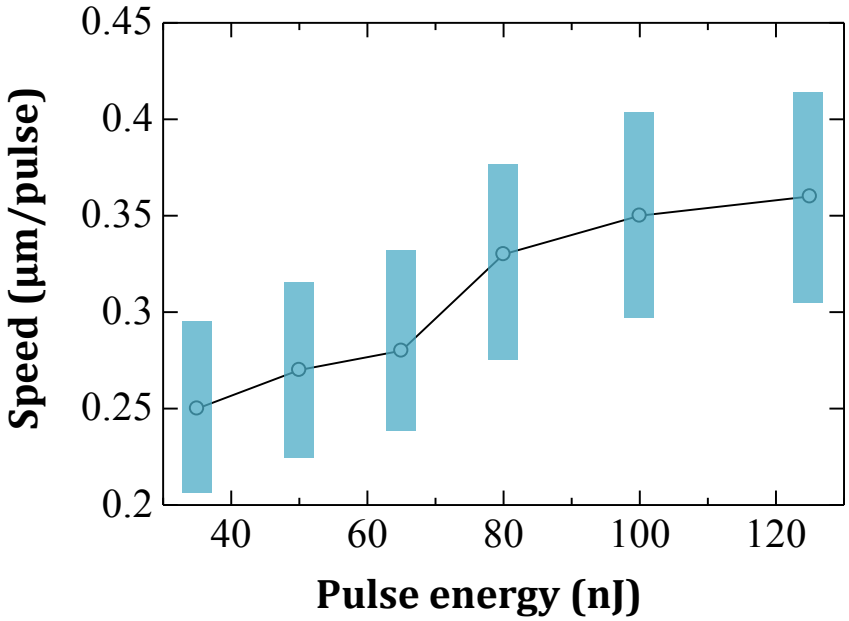

Figure 8.8: The specific combinations of laser power and fabrication speed that can create non-reciprocal graphitization when the fabrication is along <110> directions. The dots present the values shown in Table 8.1, with which the non-reciprocal effects are most obvious. The non-reciprocal effects exist if the fabrication speed is in the blue regions of the figure.

It is notable that this significant difference in the level of graphitization could only be seen for the fabrication with specific combination of laser power and translation speed. Either smaller or larger power, faster or slower speed leads to no significant difference for the fabrication along two reversed directions. The specific combinations of the laser power and fabrication speed were tested by experiments, and are shown in Table 8.1. The presented values in the table create the most obvious non-reciprocal effect, though the effect can still be seen if the fabrication speeds are within about $\pm 15\%$ range relative to the presented values. This can be clearly seen in the presentation of Figure 8.8, whereas the effective speed that can generate the non-reciprocal effect is represented as the blue regions.

8.5.2 Circular polarization

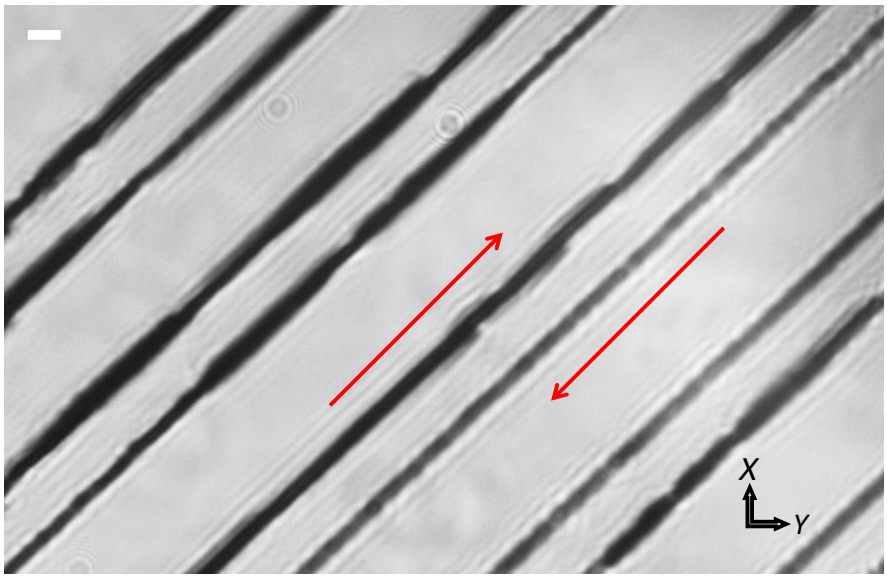

Figure 8.9: The wires fabricated with circular polarized laser light along <110> direction. All the wires were fabricated with same power (pulse energy 65 nJ), and same speed (0.28 μm/pulse). Red arrows show the fabrication directions. Images were captured from a conventional optical microscope. Scale bar is 2 μm.

We moved on to investigate the fabrication along <110> when the laser light is with a circular polarization state. A quarter waveplate was inserted into the optical system before the objective lens to change the linear polarization into circular polarization. Various combinations of laser power and fabrication speed were tested, especially for the parameters given

in Table 8.1. However, we did not see any non-reciprocal phenomenon no matter what laser power and fabrication speed were used. One example is shown in Figure 8.9. The fabrication was conducted with laser power of 65 μW (pulse energy 65 nJ), while the fabrication speed was 0.28 μm/pulse. These fabrication parameters are the same as the case in Figure 8.7. It is seen that there is no obvious difference in the graphitized wires when the fabrication direction was reversed. Similarly, there is also no feathering effect along the wires.

Similarly, there has not been a reliable explanation for this non-reciprocal effect. With these results, the non-reciprocal effect in the fabrication along <110> may be a complex phenomenon caused by the heat flow, crystal structure and specific light polarization.

8.6 Polarization microscope images

In the above descriptions, it has been demonstrated that the feathering effect generated in the fabrication along <100>, while the non-reciprocal phenomenon is seen in the fabrication along <110>. Different from diamond, graphite is not transparent to visible light, thus a visible light optical microscope is enough to characterize the graphitization status of the fabricated area. To see if there could be any change in the non-graphitized area beside the wires, we used the polarization microscope to image the strain in the diamond along the wires.

The images of the wires fabricated along <100> and <110> are shown in Figure 8.10. The changes in the image brightness represent the depolarization variation of the illumination light. This is usually caused by strain variation around the graphitized region. A variation of the strain causes birefringence (refractive index change) of the diamond, which leads to the depolarization of illumination light for the microscope. There are three possible reasons that can introduce strain variation around the graphitization area. Firstly, because the graphite has lower density than the diamond, expansion in the volume of graphite introduces strain to the surrounding diamond. In this case, larger size of graphitized region usually brings more strain than smaller size graphitized region. This is seen in Figure 8.10 (b) that the bright area is more likely to be seen around the thicker wires than the thinner wires. Secondly, in some places, graphite causes cracking to the surrounding diamond, which is usually around the thicker wires. When cracking occurs, strong stress variation generates around the cracking area. In

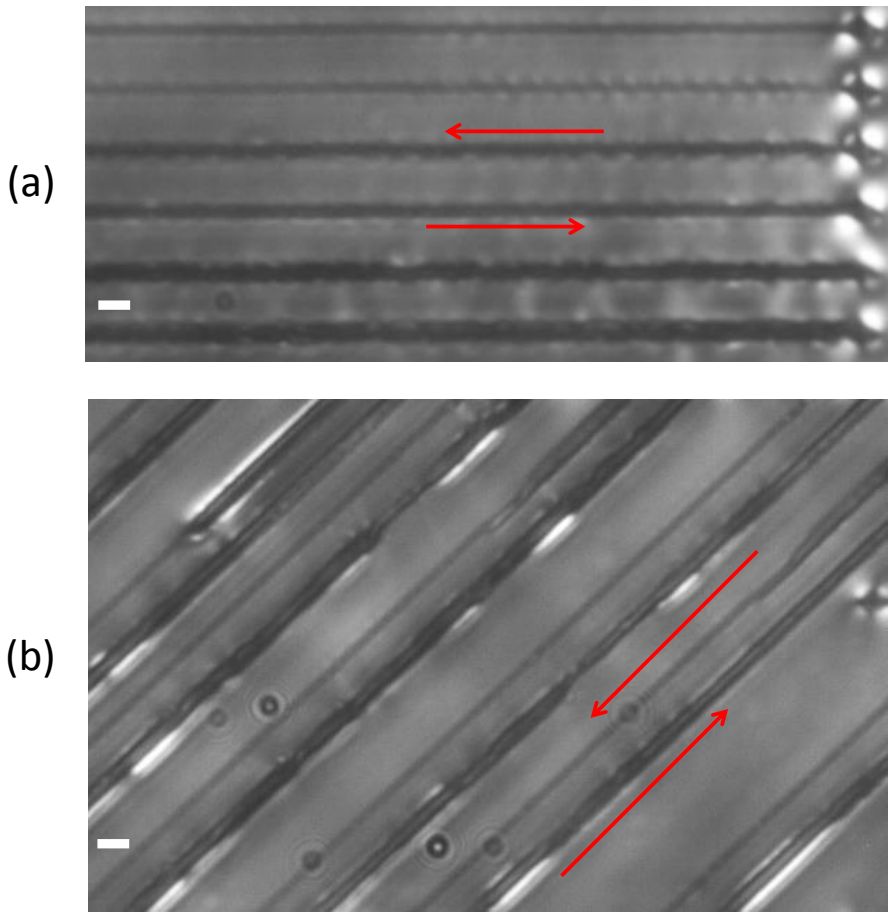

Figure 8.10: The polarization microscope images for the wires fabricated along <100> and <110>. The changes in the image brightness represent the vibration of the strain in the diamond. (a) Fabrication along <100>. The wires were fabricated with a same speed of 0.25 μm/pulse, but different pulse energy. (b) Fabrication along <110>. The wires were fabricated with pulse energy of 65 nJ, and speed of 0.28 μm/pulse. Red arrows show the fabrication directions. Scale bar is 2 μm.

Figure 8.10 (b), we can see that only part of the region around the thicker wires appears bright (caused by cracking), while other parts are pretty dark. Thirdly, the strain (and refractive index) of the diamond could be possibly changed under the low power ultrafast laser focusing without the graphitization process. We call this "weak fabrication", which could occur in the diamond region around the graphitic area. Even though the diamond is not turned into graphite, a variation of refractive index could still be introduced.

As the result observed in Figure 8.10, for the fabrication along <100>, it is seen that there are bright points along the wires, which marks the effects of the feathering effect. The end of the wires at the right side was surrounded by very bright regions, as the laser focus stayed at

the wire end for longer time, leading larger area of graphite. For the fabrication along <110>, it seems the bright region is only seen along the thicker wires. No significant strain vibration is seen along the thinner wires.

8.7 Pulse front tilt

Pulse front tilt is generally considered as an important factor causing the non-reciprocal effect in the ultrafast laser fabrication [111, 112, 160, 215]. In our experiments, it is easy to make the SLM operate as a variable grating, thus control the magnitude and direction of the pulse front tilt [125]. The pulse front tilt along <100> and <110> directions were therefore created with various magnitudes (from 0 fs to $\pm$100 fs) by SLM. The comparisons were conducted for the case without any applied PFT and the case with PFT of different magnitude and direction. However, no difference was found for the wires fabricated with and without pulse front tilt. These verifications were conducted for different laser power, fabrication speed, light polarization and fabrication directions. We therefore conclude that the pulse front tilt does not have an influence on the non-reciprocal effects in the diamond crystal fabrication. This conclusion in fact matches with the results reported in the $LiNbO_3$ crystal fabrication [216], which indicates the non-reciprocal effects in the crystal fabrication is only related to the heat flow and crystal direction.

8.8 Conclusions

As a summary, the non-reciprocal fabrication phenomenon was extensively explored in different cases. Particularly, the fabrication along <100> direction creates the feathering effect beside the wires. The fabrication along <100> presents significantly different level of graphitization when fabrication direction is reversed for linear polarized light. The influences from the laser power, fabrication speed and pulse front tilt were discussed in detail.

Several conclusions are listed as follows: 1) Feathering effect generate when the fabrication is conducted along <100> directions. The light polarization does not affect the feathering effect. 2) Significant non-reciprocal effect is seen when the laser light with linear polarization

is used for the fabrication along <110>. Specific combinations of the laser power and fabrication speed are required. This effect could not be seen in the fabrication with circular polarized light. 3) Pulse front tilt does not have any effect in the non-reciprocal effect in diamond crystal fabrication.

With those experimental evidences, it is possible that these effects are the interaction results of heat flow, light polarization and crystal structure. However, more demonstrations need to be conducted to further understand its internal mechanism.

Chapter 9

Exploring advanced applications of adaptive laser fabrication in diamond

9.1 Introduction

In past chapters, it has been shown that adaptive laser fabrication in diamond can create high quality graphitic wires with significantly reduced resistivity. The non-reciprocal effects during the diamond fabrication have also been investigated. This chapter explores several more interesting applications for the adaptive diamond fabrication technique, and concentrates on demonstrating the potential and possibility of these advanced applications. Three applications are discussed: 1) high frequency AC conductor, 2) micro-capacitors and 3) electrode arrays for radiation detectors. To begin with, the impedance measurements for the high frequency alternating current conducting through straight graphitic wire are discussed. The measurement results are compared with theoretical simulations. In the second part, a micro-capacitor with high resolution was designed and fabricated. In the third part, the graphitic electrodes were fabricated perpendicular to the diamond surface. Four arrays of electrodes were processed in a diamond sample for the application as a radiation detector.

9.2 High frequency AC conductor

9.2.1 DC and AC

It has been demonstrated in the previous Chapter that the resistivity of the graphitic wires was reduced by tens of times by using adaptive optics fabrication. Those measurements of the resistance were conducted with direct current (DC). Particular application for the DC property of the graphitic wires usually relates to the resistivity. For example, the radiation detector for high-energy physics [60,61,178–181] requires a low resistivity to achieve high efficiency. Beside those conventional applications only using DC, there are applications that need to conduct alternating current (AC). In AC electronics, the direction of the charge flow periodically reverse in a high frequency. One particular application is to use the high frequency micro-wave to control the spin-state of the nitrogen-vacancy (N-V) center inside diamond. The nitrogen-vacancy center is a point defect in the diamond lattice, which consists of a nearest-neighbor pair of a nitrogen atom and a lattice vacancy. Electron spins at N-V centers can be manipulated at room temperature by applying a high frequency micro-wave through a AC circuit [218,219]. As the spin-state of the N-V center forms an important part of quantum technology, techniques for their control have become a very crucial research in nowadays. The conventional method is to deposit electrical circuits on the surface of the diamond sample, thus the micro-waves could be conducted into the sample by applying an alternating current to the circuit. As the circuit deposition can not penetrate inside the diamond, this method has a significant limitation in the accurate positioning of the micro-wave to the specific area of diamond. The fabrication by adaptive optics has enabled high quality graphitic wires with ultra-thin size, low resistivity and arbitrary shapes [220]. Therefore, it is possible to fabricate electric circuits to conduct the high frequency AC charge inside the diamond for more accurate control of the N-V center.

There are reports on the high frequency AC property of the graphite sample [221,222], but there has not been investigation into the AC property of the laser processed wires or electric circuits inside diamond. All the current studies for the laser processed graphite in diamond were conducted with DC. In this section, I discuss the AC measurements of impedance, resistance and reactance for the single straight wires. The fabrication and characterization of

micro-capacitors are also presented.

9.2.2 Equivalent circuit for AC measurement with micro-probes

We firstly characterize the high frequency AC property for the straight wires. A wire was fabricated with 20 nJ pulse energy, 10 μm/s by a 1.4 NA oil objective lens. The depth is 20 μm, and the adaptive correction for the refractive index mismatch aberration was performed with the SLM. The wire has a length of 400 μm, and was fabricated with four passes by an axial shift of 0.5 μm each pass. The cross-section size is 1.4 $\times$ 3.2 μm. A micro-positioner rig with probe tips (diameter 10 μm) was used to make electrical contact with the embedded graphitic wires. The measurement sketch is shown in Figure 9.1 (a).

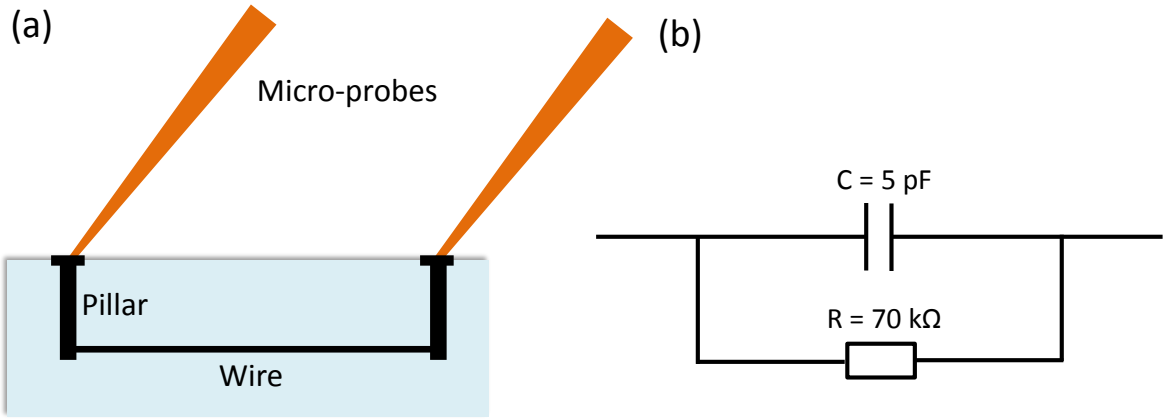

Figure 9.1: (a) The sketch showing the measurement of AC property for the graphitic wire inside diamond. Two micro-probes were used to touch the surface contacts. (b) The equivalent electrical circuit for the AC measurement. The capacitor was mostly generated from the two micro-probes. The value of the capacitance (5 pF) was evaluated by theoretical fitting of measuring data, while the value of resistance (70 kΩ) was directly measured by Impedance Analyzer.

As the two micro-probes are long (length about 10 cm), and close to each other (distance 400 μm for the tip), they form a small capacitor which is parallel to the wire circuit. Additionally, according to previous reports, the components combined by graphite and diamond particles also have capacitance effect [221]. As the wavelength of the high frequency microwave used in our investigation is much larger than the length of the wire, we therefore assume a capacitor was paralleled into the equivalent circuit, which is shown in Figure 9.1 (b). In this

case, the total impedance is calculated as:

$$\frac{1}{Z} = \frac{1}{1/iwC} + \frac{1}{R} \tag{9.1}$$

where Z is the total impedance, w is the AC frequency, C is the equivalent capacitance and R is the resistance. In a general case, the total equivalent impedance Z_0 could be expressed by the combination of equivalent resistance R_0 (real part of impedance) and equivalent reactance X_0 (imaginary part of impedance):

$$Z_0 = R_0 + iX_0 \tag{9.2}$$

The resistance is the opposition to the passage of an electric current through a conductor, while the reactance is the opposition to a change in current. The magnitude of reactance is decided by the capacitor and conductor in the circuit. The magnitude of impedance $|Z_0|$ is then calculated as:

$$|Z_0| = \sqrt{R_0^2 + X_0^2} \tag{9.3}$$

9.2.3 Results analysis

DC measurements show the total resistance including the pillar and additional losses is 70 kΩ. So that the resistivity of the wire is calculated to be 0.048 Ωcm. In the measurements of AC property, the alternating current was provided by an Agilent 4192A LF Impedance Analyzer with controllable frequency. The measurements for impedance, resistance and reactance were conducted with the AC frequency varied from zero to 3.5 MHz. The results are shown on a linear scale in Figure 9.2 (a).

It is seen that both the resistance and impedance present a decreasing trend after $\sim$200 kHz, which means that a higher passage of electric current was achieved in the higher frequency region. The magnitude of reactance presents an increasing and then decreasing trends. This confirms the existence of capacitance or conductance in the circuit. To estimate the capacitance, the theoretical simulation was conducted with the adjustment of capacitance value. Figure 9.2 (b) presents the simulation assuming the equivalent capacitance is 5 pF. Com-

paring the two figures, it seems both the parameter setting and the equivalent circuit model (Figure 9.1 (b)) make the simulation matches with the measured results well. These results confirm the previous parallel capacitor model, and also suggest that the additional capacitance was about 5 pF. We consider the additional capacitance was mostly generated from the two micro-probes, and partly from the graphitic wire itself. However, this needs more demonstration in the future.

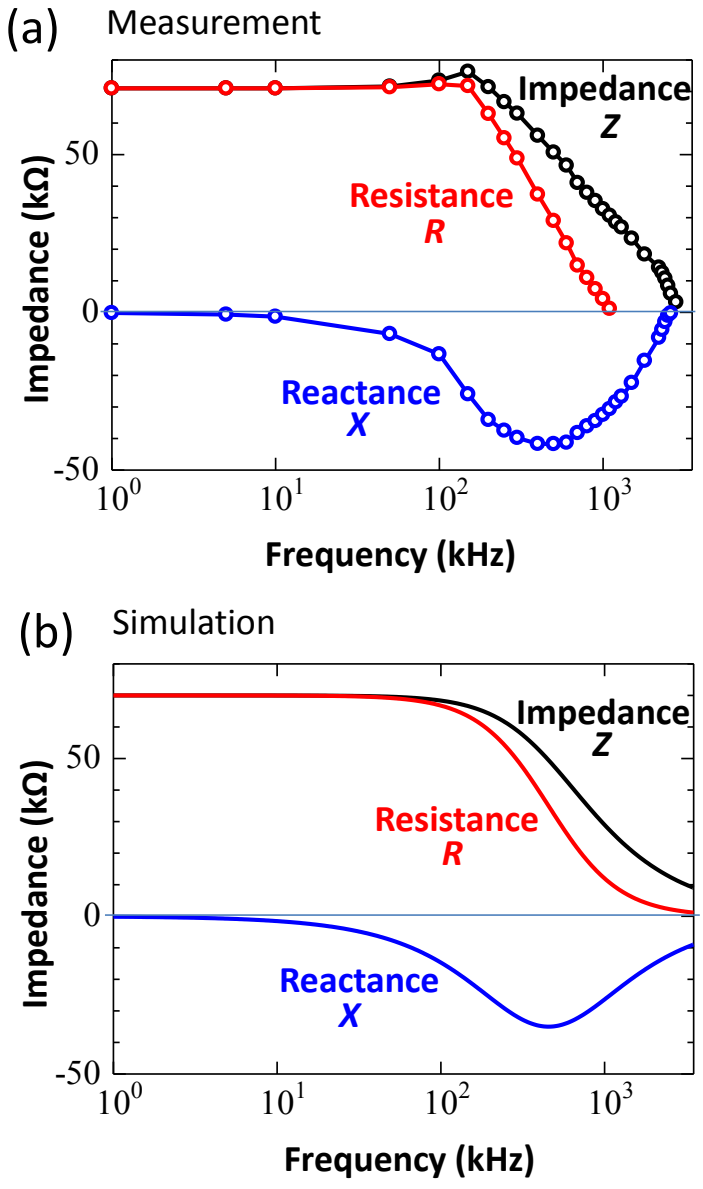

Figure 9.2: Linear display of the (a) measurement and (b) simulated results for the magnitude of impedance $|Z|$, the resistance R and the reactance X. The simulation was conducted assuming the equivalent capacitance is 5 pF.

A more usual display for the impedance is with log axis. The measurement results with the

log display are shown in Figure 9.3 (a). The reactance was shown using absolute values. Compared with the simulation results in Figure 9.3 (b), the measured data has a slightly sharper drop at the frequency larger than 1 MHz. This was due to the low resolution of the Impedance Analyzer when the measured data is with small value. Despite the sharp drop, the two figures still have excellent match.

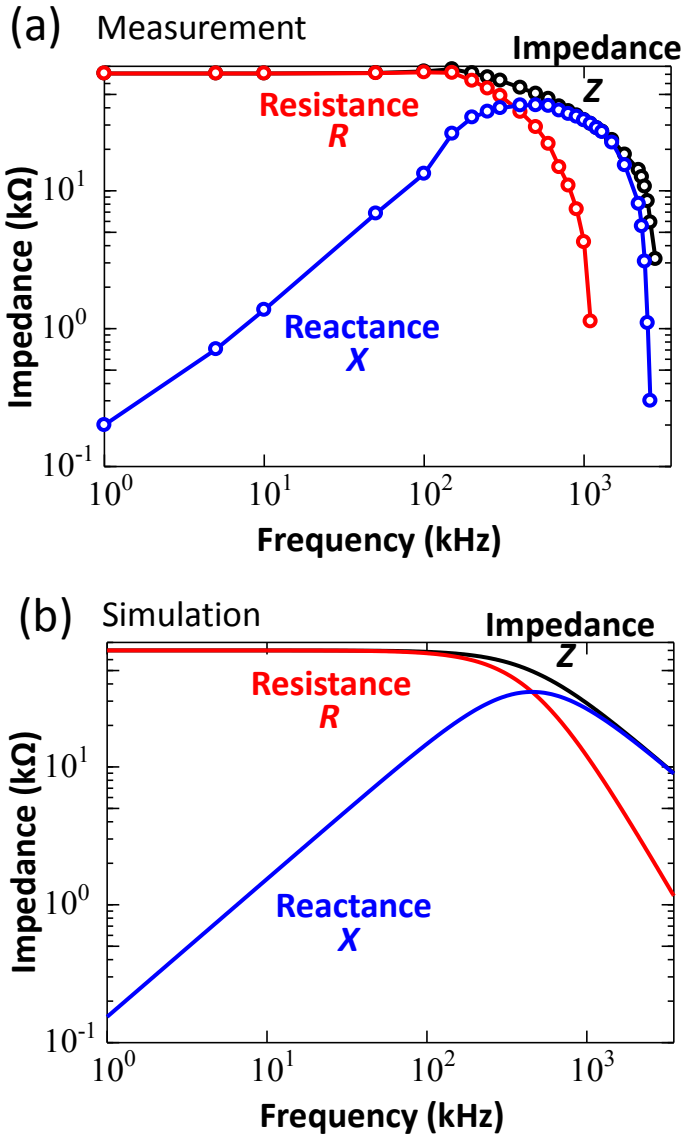

Figure 9.3: Log display of the (a) measurement and (b) simulated results for the magnitude of impedance $|Z|$, the resistance R and the reactance X. The simulation was conducted assuming the equivalent capacitance is 5 pF, while the resistance is 70 kΩ.

The meaning of electrical impedance can be understood by substituting it into Ohm's law,

which is expressed by the equation:

$$V = I\,|Z|\,e^{j\theta} \tag{9.4}$$

The magnitude of impedance $|Z|$ can be understood as the resistance. The phase factor tells us that the current lags the voltage by a phase of θ. In the time domain, the current signal is shifted $\frac{\theta}{2\pi}T$ later with respect to the voltage signal. The phase of impedance is calculated by:

$$\theta = \arctan(\frac{X}{R}) \tag{9.5}$$

The plots of the impedance phase for the fabricated graphitic wire are shown in Figure 9.4.

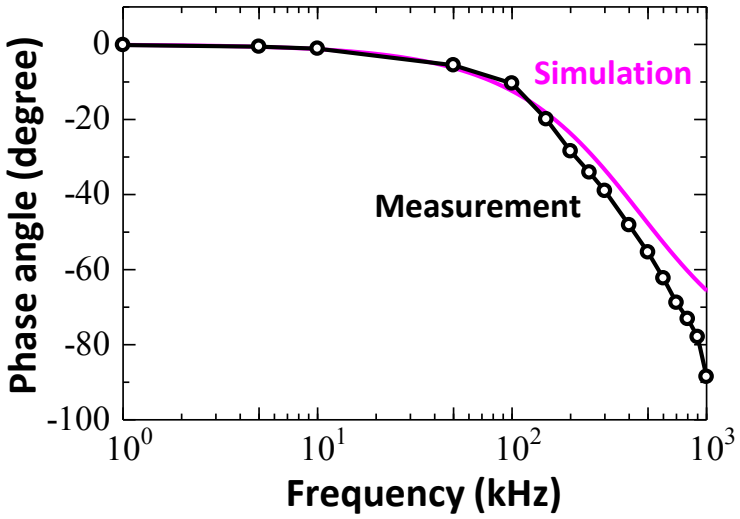

Figure 9.4: The plots of measured and simulated phase of impedance. The simulation was conducted assuming the equivalent capacitance is 5 pF, while the resistance is 70 kΩ.

9.2.4 Discussion

This section presents the conducting of high frequency AC through straight graphitic wire in a general case of measurement: the wire is connected with an outside circuit which introduces an additional capacitance effect. This is a common situation if the diamond sample is not bonded into a chip. The measured results show a nice agreement with the simulations, and also suggest that the additional capacitance effect may dominate the high frequency AC property. In future observations, the conductive property could be measured for a bonded sample in a chip, thus

any additional effects from outside circuits could be minimized. Some more research works could be conducted based on the results presented in this section, such as investigating the spin status of N-V center in diamond by introducing the micro-wave [218, 219, 223, 224].

9.3 Design and fabrication of micro-capacitor

With the adaptive laser fabrication, it is easy to create the graphitic micro-structure with a high resolution inside the diamond. One particular interesting research is to fabricate and characterize the micro-capacitors. As the capacitor could be used to create a high electrical field between its two plates by applying a DC voltage, its fabrication may also be useful for the future research of electrical field effect in the N-V center.

9.3.1 Capacitor design

For the design of the micro-capacitor, two rectangular plates could be created with their length in the y direction and width in z direction. A sketch showing the side and top views of the micro-capacitor is presented in Figure 9.5. The plates should be well-graphitized to extensively reduce the additional resistance. The fabrication of the plates could be conducted by multiple laser passes with axial shifts in z direction (Section 7.4.1). High conductivity graphitic wires could be fabricated later to connect the two plates. The equation to calculate the capacitance is given by:

$$C = \frac{\varepsilon_r \varepsilon_0 S}{4\pi k d} \tag{9.6}$$

where ε_0 is the vacuum permittivity, which equals to 8.854187817 $\times$ 10^{-12} F/m. ε_r is the permittivity of dielectric between the two plates of capacitor, and for diamond, it equals to 5.7 [225]. S is the area of the plates, while k is the Coulomb's constant and d is the distance between the two plates.

In our design, the length of the plate was 300 μm along the y direction, and the width was 10 μm along the z direction. The distance between the two plates was 1 μm. This gives a capacitance of $\sim$0.1 pF for the designed micro-capacitor.

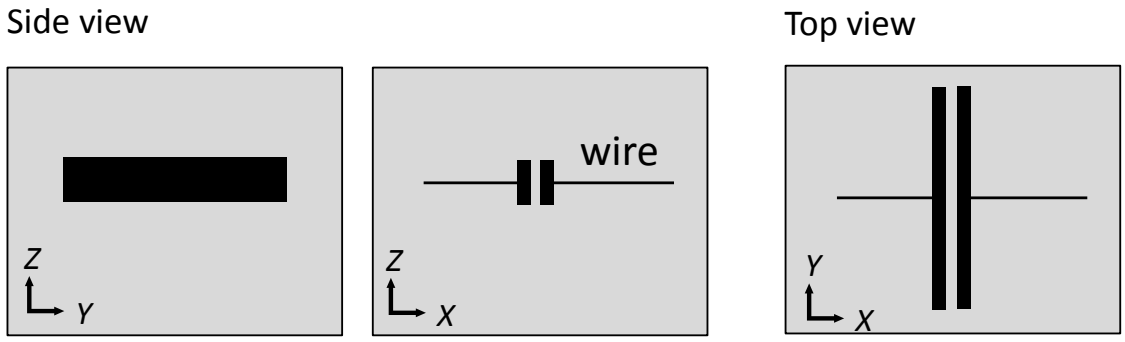

Figure 9.5: Sketch showing the side and top views of the designed micro-capacitor with two rectangular shape plates. Graphitic wires are connected to the side of the plates.

9.3.2 Connection circuits

For the design of inner connection circuits for the micro-capacitor, the simplest way is to fabricate two wires connecting each plate. The equivalent circuit is a single capacitor which is in series with two resistors (graphitic wires are considered as simple resistors, capacitance inside wire is ignored here). The equivalent circuit is shown at the left side of Figure 9.6. Assuming the resistance of the graphitic wires at each side of the plate is 40 kΩ, the simulation results for the impedance, reactance and resistance of this circuit is presented at the right side of Figure 9.6. It is seen that both the impedance and reactance are infinitely large in the low frequency region, and they drop significantly with an increase of the AC frequency. The frequency at the cross point of the reactance and resistance curves (marked by an arrow in the figure) can act as the metric for the characterization of the magnitude of the capacitance. Assuming the micro-capacitor has a capacitance of 0.1 pF, the frequency at the cross point is 22 MHz.

Another connection design for the micro-capacitor is to fabricate an additional wire which is parallel to the micro-capacitor. The equivalent circuit is shown in Figure 9.6 (b). In this design, an additional resistor is parallelled into the connection circuit. The simulations for the impedance, reactance and resistance are shown at the right side. It is seen that both the impedance and resistance begin with a constant, and they start to decrease when the AC frequency reaches to certain value (marked by an arrow). Similarly, this specific frequency acts as the metric in the capacitance characterization for this circuit model. Assuming the micro-

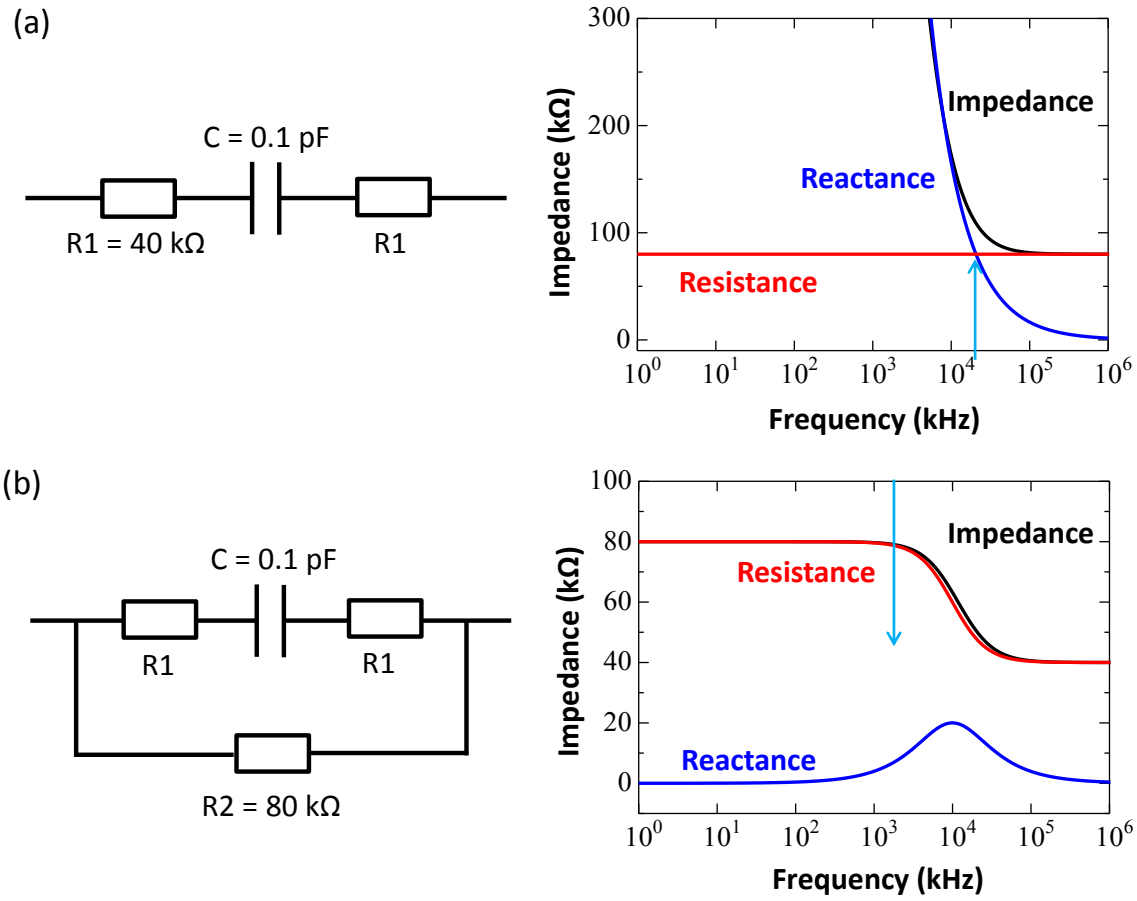

Figure 9.6: The inner connection circuits for the micro-capacitor. Two methods are presented: (a) Two wires are fabricated to connect each plate of the micro-capacitor. (b) Besides the two wires connecting the plates, an additional graphitic wire is fabricated in parallel to the micro-capacitor. The equivalent circuits are displayed on the left side of the figure, while the simulations of impedance, reactance and resistance are presented at the right side. The capacitance of 0.1 pF is the calculated value from the physical parameters of laser fabricated micro-capacitor. The possible small capacitance effect in the graphitic wire itself was not considered in the model. Arrows in the curves mark the specific frequency that can be used to determine the magnitude of capacitance.

capacitor has a capacitance of 0.1 pF, the frequency at the cross point is 2 MHz.

While both the two circuit designs are able to characterize the magnitude of the capacitance, the second one has more advantages than the first one. Firstly, the specific frequency as the metric for the capacitance in the second method (2 MHz) is more than ten times smaller than that of the first method (22 MHz). This could simplify the characterization experiments, as unexpected side effects are usually generated in the circuits for high frequency region. Secondly, in the second model, the impedance, resistance and reactance begin with constants while the frequency is zero. This enables the possibility to do the initial check for an in-

tegrity of the circuits by a DC. As a result, in our experiments, we choose the second design to connect the micro-capacitor for the AC characterization.

For the outside connection circuit, there would be an additional 5 pF capacitance if the micro-probe is used. In Equation (9.6), the capacitance is proportional to S/d. As the size of micro-probes is much larger than the graphitic micro-capacitor, the area of the micro-probes (S) is significantly greater than an embedded micron structure. If the micro-probes were used for the measurement of high frequency AC property, the capacitance of the graphitic micro-capacitor would be too small to be characterized. We therefore propose to use the surface metal deposition technique to enable the AC capacitance characterization. This technique is to use the photolithographic mask to deposit metal layers in the shape of a designed pattern on the surface of diamond [226]. External electrical wires can be bonded to the surface metal for further measurements. By using this mature technique, we are able to use the bonded metal layer to connect the graphitic surface contacts, thus characterize the AC property of the micro-capacitor without the significant influence of external capacitance.

9.3.3 Fabrication

The fabrication of the micro-capacitor plates started from a depth of 22 μm. In each xy plane, two graphitic wires with distance of 1 μm were fabricated with 20 nJ pulse energy, 10 μm/s by a 1.4 NA oil objective lens. SLM was used for the adaptive correction of the refractive index mismatch aberration. This formed a rectangular graphitic area with a size of 2.4 $\times$ 300 μm in each xy plane. After the fabrication in one xy plane, the fabrication depth was reduced by 0.6 μm to the next xy plane, then similarly, the rectangular area was fabricated. The total fabrication was conducted for 14 different planes to form one single plate for the micro-capacitor. The two plates were fabricated with the same method simultaneously.

The fabrication of the micro-wires was conducted with two passes in xy plane by a distance of 0.8 μm between each pass, and six passes in the xz plane with an axial shift of 0.5 μm. The depth of the wires was 20 μm under the diamond surface. The cross-section size of the wire was measured to be 2.2 $\times$ 4.2 μm.

The microscope image of the fabricated micro-capacitor and the connection circuit is

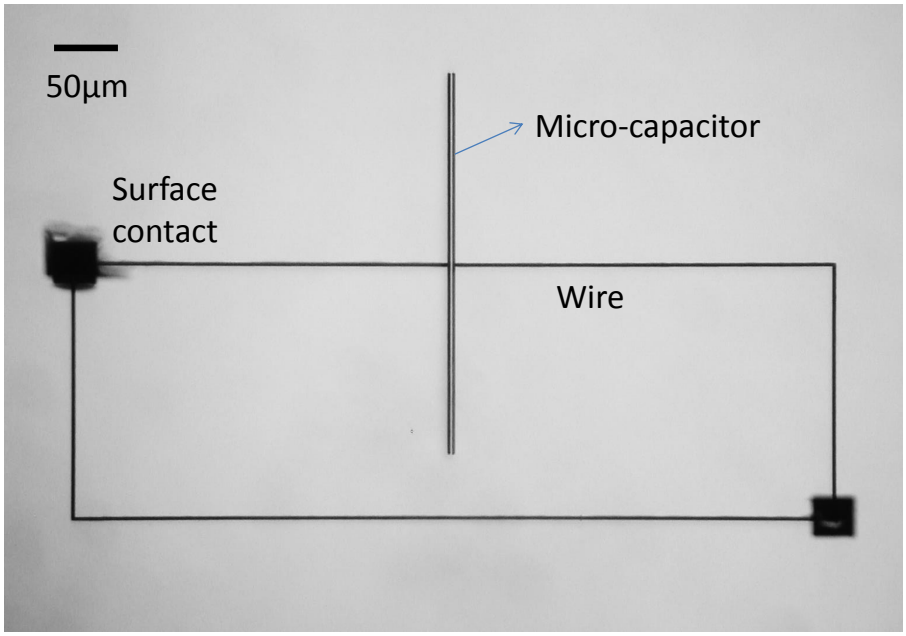

Figure 9.7: The microscopic image of the micro-capacitor. The size of capacitor is 300 $\times$ 10 μm, with a distance of 1 μm between two plates. Wires length are 600 μm and 200 μm, respectively.

shown in Figure 9.7. The lengths of the graphitic wires are 600 μm and 200 μm, respectively. Perpendicular pillars and surface contacts were fabricated at left and right sides of the circuit. The DC measurement of the circuits confirmed the resistivity of the wires was 0.036 Ωcm. This value matches well with our previous publications [220].

9.3.4 Discussion

This section firstly presents the design of micro-capacitor and its connection circuits. The detailed fabrication procedure for the micro-capacitor is then illustrated. It is seen that the capacitance of the micro-capacitor is much smaller than the additional capacitance effect generated from outside circuit, if the micro-probes are used. Therefore, alternative method such as the surface metal deposition technique may be used to characterize the micro-capacitor. Future works include investigating the electric field between the two plates when applying a high voltage DC, and finding other applications in electronics for the micro-capacitor.

9.4 Fabrication of electrode arrays for radiation detector

9.4.1 Radiation detectors

Conventional radiation detector usually uses the silicon as the base bulk material. Collecting electrodes are buried within the bulk of the detector and separated by a few dozens of microns [227]. Recently, diamond has been adopted as an alternative base bulk material for the radiation detectors. Since diamond radiation hardness is far superior to silicon for high energy particles [228, 229], one can expect for 3D structured diamond detectors to withstand higher fluences than their silicon analogues and be able to operate after unprecedented radiation levels. The most efficient way to bury the electrodes inside diamond is to use ultrafast laser material processing. The electrodes can be fabricated by translating the sample perpendicular to the direction of laser propagation. Electrode arrays are formed by fabricating tens of electrodes with certain designed pattern. These perpendicular electrodes are then connected by the graphitic wires embedded in the subsurface depth. An example of the electrode array is shown in Figure 9.8, in which, 61 electrodes were separated with 100 μm each [181]. As a result, a 3D structure which is made of two interdigitated superficial graphitic combs is engraved by the ultrafast laser. The detection of the radiation is based on the ShockleyRamo theorem [230], which calculates the instantaneous electric current induced by a charge moving in the vicinity of an electrode. In a practical application, one comb is connected with a bias voltage, the other is connected to the current detector. The change of the current measurement could inform the information of radiation status and position. As the principle of radiation detector belongs to the enormous research of radiation physics, here we only concern the laser fabrication of high quality graphitic electrode arrays.

The performance of the radiation detector significantly depends on the resistivity of the electrodes. In addition, a smaller cross section size is always preferred, as the resolution can be improved in such way. There have been lots of studies in recent years fabricating the electrodes by ultrafast laser pulses [60, 61, 178–181]. It has been found that in order to generate high quality, homogeneous and uniform graphitic wires with controllable thin sizes, it is essential to use pulses with shorter durations (such as a fs/ps laser) [61, 181, 197]. As

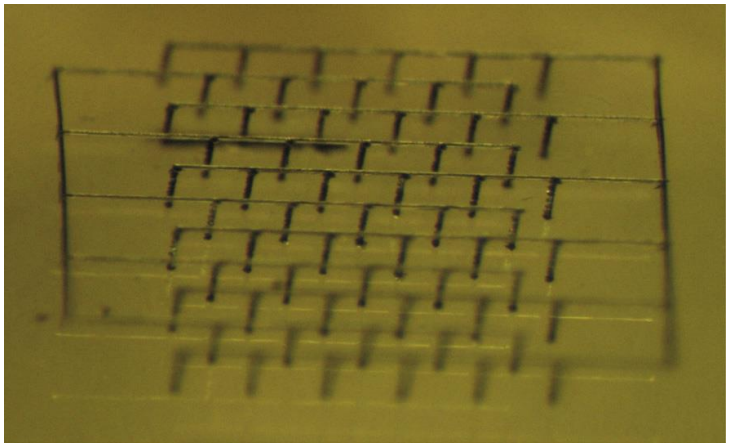

S. Lagomarsino, Diam. Relat. Mater. 2014

Figure 9.8: An example of the electrode array for radiation detector [181].

all the previous fabrications are using the objective lens with air immersion, there are two outstanding problems: 1) a large resistivity (around several Ω cm), 2) a large cross-section size (tens of micron). We have proved in Chapter 7, that the fabrication with adaptive optics and oil immersion objective lens can significantly reduce the size and resistivity of the wires. However, the electrode fabrication along a perpendicular direction is far more difficult than the fabrication of wires parallel to the diamond surface. This is due to the challenges of fabrication at much higher depths, where aberrations are much larger. This section concentrates on the detailed approach in the perpendicular electrode arrays fabrication.

9.4.2 Design and fabrication

The design of the electrodes is shown in Figure 9.9, where the detector includes four independent arrays of total 244 electrodes. Each array contains two electrode combs. 6×6 electrodes in one comb are connected together for applying the bias voltage, while the other comb contains five rows of electrodes, with five electrodes in each row. The row is designed to be connected to an outside pin. The diamond sample is a size of 4 mm×4 mm, and a thickness of 0.5 mm. Each array is 0.6 mm×0.6 mm, with a distance of 0.5 mm between each other. The electrodes are separated with a distance of 0.12 mm.

The optical system used for the electrode fabrication is similar to the system used in Chap-

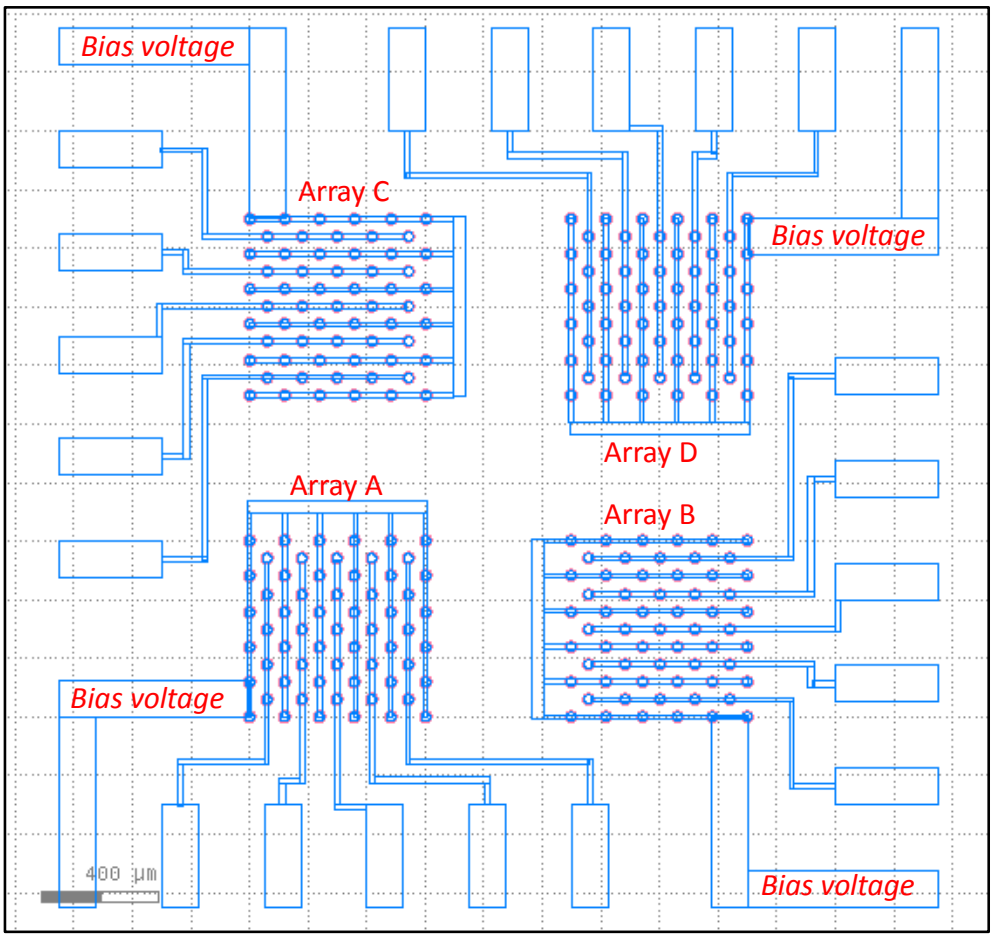

Figure 9.9: The layout of the designed electrode arrays for radiation detector. Four arrays are marked as A, B, C and D.

ter 7. For the fabrication parallel to the diamond surface, a high NA (1.4NA) oil objective lens was used. The fabrication at a depth of 100 μm was demonstrated by this objective lens. However, it is very difficult to fabricate at a depth higher than 100 μm, as the refractive index mismatch aberration became too large to compensate. In addition, the working distance of the 1.4NA lens is too short to fabricate through the diamond sample, which has a thickness of 0.5 mm. We therefore chose another oil objective lens with lower NA (0.8NA, 20×, Olympus UplanApo). A lower NA objective lens can significantly reduce the amount of the refractive index mismatch aberration that needs to be compensated (Section 2.5.2, Chapter 2). The reason to use relatively higher NA oil immersion lens rather than the lower NA air immersion lens is that better focal confinement of the laser pulses can be obtained by high NA lens. This could be useful to increase the quality of the graphitic electrodes.

When fabricating with an oil objective lens, it is difficult to graphitize the subsurface area,

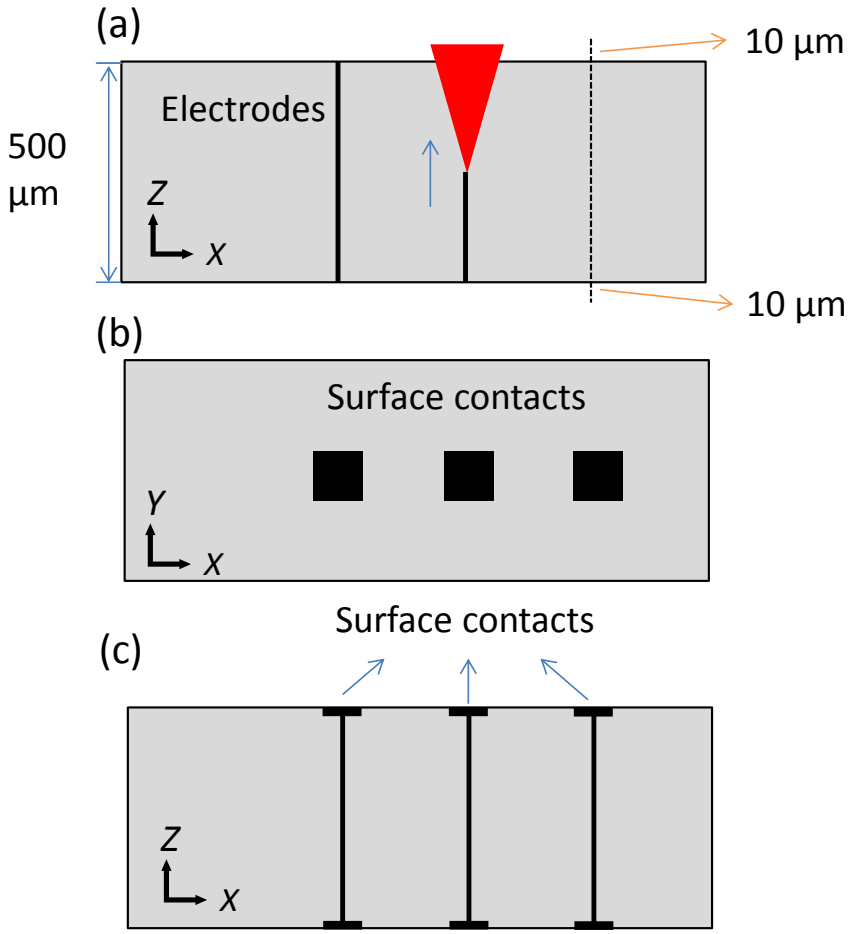

Figure 9.10: Sketches showing the fabrication of perpendicular electrodes in diamond. (a) The fabrication of the electrodes. The dashed line shows moving path of the laser focus relative to the diamond sample. (b) The surface contacts. (c) The whole fabricated electrodes with the surface contacts.

as the oil is usually boiled when the laser focus is approaching the diamond surface. Similar to the description in Chapter 7, the fabrication process can be divided into two steps: the electrode fabrication inside the diamond, and the surface contact fabrication on the diamond surface. A sketch showing the fabrication process is presented in Figure 9.10. For the fabrication of the perpendicular wires, the laser focus started 10 μm beneath the bottom surface of the diamond. The sample was then translated by 3D stage so that the focus moved up to the top surface with a fixed speed. The moving of the sample stopped while the laser focus is 10 μm above the top surface. Moving the laser focus $\pm$10 μm longer than the thickness of the sample makes sure that the electrodes were extensively fabricated till the end of the diamond surfaces. The fabrication pulse energy for array A and B was 170 nJ, while for C and

D was 260 nJ. The moving speed for A and C was 20 μm/s, while for B and D was 10 μm/s. The cross-section size of the electrodes is determined by the fabrication pulse energy. As a result, the electrodes in array A and B are with a cross-section diameter of 2.2 μm, while the electrodes in array C and D are with diameter of 2.8 μm. It was seen in the high resolution microscope that the cross-section size of each electrode is quite uniform at each depth. The surface contacts were fabricated by using an air objective lens (0.5NA). The size of the surface contacts was 10×10 μm. It is notable that the surface contacts should be fabricated at both ends of the perpendicular electrodes.

9.4.3 Microscope images

Images before the fabrication of surface contacts

Figure 9.11 shows the microscope images of the electrode array from the top view of the diamond sample. These images were taken before the fabrication of the surface contacts. Images in Figure 9.11 (a) were taken while the microscope was focused on the top surface of the sample. The size and shape of the electrodes slightly vary for each electrode. This is because some of the electrodes experienced slight cracking on the diamond surface. Images in Figure 9.11 (b) were taken while the microscope was focused with a certain depth (about 250 μm) into the diamond sample. The slight cross lines beside the electrodes were due to the shadow of electrodes in the microscope illumination. It is seen that the size and shape are quite uniform for all the electrodes, confirming that the fabrication was in of good quality. Because of the lower threshold in the laser graphitization of diamond surface, the images in (a) present slight larger size of the electrodes than that in (b).

Images after the fabrication of surface contacts

Figure 9.12 shows the microscope images after the fabrication of the surface contacts. Figure 9.12 (a) presents the images taken when the microscope was focused on the top surface of the diamond sample. It is seen that after the fabrication of the surface contacts, the size became larger on the top surface. Due to cracking, there are graphitic particles distributed around the contacts. Figure 9.12 (b) shows the images taken when the microscope was focused with a

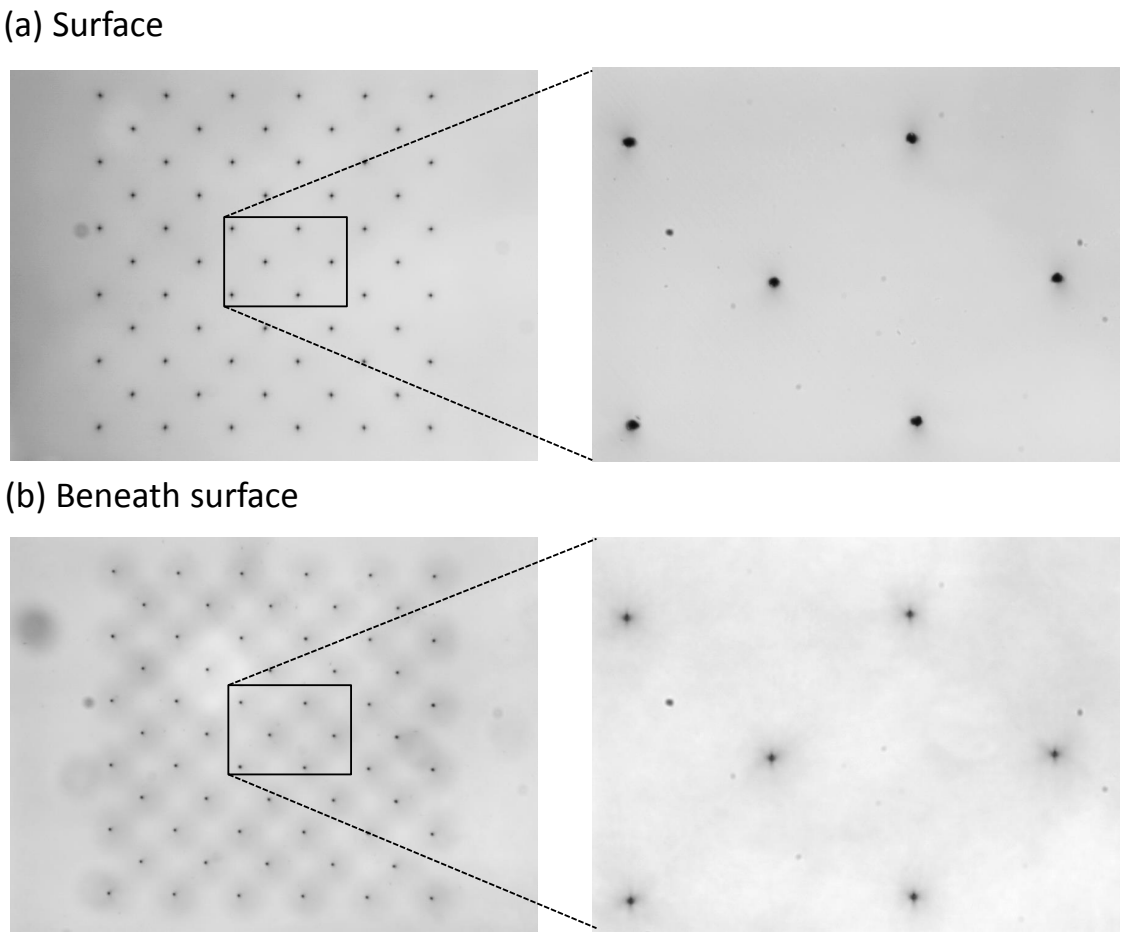

Figure 9.11: Microscope images showing the top view of the diamond sample embedded with electrode arrays. The electrodes were not fabricated with surface contacts. (a) Microscope was focused on the top surface of the sample. (b) Microscope was focused with a certain depth (about 250 μm) beneath the surface of the sample. The electrodes in each row were separated with a distance of 120 μm.

certain depth beneath the diamond surface. The size of the electrodes was smaller than that shown in (a), and the same with that shown in Figure 9.11 (b), confirming the fabrication of the surface graphitic contracts did not influence the embedded electrodes. The dark circles around the electrodes are due to the shadows of the surface contacts during the microscope illumination. To show the four arrays as well as the whole electrodes and surface contacts, the diamond sample was aligned with a tilted angle. Those images are presented in Figure 9.12 (c). The images clearly show both the surface contacts and electrodes. The difference in the size of the surface contacts and electrodes is easily seen.

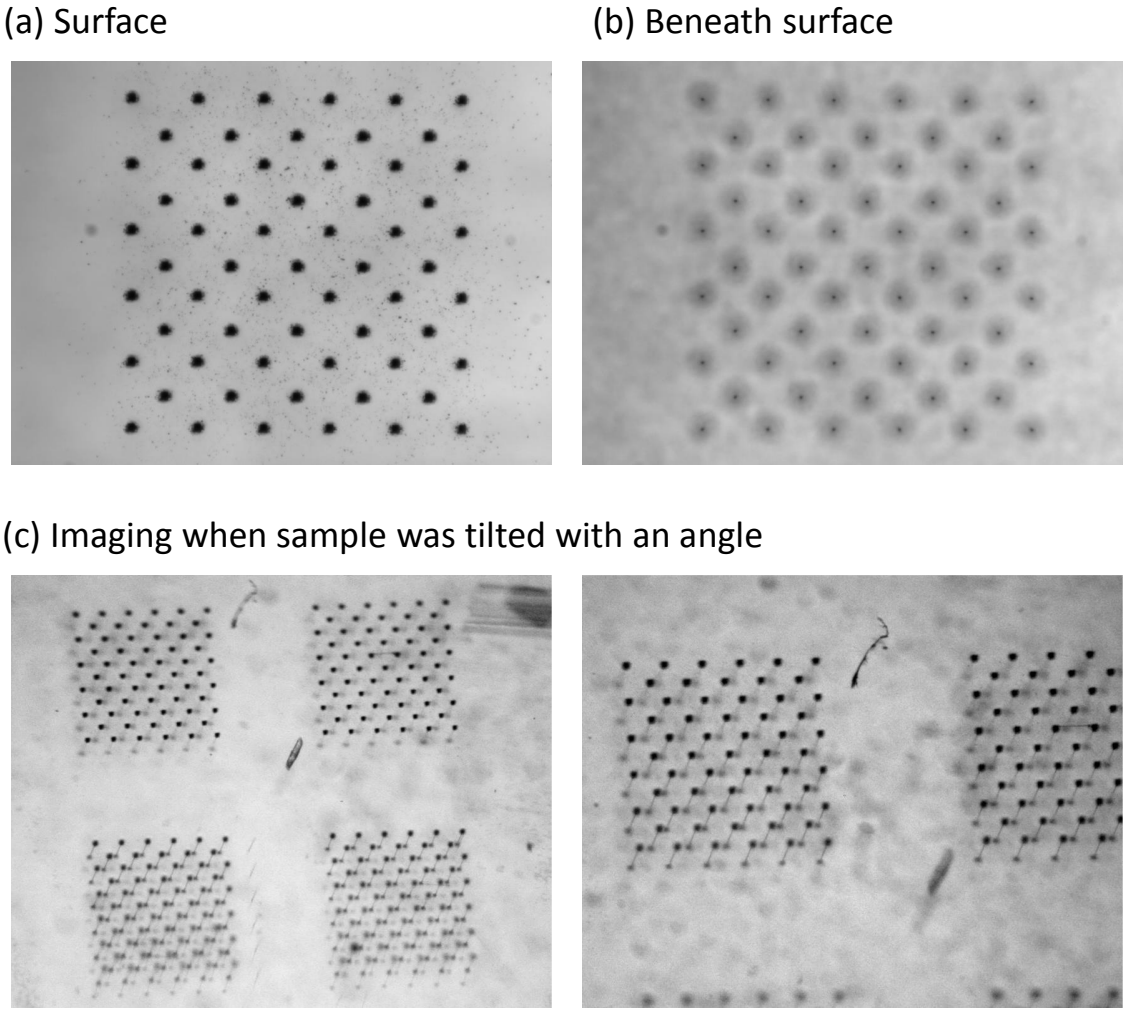

Figure 9.12: Microscope images showing the diamond sample embedded with electrode arrays. The electrodes were fabricated with surface contacts. (a) Microscope was focused on the top surface of the sample. (b) Microscope was focused with a certain depth (about 250 μm) beneath the surface of the sample. (c) The diamond sample was imaged with a tilted position to show the four arrays as well as the whole electrodes and surface contacts. The electrodes in each row were separated with a distance of 120 μm.

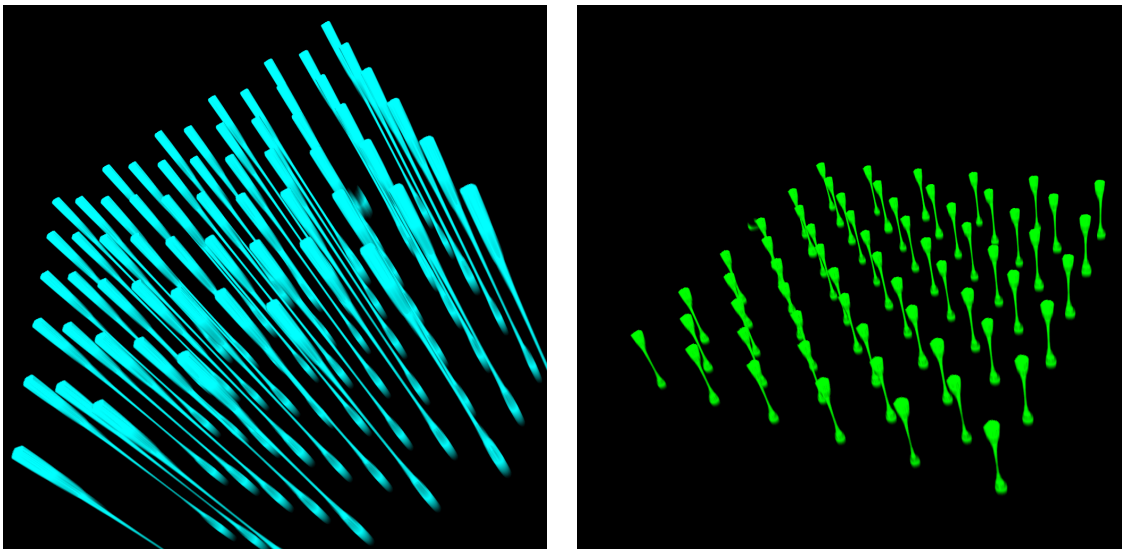

Figure 9.13: 3D images of one electrode array. The images were constructed from 20 2D images taken by a conventional microscope. Left: The 3D image showing the electrodes with real size. The electrodes have a length of 500 μm. In each row, they were separated with a distance of 120 μm. Right: The 3D image showing the electrodes with compressed length. The length shown in the image is 20% of the actual length.

3D images

3D images of the electrodes in an array are taken by a conventional optical microscope. To construct the 3D images, a number of 2D images were firstly acquired when the microscope was focused to various depths. The diamond sample was aligned at a fixed position for a set of 2D images. In our experiment, the 3D images shown in Figure 9.13 were constructed by 20 different 2D images. The image on the left hand of the figure presents the electrodes with real sizes. As the length of the electrodes (500 μm) is larger than the distance between two electrodes (120 μm), the electrodes in the back are covered by the ones in the front of the image. For a clear view of all the electrodes inside the array, the length of the electrodes was compressed to 20% of the actual length. The image with compressed length is shown in Figure 9.13 (b). It is notable that the electrodes present a tube shape in these 3D images. This is due to effect of the shadows from surface contacts during the microscope illumination. These shadows were presented in Figure 9.11 (b). They are of larger size when the microscope is focused near the diamond surface. In the real case, the cross-section size of the electrodes is fairly uniform across all depths.

9.4.4 Discussion

The design, fabrication and microscope imaging of the electrode arrays are discussed in this section. While the electrodes seem to be of a good quality in the images, there is still a need to evaluate its resistivity, which will be future work once the sample is bonded into the chip. As we expect the resistivity could be reduced compared to the previous reports, it will be interesting to see its improvement in the performance as a radiation detector.

9.5 Conclusions

This chapter concentrates on exploring new applications for the adaptive laser diamond fabrication. The description contains three potential applications. Firstly, the high frequency AC property was measured for straight wires with micro-probes. The measured results match with the theoretical simulation well. Secondly, the micro-capacitor and its connection circuits were designed. Detailed fabrication procedure is discussed. Finally, the perpendicular electrode arrays were fabricated. Various microscope images are analyzed.

Due to limitations in the necessary apparatus for surface metal deposition, this chapter could only include research from the laser micro-fabrication point of view for these new applications. Since the quality of the graphitization is demonstrated to be significantly improved with the adaptive optics, we believe that this advanced method for laser processing in diamond could generate more interesting applications in wide areas.

Chapter 10

Conclusions and summary

This thesis concentrates on advancing the theories and experimental technologies for laser material processing technique with adaptive optics. With the correction of various aberrations, adaptive optics is able to significantly improve the fabrication quality. However, there are still great vacancies in need of further study of this advanced technology. The need of theory development includes the exploration of the effects of aberrations and sample dispersion on the ultrafast laser focusing. Practical technology development includes the demand of developing new adaptive optics methods in correcting the pulse front distortions, improving the fabrication technique to obtain high quality diamond wires, and exploring more advanced applications in 3D diamond and glass structuring.

The presented calculation methods in Chapter 2 are extensively useful in understanding how different factors or parameters affect the ultrafast laser focusing. With introducing the mathematical models of Fourier optics and phase aberrations, the simulation of the focal intensity distribution is enabled. With different representations of the pupil intensity illumination, various focusing methods can be modelled. In addition, the theory of lens dispersion is valuable in evaluate the ultrafast laser focusing system, allowing the development of new adaptive optics technique to control the pulse front and correct the distortions.

As the first direct application of these mathematical modes, the focal intensity distributions are simulated for the effects of phase aberrations and sample dispersion. The aberrations and sample dispersion generally exist in all practical laser fabrication systems. Since they have not been reported before, these theoretical investigations are very useful in determine

how the aberrations and sample dispersion affect the spatial and temporal properties of the laser focus. The simulation results can reveal the significance of each phase aberration and sample dispersion in different practical scenarios, and suggest if any corrections or other system modifications are needed. Those results provide theoretical guides for operating further experimental investigations which are described in later chapters.

Beside the phase aberrations and sample dispersion, another factor which brings undesired distortions to the laser focus is the lens dispersion. The theoretical simulations for the effects of lens dispersion and pulse front distortion have already been extensively reported previously. There is only a lack of technique that can adaptively compensate this kind of distortion. The demonstration of the pulse front adaptive optics in the thesis not only greatly extended the capability of adaptive optics methods, but also provided a new method in controlling the ultrafast laser pulses to further adaptively compensate the chromatic lens dispersion. This new adaptive optics method is demonstrated to be able to practically correct the quadratic pulse front distortion in a two-photon microscope. 1.4 times improvement in the two-photon signal is demonstrated for a 80 fs laser. However, we would expect a much more significant improvement to be found in the future when lasers with shorter pulse duration are used. It is likely that more and more new applications would be enabled in ultrafast physics, adaptive optics and other laser focusing systems by controlling the laser pulse front with adopting this technique.

Those investigations of the aberration and sample dispersion effects, together with the development of the pulse front adaptive optics technique aim at improving the ultrafast laser focusing performance, which is the core part of the laser material processing. Later on, the laser processing in practical materials including diamond and silica glass is described based on those improvements of the laser focusing process.

The laser processing in diamond best reveals the advantage of adaptive optics. As diamond has a much higher refractive index of 2.4 than the that of immersion oil (1.52), in addition with a high NA objective lens used, the spherical aberration arising from the refractive index mismatch is very significant even for the fabrication in a small depth. We have demonstrated that with the correction by the SLM, the resistivity of the laser processed graphitic wires was reduced by more than 100 times. The high conductivity wires following any 3D shape were

enabled for the first time. More interesting investigations in the laser micro-fabrication are discussed. Firstly, directional effects were found in the diamond fabrication. It was seen feather effects generated when the fabrication was conducted along <100> directions. More interestingly, significant non-reciprocal effect was seen when the laser light with linear polarization was used for the fabrication along <110>. Secondly, the impedance of the straight wires was measured by using high frequency alternative current. With the advantages of the adaptive laser fabrication, the graphitic micro-capacitors were fabricated. Arrays of electrodes which are perpendicular to the diamond surface were processed for the applications in high energy particle detectors. With the advanced adaptive laser fabrication, more and more new and interesting applications could be enabled in the future with the graphite fabrication in diamond.

As a brief summary, this thesis targets at the advancing of adaptive laser micro-fabrication technology. This was realized firstly by improving the performance of ultrafast laser focusing, and then applying the technique to interesting applications. Both theories and practical techniques were developed.

For the future outlook for the adaptive laser micro-fabrication, several interesting topics could be further investigated based on the current progress described in this thesis. Firstly, various illumination patterns could be included in the modeling of ultrafast laser focusing. The modelling could be conducted for both conventional focusing and temporal focusing. Secondly, based on the experiments in the pulse front correction, theoretical simulations concentrating on the effects of pulse front correction could be performed. In particular, the simulations for the effects of pulse front distortion in the SSTF could be further investigated. Thirdly, as the newly developed pulse front adaptive optics was only in its embryo, more and more practical applications could be further developed by creating interesting pulse front shapes. Fourthly, the high frequency AC performance of the graphitic wires in diamond could be measured. More interesting applications may be found in the controlling of N-V center of the diamond sample. Fifthly, the powerful ability in the fabrication of 3D structure could enable more interesting applications when it is combined with the biomedical research.

Appendix

Laser processing of 3D funnel structure in silica glass

1. Introduction

In the previous chapters, it has been demonstrated that it is possible to create high quality 3D structures even in a material with a high refractive index. With aberration compensation by adaptive optics, both the quality and resolution have been greatly improved. On the other hand, silica glass is usually used as the target material for laser material processing. It has already been studied for its applications in optical communications and quantum physics (Section 1.2, Chapter 1).

One particular application of the laser glass fabrication is to combine laser processing and chemical etching methods. The breaking down of the bonds between molecules during laser processing makes the fabricated area more easily dissolved in chemical solution such as hydrofluoric acid (HF) than other un-fabricated regions [53, 231]. With enough etching time, functional 3D structures can be created by removing the laser processed area. An enormous number of interesting applications have been reported. One related research field is the lab-on-a-chip technique [54], which creates 3D structure in a silica glass for various biomedical investigations. With laser processing and chemical etching, interesting applications such as micron actuators [55], micro-channels [56], micro-gratings [56], monolithic [57] and surface structuring [58] have been enabled.

In this chapter, I introduce the fabrication of a specific 3D structure in silica glass - the funnel structure, for the research of neuron cell behaviors. The fabrication method of whole 3D volume is presented. The optimization in the fabrication parameters and improvement in the etching process are discussed.

2. Structure design

The live cells are sensitive to their physical surroundings, and usually they prefer to maintain movement along small angles. It is useful to create 3D micron structures in the substrate of bio-compatible material to investigate the cells' movements. Photolithography techniques have been long used in creating surface structure in polydimethylsiloxane (PDMS), which is a non-toxic and biocompatible material [232, 233]. However, there is still a need to avoid the complicated photolithography process, and to make use of materials other than PDMS. Direct laser micro-fabrication method is an ideal solution to these to problems.

For the choice of substrate material, polyethylene terephthalate (PET) has been tested. However, with some initial investigations, it was found that the pores on the PET material were rough, and that there was a build-up of material around the pores occurring during the machining process. It was deemed necessary to use a material that would result in smooth, unblocked structures after machining. Silica glass coverslip is therefore chosen for the experimental demonstration.

The design of a funnel structure is carried out to make investigations for the behaviour of neuron to neuron communications. The sketches are shown in Figure 10.1. The shapes of the funnels are designed to be different on the two sides of the coverslip. On one side (bottom side), all the funnels were designed to form a shape of small pore at the surface, as shown in the "bottom view" sketch in Figure 10.1. The pores are expected to be with a size of less than 5 μm, which reduces the chance that the cells can pass through them on the bottom side. However, these pores can still let the cells on the other side (top side) of the coverslip to grow.

On the top side of the coverslip, the funnels were designed to have different kinds of shape: the straight pillar, the circular shape funnel and rectangular shape funnel, as shown in the "top view" sketch in Figure 10.1. The circular shape was designed to have a diameter of 60 μm, while the rectangular shape was designed with a size of 30×60 μm. In addition, as presented in the "side view" sketch, for one specific shape of either circle or rectangle, the funnels were designed with different sizes. We characterize the difference in the size as difference in the angles of funnel wall, which is 45°, 57° and 72° as shown in the "side view" sketch. For the rectangular shaped funnels, the angles were characterized by the width (the 30 μm side) rather than the length. The design of the funnel structures could enable the investigation of

the cell growing behavior, especially the research in the way they interact with these different passageways.

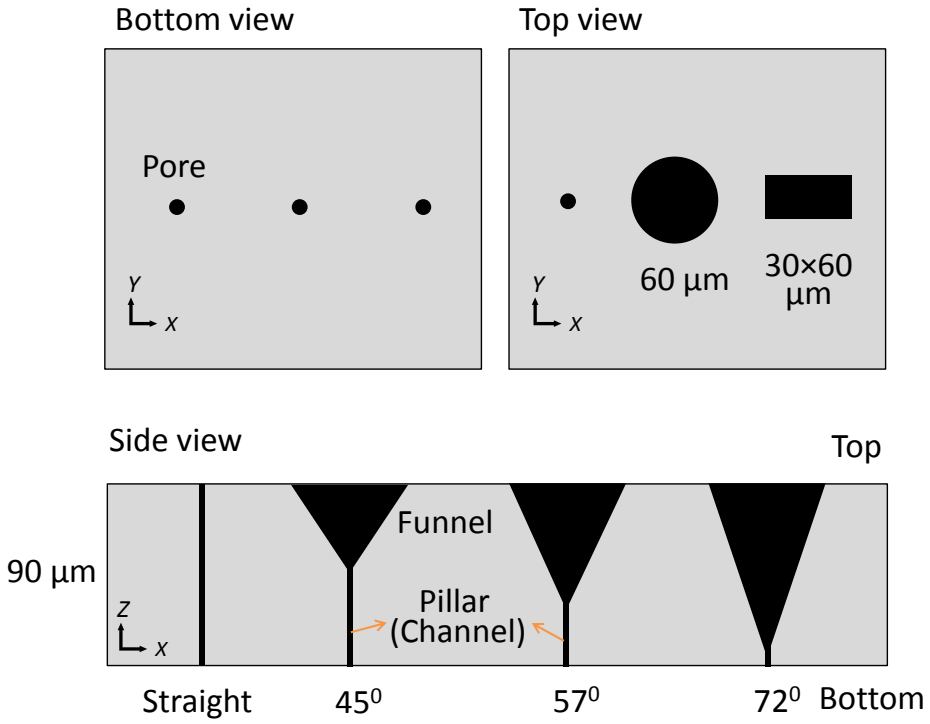

Figure 10.1: Sketches for the funnel structure design in the silica glass. The sample is a microscope coverslip. Top sketch shows the bottom and top views of the fabricated coverslip. On one side, all the funnels were designed to be with a shape of small pore. On the other side, three different shapes were fabricated: the straight pillar, the circular shape funnel and rectangular shape funnel. Bottom sketch shows the side view of the coverslip. Three different angles of the funnel are fabricated: $45°$, $57°$ and $72°$.

3. Chemical etching

The coverslip used in the fabrication was Agar Scientific, No. 0 with a thickness of 80 - 100 μm. The laser fabrication system is similar to the one used in the diamond fabrication (Chapter 7). An Zeiss 20$\times$ 0.5 NA air immersion objective lens was used for the fabrication.

As shown in Figure 10.1, the dark area shown in the sketch was designed to be processed by a high power laser focus. This area is much easier to be chemically etched by the acid. After the laser machining of the selected area, the coverslip sample was soaked inside hydrofluoric acid (HF) [53,231]. 20 ml volume of 1% working solution was made up by slowly adding 1 ml of 50% HF acid to 49 ml of deionised water. The etching time was controlled to be around 20 - 50 mins according to the requirement. The sonication was started in the same time to

increase the etching efficiency. The molecular bonds in the laser processed area were broken down, so that these area was more exposed to the acid solution and experienced a much faster etching speed than other areas of the glass coverslip. With enough time, the laser processed area should be removed by the acid. The air funnel should be obtained after the sample was rinsed in DI water and cleaned by Ethanol. The coverslip etching described in this chapter was carried out by a collaborator who was working with me.

4. Fabrication method

4.1 Two approaches

The fabrication of the funnel structure is the most critical part, as it contains a large volume which is relatively difficult to be etched through. During our experiment, we tried two approaches to fabricate the funnels. One is the side wall fabrication, and the other is the whole volume fabrication.

To increase the fabrication efficiency, a first approach to fabricate the side wall of the funnel was tried. The proposed idea was that after completely etching of the fabricated side wall, the whole glass cone would be isolated from the coverslip. After the fabrication, a way to increase the etching depth and potentially remove the remaining cone is to use a longer etching time. As the coverslip was soaked inside the HF solution, both sides were etched in the meantime. In our experiments, the size of the pore on the bottom side of the coverslip has to be small enough for the cell seeding research. However, a longer etching time would lead to a larger size for the etched pore.

To choose an appropriate time, there is a trade-off between the etching for the funnel on the top side, and the pore on the bottom side. On one hand, the funnels need longer etching time for the cone shape glass to be fully removed. On the other hand, the pores need shorter time to maintain a small size. We found the fabrication of the side wall can not achieve these two tasks at the same time. To solve this problem, we moved on to use the second method to fabricate the funnels.

4.2 Fabrication

To increase the performance of etching, the whole volume of the funnel structure was fabri-

cated, as shown in Figure 10.2 (a). The 3D cone structure, which has a large volume, is shown as the top sketch in Figure 10.2 (a). With the processing for the whole volume of the cone, the HF etching was expected to go straight from the top surface down to larger depths. As the contact area of the modified glass with the HF solution increased a lot compared to the side wall fabrication method, the etching speed was expected to be significantly raised.

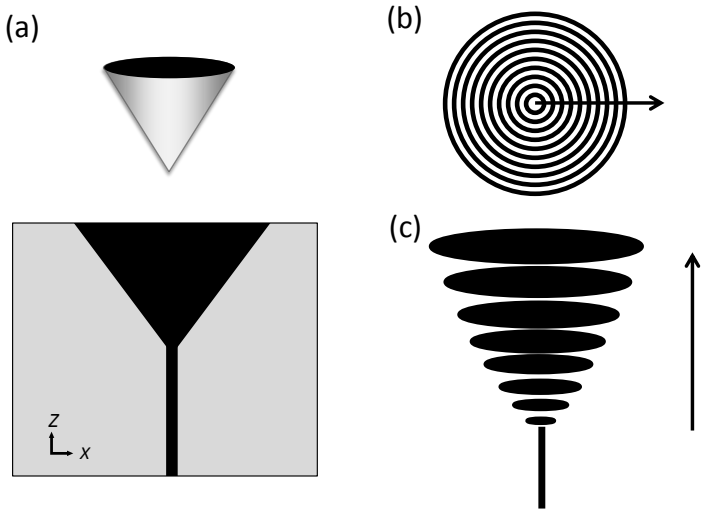

Figure 10.2: The sketch illustrating the whole volume fabrication for the funnels. (a) Side view of the coverslip with the proposed fabricated area shown in black region. The whole volume of cone is presented at the top. (b) Sketch illustrating of the fabrication in one single depth. A 2D circular (or rectangular) area was fabricated by a number of circles (or rectangles) with increments of radius. (c) The whole volume of the funnel was fabricated by a number of 2D circular area (or rectangular area) with increasing radius and decreasing depth. Arrow marks the fabrication sequence.

The fabrication process is presented in Figure 10.2 (b) and (c). The pillar was fabricated with the same procedure as described in the previous subsection. The cone structure was in fact constructed by a number of processed 2D circular areas (or rectangular areas) at different depths. Figure 10.2 (b) illustrates the fabrication process for each 2D area at one specific depth. A number of circles (or rectangles) with different radii were fabricated in sequence to form the circular area. The arrow in the sketch shows the fabrication direction. As shown in Figure 10.2 (c), these 2D circular areas were fabricated for each depth with a continuous increment of radius. Finally, the cone structure was constructed by a number of 2D circular areas with increasing radius and decreasing depth. While this method would enhance the etching efficiency, it, however, significantly increased the laser processing time which has a

linear proportional relationship with the volume of the structure. The significant consumption of the processing time may be dissolved in the future by adopting the parallel fabrication [90], or widefield temporal focusing (Chapter 3).

In the fabrication of the whole volume, a relatively higher translating speed of the laser focus was used to increase the efficiency. The fabrication of the circles was with speed of 150 μm/s, and fabrication power of 4.2 μJ. During the fabrication of each 2D circular area at one specific depth, the radius increment for each circle was 2 μm. The depth step along the axial direction to form the 3D funnel structure was also 2 μm increment for each 2D circular area. These increments in the fabrication step were determined by the fabrication power and speed. With either smaller fabrication speed, or larger laser power, the distance increment could be larger. Take an example for the funnel with 57° angle (Figure 10.1) or 45 μm height, there were 23 different fabrication depths. For the whole volume of the cone structure, 210 circles were fabricated.

4.3 Results after etching

Shown in Figure 10.1, the funnels with different angles have different heights. The heights for funnels with angles of 45°, 57° and 72° are 36 μm, 45 μm and 78 μm, respectively. We therefore differ the time for the etching according to the height of funnels. In this way, funnels with larger height need longer time, while funnels with smaller height require shorter time. The time range for the etching was set to be within 20 - 50 mins.

The SEM images after the etching process are shown in Figure 10.3. It is seen that the funnels have been completely etched through, and there is no remaining glass cone inside, even for the one with the largest cone angle (72°). The side wall of the funnels is rougher than the surface of the glass. Methods to further smoothen the side wall are: 1) reduce the fabrication speed, however with a sacrifice of the fabrication time; 2) anneal the sample after etching process.

4.4 Surface ablation

As discussed in the previous subsection, there is a trade-off between the etching time for funnels and the pillar. To maintain a small size for the pore, the etching time should be as short as possible. An additional way to further reduce the etching time is to do surface

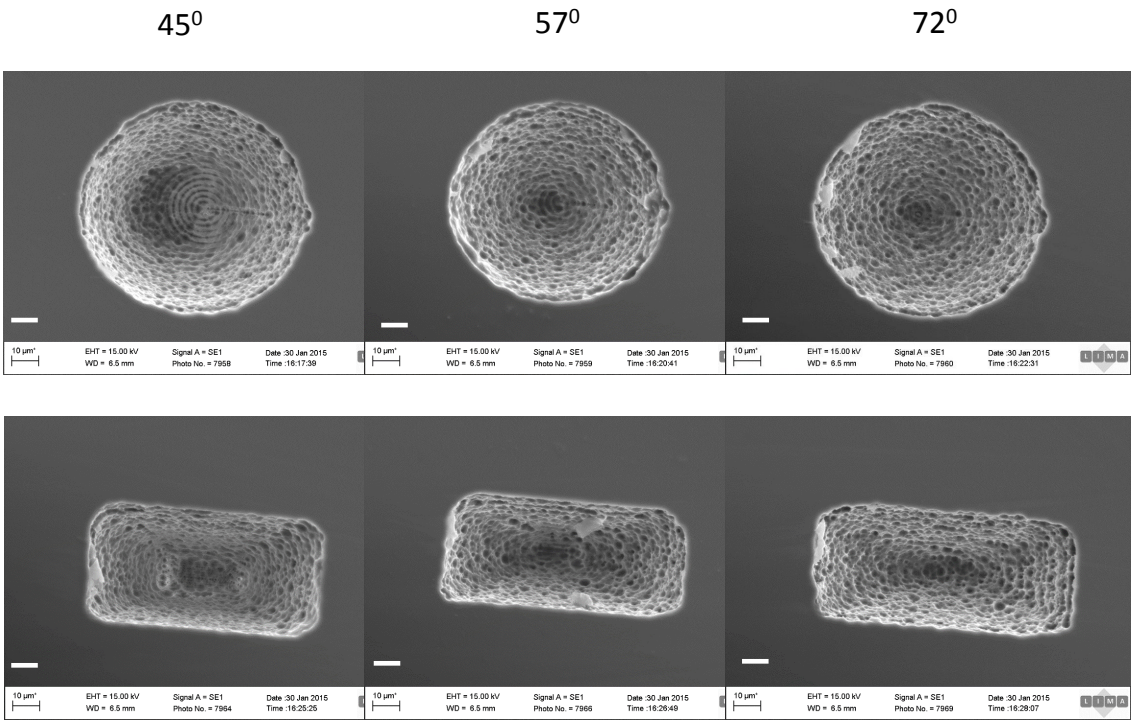

Figure 10.3: The scanning electron microscope (SEM) images of the coverslip etched by 1% hydrofluoric acid (HF). The circular and rectangular funnels were fabricated with the whole volume. Angles on the top represent the size of the funnel (refer to Figure 10.1). The scale bars in all the images represent 10 μm distance.

ablation. This process was conducted after the fabrication of the whole volume. During the ablation, the fabrication sequence was reversed, thereby the 2D circular (or rectangular) area was still fabricated for each depth, but the fabrication sequence was conducted from lower depth to higher depth (opposite to the direction marked by the arrow shown in Figure 10.2 (c)). The ablation was conducted with a higher laser power, so that the glass in the ablated area was completely broken down, becoming small debris and falling outside the funnel. Surface ablation could only be efficient in lower depth area. In our fabrication, the funnel was ablated to around 20 μm beneath the top surface.

Figure 10.4 illustrates the advantage of surface ablation. In (a), the funnel was ablated after the fabrication of the whole volume. The time to completely etch through was 20 mins. In comparison, the image in (b) shows that the funnel was not ablated after the fabrication of the whole volume, while the time needed for the full etching was 50 mins. It is clearly seen that less time was needed for the one conducted with an additional surface ablation process.

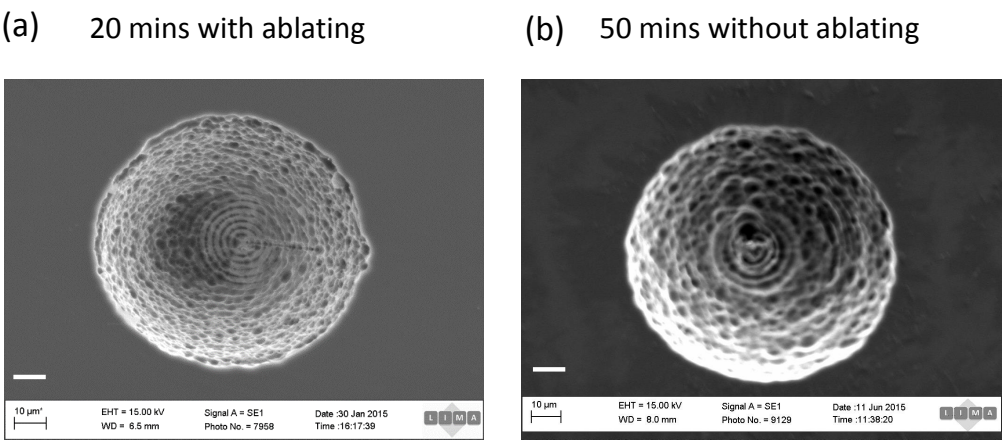

Figure 10.4: The scanning electron microscope (SEM) images of the etched coverslip. (a) The funnel was ablated after the fabrication of the whole volume. Etching time was 20 mins. (b) The funnel was without the ablation process after the fabrication of the whole volume. Etching time was 50 mins. The scale bars in both the images represent 10 μm.

5. Junction between the funnel and channel

The ultimate target is to create a 3D structure that can allow a cell to grow through the funnel and channel, reaching the other side of the coverslip. Therefore, it is also important to make sure that the junction between the funnel and the channel is etched through. In previous images, it is noticeable that most of the junctions were still filled with glass.

In the etching process, the junction was a final part to be reached by the acid, as its position is usually in the middle of the coverslip. Therefore, it was considered as the most difficult step. In our fabrication, we used an improved set-up to increase the possibility that the junction part could be fully etched. After the fabrication of the pillar, the laser power was raised to a much higher level, while the fabrication speed was reduced to a small value. As a result, the glass in the junction area was exposed under a high laser power for a long time. This set-up allowed the junction part to be more processed by the laser than any other area. Figure 10.5 shows the difference with the etching results. The images in (a) presents the process that the junction part was fabricated with the same parameter as the fabrication of the funnel, while in (b), the junctions were fabricated with much higher power and lower speed. All the funnels were etched with the same time duration. Dark holes are seen in the center of the funnels for Figure 10.5 (b), but not for (a), indicating that hollow junctions were more readily formed when a different fabrication procedure was used.

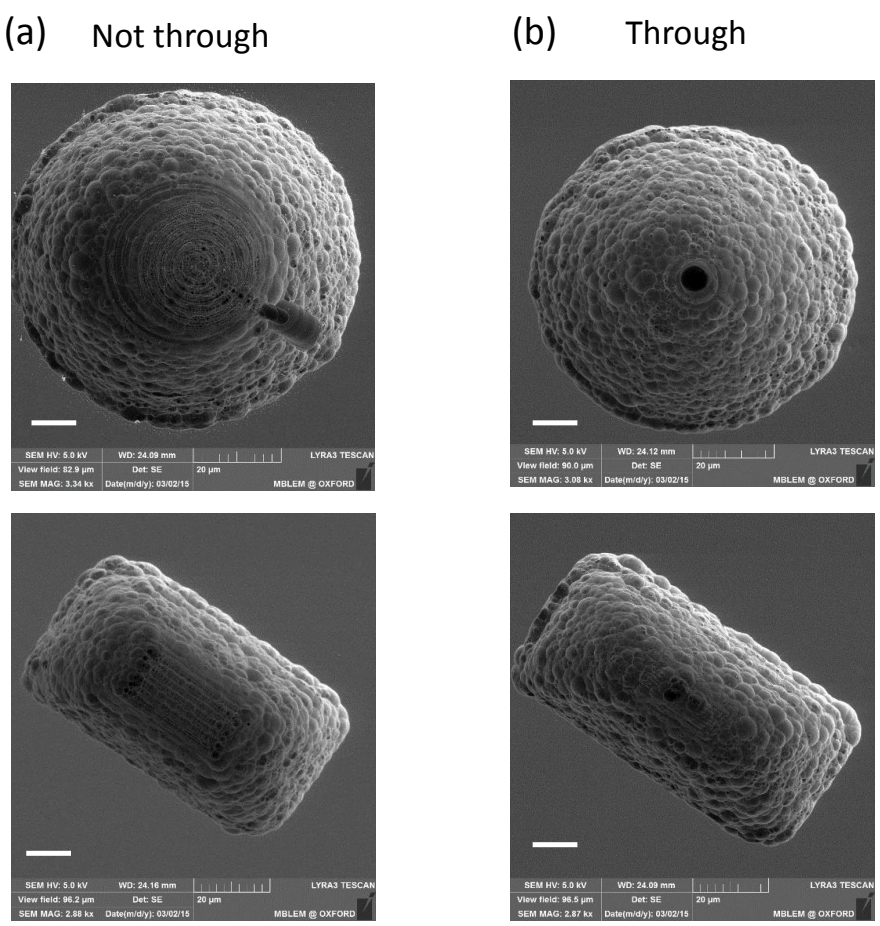

Figure 10.5: The scanning electron microscope (SEM) images of the etched coverslip. (a) The funnel and junction part were fabricated with the same parameter. (b) The junction part was fabricated with higher power and slower speed. The scale bars in all the images represent 10 μm.

6. Laser power and fabrication speed

The fabrication with a higher laser power and low translating speed creates more disruption of the glass structure, thus reducing the etching time and increasing the size of the etched area. Therefore, we would use a small power and high speed in the fabrication at the end of the pillar, relative higher power in the fabrication of the funnel and even higher power and lower speed in the fabrication of junction and pillar. Table 10.1 summarizes the laser power and fabrication speed used for the fabrication of different parts.

There are always trade-offs in choosing the fabrication parameters. For example, a higher fabrication speed is usually desired, as it leads to decreased fabrication time. On the other hand, a low fabrication speed is useful to reduce the surface roughness of the funnel wall after

Table 10.1: The laser power and fabrication speed for different parts of the structure.

Fabricated parts	Pulse energy (μJ)	Speed (μm/s)
Ablation	6.5	150
Funnel	4.2	150
Junction & Pillar	6.5	10
End of Pillar	0.12	100

etching. For another example, to further reduce the etching time, one approach is to reduce the step increments for the radius of circles and 2D areas. However, this is with a sacrifice of the fabrication efficiency, as much more number of circles have to be fabricated.

7. Conclusions

In this chapter, the 3D structure with circular and rectangular funnels connected with straight channels were designed and fabricated for the application in biology research. The method of fabrication of the side wall made it difficult to fully etch through the funnel. The method of fabricating the whole volume cost more time, but improved the etching process. The fabrication parameters such as the fabrication speed, laser power and etching time significantly affect the quality of the 3D structure. The relative influences are discussed in detail. With the powerful ultrafast laser processing technique, more complex 3D structures can be enabled for various biomedical researches.

As the thickness of the silica glass is small, the refractive index mismatch aberration is not significant for the fabrication discussed in this chapter. Therefore, the adaptive optics method was not used in this case. For the future 3D fabrication either with a larger depth or with a high NA objective lens, the adaptive optics will be useful to further increase the quality of microstrucures.

References

[1] P. M. W. French, "The generation of ultrashort laser pulses," Reports on Progress in Physics **58**, 169–262 (1999).

[2] L. E. Hargrove, R. L. Fork, and M. A. Pollack, "Locking of hene laser modes induced by synchronous intracavity modulation," Applied Physics Letters **5**, 4–5 (1964).

[3] F. Krausz, M. E. Fermann, T. Brabec, P. F. Curley, M. Hofer, M. H. Ober, C. Spielmann, E. Wintner, and A. J. Schmidt, "Femtosecond solid-state lasers," IEEE Journal of Quantum Electronics **28**, 2097–2122 (1992).

[4] O. G. Peterson, S. A. Tuccio, and B. B. Snavely, "CW Operation of an Organic Dye Solution Laser," Applied Physics Letters **17**, 245–247 (1970).

[5] E. P. Ippen, C. V. Shank, and A. Dienes, "Passive mode locking of the cw dye laser," Applied Physics Letters **21**, 348–350 (1972).

[6] L. F. Mollenauer and R. H. Stolen, "The soliton laser," Optics letters **9**, 13–15 (1984).

[7] H. Coles and S. Morris, "Liquid-crystal lasers," Nature Photonics **4**, 676–685 (2010).

[8] A. D. Ford, S. M. Morris, and H. J. Coles, "Photonics and lasing in liquid crystals," Materials Today **9**, 36–42 (2006).

[9] D. J. Gardiner, S. M. Morris, P. J. W. Hands, C. Mowatt, R. Rutledge, T. D. Wilkinson, and H. J. Coles, "Paintable band-edge liquid crystal lasers," Optics express **19**, 2432–2439 (2011).

[10] A. E. Siegman, *Lasers* (University Science Books, 1986).

[11] J. Catherall and G. New, "Role of spontaneous emission in the dynamics of mode locking by synchronous pumping," IEEE Journal of Quantum Electronics **22**, 1593–1599 (1986).

[12] U. Stamm, "Numerical Analysis of Pulse Generation in Synchronously Mode-Locked cw Dye Lasers," Appl. Phys. B **45**, 101–108 (1988).

[13] G. Steinmeyer, "Frontiers in Ultrashort Pulse Generation: Pushing the Limits in Linear and Nonlinear Optics," Science **286**, 1507–1512 (1999).

[14] T. Brabec and F. Krausz, "Intense few-cycle laser fields: Frontiers of nonlinear optics," Reviews of Modern Physics **72**, 545–591 (2000).

[15] N. Bloembergen, "A brief history of light breakdown," J. Nonlinear Opt. Phys. **6**, 377–385 (1997).

[16] J. Kruger and W. Kautek, *Polymers and Light* (Springer, Berlin, 2004).

[17] F. Dausinger, F. Lichtner, and H. Lubatschowski, *Femtosecond Technology for Technical and Medical Applications* (Springer, Berlin, 2004).

[18] G. D. Valle, R. Osellame, P. Laporta, G. Della Valle, R. Osellame, P. Laporta, and G. D. Valle, "Micromachining of photonic devices by femtosecond laser pulses," Journal of Optics A: Pure and Applied Optics **11**, 049801 (2009).

[19] M. Beresna and P. G. Kazansky, "Ultrafast laser direct writing and nanostructuring in transparent materials," Advances in Optics and Photonics **339**, 293–339 (2014).

[20] S. Maruo and J. T. Fourkas, "Recent progress in multiphoton microfabrication," Laser and Photonics Reviews **2**, 100–111 (2008).

[21] R. Narayan and P. Goering, "Laser micro- and nanofabrication of biomaterials," MRS Bulletin **36**, 973–982 (2011).

[22] R. Srinivasan, E. Sutcliffe, and B. Braren, "Ablation and etching of polymethylmethacrylate by very short (160 fs) ultraviolet (308 nm) laser pulses," Applied Physics Letters **51**, 1285–1287 (1987).

[23] S. Küper and M. Stuke, "Femtosecond uv excimer laser ablation," Applied Physics B Photophysics and Laser Chemistry **44**, 199–204 (1987).

[24] D. Du, X. Liu, G. Korn, J. Squier, and G. Mourou, "Laser-induced breakdown by impact ionization in SiO2 with pulse widths from 7 ns to 150 fs," Applied Physics Letters **64**, 3071–3073 (1994).

[25] P. Pronko, S. Dutta, J. Squier, J. Rudd, D. Du, and G. Mourou, "Machining of submicron holes using a femtosecond laser at 800 nm," Optics Communications **114**, 106–110 (1995).

[26] K. M. Davis, K. Miura, N. Sugimoto, and K. Hirao, "Writing waveguides in glass with a femtosecond laser." Optics letters **21**, 1729–1731 (1996).

[27] A. G. Okhrimchuk, A. V. Shestakov, I. Khrushchev, and J. Mitchell, "Depressed cladding, buried waveguide laser formed in a YAG:Nd3+ crystal by femtosecond laser writing." Optics letters **30**, 2248–2250 (2005).

[28] S. Maruo, O. Nakamura, and S. Kawata, "Three-dimensional microfabrication with two-photon-absorbed photopolymerization." Optics letters **22**, 132–134 (1997).

[29] S. Juodkazis, V. Mizeikis, K. K. Seet, M. Miwa, and H. Misawa, "Two-photon lithography of nanorods in SU-8 photoresist," Nanotechnology **16**, 846–849 (2005).

[30] M. F. Yanik, H. Cinar, H. N. Cinar, A. D. Chisholm, Y. Jin, and A. Ben-Yakar, "Neurosurgery: functional regeneration after laser axotomy." Nature **432**, 822 (2004).

[31] R. R. Gattass and E. Mazur, "Femtosecond laser micromachining in transparent materials," Nature Photonics **2**, 219–225 (2008).

[32] V. S. Zapasskii, "Spin-noise spectroscopy: from proof of principle to applications," Advances in Optics and Photonics **5**, 131 (2013).

[33] B. C. Stuart, M. D. Feit, A. M. Rubenchik, B. W. Shore, and M. D. Perry, "Laser-Induced Damage in Dielectrics with Nanosecond to Subpicosecond Pulses," Physical Review Letters **73**, 1919–1922 (1994).

[34] A. P. Joglekar, H.-H. Liu, E. Meyhöfer, G. Mourou, and A. J. Hunt, "Optics at critical intensity: applications to nanomorphing," P. Natl. Acad. Sci. USA **101**, 5856–61 (2004).

[35] P. Weinberger, "John Kerr and his effects found in 1877 and 1878," Philosophical Magazine Letters **88**, 897–907 (2008).

[36] E. Cumberbatch, "Self-focusing in Non-linear Optics," J. Inst. Maths Applics **6**, 250–262 (1970).

[37] R. Y. Chiao, E. Garmire, and C. H. Townes, "Self-trapping of optical beams," Phys. Rev. Lett. **13**, 479 (1964).

[38] R. Y. Chiao, T. K. Gustafson, and P. L. Kelley, "Self-focusing of optical beams," Topics in Applied Physics **114**, 129–143 (2009).

[39] P. Lallemand and N. Bloembergen, "Self-focusing of laser beams and stimulated raman gain in liquids.pdf," Phys. Rev. Lett. **15** (1965).

[40] A. Couairon and A. Mysyrowicz, "Femtosecond filamentation in transparent media," Physics Reports **441**, 47–189 (2007).

[41] Y. Shimotsuma, P. G. Kazansky, J. R. Qiu, and K. Hirao, "Self-organized nanogratings in glass irradiated by ultrashort light pulses," Phys. Rev. Lett. **91**, 247405 (2003).

[42] E. N. Glezer, M. Milosavljevic, L. Huang, R. J. Finlay, T. H. Her, J. P. Callan, and E. Mazur, "Three-dimensional optical storage inside transparent materials." Optics letters **21**, 2023–2025 (1996).

[43] C. Hnatovsky, R. S. Taylor, P. P. Rajeev, E. Simova, V. R. Bhardwaj, D. M. Rayner, and P. B. Corkum, "Pulse duration dependence of femtosecond-laser-fabricated nanogratings in fused silica," Applied Physics Letters **87**, 98–101 (2005).

[44] S. Onda, W. Watanabe, K. Yamada, K. Itoh, and J. Nishii, "Study of filamentary damage in synthesized silica induced by chirped femtosecond laser pulses," Journal of the Optical Society of America B **22**, 2437 (2005).

[45] K. Miura, J. Qiu, H. Inouye, T. Mitsuyu, and K. Hirao, "Photowritten optical waveguides in various glasses with ultrashort pulse laser," Applied Physics Letters **71**, 3329 – 3331 (1997).

[46] Y. Nasu, M. Kohtoku, and Y. Hibino, "Low-loss waveguides written with a femtosecond laser for flexible interconnection in a planar light-wave circuit," Opt. Lett. **30**, 723–725 (2005).

[47] J. B. Spring, P. S. Salter, B. J. Metcalf, C. Peter, M. Moore, N. Thomas-peter, X.-m. Jin, N. K. Langford, W. Steven, M. J. Booth, and I. A. Walmsley, "On-chip low loss heralded source of pure single photons," Optics express **21**, 5932–5935 (2013).

[48] P. C. Humphreys, B. J. Metcalf, J. B. Spring, M. Moore, P. S. Salter, M. J. Booth, W. S. Kolthammer, and I. a. Walmsley, "Strain-optic active control for quantum integrated photonics," Arxiv preprint arXiv:1405.2694 **22**, 7 (2014).

[49] G. D. Marshall, A. Politi, J. C. F. Matthews, P. Dekker, M. Ams, M. J. Withford, and J. L. OBrien, "Laser written waveguide photonic quantum circuits," Opt. Express **17**, 12546–12554 (2009).

[50] T. Gorelik, M. Will, S. Nolte, a. Tuennermann, and U. Glatzel, "Transmission electron microscopy studies of femtosecond laser induced modifications in quartz," Applied Physics A: Materials Science & Processing **76**, 309–311 (2003).

[51] V. Apostolopoulos, L. Laversenne, T. Colomb, C. Depeursinge, R. P. Salathé, M. Pollnau, R. Osellame, G. Cerullo, and P. Laporta, "Femtosecond-irradiation-induced refractive-index changes and channel waveguiding in bulk Ti3+: Sapphire," Applied Physics Letters **85**, 1122–1124 (2004).

[52] A. Baum, P. J. Scully, M. Basanta, C. L. P. Thomas, P. R. Fielden, N. J. Goddard, W. Perrie, and P. R. Chalker, "Photochemistry of refractive index structures in poly(methyl methacrylate) by femtosecond laser irradiation." Optics letters **32**, 190–192 (2007).

[53] Y. Cheng, K. Sugioka, and K. Midorikawa, "Freestanding optical fibers fabricated in a glass chip using femtosecond laser micromachining for lab-on-a-chip application," Opt Express **13**, 7225–7232 (2005).

[54] A. Schaap, T. Rohrlack, and Y. Bellouard, "Lab on a chip technologies for algae detection: A review," Journal of Biophotonics **5**, 661–672 (2012).

[55] B. Lenssen and Y. Bellouard, "Optically transparent glass micro-actuator fabricated by femtosecond laser exposure and chemical etching," Applied Physics Letters **101**, 1–5 (2012).

[56] C. Corbari, A. Champion, M. Gecevicius, M. Beresna, Y. Bellouard, and P. G. Kazansky, "Femtosecond versus picosecond laser machining of nano-gratings and microchannels in silica glass," Opt Express **21**, 3946–3958 (2013).

[57] V. Tielen and Y. Bellouard, "Three-Dimensional Glass Monolithic Micro-Flexure Fabricated by Femtosecond Laser Exposure and Chemical Etching," Micromachines **5**, 697–710 (2014).

[58] R. Drevinskas, M. Gecevičius, M. Beresna, Y. Bellouard, and P. G. Kazansky, "Tailored surface birefringence by femtosecond laser assisted wet etching," Optics Express **23**, 1428 (2015).

[59] V. I. Konov, "Laser in micro and nanoprocessing of diamond materials," Laser Photonics Rev. **6**, 739–766 (2012).

[60] A. Oh, B. Caylar, M. Pomorski, and T. Wengler, "A novel detector with graphitic electrodes in CVD diamond," Diam. Relat. Mater. **38**, 9–13 (2013).

[61] S. Lagomarsino, M. Bellini, C. Corsi, F. Gorelli, G. Parrini, M. Santoro, and S. Sciortino, "Three-dimensional diamond detectors: Charge collection efficiency of graphitic electrodes," Appl. Phys. Lett. **103**, 233507 (2013).

[62] M. Shimizu, Y. Shimotsuma, M. Sakakura, T. Yuasa, H. Homma, Y. Minowa, K. Tanaka, K. Miura, and K. Hirao, "Periodic metallo-dielectric structure in diamond," Opt. Express **17**, 46–54 (2009).

[63] J. A. Kubby, *Adaptive Optics for Biological Imaging* (FL: CRC Press, Boca Raton, 2013).

[64] J. W. Hardy, *Adaptive Optics for Astronomical Telescopes* (Oxford University Press, New York, 1998).

[65] J. Liang, D. R. Williams, and D. T. Miller, "Supernormal vision and high-resolution retinal imaging through adaptive optics." Journal of the Optical Society of America. A, Optics, image science, and vision **14**, 2884–2892 (1997).

[66] M. J. Booth, "Adaptive optics in microscopy," Philosophical Transactions Of The Royal Society A **365**, 2829–2843 (2007).

[67] G. D. Love, "Wave-front correction and production of Zernike modes with a liquid-crystal spatial light modulator," Applied optics **36**, 1517–1520 (1997).

[68] P. M. Birch, J. Gourlay, G. D. Love, and A. Purvis, "Real-time optical aberration correction with a ferroelectric liquid-crystal spatial light modulator," Applied optics **37**, 2164–2169 (1998).

[69] A. M. Weiner, "Femtosecond pulse shaping using spatial light modulators," Review of Scientific Instruments **71**, 1929–1960 (2000).

[70] V. Nikolenko, D. S. Peterka, R. Araya, A. Woodruff, and R. Yuste, "Spatial light modulator microscopy," Cold Spring Harbor Protocols **2013**, 1132–1141 (2013).

[71] B. Xu, J. M. Gunn, J. M. D. Cruz, V. V. Lozovoy, and M. Dantus, "Quantitative investigation of the multiphoton intrapulse interference phase scan method for simultaneous phase measurement and compensation of femtosecond laser pulses," Journal of the Optical Society of America B **23**, 750 (2006).

[72] "http://www.hamamatsu.com/jp/en/X10468-02.html," .

[73] F. Druon, G. Chériaux, J. Faure, J. Nees, M. Nantel, A. Maksimchuk, G. Mourou, J. C. Chanteloup, and G. Vdovin, "Wave-front correction of femtosecond terawatt lasers by deformable mirrors," Optics letters **23**, 1043–1045 (1998).

[74] E. Zeek, K. Maginnis, S. Backus, U. Russek, M. Murnane, G. Mourou, H. Kapteyn, and G. Vdovin, "Pulse compression by use of deformable mirrors," Optics letters **24**, 493–495 (1999).

[75] E. Zeek, R. Bartels, M. M. Murnane, H. C. Kapteyn, S. Backus, and G. Vdovin, "Adaptive pulse compression for transform-limited 15-fs high-energy pulse generation," Optics letters **25**, 587–589 (2000).

[76] "http://www.imagine-optic.com/en/product/mirao-52-e/0/0/," .

[77] D. Dagel, W. Cowan, O. Spahn, G. Grossetete, A. Grine, M. Shaw, P. Resnick, and B. Jokiel, "Large-stroke MEMS deformable mirrors for adaptive optics," J. Microelectromechanical Systems **15**, 572–583 (2006).

[78] T. Bifano, J. Perreault, R. Krishnamoorthy Mali, and M. Horenstein, "Microelectromechanical deformable mirrors," IEEE J. Selected Topics in Quantum Electronics **5**, 83–89 (1999).

[79] S. Bonora and L. Poletto, "Push-pull membrane mirrors for adaptive optics." Optics express **14**, 11935–11944 (2006).

[80] A. N. Simonov, S. Hong, and G. Vdovin, "Piezoelectric deformable mirror with adaptive multiplexing control," Optical Engineering **45**, 070501 (2006).

[81] J. C. Dainty, A. V. Koryabin, and A. V. Kudryashov, "Low-order adaptive deformable mirror," Applied Optics **37**, 4663–4668 (1998).

[82] E. J. Fern, L. Vabre, B. Hermann, A. Unterhuber, B. Pova, and W. Drexler, "Adaptive optics with a magnetic deformable mirror: applications in the human eye," Optics Express **14**, 631–643 (2006).

[83] G. Vdovin and M. Loktev, "Deformable mirror with thermal actuators," Optics Letters **27**, 677–679 (2002).

[84] E. M. Vuelban, N. Bhattacharya, and J. J. M. Braat, "Liquid deformable mirror for high-order wavefront correction." Optics letters **31**, 1717–1719 (2006).

[85] P. Laird, N. Caron, M. Rioux, E. F. Borra, and A. Ritcey, "Ferrofluidic adaptive mirrors," Applied Optics **45**, 3495–3500 (2006).

[86] K. Chaen, H. Takahashi, S. Hasegawa, and Y. Hayasaki, "Display method with compensation of the spatial frequency response of a liquid crystal spatial light modulator for holographic femtosecond laser processing," Optics Communications **280**, 165–172 (2007).

[87] S. Hasegawa and Y. Hayasaki, "Holographic femtosecond laser processing with multiplexed phase fresnel lenses," Optics Letters **31**, 1705–1707 (2006).

[88] Z. Kuang, W. Perrie, J. Leach, M. Sharp, S. P. Edwardson, M. Padgett, G. Dearden, and K. G. Watkins, "High throughput diffractive multi-beam femtosecond laser processing using a spatial light modulator," Applied Surface Science **255**, 2284–2289 (2008).

[89] A. Jesacher, G. D. Marshall, T. Wilson, and M. J. Booth, "Adaptive optics for direct laser writing with plasma emission aberration sensing," Optics Express **18**, 656–661 (2010).

[90] A. Jesacher and M. J. Booth, "Parallel direct laser writing in three dimensions with spatially dependent aberration correction," Opt. Express **18**, 21090–21099 (2010).

[91] P. S. Salter and M. J. Booth, "An addressable microlens array for parallel laser microfabrication," Opt. Lett. **36**, 2302–2304 (2011).

[92] G. Zhou, A. Jesacher, M. Booth, T. Wilson, A. Ródenas, D. Jaque, and M. Gu, "Axial birefringence induced focus splitting in lithium niobate," Optics express **17**, 2783–2785 (2009).

[93] R. D. Simmonds, P. S. Salter, A. Jesacher, and M. J. Booth, "Three dimensional laser microfabrication in diamond using a dual adaptive optics system," Opt. Express **19**, 24122–24128 (2011).

[94] P. S. Salter, A. Jesacher, J. B. Spring, B. J. Metcalf, and R. D. Simmonds, "Adaptive slit beam shaping for direct laser written waveguides," Opt. Lett. **37**, 470–472 (2012).

[95] M. Gu, *Advanced optical imaging theory* (Springer Science & Business Media, 2000).

[96] E. Hecht and A. Zajac, *Optics* (Addison Wesley, San Francisco, CA, 2002).

[97] Y. M. Engelberg and S. Ruschin, "Fast method for physical optics propagation of high-numerical-aperture beams," Journal Of The Optical Society Of America A **21**, 2135–2145 (2004).

[98] A. Lipson, S. G. Lipson, and H. Lipson, *Optical Physics* (Cambridge University Press, 2010).

[99] G. Zhu, J. van Howe, M. Durst, W. Zipfel, and C. Xu, "Simultaneous spatial and temporal focusing of femtosecond pulses," Opt. Express **13**, 2153–2159 (2005).

[100] M. E. Durst, G. Zhu, and C. Xu, "Simultaneous Spatial and Temporal Focusing in Nonlinear Microscopy," Optics communications **281**, 1796–1805 (2008).

[101] D. Oron and Y. Silberberg, "Harmonic generation with temporally focused ultrashort pulses," J. Opt. Soc. Am. A **22**, 2660–2663 (2005).

[102] D. Oron and Y. Silberberg, "Spatiotemporal coherent control using shaped, temporally focused pulses," Optics Express **13**, 9903–9908 (2005).

[103] D. Oron, E. Tal, and Y. Silberberg, "Scanningless depth-resolved microscopy," Optics express **13**, 1468–1476 (2005).

[104] E. Tal, D. Oron, and Y. Silberberg, "Improved depth resolution in video-rate line-scanning multiphoton microscopy using temporal focusing," Optics Letters **30**, 1686 (2005).

[105] M. E. Durst, G. Zhu, and C. Xu, "Simultaneous spatial and temporal focusing for axial scanning," Optics express **14**, 12243–54 (2006).

[106] A. Vaziri, J. Tang, H. Shroff, and C. V. Shank, "Multilayer three-dimensional super resolution imaging of thick biological samples." Proceedings of the National Academy of Sciences of the United States of America **105**, 20221–20226 (2008).

[107] E. Papagiakoumou, V. de Sars, D. Oron, and V. Emiliani, "Patterned two-photon illumination by spatiotemporal shaping of ultrashort pulses," Optics express **16**, 22039–22047 (2008).

[108] E. Papagiakoumou, V. de Sars, V. Emiliani, and D. Oron, "Temporal focusing with spatially modulated excitation," Optics express **17**, 5391–5401 (2009).

[109] E. Y. S. Yew, C. J. R. Sheppard, and P. T. C. So, "Temporally focused wide-field two-photon microscopy : Paraxial to vectorial," Opt. Express **21**, 19645–19655 (2013).

[110] F. He, H. Xu, Y. Cheng, J. Ni, H. Xiong, Z. Xu, K. Sugioka, and K. Midorikawa, "Fabrication of microfluidic channels with a circular cross section using spatiotemporally focused femtosecond laser pulses," Opt. Lett. **35**, 1106–1108 (2010).

[111] D. N. Vitek, E. Block, Y. Bellouard, D. E. Adams, S. Backus, D. Kleinfeld, C. G. Durfee, J. A. Squier, A. Johnson, and P. S. Tsai, "Spatio-temporally focused femtosecond laser pulses for nonreciprocal writing in optically transparent materials," Opt. Express **18**, 24673–24678 (2010).

[112] D. N. Vitek, D. E. Adams, A. Johnson, P. S. Tsai, S. Backus, C. G. Durfee, D. Kleinfeld, and J. A. Squier, "Temporally focused femtosecond laser pulses for low numerical aperture micromachining through optically transparent materials," Optics express **18**, 18086–94 (2010).

[113] D. Kim and P. T. C. So, "High-throughput three-dimensional lithographic microfabrication," Optics letters **35**, 1602–1604 (2010).

[114] Y.-C. Li, L.-C. Cheng, C.-Y. Chang, C.-H. Lien, P. J. Campagnola, and S.-J. Chen, "Fast multiphoton microfabrication of freeform polymer microstructures by spatiotemporal focusing and patterned excitation," Optics express **20**, 19030–19038 (2012).

[115] R. Stoian, J. P. Colombier, C. Mauclair, G. Cheng, M. K. Bhuyan, P. K. Velpula, and P. Srisungsitthisunti, "Spatial and temporal laser pulse design for material processing on ultrafast scales," Applied Physics A **114**, 119–127 (2013).

[116] M. Born and E. Wolf, *Principles of Optics* (Cambridge University, 2010), 6th ed.

[117] M. J. Booth, M. A. A. Neil, and T. Wilson, "Aberration correction for confocal imaging in refractive-index-mismatched media," Journal of Microscopy **192**, 90–98 (1998).

[118] R. L. Fork, C. H. B. Cruz, P. C. Becker, and C. V. Shank, "Compression of optical pulses to six femtoseconds by using cubic phase compensation," Optics Letters **12**, 483–485 (1988).

[119] A. Stingl, M. Lenzner, C. Spielmann, and F. Krausz, "Sub-10-fs mirror-dispersion-controlled Ti : sapphire laser," Optics Letters **20**, 602–604 (1995).

[120] Z. Wei, M. S. Pshenichnikov, and D. A. Wiersma, "Optical pulse compression to 5 fs at a 1-MHz repetition rate," Optics Letters **22**, 102–104 (1997).

[121] N. A. Papadogiannis, B. Witzel, C. Kalpouzos, and D. Charalambidis, "Observation of Attosecond Light Localization in Higher Order Harmonic Generation," Physical Review Letters **1**, 4289–4292 (1999).

[122] P. Agostini and L. F. DiMauro, "The physics of attosecond light pulses," Reports on Progress in Physics **67**, 813–855 (2004).

[123] Z. Bor, "Distortion of femtosecond laser pulses in lenses and lens systems," Journal of Modern Optics **35**, 1907–1918 (1988).

[124] S. Akturk, M. Kimmel, P. O'Shea, and R. Trebino, "Measuring pulse-front tilt in ultrashort pulses using GRENOUILLE." Optics express **11**, 491–501 (2003).

[125] P. S. Salter and M. J. Booth, "Dynamic control of directional asymmetry observed in ultrafast laser direct writing," Applied Physics Letters **141109**, 1–4 (2012).

[126] S. Akturk, X. Gu, E. Zeek, and R. Trebino, "Pulse-front tilt caused by spatial and temporal chirp," Opt. Express **12**, 4399–4410 (2004).

[127] P. Torok, P. Varga, Z. Laczik, G. R. Booker, P. Török, P. Varga, Z. Laczik, and G. R. Booker, "Electromagnetic diffraction of light focused through a planar interface between materials of mismatched refractive indices: an integral representation," J. Opt. Soc. Am. A **12**, 325 (1995).

[128] U. Fuchs, U. D. Zeitner, and A. Tünnermann, "Ultra-short pulse propagation in complex optical systems," Opt. Express **13**, 3852–3861 (2005).

[129] D. E. Zelmon, D. L. Small, and D. Jundt, "Infrared corrected Sellmeier coefficients for congruently grown lithium niobate and 5 mol.% magnesium oxide doped lithium niobate," Journal of the Optical Society of America B **14**, 3319 (1997).

[130] P. Ferraro, S. Grilli, and P. D. Natale, *Ferroelectric Crystals for Photonic Applications* (Springer Series in Materials Science, 2009).

[131] M. Daimon and A. Masumura, "Measurement of the refractive index of distilled water from the near-infrared region to the ultraviolet region," Applied Optics **46**, 3811 (2007).

[132] S. Kedenburg, M. Vieweg, T. Gissibl, and H. Giessen, "Linear refractive index and absorption measurements of nonlinear optical liquids in the visible and near-infrared spectral region," Optical Materials Express **2**, 1588 (2012).

[133] I. H. Malitson, "Interspecimen Comparison of the Refractive Index of Fused Silica," J. Opt. Soc. Am. A **55** (1965).

[134] F. Peter, "Über Brechungsindizes und Absorptionskonstanten des Diamanten zwischen 644 und 226 mμ," Zeitschrift für Physik **15**, 358–368 (1923).

[135] I. Aharonovich, A. D. Greentree, and S. Prawer, "Diamond photonics," Nat. Photonics **5**, 397–405 (2011).

[136] A. Baltuška, Z. Wei, M. S. Pshenichnikov, D. A. Wiersma, and R. Szip, "All-solid-state cavity-dumped sub-5-fs laser," Applied Physics B **188**, 175–188 (1997).

[137] H. Dana, N. Kruger, A. Ellman, and S. Shoham, "Line temporal focusing characteristics in transparent and scattering media," Optics Express **21**, 5677–5687 (2013).

[138] R. L. Fork, O. E. Martinez, and J. P. Gordon, "Negative dispersion using pairs of prisms," Optics letters **9**, 150–2 (1984).

[139] J. D. Kafka and T. Baer, "Prism-pair dispersive delay lines in optical pulse compression," Optics letters **12**, 401–3 (1987).

[140] Glass, "http://refractiveindex.info/download/data/2012/schott_optical_glass_collection_datasheets_d
.

[141] Z. Bor, Z. Gogolak, and G. Szabo, "Femtosecond-resolution pulse-front distortion measurement by time-of-flight interferometry," Optics Letters **14**, 862–864 (1989).

[142] A. Federico and O. Martinez, "Distortion of femtosecond pulses due to chromatic aberration in lenses," Optics Communications **91**, 104–110 (1992).

[143] M. Kempe, U. Stamm, B. Wilhelmi, and W. Rudolph, "Spatial and temporal transformation of femtosecond laser pulses by lenses and lens systems," JOSA B **9**, 1158–1165 (1992).

[144] D. Yelin, D. Meshulach, and Y. Silberberg, "Adaptive femtosecond pulse compression," Optics letters **22**, 1793–1795 (1997).

[145] W. Amir, T. A. Planchon, C. G. Durfee, and J. A. Squier, "Complete characterization of a spatiotemporal pulse shaper with two-dimensional Fourier transform spectral interferometry," Optics letters **32**, 939–941 (2007).

[146] A. M. Weiner, "Ultrafast optical pulse shaping: A tutorial review," Optics Communications **284**, 3669–3692 (2011).

[147] R. Piestun and D. A. Miller, "Spatiotemporal control of ultrashort optical pulses by refractive-diffractive-dispersive structured optical elements," Optics letters **26**, 1373–1375 (2001).

[148] U. Fuchs, U. D. Zeitner, and A. Tünnermann, "Hybrid optics for focusing ultrashort laser pulses," Optics Letters **31**, 1516–1518 (2006).

[149] M. J. Booth, T. Wilson, H. Sun, T. Ota, and S. Kawata, "Methods for the characterization of deformable membrane mirrors," Applied Optics **44**, 5131–5139 (2005).

[150] T. A. Planchon, S. Ferré, G. Hamoniaux, G. Chériaux, and J.-P. Chambaret, "Experimental evidence of 25-fs laser pulse distortion in singlet beam expanders," Optics letters **29**, 2300–2302 (2004).

[151] Z. Bor, "Distortion of femtosecond laser pulses in lenses," Optics letters **14**, 119–121 (1989).

[152] M. Kempe and W. Rudolph, "Femtosecond pulses in the focal region of lenses," Physical review. A **48**, 4721–4729 (1993).

[153] S. Szatmári and G. Kühnle, "Pulse front and pulse duration distortion in refractive optics, and its compensation," Optics Communications **69**, 60–65 (1988).

[154] S.-W. Bahk, J. Bromage, and J. D. Zuegel, "Offner radial group delay compensator for ultra-broadband laser beam transport," Opt. Lett. **39**, 1081–1084 (2014).

[155] K. Wang, D. E. Milkie, A. Saxena, P. Engerer, T. Misgeld, M. E. Bronner, J. Mumm, and E. Betzig, "Rapid adaptive optical recovery of optimal resolution over large volumes," Nature methods **11**, 1–7 (2014).

[156] R. Netz, T. Feurer, R. Wolleschensky, and R. Sauerbrey, "Measurement of the pulse-front distortion in high-numerical-aperture optics," Applied Physics B **70**, 833–837 (2000).

[157] J. Jasapara and W. Rudolph, "Characterization of sub-10-fs pulse focusing with high-numerical-aperture microscope objectives," Optics letters **24**, 777–9 (1999).

[158] P. Bowlan, P. Gabolde, and R. Trebino, "Directly measuring the spatio-temporal electric field of focusing ultrashort pulses," Optics express **15**, 10219–30 (2007).

[159] M. K. Trubetskov, M. von Pechmann, I. B. Angelov, K. L. Vodopyanov, F. Krausz, and V. Pervak, "Measurements of the group delay and the group delay dispersion with resonance scanning interferometer," Optics express **21**, 6658–69 (2013).

[160] P. G. Kazansky, W. Yang, E. Bricchi, J. Bovatsek, A. Arai, Y. Shimotsuma, K. Miura, and K. Hirao, "Quill writing with ultrashort light pulses in transparent materials," Appl. Phys. Lett. **90**, 151120 (2007).

[161] W. Denk, J. H. Strickler, and W. W. Webb, "Two-Photon Laser Scanning Fluorescence Microscopy," Science **248**, 73–76 (1990).

[162] W. Amir, T. A. Planchon, C. G. Durfee, J. A. Squier, P. Gabolde, R. Trebino, and M. Müller, "Simultaneous visualization of spatial and chromatic aberrations by two-dimensional Fourier transform spectral interferometry," Optics letters **31**, 2927–9 (2006).

[163] P. Bowlan, U. Fuchs, R. Trebino, and U. D. Zeitner, "Measuring the spatiotemporal electric field of tightly focused ultrashort pulses with sub-micron spatial resolution," Optics express **16**, 13663–75 (2008).

[164] C. Radzewicz, M. la Grone, and J. Krasinski, "Interferometric measurement of femtosecond pulse distortion by lenses," Optics Communications **126**, 185–190 (1996).

[165] R. D. Simmonds, T. Wilson, and M. J. Booth, "Effects of aberrations and specimen structure in conventional, confocal and two-photon fluorescence microscopy," Journal of microscopy **245**, 63–71 (2012).

[166] B. Sun, P. S. Salter, and M. J. Booth, "Pulse front adaptive optics: a new method for control of ultrashort laser pulses," Optics Express **23**, 19348 (2015).

[167] D. Débarre, T. Vieille, and E. Beaurepaire, "Simple characterisation of a deformable mirror inside a high numerical aperture microscope using phase diversity." Journal of microscopy **244**, 136–143 (2011).

[168] D. Débarre, E. J. J. Botcherby, T. Watanabe, S. Srinivas, M. J. Booth, and T. Wilson, "Image-based adaptive optics for two-photon microscopy," Optics Letters **34**, 2495–2497 (2009).

[169] E. B. Kromann, T. J. Gould, M. F. Juette, J. E. Wilhjelm, and J. Bewersdorf, "Quantitative pupil analysis in stimulated emission depletion microscopy using phase retrieval," Optics letters **37**, 1805–1807 (2012).

[170] B. Sun, P. S. Salter, and M. J. Booth, "Effects of aberrations in spatiotemporal focusing of ultrashort laser pulses," J. Opt. Soc. Am. A **31**, 765 (2014).

[171] P. S. Salter, Z. Iqbal, and M. J. Booth, "Analysis of the Three-Dimensional Focal Positioning Capability of Adaptive Optic Elements," International Journal of Optomechatronics **7**, 37–41 (2013).

[172] R. S. Balmer, J. R. Brandon, S. L. Clewes, H. K. Dhillon, J. M. Dodson, I. Friel, P. N. Inglis, T. D. Madgwick, M. L. Markham, T. P. Mollart, N. Perkins, G. A. Scarsbrook, D. J. Twitchen, A. J. Whitehead, J. J. Wilman, and S. M. Woollard, "Chemical vapour deposition synthetic diamond: materials, technology and applications," J. Phys. Condens. Matter **21**, 364221 (2009).

[173] W. Yang, O. Auciello, J. E. Butler, W. E. I. Cai, J. A. Carlisle, J. E. Gerbi, D. M. Gruen, T. Knickerbocker, T. L. Lasseter, J. N. Russell, L. M. Smith, and R. J. Hamers, "DNA-modified nanocrystalline diamond thin- films as stable, biologically active substrates," Nat. Materials **1**, 253–258 (2002).

[174] F. Picollo, S. Gosso, E. Vittone, A. Pasquarelli, E. Carbone, P. Olivero, and V. Carabelli, "A new diamond biosensor with integrated graphitic microchannels for detecting quantal exocytic events from chromaffin cells," Adv. Mater. **25**, 4696–700 (2013).

[175] D. D. Awschalom, R. Epstein, and R. Hanson, "The diamond age of spintronics," Sci. Am. **297**, 84–91 (2007).

[176] M. C. Granger, M. Witek, J. Xu, J. Wang, M. Hupert, A. Hanks, M. D. Koppang, J. E. Butler, G. Lucazeau, M. Mermoux, J. W. Strojek, and G. M. Swain, "Standard Electrochemical Behavior of High-Quality, Boron-Doped Polycrystalline Diamond Thin-Film Electrodes," Anal. Chem. **72**, 3793–3804 (2000).

[177] M. Nesladek, D. Tromson, C. Mer, P. Bergonzo, P. Hubik, and J. J. Mares, "Superconductive B-doped nanocrystalline diamond thin films: Electrical transport and Raman spectra," Appl. Phys. Lett. **88**, 232111 (2006).

[178] B. Caylar, M. Pomorski, and P. Bergonzo, "Laser-processed three dimensional graphitic electrodes for diamond radiation detectors," Appl. Phys. Lett. **103**, 043504 (2013).

[179] T. Kononenko, V. Ralchenko, A. Bolshakov, V. Konov, P. Allegrini, M. Pacilli, G. Conte, and E. Spiriti, "All-carbon detector with buried graphite pillars in CVD diamond," Appl. Phys. A **114**, 297–300 (2013).

[180] M. Pacilli, P. Allegrini, G. Conte, E. Spiriti, V. G. Ralchenko, M. S. Komlenok, A. P. Bolshakov, A. A. Khomic, and V. I. Konov, "Diamond-graphite pixel array for particles detection," J. Instrum. **8**, C10013–C10013 (2013).

[181] S. Lagomarsino, M. Bellini, C. Corsi, S. Fanetti, F. Gorelli, I. Liontos, G. Parrini, M. Santoro, and S. Sciortino, "Electrical and Raman-imaging characterization of laser-made electrodes for 3D diamond detectors," Diam. Relat. Mater. **43**, 23–28 (2014).

[182] Y. G. Chen, M. Hasegawa, H. Okushi, S. Koizumi, H. Yoshida, T. Sakai, and N. Kobayashi, "Electrical properties of graphite/homoepitaxial diamond contact," Diam. Relat. Mater. **11**, 451–457 (2002).

[183] S. Prawer, A. D. Devir, L. S. Balfour, and R. Kalish, "Infrared emission from selected areas in ion-beam-irradiated diamond." Appl. Opt. **34**, 636–40 (1995).

[184] A. V. Karabutov, V. G. Ralchenko, I. I. Vlasov, R. A. Khmelnitsky, M. A. Negodaev, V. P. Varnin, and I. G. Teremetskaya, "Surface engineering of diamond tips for improved field electron emission," Diam. Relat. Mater. **10**, 2178–2183 (2001).

[185] T. I. Galkina, A. Y. Klokov, A. I. Sharkov, R. A. Khmelnitski, A. A. Gippius, V. A. Dravin, V. G. Ralchenko, and A. V. Savelev, "Bolometric detector embedded in a polycrystalline diamond grown by chemical vapor deposition," Phys. Solid State **49**, 654–659 (2007).

[186] V. S. Vavilov, V. V. Krasnopevtsev, Y. V. Miljutin, A. E. Gorodetsky, and A. P. Zakharov, "On structural transitions in ion-implanted diamond," Radiat. Eff. **22**, 141–143 (1974).

[187] P. Olivero, S. Rubanov, P. Reichart, B. C. Gibson, S. T. Huntington, J. Rabeau, A. D. Greentree, J. Salzman, D. Moore, D. N. Jamieson, and S. Prawer, "Ion-Beam-Assisted Lift-Off Technique for Three-Dimensional Micromachining of Freestanding Single-Crystal Diamond," Advanced Materials **17**, 2427–2430 (2005).

[188] B. A. Fairchild, P. Olivero, S. Rubanov, A. D. Greentree, F. Waldermann, R. A. Taylor, I. Walmsley, J. M. Smith, S. T. Huntington, B. C. Gibson, D. N. Jamieson, and S. Prawer, "Fabrication of Ultrathin Single-Crystal Diamond Membranes," Advanced Materials **20**, 4793–4798 (2008).

[189] M. Liao, S. Hishita, E. Watanabe, S. Koizumi, and Y. Koide, "Suspended single-crystal diamond nanowires for high-performance nanoelectromechanical switches," Adv. Mater. **22**, 5393–7 (2010).

[190] F. Picollo, D. Gatto Monticone, P. Olivero, B. A. Fairchild, S. Rubanov, S. Prawer, and E. Vittone, "Fabrication and electrical characterization of three-dimensional graphitic microchannels in single crystal diamond," New J. Phys. **14**, 053011 (2012).

[191] A. Reznik, V. Richter, and R. Kalish, "Kinetics of the conversion of broken diamond (sp3) bonds to graphitic (sp2) bonds," Phys. Rev. B **56**, 7930–7934 (1997).

[192] M. L. Tseng, P. C. Wu, S. Sun, C. M. Chang, W. T. Chen, C. H. Chu, P. L. Chen, L. Zhou, D. W. Huang, T. J. Yen, and D. P. Tsai, "Fabrication of multilayer metamaterials by femtosecond laser-induced forward-transfer technique," Laser Photonics Rev. **6**, 702–707 (2012).

[193] M. Huang and Z. Xu, "Spontaneous scaling down of femtosecond laser-induced apertures towards the 10-nanometer level: the excitation of quasistatic surface plasmons," Laser Photonics Rev. **8**, 633–652 (2014).

[194] J. Li, J. Mu, B. Wang, W. Ding, J. Liu, H. Guo, W. Li, C. Gu, and Z.-Y. Li, "Direct laser writing of symmetry-broken spiral tapers for polarization-insensitive three-dimensional plasmonic focusing," Laser Photonics Rev. **8**, 602–609 (2014).

[195] D.-X. Liu, Y.-L. Sun, W.-F. Dong, R.-Z. Yang, Q.-D. Chen, and H.-B. Sun, "Dynamic laser prototyping for biomimetic nanofabrication," Laser Photonics Rev. **7** (2014).

[196] D. Wu, S.-Z. Wu, J. Xu, L.-G. Niu, K. Midorikawa, and K. Sugioka, "Hybrid femtosecond laser microfabrication to achieve true 3D glass/polymer composite biochips with multiscale features and high performance: the concept of ship-in-a-bottle biochip," Laser Photonics Rev. **8**, 458–467 (2014).

[197] T. V. Kononenko, M. S. Komlenok, V. P. Pashinin, S. M. Pimenov, V. I. Konov, M. Neff, V. Romano, and W. Lüthy, "Femtosecond laser microstructuring in the bulk of diamond," Diam. Relat. Mater. **18**, 196–199 (2009).

[198] T. V. Kononenko, V. I. Konov, S. M. Pimenov, N. M. Rossukanyi, A. I. Rukovishnikov, and V. Romano, "Three-dimensional laser writing in diamond bulk," Diam. Relat. Mater. **20**, 264–268 (2011).

[199] V. N. Strekalov, V. I. Konov, V. V. Kononenko, and S. M. Pimenov, "Early stages of laser graphitization of diamond," Appl. Phys. A **76**, 603–607 (2003).

[200] T. V. Kononenko, M. Meier, M. S. Komlenok, S. M. Pimenov, V. Romano, V. P. Pashinin, and V. I. Konov, "Microstructuring of diamond bulk by IR femtosecond laser pulses," Appl. Phys. A **90**, 645–651 (2007).

[201] M. Neff, T. V. Kononenko, S. M. Pimenov, V. Romano, W. Lüthy, and V. I. Konov, "Femtosecond laser writing of buried graphitic structures in bulk diamond," Appl. Phys. A **97**, 543–547 (2009).

[202] S. M. Pimenov, I. I. Vlasov, A. A. Khomich, B. Neuenschwander, M. Muralt, and V. Romano, "Picosecond-laser-induced structural modifications in the bulk of single-crystal diamond," Appl. Phys. A **105**, 673–677 (2011).

[203] T. V. Kononenko, A. A. Khomich, and V. I. Konov, "Peculiarities of laser-induced material transformation inside diamond bulk," Diam. Relat. Mater. **37**, 50–54 (2013).

[204] P. S. Salter and M. J. Booth, "Ultrafast laser processing of diamond," SPIE MOEMS-MEMS **10100**, 89740T (2014).

[205] D. S. Knight and W. B. White, "Characterization of diamond films by Raman spectroscopy," Journal of Materials Research **4**, 385–393 (1989).

[206] R. D. Simmonds, P. S. Salter, A. Jesacher, and M. J. Booth, "Aberration correction in laser micro-fabrication," Opt. Express **19**, 24122–24128 (2011).

[207] J. D. Cutnell and K. W. Johnson, *Resistivity of Various Materials in Physics* (Wiley, New York, 2004).

[208] R. Kalish, A. Reznik, K. W. Nugent, and S. Prawer, "The nature of damage in ion-implanted and annealed diamond," Nucl. Instrum. Meth. B **148**, 626–633 (1999).

[209] S. Kawata, H. B. Sun, T. Tanaka, and K. Takada, "Finer features for functional microdevices." Nature **412**, 697–8 (2001).

[210] G. D. Marshall, A. Jesacher, A. Thayil, M. J. Withford, and M. Booth, "Three-dimensional imaging of direct-written photonic structures," Opt. Lett. **36**, 695–697 (2011).

[211] M. W. Doherty, N. B. Manson, P. Delaney, F. Jelezko, J. Wrachtrup, and L. C. Hollenberg, "The nitrogen-vacancy colour centre in diamond," Phys. Rep. **528**, 1–45 (2013).

[212] F. Jelezko and J. Wrachtrup, "Single defect centres in diamond: A review," Phys. Status Solidi A **203**, 3207–3225 (2006).

[213] S. A. O. Russell, S. Sharabi, A. Tallaire, and D. A. J. Moran, "Hydrogen-Terminated Diamond Field-Effect Transistors With Cutoff Frequency of 53 GHz," IEEE Electr. Device L. **33**, 1471–1473 (2012).

[214] S. D. Janssens, S. Drijkoningen, and K. Haenen, "Ultra-thin nanocrystalline diamond membranes as pressure sensors for harsh environments," Appl. Phys. Lett. **104**, 073107 (2014).

[215] W. Yang, P. G. Kazansky, Y. Shimotsuma, M. Sakakura, K. Miura, and K. Hirao, "Ultrashort-pulse laser calligraphy," Appl. Phys. Lett. **93**, 171109 (2008).

[216] W. Yang, P. G. Kazansky, and Y. P. Svirko, "Non-reciprocal ultrafast laser writing," Nature Photonics **2**, 99–104 (2008).

[217] T. Hahn and A. Looijenga-Vos, *International Tables for Crystallography* (International Union of Crystallography, 1999).

[218] K. Bayat, J. Choy, M. Farrokh Baroughi, S. Meesala, and M. Loncar, "Efficient, uniform, and large area microwave magnetic coupling to NV centers in diamond using double split-ring resonators," Nano Letters **14**, 1208–1213 (2014).

[219] G. de Lange, T. van der Sar, M. Blok, Z.-H. Wang, V. Dobrovitski, and R. Hanson, "Controlling the quantum dynamics of a mesoscopic spin bath in diamond," Scientific Reports **2**, 1–5 (2012).

[220] B. Sun, P. S. Salter, and M. J. Booth, "High conductivity micro-wires in diamond following arbitrary paths," Applied Physics Letters **105**, 231105 (2014).

[221] S. A. Mansour, E. Shalaan, and M. H. I. E. Eraki, "Dielectric Dispersion and AC Conductivity of Acrylonitrile Butadiene Rubber-Poly (vinyl chloride)/ Graphite Composite," Journal of Applied Polymer Science (2011).

[222] B. Ramanujam, R. Y. Mahale, and S. Radhakrishnan, "Polyethersulfone-expanded graphite nanocomposites: Charge transport and impedance characteristics," Composites Science and Technology **70**, 2111–2116 (2010).

[223] N. D. Lai, D. Zheng, F. Jelezko, F. Treussart, and J. F. Roch, "Influence of a static magnetic field on the photoluminescence of an ensemble of nitrogen-vacancy color centers in a diamond single-crystal," Applied Physics Letters **95**, 2009–2011 (2009).

[224] P. L. Stanwix, L. M. Pham, J. R. Maze, D. Le Sage, T. K. Yeung, P. Cappellaro, P. R. Hemmer, a. Yacoby, M. D. Lukin, and R. L. Walsworth, "Coherence of nitrogen-vacancy electronic spin ensembles in diamond," Physical Review B - Condensed Matter and Materials Physics **82**, 7–10 (2010).

[225] J. M. Le Floch, R. Bara, J. G. Hartnett, M. E. Tobar, D. Mouneyrac, D. Passerieux, D. Cros, J. Krupka, P. Goy, and S. Caroopen, "Electromagnetic properties of polycrystalline diamond from 35 K to room temperature and microwave to terahertz frequencies," Journal of Applied Physics **109**, 1–7 (2011).

[226] K. L. Moazed, J. R. Zeidler, and M. J. Taylor, "A thermally activated solid state reaction process for fabricating ohmic contacts to semiconducting diamond," Journal of Applied Physics **68**, 2246–2254 (1990).

[227] S. I. Parker, C. J. Kenney, and J. Segal, "3D - A proposed new architecture for solid-state radiation detectors," Nuclear Instruments and Methods in Physics Research, Section A: Accelerators, Spectrometers, Detectors and Associated Equipment **395**, 328–343 (1997).

[228] W. De Boer, J. Bol, A. Furgeri, S. Müller, C. Sander, E. Berdermann, M. Pomorski, and M. Huhtinen, "Radiation hardness of diamond and silicon sensors compared," Physica Status Solidi (A) Applications and Materials Science **204**, 3004–3010 (2007).

[229] M. Bruzzi, H. F. W. Sadrozinski, and A. Seiden, "Comparing radiation tolerant materials and devices for ultra rad-hard tracking detectors," Nuclear Instruments and Methods in Physics Research, Section A: Accelerators, Spectrometers, Detectors and Associated Equipment **579**, 754–761 (2007).

[230] H. Spieler, *Introduction to radiation detectors and electronics* (UC Berkeley, 1998).

[231] R. An, J. D. Uram, E. C. Yusko, K. Ke, M. Mayer, and A. J. Hunt, "Ultrafast laser fabrication of submicrometer pores in borosilicate glass," Opt Lett **33**, 1153–1155 (2008).

[232] J. H. Choi, H. Lee, H. K. Jin, J.-s. Bae, and G. M. Kim, "Micropatterning of neural stem cells and Purkinje neurons using a polydimethylsiloxane (PDMS) stencil," Lab on a Chip **12**, 5045 (2012).

[233] A. C. Saito, T. S. Matsui, T. Ohishi, M. Sato, and S. Deguchi, "Contact guidance of smooth muscle cells is associated with tension-mediated adhesion maturation," Experimental Cell Research **327**, 1–11 (2014).

Journal Publications

1. **Bangshan Sun**, Patrick S. Salter, and Martin J. Booth, "Pulse front adaptive optics in two-photon microscopy," ***Opt. Lett.***, vol. 40, no. 21, p. 4999-5002, 2015.

2. **Bangshan Sun**, Patrick S. Salter, and Martin J. Booth, "Pulse front adaptive optics: a new method for control of ultrashort laser pulses," ***Opt. Express***, vol. 23, no. 15, p. 19348, 2015.

3. **Bangshan Sun**, Patrick S. Salter, and Martin J. Booth, "Effects of sample dispersion on ultrafast laser focusing," ***J. Opt. Soc. Am. B***, vol. 32, no. 7, p. 1272-1280, 2015.

4. **Bangshan Sun**, Patrick S. Salter, and Martin J. Booth, "High conductivity micro-wires in diamond following arbitrary paths," ***Appl. Phys. Lett.***, vol. 105, p. 231105, 2014.

5. **Bangshan Sun**, Patrick S. Salter, and Martin J. Booth, "Effects of aberrations in spatiotemporal focusing of ultrashort laser pulses," ***J. Opt. Soc. Am. A***, vol. 31, no. 4, p. 765, 2014.

Participated Conferences

Oral presentation

"Three dimensional laser micro-fabrication in diamond", LAMP 2015, The 7th International Congress on Laser Advanced Materials Processing, Kitakyushu, Fukuoka, Japan, May 26-29, 2015.

Conference including:

LPM2015The 16th International Symposium on Laser Precision Microfabrication

HPL2015The 7th International Symposium on High Power Laser Processing.

Won conference prize: "Outstanding Student Paper Award (Oral)"

Post presentation

"Laser fabricated high conductivity micro-wires in diamond", Seventh Photonics day, University of Oxford, Oxford, UK, Apr. 20, 2015.

Won conference prize: "Outstanding Student Post Award"

Oral presentation

"Wave and pulse front distortions in laser fabrication", Photon14 (Optics and Photonics 2014), Imperial College London, London, UK, Sept. 1-4, 2014.

Oral presentation

"Wave front distortions in focusing of ultrashort pulses for laser machining", LPM 2014, The 15th International Symposium on Laser Precision Microfabrication, Vilnius, Lithuania, June 17-20, 2014.